Doctoral Thesis

Investigation on Energy Harvesting System in Polymer Solar Cells

Taehyo Kim

Department of Energy Engineering

(Energy Engineering)

Graduate School of UNIST

2018

Investigation on Energy Harvesting System in Polymer Solar Cells

Taehyo Kim

Department of Energy Engineering

(Energy Engineering)

Graduate School of UNIST

Investigation on Energy Harvesting System in Polymer Solar Cells

A thesis/dissertation
submitted to the Graduate School of UNIST
in partial fulfillment of the
requirements for the degree of
Doctor of Philosophy

Taehyo Kim

12/14/2017 of submission

Approved by

Advisor
Jin Young Kim

Investigation on Energy Harvesting System in Polymer Solar Cells

Taehyo Kim

This certifies that the thesis of Taehyo Kim is approved.

12/14/2017 of submission

signature

Advisor: Jin Young Kim

signature

Hyunhyub Ko: Thesis Committee Member #1

signature

Myoung Hoon Song: Thesis Committee Member #2

signature

Tae-Hyuk Kwon: Thesis Committee Member #3

signature

Han Young Woo: Thesis Committee Member #4

Abstract

Polymer solar cells (PSCs) have made remarkable progress and attracted great attention as the promising clean renewable energy sources due to their many advantages including flexibility, light weight, and low fabrication cost. Among various strategies, development of highly transparent conducting electrode such as silver nanowire (AgNW) by alignment process for flexible, hybridized surface plasmon effect using plasmonic electrode consisting of align AgNW and Ag@SiO_2 NPs and the development of Ternary polymer solar cell can improve device performance by improving photon harvesting of active layers through complementary absorption of each components as well as limitation of binary PSCs.

Here, I present the promising alternative TCE materials instead of ITO using align AgNW electrode by capillary printing technique for high performance polymer solar cell and polymer light emitting diodes (PLEDs). The aligned AgNW electrode exhibited using a capillary printing technique is simple and easy for device fabrication and showed superior electrical and optical properties. The aligned AgNW electrode contributes to improvement in light absorption and emission in the active layer by enhanced transmittance and scattering effect, resulting in an improved device performance compared to nanowire electrode with other techniques. Furthermore, I report nanoparticle (NP) enhanced plasmonic AgNW electrode consisting of align AgNW and Ag@SiO_2 NPs. This plasmonic electrode enables substantially enhanced light absorption efficiency due to strong hybridized plasmon coupling effect between localized surface plasmons (LSPs) and surface propagating plasmons (SPPs), which leads to the improvement of device performance of OPVs.

I also report on various morphology engineering strategies of active layer introducing processing additives and designing planar polymer with better chain packing to facilitate charge carrier transport for device application.

Finally, I report highly efficient ternary PSC using two acceptors with $PC_{71}BM$ and ITIC mixture with a promising large band gap conjugated polymer. This ternary PSCs results in improved device efficiency by improving photon harvesting of active layers through complementary absorption of each materials and manipulating morphology enhanced efficient charge transfer and transport pathways.

This brilliant and promising strategies using align metal nanowire electrode, plasmonic NW-NP electrode and ternary blend bulk-heterojunction system may be of great utility in the development and mass production of next-generation photovoltaic devices.

Keywords: Polymer solar cells, Transparent conducting oxide, Silver nanowire, Surface plasmon, metal nanoparticles, Ternary blend polymer solar cell, Conjugated polymer

Table of Contents

List of Figures

Figure 2.3 Quantitative FFT analyses of the degree of alignment of capillary-printed AgNW networks. (a) Optical micrographs of aligned AgNW networks fabricated using different coating speeds (0.5-10 mm s^{-1}) and solution concentrations (0.1-0.5 wt.%) on PLL-coated substrates. FFT images in the insets of the optical micrographs indicate unidirectional structures with anisotropic features. The scale bar is 20 μm. FWHM fitting data, calculated from the radial summation of pixel intensity in the FFT images, indicates the degree of alignment for printed AgNW networks fabricated with (b) different solution concentrations and (c) different coating speeds.

Figure 2.4 Dark-field optical micrographs of AgNW networks fabricated with a concentration of 0.1 wt.% by capillary printing using (a,b) nano-patterned, (c,d) micro-patterned and (e) flat PDMS stamps, respectively. The printing conditions include a speed of 1.5 mm/s and a pressure of 1.57 kPa. Alignment using nano-patterned PDMS stamps provides aligned AgNW networks 400 nm width 10 μm width 20 μm width c Micro-patterned PDMS d Micro-patterned PDMS e Flat PDMS 150 nm width a Nano-patterned PDMS b Nano-patterned PDMS 7 with a characteristic line-shaped FFT pattern, in contrast to the blurred circular FFT pattern produced from networks using a flat PDMS stamp. All scale bars are 40 μm.

Figure 2.5 Effect of the angle of the triangular PDMS stamp on the NW alignment process. Photographic images of AgNW arrays prepared using triangular PDMS stamps with angles of (a) 5°, (b) 10°, (c) 20°, and (d) 30°. (e-h) Close-up images of the meniscuses formed using triangular PDMS stamps with different angles (5°-30°). (i-l) Dark-field images of aligned AgNW arrays coated using triangular PDMS stamps with different angles on glass treated by O2 plasma. The scale bar is 40 μm.

Figure 2.6 (a) Schematic illustration showing the measurement of contact pressure between the nano-patterned PDMS stamp and the substrate. (b) Dark-field optical micrographs of aligned AgNW networks fabricated with a concentration of 0.5 wt.% using different contact pressures (0-3.14 kPa). Line-shaped FFT patterns in the insets demonstrate that the alignment degree is increased with increasing contact pressure. The scale bar is 40 μm.

Figure 2.7 Dark-field optical micrographs of aligned AgNWs deposited on substrates chemically modified by (a) hexamethyldisilazane (HDMS), (b) O2 plasma treatment, (c) (3- Aminopropyl)triethoxysilane (APTES), (d) poly-L-lysine (PLL), and (e) 3-(2- Aminoethylamino)propyltrimethoxysilane (AAPTS). The scale bar is 40 μm. (f) The surface density of aligned AgNWs deposited on differently modified substrates.

Figure 2.8 (a) Photographs of glass, PET, and PDMS substrates deposited with aligned AgNW arrays. (b)

Dark-field optical micrographs of highly aligned AgNW arrays using a concentration of 0.05 wt.% measured at three points on the glass substrate with a size of 25 mm × 25 mm. All scale bars are 40 μm.

Figure 2.9 (a) Dark-field optical micrographs of random AgNW network fabricated by spincoating. The scale bar is 40 μm. FFT image provided in inset. (b) Radial summation of pixel intensity distribution between 0° and 360° in the FFT analyses of AgNW networks with aligned and random structures. (c) Radial summation of pixel intensity distribution between 0° and 360° in the FFT analyses of different geometric (45°, 60°, 90° crossed) AgNW networks fabricated via multi-step capillary printing alignment process.

Figure 2.10 Radial summation of pixel intensity between 0° and 180° in FFT analyses of darkfield optical micrographs for aligned AgNW networks coated using (a) different solution concentrations (0.1-0.5 wt.%) and (b) different coating speeds (0.5-10.0 mm s^{-1}).

Figure 2.11 Electrical percolation behaviors of AgNW networks with different geometries. (a) Comparison of Rs in aligned and random AgNW networks as a function of surface area density. Power-law fits of Rs for (b) aligned and (c) random AgNWs as a function of (S - Sc), where Sc (%) is the critical surface area density for the onset of conductivity

Figure 2.12 Comparison of optical and electrical performances of AgNWs with aligned and randomly oriented networks. (a) SEM images of aligned AgNW and random AgNW networks show good agreement with corresponding geometric structures. Schematics provide a basis for the understanding of the electrical percolation behavior of the networks. All scale bars are 2μm. (b) Sheet resistance (R_s) for AgNW networks with aligned and randomly oriented geometries as a function of NW linear density. (c) Optical transmittance T (solid lines) and haze factor (dashed lines) over the visible spectrum for aligned (blue) and random (red) AgNWs with similar R_s values. The substrate was used as a reference. (d) Change in the R_s of aligned AgNW networks as a function of the alignment degree, wherein FWHM values are calculated from the radial summation of the pixel intensity in FFT patterns. Comparison of (e) the R_s-T performance and (f) FoM values of different AgNW electrodes.

Figure 2.13 (a) Change in NW linear density and (b) T over the visible light range (400-800 nm wavelength) for aligned AgNW networks fabricated with different coating speeds. (c) The comparison of NW density of our work with the NW densities of other assembly techniques estimated from the reported results.

Figure 2.14 Sheet resistances of aligned AgNW networks for different measurement directions as a function

of FWHM values. Aligned AgNW networks with various alignment degrees were fabricated with solution concentrations of 0.05-0.5 wt.%, coating speed of 1.5 mm/sec, and coating pressure of 1.57 kPa.

Figure 2.15 Mechanical properties of aligned AgNW films on PET substrates. (a) Variations in resistance of aligned AgNW film as a function of bending radius. (b) Resistance change over the course of 1000 bending cycles at the bending radius of 1.25 mm. Resistance was measured after the films were released and had resumed the lengths measured prior to bending.

Figure 2.16 Device structure and characteristics of PLEDs using aligned AgNW electrodes. (a) Schematic PLED structure. (b) Schematic energy level diagrams under the flat-band condition for PLEDs with AgNW electrodes. (c) Current density, (d) luminance, (e) luminous efficiency, and (f) power efficiency with changes in the applied voltage for PLEDs with ITO, random, and aligned AgNW electrodes.

Figure 2.17 AFM images of (a) aligned AgNW networks and (b) random AgNW networks. The surface roughness of aligned AgNWs films is lower than that of random AgNWs films. The scale bars are 2 μm. Optical images for the surface of PEDOT:PSS coated onto (c) aligned and (d) random AgNW films. The scale bars are 100 μm. The surface of random AgNWs films shows the protrusion of NWs through the PEDOT:PSS layer. The scale bars of the magnifications are 20 μm.

Figure 2.18 Transmittance spectra of ITO, random AgNW, and aligned AgNW films on glass substrates.

Figure 2.19 Device structure and characteristics of PSCs using aligned AgNW electrodes. (a) Schematic PSC structure. (b) Schematic energy level diagrams under the flat-band condition. (c) *J-V* characteristics under AM 1.5 illumination at 100 mW cm^{-2} and (d) IPCE of PSCs with ITO, random, and aligned AgNW electrodes.

Figure 2.20 Light-emitting characteristics. Variations in (a) current density, (b) luminance, (c) EL efficiency, and (d) power efficiency with applied voltage using ITO-coated and random or aligned AgNW-based electrodes on flexible substrates.

Figure 2.21 *J-V* characteristics under AM 1.5 illumination at 100 mW cm-2 with ITO and aligned AgNWs for flexible PSCs.

NW length (bottom). (d,e) Raman analysis of a NP-NW system with different polarization angles of incident light. (d) SEM image of a single AgNW decorated with an AgNP for Raman analysis. The arrows indicate incident light with perpendicular (purple) and parallel (red) polarization along the NW direction, respectively. The scale bar is 100nm. (e) Raman spectra of poly-L-lysine (PLL) adsorbed on NP-NW junction by using incident laser with 532 nm wavelength, polarized perpendicular (purple) and parallel (red) along the NW direction. (f) Raman spectra of PLL adsorbed onto NW and NP-NW junction networks. (g-i) Surface-enhanced Raman spectroscopy (SERS) images. Raman mapping images of PLL adsorbed on AgNW, Ag@SiO_2NPs-AgNWs and Ag@SiO_2NPs on glass substrates.

Figure 3.9 E-field distribution for single AgNW and AgNW decorated with Ag@SiO2NP when the incident light at 416 nm, polarized in parallel direction to NW.

Figure 3.10 (a-c) SEM images for three different structures of (a) AgNW, (b) AgNW-Ag@SiO_2NPs, and (c) Ag@SiO_2NPs. All scale bars indicate 1 μm.

Figure 3.11 Photoluminescence behavior of fluorescent SY films on NP-enhanced plasmonic AgNW electrodes. Confocal images of (a) an aligned AgNW network and (b) an aligned AgNW network decorated by Ag@SiO_2NPs coated by SY. The scale bars indicate 5 μm. (c) Confocal image with high resolution of a single AgNW decorated by Ag@SiO_2NP, coated by SY where significant enhancement of fluorescence emission is observed at the NW-NP junction. The scale bar is 4 μm. (d) Steady-state photoluminescence spectra of the SY film with aligned an aligned AgNW network and an aligned AgNW network decorated by Ag@SiO_2NPs.

Figure 3.12 Device structure and characteristics of OLEDs using NP-enhanced plasmonic AgNW electrodes. (a) Schematic device structure of OLEDs with NP-enhanced plasmonic AgNW electrodes. (b) Schematic energy level diagram under the flat-band condition. (c) Current density, (d) luminance, (e) luminous efficiency and (f) power efficiency versus applied voltage for OLEDs with ITO, aligned AgNW, and NP-enhanced plasmonic AgNW electrodes.

Figure 3.13 Device structure and characteristics of OSCs using NP-enhanced plasmonic AgNW electrodes. (a) Schematic device structure of OSCs with NP-enhanced plasmonic AgNW electrodes. (b) Schematic energy level diagram under the flat-band condition. (c) *J-V* characteristics of under AM 1.5G illumination at 100mW cm^{-2}. (d) IPCE spectra of OSCs using ITO, aligned AgNW and NP-enhanced plasmonic AgNW electrodes.

Figure 7.8 Photocurrent measurement as a function of effective voltage for (a) **PCTTPD**:$PC_{71}BM$, (b) **PCTTTPD**:$PC_{71}BM$ and (c) **PCBTTPD**:$PC_{71}BM$.

List of Tables

Chapter 1. Introduction

1.1 History of Organic Solar Cells (OSCs)

Becquerel who created and analyzed the first solar cell began the discovery of photovoltaic effect in 1839.[1] He explained a production of electrical current when two same electrodes immersed in weak conducting solution are exposed to solar radiation. At first, Smith and Adams made reported on photoconductivity by using selenium in 1873 and 1876, respectively.[2] Pochettino and Volmer reported the first organic compound such as anthracene and studied photoconductivity in 1906 and 1913, respectively.[3] In the 1950s and 1960s the potential use of organic materials as photo-sensitizers for imaging system was recognized by many researchers. The growing scientific interest and attention the toward commercial potentials led to active research toward photoconductivity and related field. In the early 1960s it was discovered that many common dyes had semiconducting properties.

After the oil crisis in the early 1970s, many researchers insisted the necessity of alternative sources of energy, leading to development of photovoltaic cell. In the 1980s, the industry attempted to begin to nature due to costs grew and manufacturing facilities for producing photovoltaic modules from silicon-based p-n junction solar cells were built in many countries. Therefore, low cost photovoltaic cells were needed to use extensively, and organic materials are also applied to the photovoltaic cell.

Tang *et al*. reported organic solar cells using two organic materials such as copper phthalocyanine (CuPc) and perylene tetracarboxylic derivatives with an efficiency of 0.95% in 1986.[4] Sariciftci *et al*. had discovered efficient photoinduced electron transfer from excited conjugated polymers to the fullerene composite such as C_{60} molecule in 1992.[5] This discovery made a new era in development of organic solar cells via the polymer-fullerene composite. Furthermore, Yu *et al.* introduced bulk heterojunction structure to improve the efficiency of organic solar cells.[6] He achieved breakthrough in organic solar cell technology. Recently, power conversion efficiencies of organic solar cells have improved up to 12% by using new synthesized materials, device architectures, various technologies.

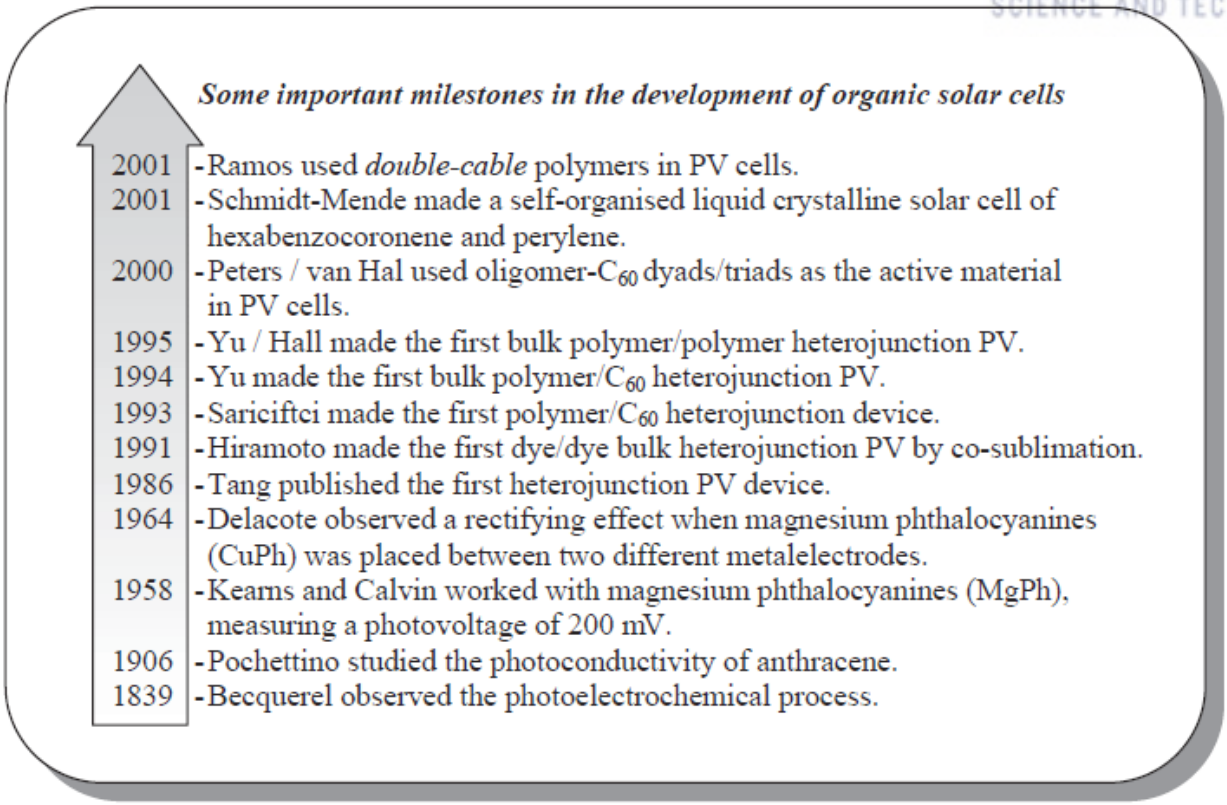

Figure 1.1 The development history of organic solar cells

1.2 Physics of OSCs

1.2.1 Principle of OSCs

The Solar cell is the device that can convert to the electricity from sunlight. Under illumination state, active layer absorbed photon into the device and then electron-hole pairs are generated as excitons. The generated excitons need to diffuse at a donor–acceptor (DA) interface to dissociate into free charges. After that, electrons and holes need to transfer to electrodes through their corresponding percolation pathway.[7] The operating principles of organic solar cell can be schematically shown by following steps. (**Figure 1.2**): i) light absorption (η_A), ii) exciton diffusion (η_{ED}), iii) exciton dissociation and charge transport (η_{CT}), vi) charge collection (η_{CC}). The photovoltaic power conversion efficiency (η) is determined by result of each process.

External quantum efficiency (EQE) of a device was also determined by these four processes that closely involved a solar cell performance. EQE is defined as a percentage of the number of charge carriers collected at the electrode under short-circuit condition to the number of photons incident on the device.[8]

EQE can be expressed as the product of the above steps.

$$EQE = \eta_A \times \eta_{ED} \times \eta_{CT} \times \eta_{CC}$$

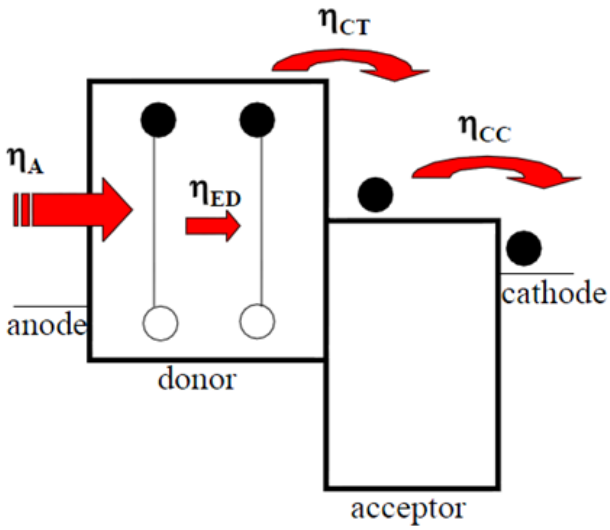

Figure 1.2 Key processes to generate electricity from sun-light in organic solar cells.

Light absorption (η_A)

The absorption spectral band, optical absorption coefficient, and thickness of a photoactive layer, as well as internal reflection determined photon absorption. Most of semiconducting polymers as donor materials have a bandgap larger than 2.0 eV, indicating limits light absorption range less than 650 nm. Thus, only a small portion of sunlight can be absorbed in polymer solar cells. Usually, most of organic solar cell devices were observed thickness of an active layer with 100 nm to avoid exciton and charge transport loss. To well balance sufficient light absorption and efficient charge transport, both a wide absorption spectral band and a high absorption coefficient become important for absorbing enough sunlight. The absorption coefficients of conjugated polymers were reported to be much higher than that of silicon so that a thin layer (e.g., 100 nm) of polymer is enough to absorb light sufficiently.

Exciton diffusion (η_{ED})

The efficiency of exciton diffusion at a DA interface is related to its exciton diffusion length (L_D) and distance (L_i) between photoexciton location and DA interface which serves as a dissociation center.[9] The L_D is equal to $(D\tau)^{1/2}$, where D is diffusion coefficient and τ is exciton lifetime.[10] Excitons can diffuse to a DA interface with $L_i \leq L_D$, otherwise they may recombine with a reduced η_{ED}. Typically, exciton diffusion length is in the range of 4~20 nm for conjugated polymers.[11-13]

Exciton dissociation and charge transport (η_{CT})

The efficiency of exciton dissociation into free holes and electrons relies on DA LUMO energy offsets and internal electric field at a DA heterojunction.[8] From current understanding, the minimum energy required to dissociate an exciton in a conjugated polymer is what is needed to overcome the exciton binding energy.[14] This energy can be provided by the offset between the LUMO energy levels of the donor and the acceptor.

The η_{CT} is charge transport efficiency. The holes are transported in a conjugated polymer, while the electrons are transported in an inorganic semiconductor. Both the donor and acceptor materials are required to form highly efficient percolation networks spanning the entire active layer to provide efficient charge transport.[15] The polymers need to have a higher degree of planarity for efficient backbone stacking for a high hole mobility. Through the treatments such as thermal and solvent annealing, the polymers should also be able to self-assemble into a more organized structure.

Collection of charge-carriers (η_{CC})

It is the fraction of the charges transported from the active layer to the electrodes with respect to the total free charges that are supposed to transport to the electrodes. The η_{CC} depends on the energy levels of the active layer, the electrodes and the interface between them.[8]

1.2.2 Characterization of OSCs

Solar cell efficiency can be calculated from its current density-voltage (*J-V*) characteristic curves. From such curves, open circuit voltage (V_{oc}), short-circuit current density (J_{sc}) and fill factor (*FF*) can be obtained. Then energy conversion efficiency can be determined by equation 1.1

$$\eta = \frac{J_{sc}\, V_{oc}\, FF}{P_s} \times 100 \quad (1.1)$$

Where P_S is the incident light power density. A standard test condition for solar cells is Air Mass 1.5 global (AM 1.5 G) with an incident power density of 100 mW cm^{-2} at a temperature of 25° C, as shown in **Figure 1.3**. Equivalent circuit of a solar cell is shown as Figure 1.2. A series resistance (R_S) originates from contact and bulk semiconductor, and a shunt resistance (R_{sh}) comes from poor diode contact. The *J-V* characteristics can be described as equation 1.2,[16]

$$J = J_0 \left\{ \exp\left[\frac{q(V - JR_S A)}{nKT} \right] - 1 \right\} + \frac{V - JR_S A}{R_{sh} A} - J_{ph} \quad (1.2)$$

Where k is Boltzmann's constant, T is temperature, q is elementary charge, A is device area, n is ideality factor of the diode, J_0 is reverse saturation current density, J_{ph} is photocurrent, R_S is series resistance and R_{sh} is shunt resistance. Each parameters such as n, J_0, R_S, and R_{sh} strongly affected the *J-V* curves and photovoltaic parameters including V_{OC} and *FF*.

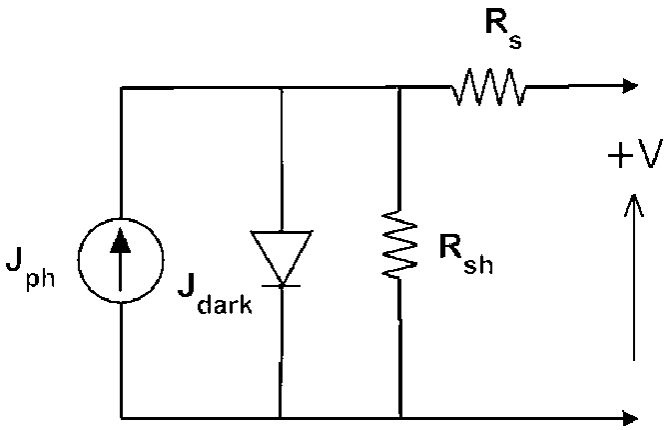

Figure 1.3 Equivalent circuit of a solar cell.

Figure 1.3 shows typical dark and illuminated current density-voltage (*J-V*) curves, in which three distinctive regions can be seen.[17] The first (I) is the linear region in negative potentials and low positive potentials, in which the current density is dominated by the shunt resistance (R_{sh}). The second (II) is the region at mediate positive regions where the curve shows an exponential behavior and the current density is related to the diode. The third (III) is another linear region in high positive potentials where the current density is related to the series resistance (R_S).[17]

The ideality factor (n) is a figure which shows how closely a diode behaves like an ideal diode and it is typically deviated from the ideal by recombination in the junction. In polymer-fullerene solar cells that can be pictured as an ''extended pn junction'', recombination can happen at the DA interface (junction) when the separated electrons and holes meet,[18] causing n to deviate from 1. Thus, the ideality factor (n) can be regarded as an indicator of DA morphology, phase separation and their interfacial area. Waldauf *et al.*

reported that bulk heterojunction solar cells with their active layers made from the same production batch have comparable diode idealities, indicated by similar slopes in the exponential regime of their *J-V* curves. It was also found that different solvents led to different morphologies in organic solar cells, resulting in different idealities.[19]

The reverse saturation current density (J_0) is also an important parameter affecting the *J-V* curves in the exponential regimes and thus cell performance. The J_0 is an indicator of how many charges can overcome the energetic barrier in the reverse direction. These charges are regarded as minority charges at the donor/acceptor interface. In a typical pn junction, J_0 can be described as equation 1.3

$$J_0 = J_{\mathrm{i}} \exp\left[\frac{-\mathrm{q}\phi}{\mathrm{nKT}}\right] \quad (1.3)$$

Where J_{i} depends on material purity and f is energetic barrier voltage. ϕ was found to be in good agreement with energy difference of the acceptor's LUMO and the donor's HOMO. The J_0 value increases with increasing temperature (T), but decreases as the material quality (purity) and energetic barrier improve.

The series resistance (R_S) is another parameter that affects the *J-V* characteristics and solar cell performance. The R_S results from limited conductivity of organic layer, contact resistance between organic layer and its corresponding electrodes, and connecting resistance between the electrodes and external circuit. The R_S can reduce the *FF* and it can also reduce the J_{SC} if it is too high. Generally, the R_S has no impact on open circuit voltage (V_{OC}) since the entire current flows through the diode at the V_{OC} condition, but no current flows though the R_S. However, at the points close to the V_{OC}, the R_S greatly affects the *J-V* curves, providing a simplified method to estimate the R_S by measuring the slope of the *J-V* curves in the regime close to the V_{OC}. The R_S should be minimized to reduce the energy loss, especially in large area solar cells.[20]

The shunt resistance (R_{sh}) is also a parameter affecting the *J-V* characteristics and solar cell performance. The R_{sh} may be related to the device structure and film morphology. For example, R_{sh} can be lowered by the leakage current through the pinholes and recombination of charge carriers in the devices.[21] The morphology and thickness can be processed with care to reduce the pinholes and recombination in the devices so that the R_{sh} can be increased. The R_{sh} needs to be maximized to reduce the power loss caused by the current that by passes the solar cell junction and load through an alternate current path from the low R_{sh}. A small R_{sh} lowers the current flowing through the diode (junction) and thus reduces the V_{OC}. A simplified way to approximately calculate the R_{sh} is to measure the slope of the *J-V* curves in the regime close to the J_{SC}.

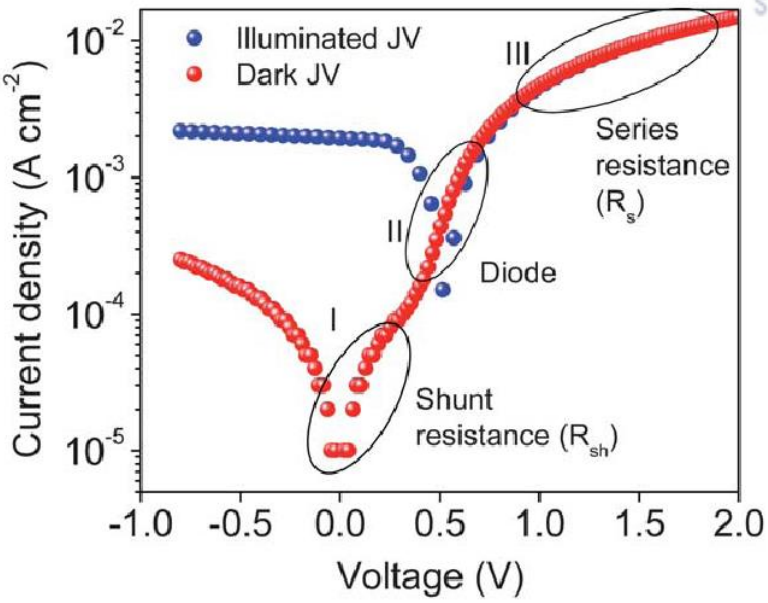

Figure 1.4 Current density-voltage (*J-V*) characteristics of solar cell.

The above discussed n, J_0, R_s and R_{sh} can strongly affect the photovoltaic parameters including V_{OC}, *FF*, J_{SC} and cell efficiency (η). V_{OC} is defined as the voltage across the cell under illumination with a zero current at which the dark current and short circuit photocurrent was exactly cancelled out. By solving the current density verse voltage equation (equation 1.3) at J=0 and V= V_{OC} can be derived as equation 1.4

$$V_{oc} = \frac{nKT}{q} \ln\left(\frac{J_{ph}}{J_0} + 1 - \frac{V_{oc}}{J_0 R_{sh}}\right) \quad (1.4)$$

Figure 1.5 shows the dependence of V_{OC} on n and J_0, calculated using equation 1.5 that is derived from equation 1.4 by assuming an infinitely large R_{sh}.

$$V_{oc} = \frac{nKT}{q} \ln\left(\frac{J_{ph}}{J_0} + 1\right) \quad (1.5)$$

When the R_{sh} is not large enough, it can also affect the V_{OC} of organic solar cells.

The *FF* is greatly affected by the R_S and R_{sh}. The relationship has been reported previously. High FF can be achieved with low R_S and high R_{sh} (ideally R_S = 0, R_{sh} = ∞). Therefore, the R_S needs to be minimized and the R_{sh} should be maximized to ensure a high *FF*. The dependence of *FF* on R_S and R_{sh} can be approximated as equation 1.6

$$FF(R_s, R_{sh}) = FF(0, \infty)[\left(1 - \frac{J_{sc} R_s}{V_{oc}}\right) - (\frac{V_{oc}}{J_{sc} R_{sh}})] \quad (1.6)$$

Another useful measurement is the incident photon-to-current conversion efficiency (IPCE), which is also called EQE, for monochromatic radiation. The IPCE value is the ratio of the observed photocurrent divided by the incident photon flux, uncorrected for reflective losses during optical excitation through the conducting glass electrode. The IPCE is a percentage of incident photons converted to electrons and predominantly coincident with the absorbance spectrum of the solar cells.

$$\mathrm{IPCE} = \frac{\text{number of electrons through the external circuit}}{\text{number of photons incident}} = \frac{[1240\ (\text{eV nm})][\text{photocurrent density}(\mu\text{A cm}^{-2})]}{[\text{wavelength (nm)}][\text{irradiation}(\text{mW cm}^{-2})]} \quad (1.7)$$

Solar irradiance varies with wavelength and roughly traces out a curve in the visible and infrared regions. Additional changes in intensity occur because of different pathways by which the sun's rays traverse through the earth's atmosphere. The property of light illuminated on a solar cell is expressed by Air Mass which is a measure of how absorption in the atmosphere affects the spectral content and intensity of the solar radiation reaching the earth's surface.

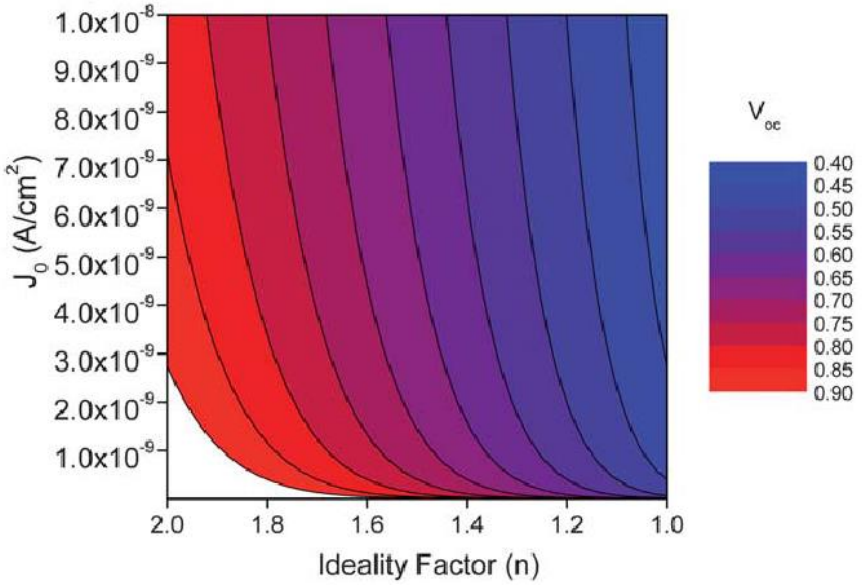

Figure 1.5 Dependence of V_{OC} on ideality factor and reverse saturation current density.

1.3 Development of Polymer Solar Cells (PSCs)

The PSCs have great potential to achieve low-cost solar energy harvesting due to their advantages such as solution processable, various materials and manufacturing techniques. The PSCs can be applied to many applications such as flexible solar modules and semitransparent solar cells in windows, even used to building applications and photon recycling in liquid-crystal displays. Various approaches, such as a novel TCE materials using AgNW electrode by alignment process, hybridized surface plasmon effect using plasmonic electrode consisting of align AgNW and Ag@SiO_2 NPs electrode, ternary PSC using two acceptors with $PC_{71}BM$ and ITIC mixture with a promising conjugated donor polymer and processing additives for morphology engineering have led to the dramatic improvement of device performance more than 10%.

1.3.1 Surface plasmon effect

Plasmonic metal nanostructures such as nanoparticles (NPs), nanorods (NRs), and nanowires (NWs) have been introduced as an efficient way to improve device efficiency via scattering or trapping of light.[22-24] Surface plasmons (SP) are the resonant oscillation of free electrons at the dielectric interface in a metal by light. Induced excitation by electric field at the specific incident wavelength lead to strong light scattering and significant enhancement of the local electromagnetic field. Surface plasmon are demonstrated different plasmon mode, classified into light scattering and light concentration using localized surface plasmons (LSPs) excited in metal nanostructure or light trapping using surface plasmon polaritons (SPPs) propagating at metal-dielectric interface.[25-28] SP can be demonstrated as the resonant photon-induced collective oscillation of valence electrons, established when the frequency of photons matches the natural frequency of surface electrons oscillating against the restoring force of positive nuclei. The resonant photon wavelength is different for different metals. For example, gold, silver, and copper nanostructures exhibit resonant behavior when interacting with ultraviolet (UV) and visible (vis) photons. Because a large fraction of the abundant solar flux consists of UV-vis photons, these noble metals are of particular interest. The resonant wavelength and SPR intensity depend not only on the nature of the metal, but also on the size and shape of metallic nanostructures.[21, 29-32] By manipulating the composition, shape and size of plasmonic nanoparticles, it is possible to design nanostructures that interact with the entire solar spectrum and beyond (**Figure 1.6**).[33, 34]

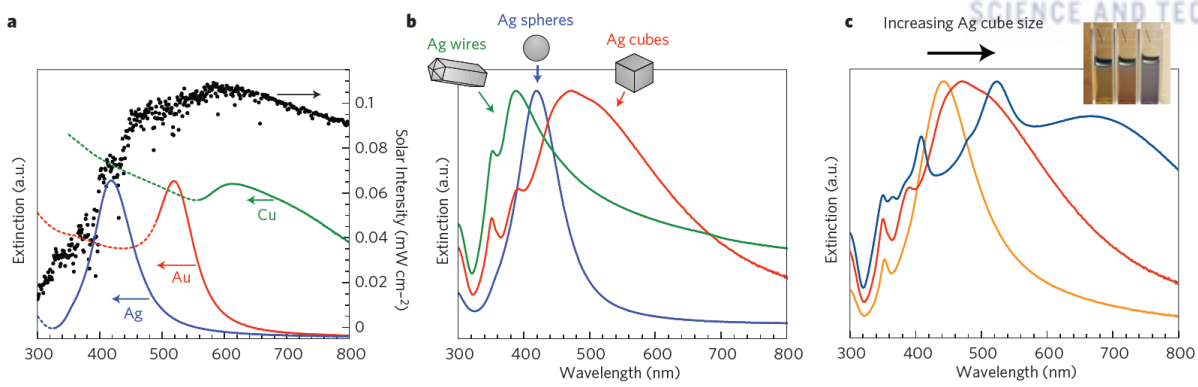

Figure 1.6 Normalized extinction spectra of a) different metal NPs, b) NPs with different shape, and c) Ag nanocubes with different size.

Plasmonic structures can offer at least three ways of reducing the physical thickness of the photovoltaic absorber layers while keeping their optical thickness constant.[28] First, metallic nanoparticles can be used as subwavelength scattering elements to couple and trap freely propagating plane waves from the Sun into an absorbing semiconductor thin film, by folding the light into a thin absorber layer (**Figure 1.7a**). Second, metallic nanoparticles can be used as subwavelength antennas in which the plasmonic near-field is coupled to the semiconductor, increasing its effective absorption cross-section (**Figure 1.7b**). Third, a corrugated metallic film on the back surface of a thin photovoltaic absorber layer can couple sunlight into SPP modes supported at the metal/semiconductor interface as well as guided modes in the semiconductor slab, whereupon the light is converted to photocarriers in the semiconductor (**Figure 1.7c**).

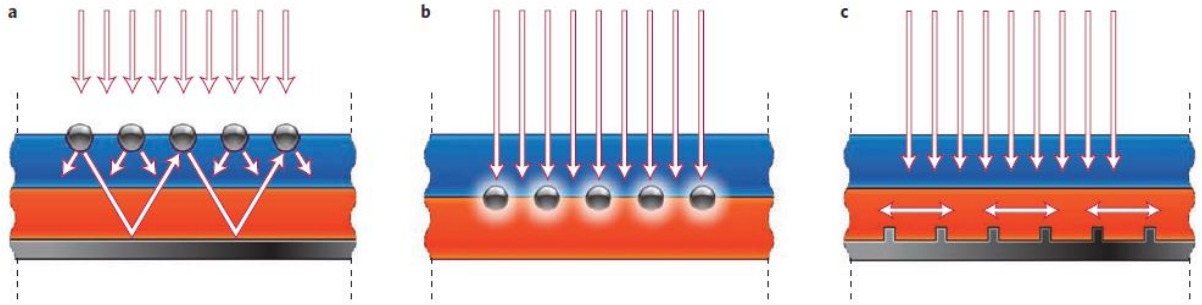

Figure 1.7 a) Light trapping by scattering from metal nanoparticles at the surface of the solar cell. Light is preferentially scattered and trapped into the semiconductor thin film by multiple and high-angle scattering, causing an increase in the effective optical path length in the cell. b) Light trapping by the excitation of localized surface plasmons in metal nanoparticles embedded in the semiconductor. The excited particles near-field causes the creation of electron–hole pairs in the semiconductor. c) Light trapping by the excitation of surface plasmon polaritons at the metal/semiconductor interface.

Metal Nanowire electrode

Investigations on nanoscale structures such as nanowire have appeared around the middle of 1990s.[35-37] The novel ideas of nanostructures forming functional conductive contacts in electronic devices have emerged around 2002.[38-40] Also the nature of conductance on nanoscale structures have been investigated since that time more detail.[41-43] The most of scientific attention was placed on silver, because it is the best conducting metal available and also exhibits chemical stability. Other metals like Copper, Gold or Platinum have been investigated as possible basis for percolation type electrodes as well, either due to higher availability (therefore lower price) or yet higher chemical stability for specialized devices. [42, 44-47] Statistically the distribution for each metal within scientific publications are > 90 % for silver based Ag NWs, copper based 5 % of publications[48, 49] and the rest for other metals and material combinations. Special attempts are reported to incorporate the nanowire design on TCOs or a carbon- based materials.[50, 51] Due to the relevance of nanowires, they will be introduced in greater detail than other potential alternative compounds, for application as preferably solution processable and transparent electrode layers in thin film electronic device.

Typically, the dimensions of nanowire are found to be less than 100㎛ in length and 1㎛ in diameter. Aspect ratio is defined by the ratio between length and diameter. From simulations and experiments it is known that nanowires with a higher aspect ratio (very long, very thin) have superior electrode performance compared to wires that rather fall into the shape category of tubes or rods.[52-54] Investigations on the concept of percolation were already executed in the 1970's.[53, 54] However, it was not until 2004 that this concept was applied to predict the conductive behavior of nanowire based electrode systems in technological relevant applications.[55]

For low aspect ratio wires the morphology is a limiting factor, as shorter wires lack of interconnections with other nanowires and nanowires with a larger diameter introduce extreme electrode surface roughness, that prevents successful application as bottom electrode in thin film devices. Most of nanowires can be used as transparent and high performance electrode layers presented in scientific literature are typically found to be about 10-50㎛ in length and have a diameter of about 50-200 nm. Due to their dimensions in the nanometer regime, NWs introduce Quantum Physics into the design of electrode layers. Nanowires exhibit so called plasmonic effects originating from the high electron density of metals and are well studied in the case of Ag NWs. The most striking observation for transparent Ag NW films is the ratio between light transmission through a nanowire electrode in comparison to how much of the illuminated area is covered by nanowires (geometric aperture). Typically observed transmissive performance is higher than expected according to classical optical physics. Coupled with the high intrinsic conductivity of silver, Ag NWs appear to be an ideal candidate for highly conductive and transparent electrodes processed from solution. This

enables a large variety of possible applications.

Incorporation of Metallic Nanostructures with the Electrodes

Metal films are inherently required as electrodes in almost all optoelectronic devices due to their excellent electrical conductivity. For instance, in light-emitting diodes and lasers they are used for charge-carrier injection. High work function metal films (e.g., Ag, Al, Au) are widely used as electrodes for organic optoelectronic devices that do not require transparent anodes and/or cathodes, whereas indium tin oxide (ITO) patterned glasses are typically used as transparent electrodes. In a recent independent study, the substrate cost (including the ITO coated glasses) was identified as the most important factor in the manufacturing cost of OSCs.[56] In addition to the intrinsic cost limitation associated with the ITO layers, there are several other important drawbacks that in some cases limit the performance of OSCs. For instance, ITO cracks easily upon bending and is not compatible with flexible plastic substrates.[57] The optical, electrical, and surface properties of ITO depend strongly on the method of deposition and cleaning.[58-60] In addition, since organic semiconductors are susceptible to damage resulting from localized heating and/or unintentional doping by metal ions leaching from the electrodes, the electrical and topographic inhomogeneity of its surface combined with its chemically ill-defined nature are particularly problematic for OSCs.[61-63] Consequently, a lower cost material that is abundant in nature would be desirable for use as an alternative transparent electrode.[64, 65] Recent studies have explored the dual use of metallic nanostructures as electrodes as well as for light trapping in order to achieve electrical and optical functionalities simultaneously. Nanopatterned metallic films, such as a 30 nm-thick Ag film with 1D nano-slit arrays, were employed as the front electrode of an OSC using CuPc:C_{60} as the active light-harvesting layer.[66] Compared with a device with a flat Ag anode, the PCE was enhanced by a factor of 3.2. However, the enhanced PCE was only 0.2%. Self-assembled nano-sphere lithography was employed to fabricate nanohole arrays on a 12 nm-thick Ag anode of an OSC with a similar CuPc:C_{60} active layer and an enhanced PCE from 0.6% to 1.2% was achieved.[67] Randomly perforated nanoholes on metal films can also function as the front electrode and were incorporated in an OSC structure based on P3HT:PCBM, resulting in enhanced incident photon to current conversion efficiency.[68] By introducing nanoholes (350 nm in diameter) on a 30 nm-thick Ag film, the PCE was enhanced from 1.03% to 1.22% compared to a reference device with a flat Ag electrode. However, the overall performance of this OSC employing the nanopatterned Ag electrode was not as good as the reference device using ITO. Recently, electrodes fabricated from metallic nanowires using low-cost nano-imprint lithography showed promise as an alternative to ITO electrodes. By choosing the proper metal and optimizing the geometric parameters of the nanowire electrode in a P3HT:PCBM device (**Figure 1.8a**), one can achieve a PCE comparable to that of devices using an ITO electrode (< 2%).[69] Even better, the PCE of a CuPc:C_{60} OSC with a metallic nanowire electrode can be

enhanced (< 1.32%) compared to that using an ITO electrode (0.96%) (**Figure 1.8b and c**).[70] However, for 1D patterned metallic nanostructures, the polarization dependence will potentially lead to weak absorption for TE polarized light.[66, 69, 70] For front electrodes with randomly perforated nanoholes, most of the front area of the OSC device is often still covered by the absorbing metal film leading to inefficient collection of the incident light.[67, 68] To address these limitations of front electrodes, a back electrode (i.e. cathode) constructed using Au nanoparticles on flat Al separated by a thin-film of LiF was recently introduced in an OSC based on P3HT:PCBM and led to an increase in PCE from 2.8%-2.9% to < 3.6% in comparison with a reference OSC using a flat LiF/Al cathode.[71] This increase in device performance was attributed to the localized SPP enhancement from the textured Au nanoparticles. In addition, 1D and 2D periodic nanopatterns were also introduced to excite SPP modes in these back electrodes.[72, 73] More recently, a patterned Au anode was introduced in an OSC based on the light-harvesting layer P3HT:PCBM with a flat Al cathode. This omnidirectional perfect absorber OSC structure resulted in a PCE of 4.4%, which is 52% higher than the reference OSC using an ITO anode.[74] To address the relatively high cost of nanofabrication, novel transparent electrodes based on metallic nanowire networks were also realized using bottom-up fabrication (**Figure 1.8d**), and open up new avenues to control light, heat and mass transport at the nanoscale level. This fabrication process could be realized on plastic substrates, and will lead to significant reduction in manufacturing cost.[75]

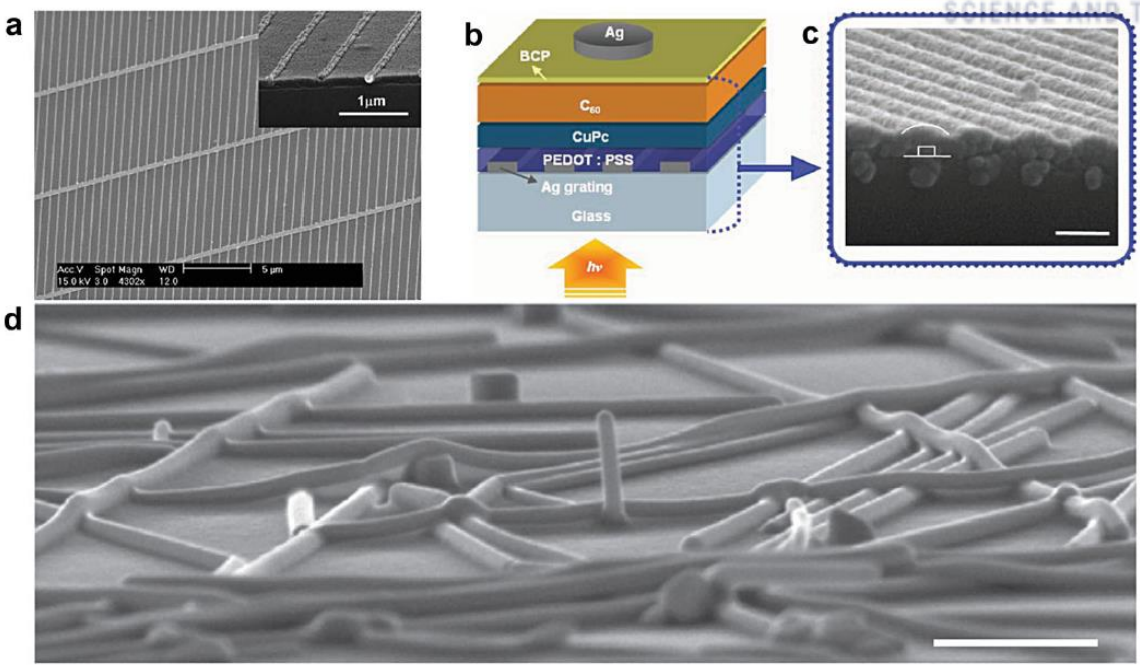

Figure 1.8 Integration/incorporation of metallic nanostructures with the electrodes: a) SEM image of the Cu electrode after transfer to the PEDOT:PSS-coated substrate where the inset shows the cross-section of the transferred metal electrode; b) schematic diagram of the fabricated molecular OSC; c) cross-sectional view of a fabricated device, without the 70 nm thick Ag cathode. The sinusoidal shape of the deposit organic films is due to their conforming to the shape and the height of the Ag nanowire array. The scale bar is 200 nm; d) a tilted SEM image of silver nanowire networks where the scale bar is 500 nm.

Metal nanoparticles

The introduction of metal nanoparticles is an effective strategy for improving the performance of polymer solar cells because of its easy application to device fabrication. Various designs using metal nanoparticles have been extensively explored for inorganic solar cells.[76] In OSCs, metal nanoparticles with different types, concentrations, shapes, sizes, distributions, etc. have been introduced into various layers and at interfaces within the devices.[77, 78]

Metal nanoparticles outside the active layer

Device structure of OSC with metallic nanoparticles outside the active layer(s) is as shown in **Figure 1.9a**. Various method such as vapor phase deposition, pulse-current electrodeposition, and thermal annealing, have been used to deposit metal nanoparticles on ITO or inside a PEDOT:PSS buffer layer.[79-81] Metal nanoparticles synthesized by chemical method were assembled on top of or embedded in a PEDOT:PSS layer (Figure 1.9 b).[82-84] The dependence of the localized surface plasmon resonance (LSPR) on the size and composition of the nanoparticles have been investigated, and there were many reports on

the enhancement in the PCE of OSCs by LSPR of metal nanoparticles. For instance, the PCEs of OSCs based on P3HT:PCBM as the active layer were increased by 20~70% by adding Ag or Au nanoparticles within the PEDOT:PSS buffer layer.[83, 85] As shown in Figure 1.9c, LSPR effect of Au nanoparticles enhanced the photocurrent by increasing light absorption in the active layer. The addition of Au nanoparticles (~15 nm in diameter) into PEDOT:PSS layer led to the enhancement in PCE from 1.99% to 2.36% in OSC based on poly(2-methoxy-5(20-ethylhexyloxy)-1,4-phenylenevinylene (MEH-PPV) as the active layer.[86] In order to enhance the plasmon excitation and far-field scattering, Au nanowire and nanomesh with random distribution were also introduced at the interface between PEDOT:PSS and ITO layers, and improved PCE (Au nanowires: 2.31% → 2.45%, Au mesh: 1.9% → 3.2%).[87] The introduction of a mixture of Ag and Au nanoparticles (40~50 nm in diameter) into PEDOT:PSS layer showed a PCE of 8.67% in OSC based a polythieno[3,4-b]-thiophene/benzodithiophene (PTB7) and $PC_{71}BM$. Cooperative plasmonic effect from dual resonant enhancement of Ag and Au nanoparticles resulted in 20% increase in PCE, and this enhancement was larger than those of devices with only Ag or Au NPs in same buffer layer.[88]

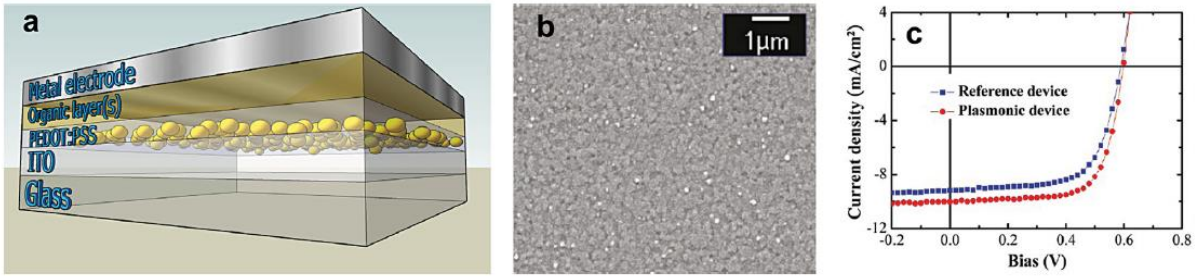

Figure 1.9 Metal nanoparticles outside the active OSC layer: a) Conceptual illustration of a plasmonic-assisted OSC with nanoparticles outside the active light-harvesting layer. b) SEM image of an anodic buffer layer consisting of Au nanoparticles (white dots) embedded in PEDOT:PSS. c) Current density versus bias (*J*-*V*) characteristics of polymer solar cells with (plasmonic device) and without (reference device) Au nanoparticles dispersed in the PEDOT:PSS layer.

Recently, surface modification of metal nanoparticles for manipulating chemical and electrical properties led to the enhancement in PCE and device stability.[89, 90] For example, plasma-polymerized fluorocarbon (CF_x)-modified Ag nanoparticles embedded at the interface between ITO and OSC layers enhanced the PCE of a zinc phthalocyanine (ZnPc): fullerene-based OSCs from 2.7% to 3.5%. This enhancement was attributed to increased light absorption in the active layer due to broadband scattering from the Ag nanoparticles. The CF_x played important role to improve charge collection at the electrode/organic interface due to an increase of 1 eV in the work function of the modified electrode. In addition, metallic nanoparticles or clusters were also applied to enhance the PCE of tandem solar cells. Originally, Forrest's group proposed

that metallic clusters (5 nm-diameter Ag clusters) can be effective recombination centers for electrons and holes at multiple junction interfaces of tandem solar cells.[91] More recently, metallic nanoparticles act as a sub-wavelength scattering element which couples and traps freely propagating plane waves in the absorbing OSC layers.[92] For instance, Au nanoparticles (~72 nm in diameter) were deposited in the interconnecting layer of an inverted tandem polymer solar cell consisting of a cell based on a P3HT:indene-C_{60} bis-adduct ($IC_{60}BA$) and another based on poly[(4,4′-bis(2-ethylhexyl)dithieno[3,2-b:2′,3′-d]silole)-2,6-diyl-alt-(2,1,3-benzothiadiazole)-4,7-diyl] (PSBTBT):$PC_{71}BM$, and resulted in an enhancement of PCE from 5.22% to 6.24%.[93] In addition to light scattering effect, the introduction of the metallic nanoparticles can affect the electrical properties of OSC devices. For instance, PEDOT:PSS layer with Ag nanoparticles on top of the ITO substrate remarkably reduced series resistance, and improved the performance of P3HT:PCBM OSCs.[94] Since the nanoparticles were located relatively far from the active organic layer, the absorption enhancement resulted mainly from light concentration/scattering from the LSPR modes of the nanoparticles rather than any near-field enhanced LSPR modes. In summary, when plasmonic materials including metallic nanoparticles, nanowires and nanomeshes were placed outside the active light-harvesting layer, strong localized plasmon field enhancement and/or increased light scattering enhanced device performances.

1.3.2 Molecular designs

The development of polymer solar cells (PSCs) have always been supported by innovations in electron donors and acceptors. First, the development of materials is a prerequisite to fulfill these requirement in PSCs to improve a power conversion efficiency (PCE). Chemical structures of some representative electron donors and acceptors were shown in **Figure 1.10**. Wudl *et al. synthesized* one of the earliest PSC polymers, poly[2-methoxy-5-(2′-ethylhexyloxy)-*p*-phenylene vinylene] (MEH-PPV).[95] He also invented one of important fullerene derivatives, PCBM, which is widely used as an electron acceptor in the PSC today. In 1995, Yu *et al.* blended MEH-PPV with C_{60} and it is reported as a first bulk heterojunction (BHJ) PSC with a high PCE.[96] From this work, most of researchers have concentrated on polymer materials for use in solar energy conversion. After significant device optimization, researcher achieved PCEs over 3.0% for PPV-based PSCs.[97, 98] However, further enhancement in device efficiency was limited due to low hole mobility and narrow light absorption range, relatively. Soluble polythiophenes, especially poly(3-hexylthiphene) (P3HT),[99] which has broader absorption than MEH-PPV and higher hole mobility,[100] have become a standard conjugated polymer for PSCs in the 2000s. The optimization of active layer morphology has led to PCEs of 4–5%, thus attracting much attention in PSCs.[101, 102]

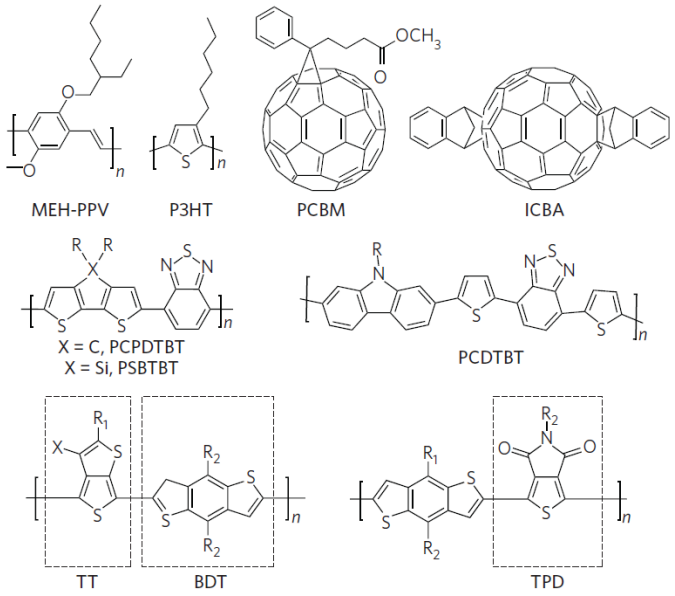

Figure 1.10 Chemical structures of representative electron donors and acceptors used in PSCs

Many researchers have developed quite a various of high-performance polymers in recent years. Among them, low bandgap polymer, poly[2,6-(4,4-bis-(2-ethylhexyl)-4*H*-cyclopenta[2,1-*b*;3,4-*b*']dithiophene)-alt-4,7-(2,1,3-benzothiadiazole)] (PCPDTBT) has broad absorption up to 900 nm. The PSCs based on made from PCPDTBT have showed an initial efficiency of around 3%.[103] However, by incorporating processing additives, the efficiencies around 5.5% were achieved.[104] Poly[*N*-9''-hepta-decanyl-2,7-carbazole-alt-5,5-(4',7'-di-2-thienyl-2',1',3'-benzothiadiazole)] (PCDTBT) reported by Leclerc *et al.* showed a PCE of 3.6%.[105] In 2009, introduction of titanium oxide (TiO_X) layer as an optical spacer improved PCEs up to 6.1% by.[106] Yu *et al.* developed impressive high performance conjugated polymers, which consist of thieno[3,4-*b*]-thiophene (TT) and benzodithiophene (BDT) alternating units.[107-110] The PSCs based on this polymer first reached PCEs of 7–8% among many polymer donor system. Researchers reported the devices with PCEs of more than 7% by using either new materials or novel device optimization techniques.[111-114]

The exploitation of novel materials is important points for improving the device performance. The key issues of polymer design include engineering the bandgap and tuning the energy levels for achieving high J_{SC} and V_{OC}, enhancing planarity of molecular backbone to obtain high charge-carrier mobility, and materials stability.[115, 116] All of these issues are related each other. In the dial case, all factors should be optimized in a conjugated polymer, but it remains a significant challenge. The knowledge on the relationship between polymer design and these parameters has been significantly improved over the past decade. The value of V_{OC} for a PSC can be expressed by following equation $V_{OC} = e^{-1} \times (|E_{HOMO}{}^{donor}| - |$

$E_{LUMO}^{acceptor}| - 0.3$ eV), where e is the elementary charge, E is the energy level and 0.3 eV is an empirical value for efficient charge separation.[117] A donor polymer with a lower HOMO level contribute to higher V_{OC}. P3HT is the most famous donor until now, with a HOMO level of ~4.9 eV,[118] which corresponds to a V_{OC} value of around 0.6 V and serves as a reference for polymer design. Thiophene is an electron-rich part.[119] The HOMO level of the polymer in a PSC can be effectively lowered by inserting groups that are less electron-rich.[120, 121] For example, fluorene and carbazole are commonly used units in wide-bandgap materials because they are less electron-rich than thiophene. By adding these units into a polymer donor, V_{OC} can be significantly increased. Cao *et al.* reported a polymer containing a fluorene unit that achieved $V_{OC} \approx$ 1.0 V.[120] Inganas *et al.* also reported a polymer composed of fluorene and quinoxaline alternating units that reached $V_{OC} \approx$ 1.0 V.[121] Another material is PCDTBT, which incorporates carbazole units in the polymer chain, from which researchers achieved $V_{OC} \approx$ 0.89 V.[105] V_{OC} is also affected by non-radiative recombination between the donor and the acceptor. Eliminating these non-radiative pathways will help to improve V_{OC}. However, there is a significant challenge about the linking polymer design with elimination process.[122]

The J_{SC} is another important parameter that affects the performance of PSCs. The most powerful approach for achieving high J_{SC} is to narrow the bandgap (<1.8 eV) for a broader absorption region of the solar spectrum.[123] The common approaches for achieving this include utilizing donor–acceptor (DA) alternating structure, stabilizing the quinoid structure, controlling the degree of planarity of polymer chain, and increasing the effective conjugation length. The alternating donor–acceptor (DA) structure is the most common approach, in which the push–pull energy between the donor and acceptor units, together with the photoinduced intra-molecular charge transfer, facilitates electron delocalization and the formation of low-bandgap quinoid mesomeric structures over the polymer backbone.[124, 125] According to molecular orbital perturbation theory, electron delocalization contributes to the hybridization of molecular orbitals, leads to electron redistribution throughout the interacting orbitals. This provides two types of new hybridized orbitals (higher HOMO level and a lower LUMO level), resulting in a narrower bandgap. Among many polymers, PCPDTBT is one of the most successful examples of DA alternating structure.[103] The bandgap of PCPDTBT is 1.4 eV (around 900 nm) by combining a dialkyl-cyclopentabithiophene donor unit and benzothiadiazole acceptor unit. This DA structure is not limited to the side chain of polymers. Huang *et al.* reported that DA structure consisting of an acceptor-based side chain and a donor-based main chain also results in a lower bandgap.[126] Another successful strategy of reducing the bandgap is stabilizing the quinoid structure of conjugated units.[123] There are two resonance structures in the ground state of a conjugated structure (aromatic and quinoidal form).[115] The quinoidal form is energetically less stable because of its smaller bandgap. Achieving quinoidal form stable can reduce the bandgap of polymer. Yu *et al.*

demonstrated that stable quinoidal structure can be stabilized by introducing fused thiophene ring into an thieno[3,4-*b*]thiophene (TT) unit.[108, 123] Polymers consisting of TT and BDT alternating units have bandgaps of around 1.6 eV.

Narrowing the bandgap of polymers is insufficient for achieving high J_{SC}. Other parameters, such as charge mobility, intermolecular interaction and molecular stacking, also affect J_{SC}. For example, tuning the chemical structure of polymers provides effective ways to improve hole mobility. Yang *et al.* was developed poly(4,4-dioctyldithieno(3,2-*b*:2',3'-*d*)silole)-2,6-diyl-alt-(2,1,3-benzothiadiazole)-4,7-diyl) (PSBTBT) by replacing the bridging carbon atom with Si atom in PCPDTBT.[127, 128] The PSBTBT polymer has a higher crystallinity than PCPDTBT and thus improved hole mobility, leading to improved J_{SC}. Using high degree of planarity structure can improve charge transport by enhancing molecule stacking.[129, 130]

Although these following strategies significantly improved V_{OC} and J_{SC}, it remains a challenge to improve for improving both values at the same time. Polymer with narrowing the bandgap can improve J_{SC}, whereas V_{OC} may be reduced due to deep HOMO level of polymer. Recently, many research groups reported that fine-tuning of the chemical structure is a powerful approach for improving both V_{OC} and J_{SC} at the same time. For example, both HOMO and LUMO levels were decreased by adding a fluorine atom into the TT unit, whereas enhancing V_{OC} and retaining the bandgap of polymer.[108] Fine-tuning the side-chain structure also showed a similar effect. For example, replacing the electron-rich alkoxy side chain with the less electron-rich alkyl chain caused to decreased HOMO and LUMO levels at the same time.[109]

The final important photovoltaic parameter for high efficiency PSC is the *FF*, which is currently the least understood one among three parameters. The *FF* is the ratio between the maximum obtainable power and the product of J_{SC} and V_{OC}. It is affected by many factors, such as charge-carrier mobility and balance, interfacial recombination, series and shunt resistances, film morphology and miscibility between the donor and acceptor.[131] However, clear understanding about *FF* still remains a challenge in the development of PSCs. To optimize molecular design, we should consider many factors including planarity of polymer chain, intermolecular interactions, molecular stacking and crystallinity, and charge-carrier mobility in structural designs. Tuning side chain in polymer also has remarkable effects on enhancing the *FF*. For example, *N*-alkylthieno[3,4-*c*]pyrrole-4,6-dione (TPD)-based polymers optimize π-stacking, polymer crystallinity and material miscibility by tuning side groups, resulting in increased *FF* from 55% to 68%.[132] It was recently reported that efficiency of 7% was achieved by using TPD–silole copolymer.[113]

Developing novel acceptors is also one of the efficient strategies to improve the PCE.[133-137] For example, C_{70} derivatives exhibited better absorption in UV-visible range than those of C_{60}. Replacing C_{60} derivatives with C_{70} derivatives often improves J_{SC} by increasing absorption in UV-visible region. Moreover, novel fullerene derivatives as the electron acceptor can also enhance V_{OC}. From the energy band diagram in Figure 1.6, V_{OC} is also determined by the LUMO level of acceptors. One of promising electron acceptor is C_{60} with

an indene bisadduct. C_{60} symmetrically adding electron-rich indene units upshifted the LUMO level by 0.17 eV, compared to $PC_{61}BM$, resulting in a 40% improvement in V_{OC} (0.84 V) in the PSCs with P3HT based PSCs. Although the BHJ PSCs based on indene bisadduct and P3HT show superior device performance, it needed to solve compatibility (or miscibility) with other polymers donor remains a challenge.

The fullerene derivatives, such as $PC_{61}BM$ and $PC_{71}BM$, are still the dominant acceptors due to their superior charge transporting properties. Unfortunately, these two acceptors suffer from some intrinsic shortcomings such as limited absorption, difficult functionalization, high production cost and air degradation issues.[138] Therefore, developing novel non-fullerene acceptors that can overcome the abovementioned disadvantages is highly desirable. As a matter of fact, research on non-fullerene acceptors has made considerable progress in the last two years and a highest PCE of around 12% has been achieved.[139] As shown in **Figure 1.11**, we will summarize recent research progress in non-fullerene small molecule acceptors Moreover, the acceptors with excellent photovoltaic performance are highlighted.. Finally, we aim to compare the performance of the as-reported non-fullerene acceptors based on the different types of conjugated polymer donors and try to provide some useful clues for further development in this area.

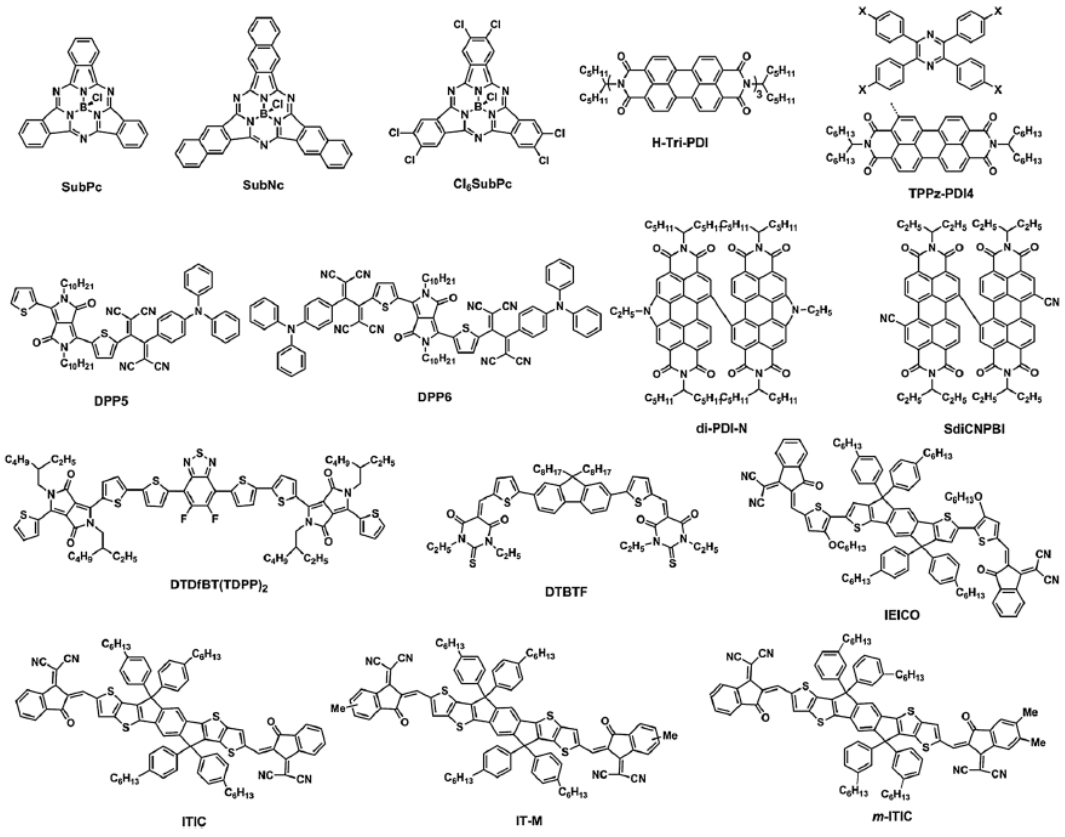

Figure 1.11 Chemical structures of the non-fullerene acceptors using various donor materials.

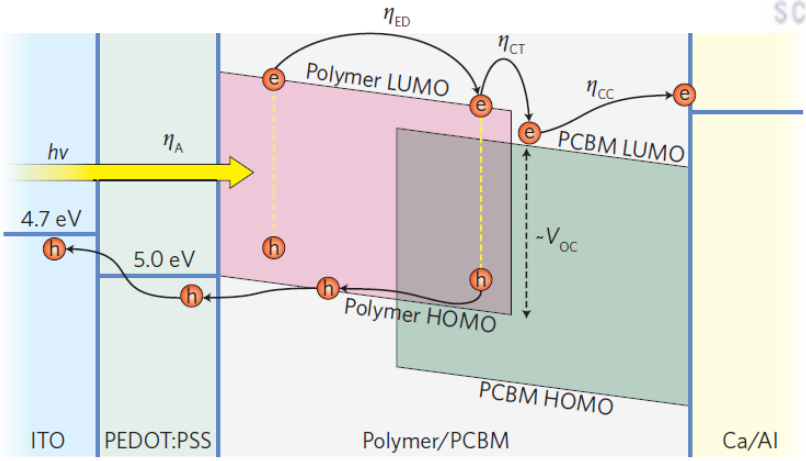

Figure 1.12 The operating mechanism and energy band diagram of PSCs.

1.3.3 Morphology control

Morphology control such as thermal annealing[140] and solvent annealing[141] is critical in bulk-heterojunction PSCs. However, the effects of thermal and solvent annealing were shown to enhance PSC efficiency by a significant amount until 2005.[142] Many approaches are also effective for improving polymer–fullerene morphology, such as solvent selection[143] and solvent mixture[144] techniques, and the use of additives.[145]

Effect of Annealing

A variety of post-treatment methods can improve the optoelectronic properties of the polymer-blend films. Annealing processes in polymer solar cells can be divided into two categories: thermal annealing[146-148] and solvent annealing.[13, 141, 142, 149] Both techniques concentrate on improving the nanoscale lateral phase separation of both the crystalline P3HT aggregates and PCBM domains.

Thermal annealing can be applied either on the final device (post-annealing) or on the polymer film only (pre-annealing). The annealing temperature and time are also the two most critical parameters in this approach. However, the selection of solvent as well as metal electrodes could also affect the ultimate device performance. The device performance of the polythiophene/fullerene-blend solar cell is crucially dependent on the processing condition, which influences the polymer self-organization and the corresponding optical and electrical properties.

The solvent annealing approach can control the polymer nanomorphology through the solvent removal time. Zhao et al. described a solvent-vapor-annealing approach with similar principles.[150] The benefits of "solvent annealing" have been previously reported by Yang Yang group.[13, 141, 142, 149] A systematic study of the spin-coating time reveal the advantage of solvent annealing over thermal annealing by sustaining the

P3HTordered structure upon higher PCBM loadings.[151] The effects of solvent boiling point and film drying time on the polymer crystallinity and absorption were studied by Chu et al. Controlling the solvent evaporation rate improved the molecular ordering of the P3HT chains, as was verified by grazing-incidence x-ray diffraction (GIXRD) results. High-precision synchrotron GIXRD provided clear evidence that the packing of the polymer chain is strongly affected by the solvent-removal rate. Fast solvent removal leads to not only the reduction of P3HT crystallinity, but also increases the interlayer distance of the polymer in the blend film.

Various annealing processes can dramatically improve the crystallinity, resulting in higher hole mobility; thus to date annealing has become the most commonly used method for device-performance improvement.

Effect of Solvents

Solution processing has many advantages among the film fabrication technologies, which usually require complicated instruments as well as costly and time-consuming procedures. Therefore, solution processing has developed into the most-favored methodology for fabricating organic optoelectronic devices. Solution processing also allows the freedom to control phase separation and molecular self-organization during solvent evaporation and/or film treatment. The solvent establishes the film evolution environment, and thus has foreseeable impact on the final film morphology. Selection and combination of solvents have been shown to be critical for the morphology in polymer-blend films, and are well-documented in the literature.[13, 152]

Spin-coating from one solvent solution results in thin films, which possess optoelectronic properties determined by the solution parameters and the spin-coating process, for example concentration, blending ratio, spin speed and time, etc.

Meanwhile, solvent properties, such as boiling point, vapor pressure, solubility, and polarity, also have considerable impact on the final film morphology. The wettability of the organic solvent on the poly(3,4-ethylenedioxythiophene) poly(styrenesulfonate) (PEDOT:PSS) surface is usually sufficiently good and not taken into account as a factor on the film morphology. However, it is worth noting that different solution processes have dissimilar requirements for achieving optimal morphology.[153]

In 2001, Shaheen *et al.* reported the effect of solvent and morphology on device performance for the poly-[2-(3,7-dimethyloctyloxy)-5-methyloxy]-para-phenylene-vinylene (MDMO-PPV):[6,6]-phenyl-C_{61}-butyric acid methyl ester (PCBM) blend system.[143] By replacing toluene with chlorobenzene (CB), the PCE of the device dramatically increased up to 2.5%. A more intimate mixing and stronger interchain interaction accounted for this improvement of device performance. The solubility of the polymer blend is much better in chlorobenzene than in toluene; thus, a much more uniform mixing of the donor and acceptor is expected. This improved intermixing is evidenced by the roughness of the blend film, where the chlorobenzene-based

sample has a much smoother film surface. Liu *et al.* investigated the poly(2-methoxy-5-(20-ethoyl-hexyloxy)-1,4-phenylene vinylene (MEH-PPV):C_{60} blend devices and observed the effect of solvation-induced morphology on device performance.[154] Using nonaromatic solvents, such as tetrahydrofuran (THF) and chloroform, resulted in larger V_{OC} and smaller J_{SC}, because of the fact that MEH-PPV side groups prevented intimate contact and thus efficient charge transfer between the MEH-PPV and C_{60} molecules. Ma *et al.* also observed that P3HT:PCBM polymer films were smoother and more uniform by replacing chloroform with CB.[148] The results of improved morphology, crystallinity, and cathode contact attributed to the high efficiency due to better choice of solvent as well as post-annealing treatment. Because of the better solubility of fullerenes in CB, its use instead of toluene resulted in a finer phase separation, while thermal annealing in both cases led to coarsening of the phases.[155] **Figure 1.13a** and **b** show the scanning electron microscopy (SEM) cross-section views of the MDMO-PPV:PCBM system casted from CB and toluene, respectively. One interesting observation is the 20–40nm thick ‘‘skin’’ layer observed in the toluene-casted film, in which the PCBM nanocrystallites were generally covered by this ‘‘skin’’ layer, identified as polymer nanospheres. However, for most chlorobenzene-cast films, the polymer nanospheres were homogeneously distributed; therefore, only at very-high PCBM loadings can this phenomenon of PCBM clusters surrounded by a ‘‘skin’’ layer be perceived. The CB-cast films have a finer phase separation and higher J_{SC} in comparison to the toluene-cast films. However, the J_{SC} of CB-cast films decreased with heavier PCBM loadings, indicating that an optimal phase-separated domain size is imperative for good device performance. Hoppe *et al.* also reported measured the localized work function using Kelvin probe force microscopy.[151] CB-cast films showed a uniform work function at the surface but an approximately 0.3 eV decrease upon illumination, while the work function of the toluene-cast films was directly topography-related, increasing in the PCBM clusters under illumination. The work function correlates to the Fermi level, that is, electron density. Under illumination, CB-cast films showed an enrichment of electrons at the surface due to charge generation, while the surface of the toluene-cast films was covered by the polymer skin-layer, causing substantial charge recombination, and a lower J_{SC}. The proposed film morphology and respective charge transport for CB- and toluene-cast films are depicted in **Figure 1.13c** and **d**. The solubility of the fullerene phase can remarkably affect the solvent selection. Larger fullerene balls tend to be less soluble, and different solvents have been used for optimal processing conditions. The key point is likely to be the formation of proper nanoscale phase separation.

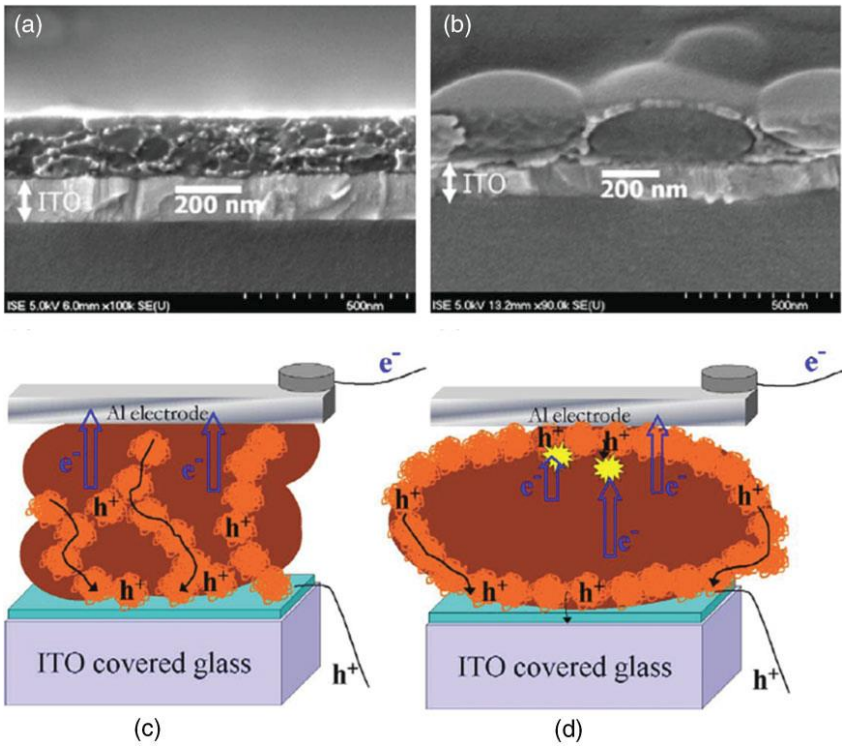

Figure 1.13 SEM cross-section images of MDMO-PPV:PCBM blend films cast on ITO-glass from a) CB and b) toluene solution. The brighter objects in a) are polymer nanospheres, whereas the darker embedments are PCBM clusters. Schematic of film morphology of c) CB- and d) toluene-cast MDMO-PPV: PCBM blend active layers. In c), carriers form percolated pathways to reach their respective electrodes. In d), electrons and holes suffer from recombination due to undesirable phase separation.

Effect of Additives

In general, device performance can be improved though post-treatments such as various annealing processes. However, for some material systems, such as the novel low-band-gap polymer poly[2,6-(4,4-bis-(2-ethylhexyl)-4H-cyclopenta[2,1-b;3,4-b0]-dithiophene)-alt-4,7-(2,1,3-benzothiadiazole)] PCPDTBT), which has a better overlap with the solar spectrum, typical post-treatments are incapable of improving the device characteristics.[156, 157] It has been demonstrated that solvent mixtures have a significant effect on film morphology and device parameter, namely on J_{SC}, V_{OC}, and *FF* in the polyfluorene copolymer/fullerene system.[144] In the poly(2,7-(9,9-dioctyl-fluorene)-alt-5,5-(40,70-di-2-thienyl-20,10,3-benzothiadiazole)):$PC_{61}BM$ blend system, mixing a small volume of CB into chloroform developed a finer and more uniform distribution of domains, which enhanced the J_{SC}. In contrast, adding xylene or toluene into chloroform resulted in larger domain sizes that decreased J_{SC} and caused significant light-intensity-dependent recombination of free charge carriers. Time-resolved spectroscopy on the picosecond scale

revealed that charge mobility was considerably improved by adding CB into chloroform, due to an enhanced free-charge-carrier generation from a finer morphology.

Earlier efforts on the solvent-mixture approach concentrated on two miscible solvents, in which both the polymers and fullerenes have considerable solubility. Advances in cooperative effect of solvent mixtures using solvents with distinct solubilities have been obtained.[145, 158] The incorporation of additives into a host solvent represents progressive method and important trend capable of controlling the BHJ morphology. It also provides a unique viewing angle to study the film-formation dynamics of the spin-coating process. However, it is vital to mention that solvent mixtures caused a more sophisticated circumstance in both the solution and film evolutions, because the solutions became multicomponent (phase) systems. Thus, to maintain simplicity, only two solvents are usually involved in the solution system while studying the fundamental principles and improving the performance. It should also be noted that the solvent-mixture method should not be restricted to only two solvents; ternary- or even quaternary-solvent systems are also realistic approaches.

Recently, the mixture-solvent systems have been widely explored by many research groups, bringing a rather clear understanding of solvent-selection rules for desirable morphology.[145, 158-160] Peet *et al.* reported that by incorporating a few volume percent of alkanedithiols into the PCPDTBT: $PC_{71}BM$ polymer blend solution, the efficiency doubled from 2.8% to 5.5%, with J_{SC} as high as 16.2 $mAcm^{-2}$.[145] The vast improvement was attributed to the enhanced interactions between the polymer chains and/or between the polymer and fullerene phases upon alkanedithiol addition, which was evidenced by the absorption data. A systematic study of alkanedithiol incorporation was carried out by Lee *et al.* to investigate the morphology-controlling mechanism, where the alkanedithiols played the role of ‘‘processing additive’’, without reacting with either the polymer or fullerene components.[161] The alkanedithiol selectively dissolved the fullerene phase, whereas the PCPDTBT was relatively insoluble. The fullerene phase stayed in the solution longer than the polymer because of the higher boiling points of the alkanedithiols (b.p. >160 ℃), providing more freedom to self-align and crystallize. Consequently, the phase-separation morphology can be exploited by various alkanedithiols and by tailoring their relative ratios. In addition, the polymer domains are maintained after removal of the fullerene phase, which allowed the direct observation of the exposed polymer network. **Figure 1.14** shows the atomic force microscopy (AFM) and transmission electron microscopy (TEM) images of the PCPDTBT:$PC_{71}BM$ films with and without 1,8-octanedithiol (OT), as well as the exposed PCPDTBT network after selective dissolution of the $PC_{71}BM$. These images clearly show larger PCPDTBT and $PC_{71}BM$ domains as a result of OT addition, indicating that the improved device performance is related to the better percolating pathways for both carriers from the larger interconnected domains. Carrier-transport analysis also pointed out the enhanced network by the increased electron mobility.[162]

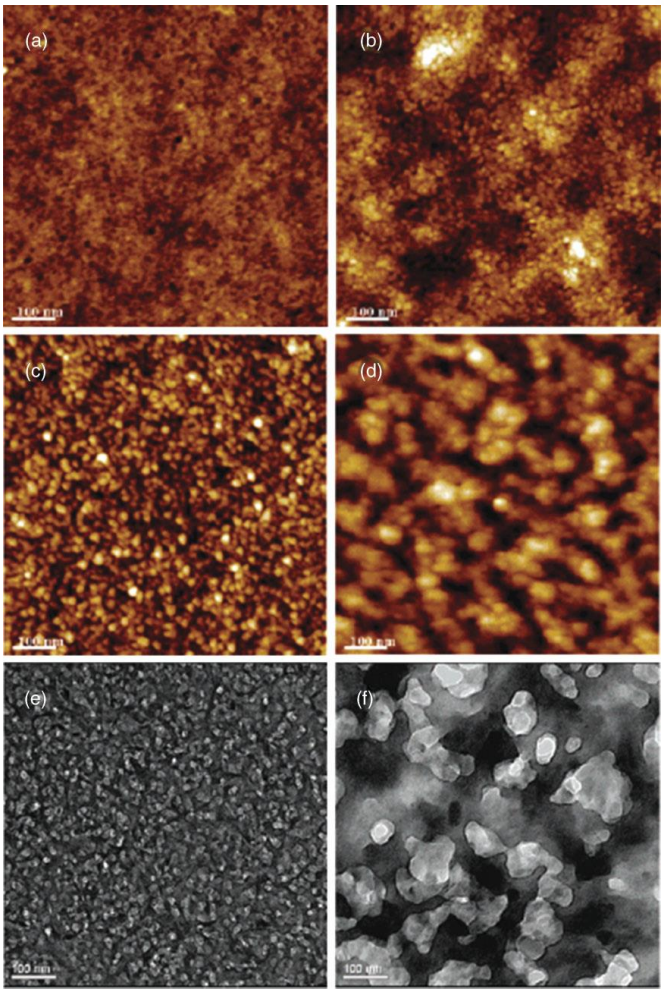

Figure 1.14 AFM and TEM images of PCPCTBT/$PC_{71}BM$ films without and with 1,8-octanedithiol and exposed PCPDTBT networks after removal of $PC_{71}BM$. AFM image of BHJ film a) without and b) with 1,8-octanedithiol. AFM image of exposed polymer networks c) without and d) with 1,8-octanedithiol. TEM image of exposed polymer networks e) without and f) with 1,8-octanedithiol.

Accordingly, two criteria for incorporating alkanedithiols to control the blend-film morphology were proposed: i) selective solubility of the fullerene component and ii) a higher boiling point (lower vapor pressure) than the host solvent. It provided insight into the mechanism of film-morphology evolution regarding a ‘‘bad’’ solvent addition, and indicated a guideline for alternative solvent-additive selection.

In conclusion, the results of various morphology control study, vertical stratification can be attributed to the different solubilities and surface energies of the blend components as well as the dynamics of the spin-coating process. A volatile solvent is likely to form a more homogeneous film, whereas a viscous solvent allows vertical phase separation. Upon vertical phase separation, the low-surface-energy component preferentially segregates at the surface or interface to reduce the overall energy. By controlling the drying rate of film through solvent viscosity and spin-coating condition, as well as surface treatment, a closer to

optimal, both laterally and vertically segregated morphology can be formed. Furthermore, certain "bad" solvents can function as "processing additives" to preform PCBM aggregates, which assist in the self-organization of both components, and thus induce vertical phase separation. If the vertical segregation can be exploited to the desired morphology, with a donor-enriched anode and acceptor enriched cathode, efficient charge dissociation through the interpenetrating network and efficient charge transport into the interconnected pathways are expected to substantially improve the device performance.

1.3.4 Ternary Polymer Solar Cells

Generally, the ternary solar cells composed three components in the active layers: the dominant donor:acceptor (D:A) and the third component. Compared with binary OSCs, ternary systems exhibit several advantages:[163-166] (a) the third component in ternary systems can enhance photon harvesting of active layers through complementary absorption of donor:acceptor. (b) It also provides an enhanced efficient charge transfer and transport pathways, thereby providing a potentially effective approach to obtain high J_{SC} and thus high PCE performance. (c) The morphology of active layers may be improved with the third component to achieve appropriate phase separation by intermolecular interactions. (d) Ternary systems can also maintain simplicity of single active-layer fabrication conditions. (e) The same optimizing strategies of BHJ solar cells, such as adding additives, tuning the energy levels, adjusting the ratio of donors and acceptors, controlling the morphology etc., can be employed to further improve V_{OC} J_{SC}, and *FF* individually or simultaneously, thereby increasing the efficiency.[163, 164] To date, due to new developments in donor:acceptor materials and device fabrication techniques, ternary PSCs have rapidly developed as a new horizon in this field,20,21 and their PCEs have exceeded 10%.[167, 168]

Based on the functionality of the third component, ternary solar cells have been classified into three categories (**Figure 1.15**) the charge-transfer mechanism.

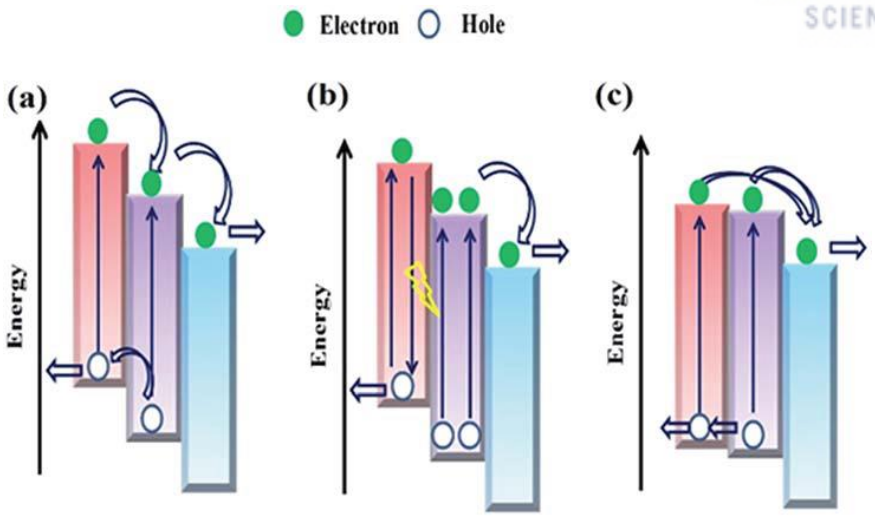

Figure 1.15 Schematic of the mechanism in ternary solar cells: (a) charge transfer mechanism, (b) energy-transfer mechanism and (c) parallel-like or alloy model. The arrows indicate the possible charge transfer and transport pathway.

The cascade-like energy levels or ternary system can facilitate charge separation and charge transfer at the host donor:acceptor interface because of the bridging effect to reduce the energy lose.[169, 170] Therefore, the third component play a role as a charge relay between the D:A materials. (b) The energy-transfer mechanism. Either a Förster resonance energy transfer (FRET) or a Dexter energy transfer occurred between the third component and the host donor:acceptor materials. The emission spectrum of the third component should show substantial overlapping with the absorption spectrum of the other materials. (c) The parallel-like or alloy model. The third component works as an individual hole/electron-transport channel or the third component and the host donor or acceptor materials electronically coupled into a new charge transfer state. Typically, there is no strict limitation to the energy level and bandgap for the third component as long as the driving force between the donor and acceptor is sufficient for exciton dissociation. Photoluminescence (PL) or transient absorption spectroscopy (TAS) measurements are the most popular and convenient tools to study charge transfer and energy transfer as well as the parallel-like model between different materials. Actually, however, it is still common that these mechanisms are involved, namely, different processes occur in the same ternary solar cell. Cyclic voltammetry (CV) measurement is useful to study the shared HOMO[171] or LUMO[172, 173] of the donor alloy or the acceptor alloy. At the same time, using crystalline small molecules to form the donor alloy with conjugated polymers can facilitate face-on orientation crystallization of donor materials which can enhance the hole mobility.[174] Although all three mechanisms are not precisely determined by the energy levels (HOMO and LUMO) and bandgap of the third component compared to the D:A system, the energy levels, as instinct properties of organic semiconductors, always play a significant role in interpreting the functionality of the third component in ternary solar cells.

1.4 Research Overview and Objective

Polymer solar cells (PSCs) is extensively considered as an attractive renewable energy sources due to many advantages including lightweight, low cost eco-friendly, solution processability and mechanical flexibility. Many research group reported superior efficient strategies to achieve high performance PSCs such as improving stability and compatibility, introducing plasmonic nanostructures and interfacial engineering, etc. These excellent strategies can contribute to break up to 10% of power conversion efficiency as promising candidates for commercialization of PSCs. Specifically, among several strategies, maximizing the light absorption in the active layer is important for high performance PSCs whereas minimizing the thickness of active layer films due to low carrier mobility of organic semiconductors caused lower *FF*, and development of highly transparent conducting electrode such as silver nanowire (AgNW) by alignment process for flexible PSCs to overcome disadvantages of ITO electrode for flexible application. Furthermore, the development of Ternary polymer solar cell can improve device performance by improving photon harvesting of active layers through complementary absorption of each components as well as limitation of binary PSCs.

In this thesis, I focused on various engineering strategies employing novel TCE materials, such as AgNW electrode by alignment process, and hybridized surface plasmon effect using plasmonic electrode consisting of align AgNW and Ag@SiO_2 NPs electrode. Especially, this plasmonic electrode led to remarkable improvement in device performance cause by enhanced light absorption and scattering through strong electromagnetic field.

I also focused on various morphology engineering strategies, introducing processing additives with conjugated polymers and enhancing planarity of molecular backbone and development of ternary PSC using two acceptors with $PC_{71}BM$ and ITIC mixture with a promising conjugated donor polymer, resulting in improved device performance by manipulating morphology, showing suitable phase separation, which contributed to the high charge transport and dissociation probability efficiency.

Chapter 2. Capillary Printing of Highly Aligned Silver Nanowire Transparent Electrodes for High-Performance Optoelectronic Device

2.1 Research background

Transparent conductive electrodes (TCEs) are essential components in many optoelectronic devices such as solar cells, touch panels and organic light-emitting diodes (OLEDs).[175-179] While indium tin oxide (ITO) has been widely used in commercial transparent electrodes, the further development and application of ITO has been limited by the cost and inherent brittleness of the material.[177, 178, 180] One promising alternative to ITO as a TCE material includes random networks of Ag nanowires (AgNWs),[181-184] which can provide lower sheet resistance (R_s) and higher optical transmittance (T) than other TCE candidates such as carbon nanotubes (CNTs),[175, 185, 186] graphene[187-191] Cu NWs,[192] and conducting polymer.[193] Moreover, AgNW networks can be readily prepared by low-cost solution-based processes, such as spin coating,[194] drop casting,[195] rod-coating[196, 197] and spray coating.[198-201]

However, for the use of random AgNW networks in high-performance solar cells and OLEDs, the junction resistance between nanowires and the large surface roughness are two critical issues that need to be addressed. Junction resistance prevents NW networks from achieving low R_s, while high density of NWs lower the optical transmittance of the electrodes.[202] The protruding NWs of overlapping random NW network structures can cause electrical short-circuits and leakages in multilayered device configurations.[203, 204] In addition, the optical haze, defined as the ratio of diffusive transmittance to total transmittance, of random NW networks may blur pixels or reduce the resolution in touch-screen and OLED devices.[197, 200, 205]

To overcome the issue of junction resistance between NWs, several approaches including thermal annealing,[195] hybridization with metal oxides and graphenes,[198, 206] mechanical pressing[207] and plasmonic weldings[182] have been introduced. The surface roughness issue has been addressed by the addition of coatings and laminations with polymers,[204, 208] metal oxides,[202] and graphene sheets.[209] However, these additional processes complicate the fabrication process or are incompatible with large-scale solution processing.

To overcome the trade-off between electrical conductivity and optical transmittance in a one-step solution process, conductive percolation networks within NW structures must be precisely controlled.[210-213] The percolation-limited performances of random NW networks in applications as TCEs have been addressed by several approaches.[214-220] One such approach utilizes high-aspect-ratio metallic NWs, generating conductive pathways with low NW densities.[214] Another approach uses lithographic[215-218] or electrospinning techniques[219, 220] to design ordered conductive networks; very low R_s values have been

obtained via the formation of junction-free conductive networks using these methods. However, these fabrication processes are complicated and unsuitable for the cost-effective and scalable production of TCEs.

Here, we introduce a simple and high-throughput fabrication strategy for the assembly of aligned AgNWs using a capillary printing technique for the fabrication of highly conductive and transparent electrodes with low surface roughness. In this approach, AgNW solutions are dragged and deposited by polydimethylsiloxane (PDMS) nanochannels, in which AgNWs are partially aligned prior to unidirectional alignment by meniscus surface tensions. Previously, various techniques including Lagmuir-Blodgett,[221] contact printing,[222] post-alignment shrinkage,[223] nanocombing,[224] nanotrench-assisted capillary force,[225] and fluid flow[226] have been employed for the alignment of semiconducting or metallic NWs. Although significant progress has been made to improve the alignment degree and density of assembled NWs, many of previous techniques require essential necessities such as pre-grown vertical NW arrays, additional transfer process, and substrate pre-patterning, which limit the cost-effective and scalable assembly of high-density NWs with a controllable NW alignment degree. Our capillary printing method can overcome these limitations and has several advantages in the fabrication of TCEs based on AgNW networks. First, the alignment technique provides large areas of highly aligned AgNWs via a one-step solution-based process that is both cost-effective and compatible with rapid roll-to-roll processes. Second, the aligned AgNWs overcome the trade-off between the electrical conductivity and optical transmittance that occurs in random NW networks, because the alignment of the AgNW networks significantly decreases the NW density; the electrical percolation threshold is lower in the aligned networks than in random NW networks. Third, the aligned AgNW networks exhibit lower surface roughness than random networks without the need for additional smoothing processes, thus providing good device compatibility in optoelectronic applications.

2.2 Experimental

Preparation of patterned PDMS stamp

Polydimethylsiloxane (PDMS) base and curing agent (Sylgard 184, Dow-corning) were completely mixed in a 10:1 weight ratio. The air-bubble in PDMS mixture during the mixing process was subsequently removed in a vacuum desiccator for 20 min. For the fabrication of the line patterned PDMS stamp, the PDMS mixture was cast onto a silicon micromold with periodic line pattern with 400 nm line width and 800 nm periodicity. Then, the PDMS mixture were thermally cured at 80°C for 4 hr on a hot-plate.

Preparation of the functionalized substrates

Glass substrates were cleaned with IPA and D.I water by sonication for 10 min. After blown-drying with N_2 gas, the substrate was treated with O_2 plasma for 5 min to increase the wettability of glass substrates. To

further increase the AgNW adhesion on the substrate, poly-l-lysine (PLL) layers with amine functional groups were coated on the substrates by spin-coating the PLL solution (0.1% concentration i[227]n H_2O)) at 4000 rpm for 60 sec.

Alignment of AgNW by capillary printing process

For the formation of triangular-shaped PDMS stamp, nano-patterned PDMS stamp was attached on a trigonal prism-shaped aluminum frame. The aluminum frame was subsequently installed onto the micro-stage, where the PDMS stamp can be freely moved back and forward with a controlled constant speed. When the PDMS stamp was put into contact with the target substrate, the contact pressure was controlled by using an electronic scale supporting the substrate. Next, AgNW dispersion (L= 35 um, D= 30 nm, purchased from Nanopyxis corporation) was dropped on the target substrate, which was subsequently sucked into PDMS line-patterns. Then, the sliding of the PDMS stamp with constant speed produced highly aligned AgNW arrays along the coating direction. Finally, the aligned AgNWs are dried in ambient environment conditions and treated by O_2 plasma for 1 min to remove organic impurities and enhance electrical conductivity.

Characterization

The sheet resistance of aligned AgNW networks was measured by using four-point probe measurement (Kiethley 2400 equipment). The optical transmittance of aligned AgNW networks was measured by UV-visible spectrophotometer (Jasco V-670). The haze factor was calculated using the diffusive and total transmittances over visible light range. To investigate the mechanical robustness of aligned AgNW films, the change in sheet resistance of aligned AgNWs on PET under various bending radius and cycles was measured using a two-probe method, in which copper tapes were attached to each side of aligned AgNWs with silver paste.

2.3 Results and discussion

The alignment of AgNWs by capillary printing was performed by dragging nano-patterned PDMS stamps over AgNW solutions on target substrates under constant velocity and pressure. Figure 1a shows a schematic of the preparation of the aligned AgNW assemblies using this capillary printing technique. In this work, we utilized a nano-patterned PDMS stamp with a line pattern spacing of 400 nm to create the nanochannels inducing the alignment of the AgNWs in the printing direction. The nano-patterned PDMS stamp was attached to a trigonal prismatic frame (**Figure 2.1a** and **Figure 2.2**), that placed the sharp peak of the PDMS stamp in contact with the substrate during the dragging of the AgNW solutions. This facilitated

the uniform formation of air-liquid-solid meniscus lines behind the contact points between the stamp and substrate. The capillary force induced by solvent evaporation further facilitated the unidirectional alignment of the AgNWs. **Figure 2.2b** illustrates the principle of AgNW alignment via capillary forces.

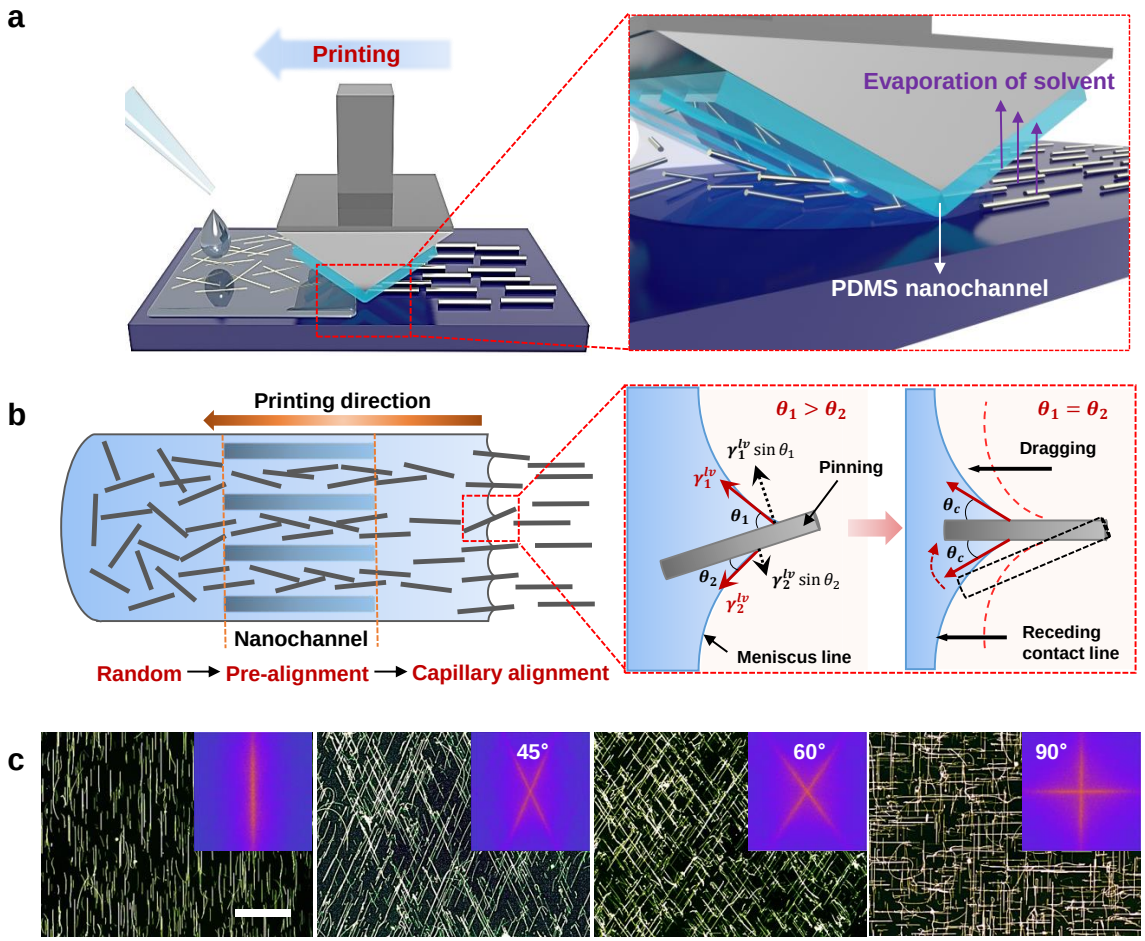

Figure 2.1. Solution-printed highly aligned AgNW arrays. (a) Schematic of the capillary printing process using a nano-patterned PDMS stamp to produce highly aligned AgNW arrays. (b) Schematic showing the alignment process during capillary printing of unidirectional AgNW arrays. The solvent-evaporation-induced capillary force produces highly aligned networks by dragging confined AgNWs at the solid-liquid-vapor contact line. (c) Dark-field optical images of differently oriented AgNW structures fabricated with a solution concentration of 0.05 wt% via one-step (unidirectional) and multi-step (45°, 60°, and 90° crossed) capillary alignments. The scale bar is 40 μm. The fast Fourier transform (FFT) analyses of the images, presented in the insets, show the corresponding geometric structures.

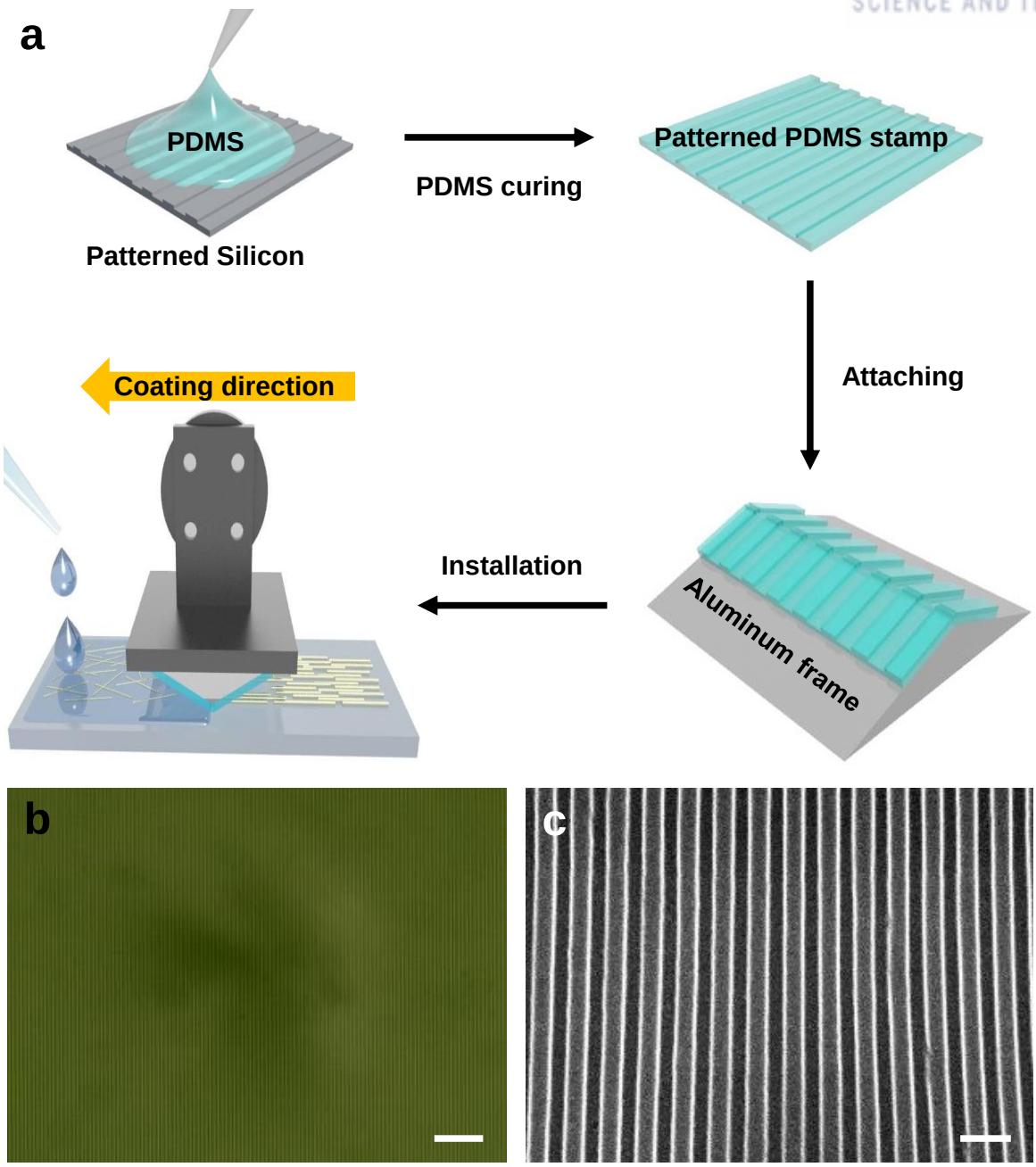

Figure 2.2 (a) Schematic of the procedure for capillary printing using a nano-patterned PDMS stamp for alignment of AgNW array. Optical microscopy (b) and scanning electron microscopy (c) images indicate the nano-patterned PDMS stamp with 400 nm of line width. Scale bars are 10 μm (b) and 1 μm (c).

First, droplets of the AgNW solution are deposited on the target substrate and soaked into the line-patterned PDMS stamp. Next, the dragging of the AgNW solution, confined between the PDMS line-pattern

and the target substrate, induces the partial pre-alignment of AgNWs in the dragging direction. This nanochannel-confined pre-alignment step is followed by the pinning of AgNWs by the evaporating air-liquid-solid meniscus line. The continued evaporation and movement of the meniscus contact line induces the further alignment of AgNWs in the dragging direction by the influence of the meniscus surface tension. In this capillary printing technique, the PDMS nanochannels are crucial in the pre-alignment of AgNWs and the uniform formation of the meniscus line. We observed that the alignment of the AgNWs was not achieved when a flat PDMS stamp without nanochannels was used (**Figure 2.3**).

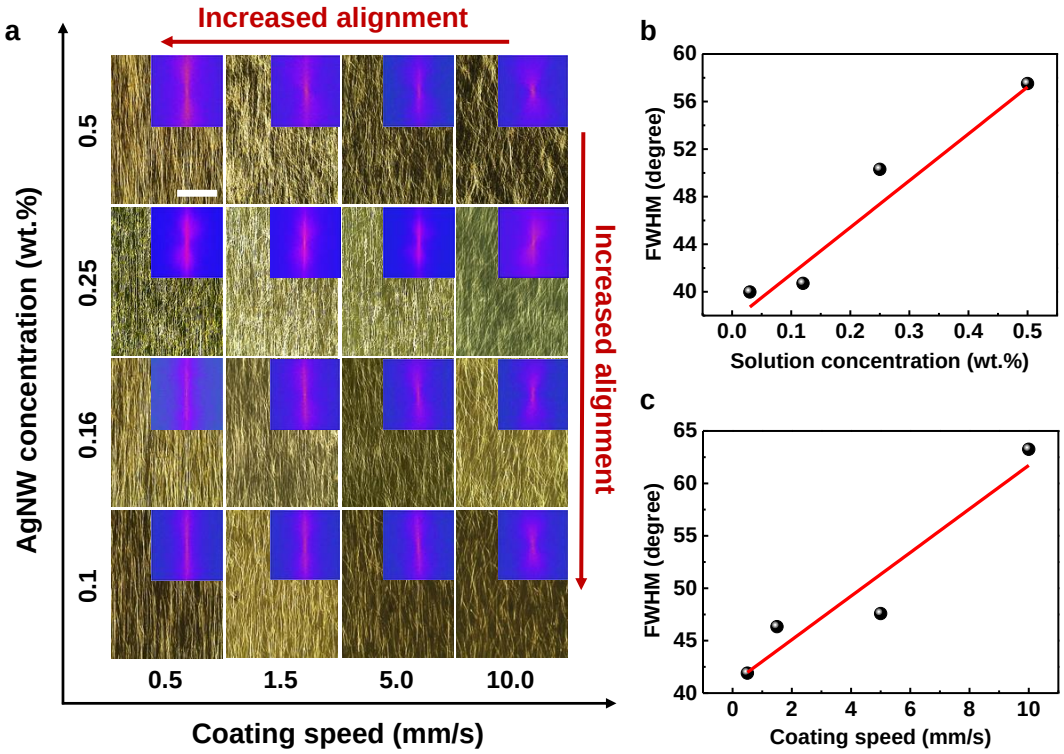

Figure 2.3 Quantitative FFT analyses of the degree of alignment of capillary-printed AgNW networks. (a) Optical micrographs of aligned AgNW networks fabricated using different coating speeds (0.5-10 mm s^{-1}) and solution concentrations (0.1-0.5 wt.%) on PLL-coated substrates. FFT images in the insets of the optical micrographs indicate unidirectional structures with anisotropic features. The scale bar is 20 μm. FWHM fitting data, calculated from the radial summation of pixel intensity in the FFT images, indicates the degree of alignment for printed AgNW networks fabricated with (b) different solution concentrations and (c) different coating speeds.

When the PDMS channel width (10, 20 μm) is comparable to the NW length (20-30 μm), the weak physical confinement of NWs within the PDMS channels results in the increase of misaligned NWs (Supporting Information **Figure 2.4**). The smaller PDMS channel width (150 nm) than the 400 nm width results in a similar NW alignment degree (**Figure 2.4**), indicating that the 400 nm cahnnel width is sufficient to physically confine long NWs (20-30 μm) and induce NW alignments in the channel direction. Because the nanochannel-confined pre-alignment step was followed by the alignment of AgNWs by the meniscus line, the distance between the nanochannel contact area and the meniscus contact line affected the degree of AgNW alignment. When the meniscus contact line was located too far from the nanochannel contact area, the pre-aligned AgNWs had a higher probability of random re-orientation within the solution before further alignment could be induced by the meniscus contact line. We varied the peak angle of the PDMS stamp, which affected the distance between the nanochannel contact area and the meniscus line. When the peak angle of the stamp was increased from 5 to 30° which resulted in a decreased distance, the degree of AgNW alignment increased (**Figure 2.5**). The contact pressure of the PDMS stamp also affected the degree of nanochannel confinement and thus the NW alignment. When the contact pressure between the stamp and the target substrate was increased from 0 to 3.14 kPa, we observed an increased degree of alignment with sharper and clearer fast Fourier transform (FFT) spectral line shapes (**Figure 2.6**).

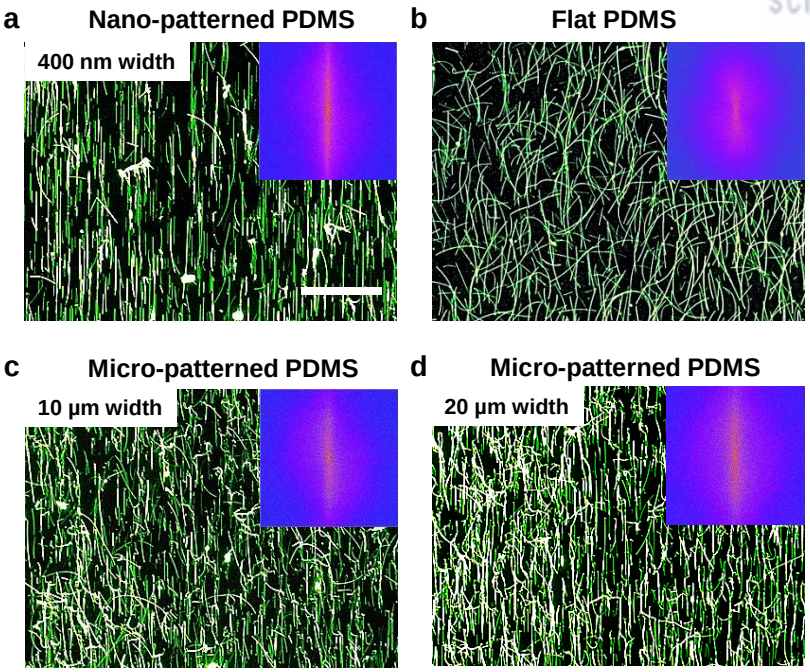

Figure 2.4 Dark-field optical micrographs of AgNW networks fabricated with a concentration of 0.1 wt.% by capillary printing using (a,b) nano-patterned, (c,d) micro-patterned and (e) flat PDMS stamps, respectively. The printing conditions include a speed of 1.5 mm/s and a pressure of 1.57 kPa. Alignment using nano-patterned PDMS stamps provides aligned AgNW networks 400 nm width 10 μm width 20 μm width c Micro-patterned PDMS d Micro-patterned PDMS e Flat PDMS 150 nm width a Nano-patterned PDMS b Nano-patterned PDMS 7 with a characteristic line-shaped FFT pattern, in contrast to the blurred circular FFT pattern produced from networks using a flat PDMS stamp. All scale bars are 40 μm.

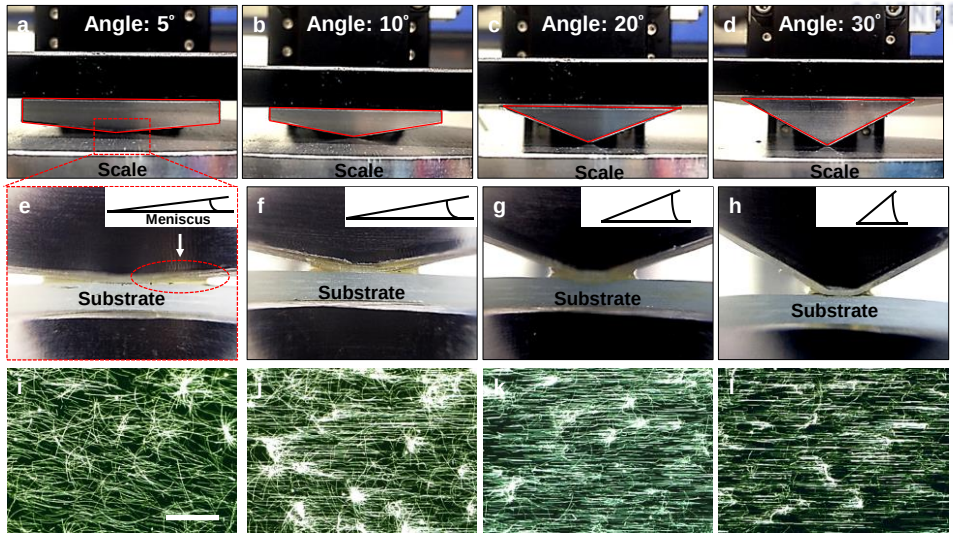

Figure 2.5 Effect of the angle of the triangular PDMS stamp on the NW alignment process. Photographic images of AgNW arrays prepared using triangular PDMS stamps with angles of (a) 5°, (b) 10°, (c) 20°, and (d) 30°. (e-h) Close-up images of the meniscuses formed using triangular PDMS stamps with different angles (5°-30°). (i-l) Dark-field images of aligned AgNW arrays coated using triangular PDMS stamps with different angles on glass treated by O2 plasma. The scale bar is 40 μm.

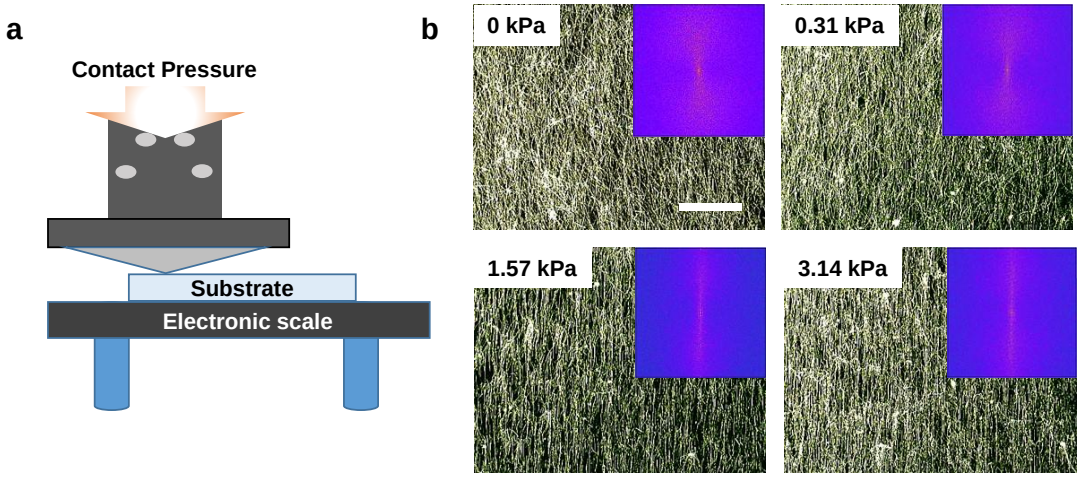

Figure 2.6 (a) Schematic illustration showing the measurement of contact pressure between the nano-patterned PDMS stamp and the substrate. (b) Dark-field optical micrographs of aligned AgNW networks fabricated with a concentration of 0.5 wt.% using different contact pressures (0-3.14 kPa). Line-shaped FFT patterns in the insets demonstrate that the alignment degree is increased with increasing contact pressure. The scale bar is 40 μm.

The inset in **Figure 2.1b** illustrates the principle of the capillary alignment of AgNWs at the meniscus contact line. Here, AgNWs are aligned perpendicular to the receding meniscus contact line by capillary forces, which can be defined as $F_s \approx 2\pi r\gamma$ where γ is the liquid surface tension and r is the radius of the NWs.[53] An estimation using r = 16 nm for the AgNWs and γ = 22.39 mN/m for the ethanol solvent provides $F_s \approx 2.2$ nN. When the AgNW is not perfectly aligned in the dragging direction by the solvent evaporation, as in the left-hand inset of Figure 1b, the slanted AgNW deforms the meniscus, resulting in the different dynamic contact angles of θ_1 and θ_2 on each side of the slanted AgNW. When θ_1 is larger than θ_2 for the slanted NW, the vertical component of the surface tension on one side is larger than that on the other ($\gamma^{lv} sin\theta_1 > \gamma^{lv} sin\theta_2$). This results in the rotation of the slanted AgNW toward the $\gamma^{lv} sin\theta_1$ direction, thus correcting the slant of the NW. When $\theta_1 = \theta_2$ after this rotation of the NW, the surface tensions are balanced ($\gamma^{lv} sin\theta_1 = \gamma^{lv} sin\theta_2$), which maintains the perpendicularity of the NW with respect to the meniscus line. The alignment of the AgNW can also be partially attributed to a hydrodynamic force, $F_{\text{hydrodynamic}} \approx \eta l V$, where η is the liquid viscosity, l is the length of the NW, and V is the printing velocity.[228] The estimated hydrodynamic dragging force is ~13 pN, using η = 1.074 mPa·s, l = 25 μm, and V = 0.5 mm/s, which is negligible compared to the capillary forces.

The friction force between the NWs and the substrate surface can also disrupt the movement of the AgNWs during the alignment process. Because the friction force strongly depends on the surface chemistry,[229] we investigated the influences of surface chemical modifications on the NW alignment (**Figure 2.7**). On CH_3-terminated surfaces, which are known to have low friction and adhesion forces,[229] the AgNWs were highly aligned along the dragging direction because of the low friction force, but the density of the assembled NWs was very low as a result of the low adhesion force between the AgNWs and the surface. In contrast, the stronger friction and adhesion forces on surfaces modified with amine monolayers led to poor NW alignment but larger NW density. Among the various surface treatments, modification with poly-L-lysine (PLL) produced the best conditions with good alignment, high NW density, and uniform NW assembly over a large area. The PLL modification can be employed on various substrate materials for the uniform alignment of AgNWs over large areas (**Figure 2.8**).

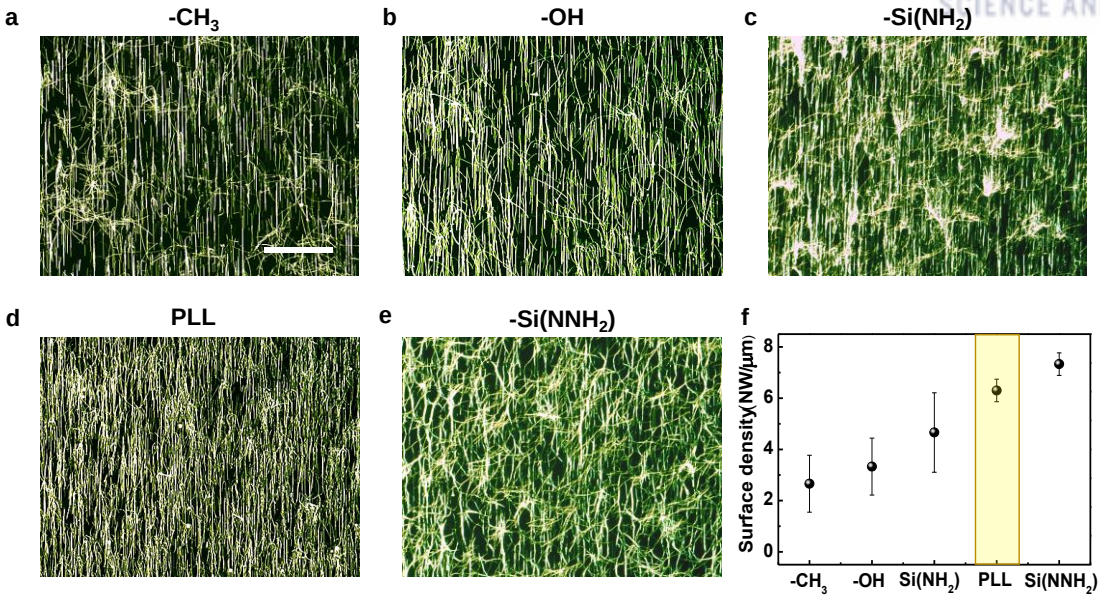

Figure 2.7 Dark-field optical micrographs of aligned AgNWs deposited on substrates chemically modified by (a) hexamethyldisilazane (HDMS), (b) O2 plasma treatment, (c) (3- Aminopropyl)triethoxysilane (APTES), (d) poly-L-lysine (PLL), and (e) 3-(2- Aminoethylamino)propyltrimethoxysilane (AAPTS). The scale bar is 40 μm. (f) The surface density of aligned AgNWs deposited on differently modified substrates.

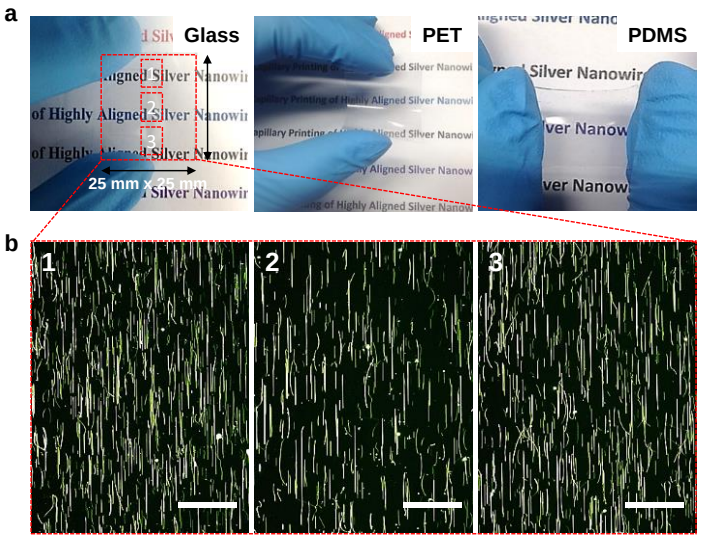

Figure 2.8 (a) Photographs of glass, PET, and PDMS substrates deposited with aligned AgNW arrays. (b) Dark-field optical micrographs of highly aligned AgNW arrays using a concentration of 0.05 wt.% measured at three points on the glass substrate with a size of 25 mm × 25 mm. All scale bars are 40 μm.

The capillary printing technique not only generates uniformly aligned AgNWs, but also enables the formation of diverse morphologies of crossed AgNW arrays via multi-step printing processes without interference by the pre-aligned AgNW array. Figure 1c shows dark-field optical micrographs of differently oriented structures, including unidirectional, 45°-crossed, 60°-crossed, and rectangular AgNW networks. The FFT image of the unidirectional AgNWs exhibits a pattern of sharp lines, while those of crossed AgNWs at various angles of 45°, 60°, and 90° show crossed line patterns. By contrast, FFT imaging of random AgNWs exhibit blurry circular patterns, indicating isotropic surface structures (**Figure 2.9a**). To further corroborate the quantitative analysis of the degree of alignment, a radial summation of the pixel intensity of the FFT data was plotted as a function of the radial angle (0-360°). As shown in **Figure 2.9b**, the unidirectional AgNW array shows clear peaks at 90° and 270°, indicating AgNW orientation in one direction. In contrast, random AgNWs shows no clear peak, resulting from the absence of any particular orientation of the AgNWs. Likewise, 45°-crossed, 60°-crossed, and rectangular AgNW arrays show four peaks centered at each corresponding radial angle, indicating that, in each case, the AgNWs are aligned in two discrete directions (**Figure 2.9c**).

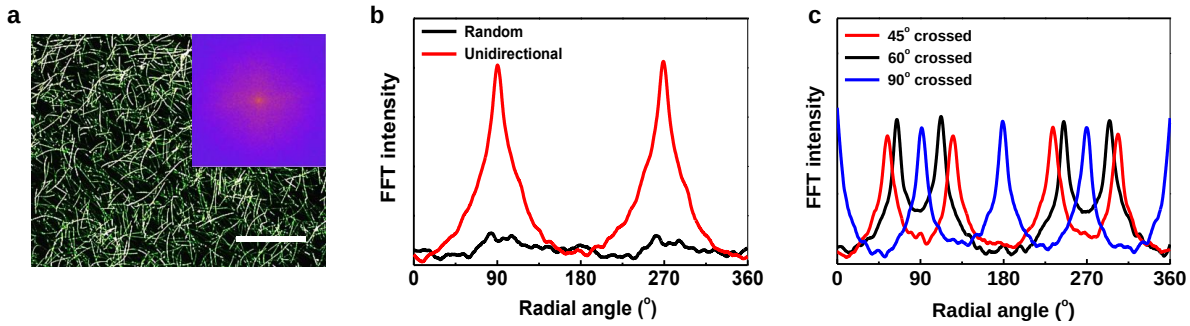

Figure 2.9 (a) Dark-field optical micrographs of random AgNW network fabricated by spincoating. The scale bar is 40 μm. FFT image provided in inset. (b) Radial summation of pixel intensity distribution between 0° and 360° in the FFT analyses of AgNW networks with aligned and random structures. (c) Radial summation of pixel intensity distribution between 0° and 360° in the FFT analyses of different geometric (45°, 60°, 90° crossed) AgNW networks fabricated via multi-step capillary printing alignment process.

To quantitatively characterize the AgNW alignment in the capillary printing process, the degree of AgNW alignment was monitored as a function of AgNW concentration and printing speed. **Figure 2.2a**

shows that the degree of alignment increases as the NW density and coating speed decrease. In order to quantitatively compare the degree of alignment, the full width at half maximum (FWHM) of the FFT spectra were plotted as functions of NW density and printing speed (**Figure 2.2b,c**). The FFT spectra were acquired by plotting the pixel intensities as a function of radial summation from the 2D FFT patterns and fitting this plot by a Gauss function (**Figure 2.10**), in which the FWHM value quantified the degree of AgNW alignment by an inverse relationship. The FWHM value increases with the increase of NW concentration, indicating the decrease of the degree of alignment. This behavior can be attributed to the increased entanglement and cohesion between AgNWs at higher concentrations, which would prevent the pre-alignment of AgNWs in the nanochannels during the printing process.

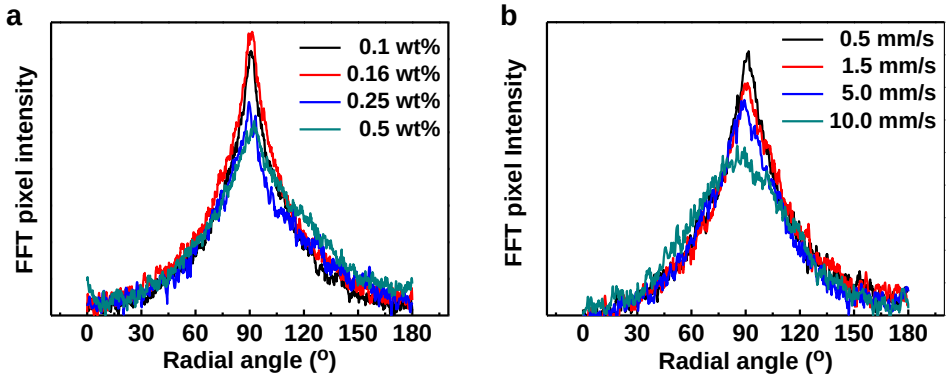

Figure 2.10 Radial summation of pixel intensity between 0° and 180° in FFT analyses of darkfield optical micrographs for aligned AgNW networks coated using (a) different solution concentrations (0.1-0.5 wt.%) and (b) different coating speeds (0.5-10.0 mm s^{-1}).

The increase of printing speed results in the increase of the FWHM value, correlating to the decrease of the alignment degree. This can be attributed to the disturbance of the uniform formation of meniscus contact lines when the movement of the receding meniscus contact line is impeded by the movement of the line-patterned stamp. This indicates that the alignment degree of the AgNW network can be decisively modulated by controlling the printing speed and NW concentration, enabling the precise control of the electrical properties of conductive percolation networks.

The aligned AgNW network showed a lower electrical percolation threshold than the random AgNW network. This is beneficial for the achievement of higher T at similar R_s or that of lower R_s at similar T. According to percolation theory, the electrical percolation threshold of AgNW networks can be determined

by using the relation, $R_s \propto (m\text{-}m_c)^{-\alpha}$, where m_c is the threshold concentration of NWs and α is the critical exponent. The critical exponent reflects the dimensionality of the conductive network, with approximate values of 1.3 and 2.0 for 2D and 3D percolation networks, repectively.[52, 230] The analysis of R_s as a function of NW areal density (S) reveals conductive percolation thresholds at S = 6.05% and 9.04% for aligned and random AgNWs, respectively (**Figure 2.11a**). The best fit to R_s as a function of ($S - S_c$), where S_c is the critical percolation threshold, was obtained using α = 1.27 and 1.30 for aligned and random AgNWs, respectively, both of which are close to the 2D theoretical values (**Figure 2.11b,c**).

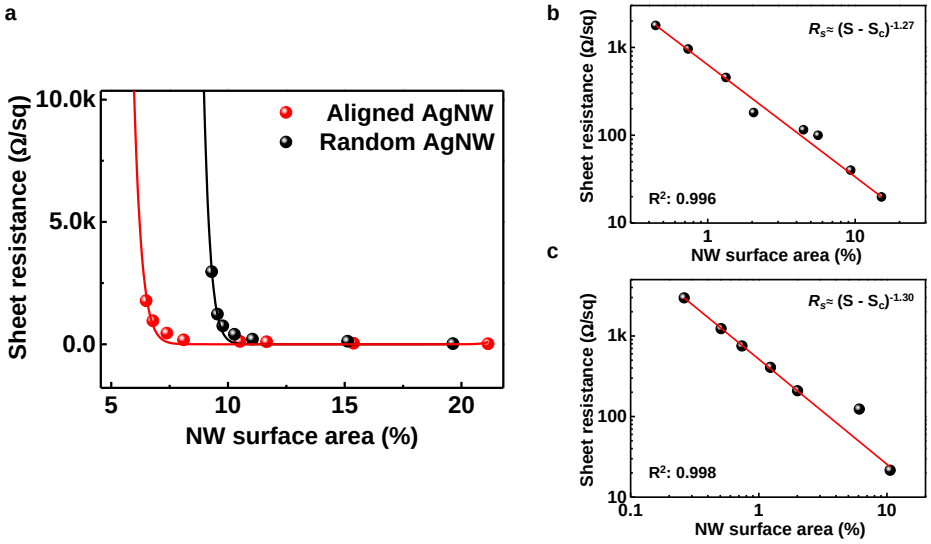

Figure 2.11 Electrical percolation behaviors of AgNW networks with different geometries. (a) Comparison of Rs in aligned and random AgNW networks as a function of surface area density. Power-law fits of Rs for (b) aligned and (c) random AgNWs as a function of (S - Sc), where Sc (%) is the critical surface area density for the onset of conductivity

Figure 2.12a shows SEM images of different morphologies of NW networks with similar electrical conductivities (~22 Ω sq^{-1}) and corresponding schematic representations of the electrical percolation networks for the aligned and random AgNW networks. For similar R_s, the aligned AgNW network displays a lower NW density compared to the random AgNW network because of the lower percolation threshold. To compare the electrical performances of aligned and random AgNW structures, R_s values of the AgNW networks have been plotted as a function of NW surface densities (**Figure 2.12b**). Here, the surface densities of the aligned AgNW networks were controlled by the coating speed (**Figure 2.13**). One major advantage

of our alignment technique is the production of high density NW assembly via a one-step solution-based process. At a coating speed of 0.5 mm/s, the NW density is ~14 NWs/μm, which is higher than those of most previous NW assembly techniques (**Figure 2.13**). The aligned AgNW films showed significantly lower R_s by a factor of ~1.7–3.4 at the same NW surface density, or significantly lower NW surface density by a factor of ~1.4–1.8 at the same R_s in comparison with those of random AgNW films (**Figure 2.13b**).

The lower percolation thresholds of the aligned AgNW networks allow higher T values than those of random AgNW films at similar R_s. **Figure 2.12c** shows T, as well as the haze factor, of aligned and random AgNW networks with similar R_s values of 22.4 Ω/sq and 22 Ω/sq, respectively. The aligned AgNW networks exhibit ~3% higher T and 2.4 times lower haze values at 550 nm wavelength compared to the random AgNW networks. These enhanced optical properties of the aligned AgNW networks can be attributed to the decreased light scattering resulting from the reduced percolation threshold and thus the lower NW surface density.

The R_s values of the aligned AgNW networks depend on the degree of alignment. **Figure 2.12d** shows the variation of R_s and T of the aligned AgNWs as a function of the FWHM value, as acquired from FFT analysis of optical images. The R_s decreases with the decrease of the FWHM value from 62° to 45°, indicating that the increase of alignment degree lowers R_s. However, T remains constant with the increase of alignment. The R_s value of the aligned AgNW networks is the lowest at 19.5 Ω/sq at the FWHM value of 50.6°. Further increase in the degree of alignment, with a FWHM of 45°, does not lead to the further decrease of R_s. The existence of this critical FWHM value, corresponding to a critical degree of alignment, indicates that the probability of contact between AgNWs decreases and therefore the percolation networks are disturbed when the degree of alignment in the AgNW network is greater than a critical point. Similar behaviors have been observed for aligned CNTs, where partially aligned networks provide lower percolation thresholds and higher conductivities than either randomly or perfectly aligned networks.[231-233] We also note that R_s values of the aligned AgNW networks do not depend on the measurement directions (parallel and orthogonal directions) for aligned AgNW networks when the alignment degree is below the critical FWHM value (50.6°) (**Figure 2.14**). When the alignment degree further increases over the critical FWHM value, the aligned AgNW networks exhibit an increasing discrepancy of R_s values in the parallel and orthogonal directions.

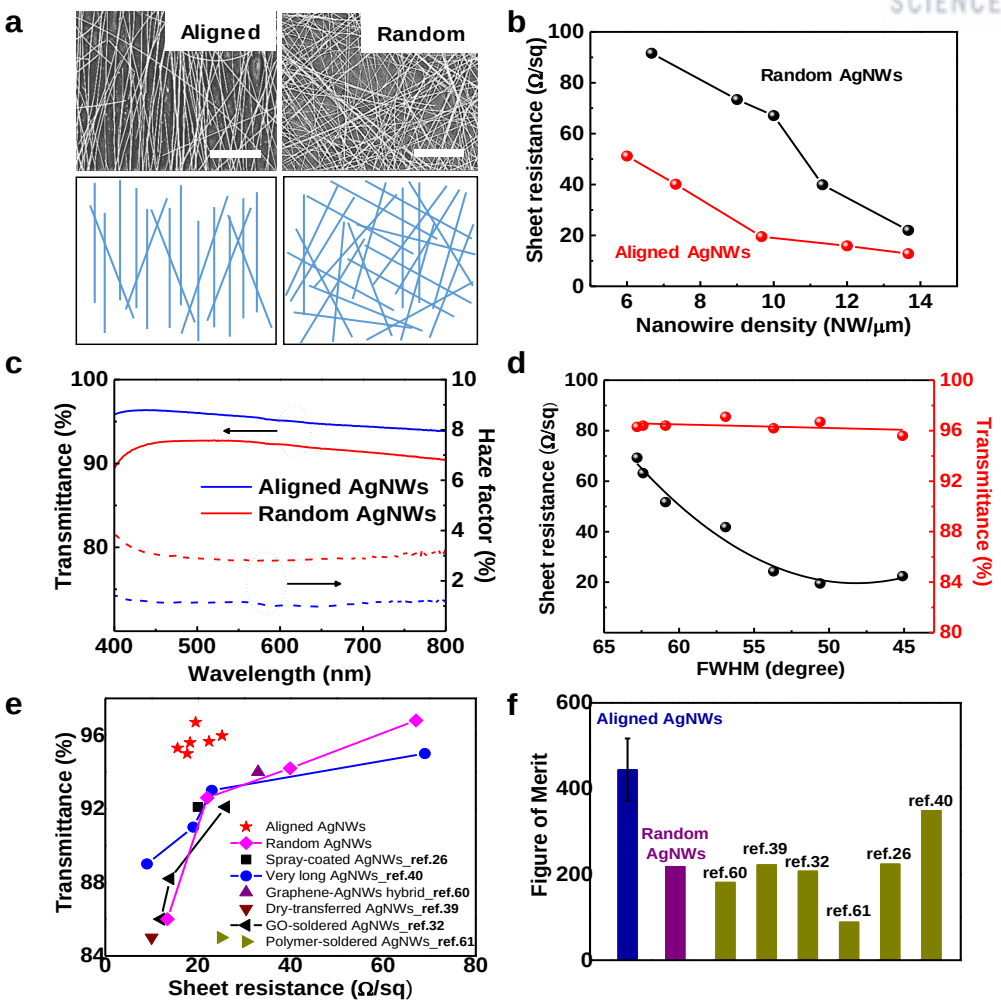

Figure 2.12 Comparison of optical and electrical performances of AgNWs with aligned and randomly oriented networks. (a) SEM images of aligned AgNW and random AgNW networks show good agreement with corresponding geometric structures. Schematics provide a basis for the understanding of the electrical percolation behavior of the networks. All scale bars are 2μm. (b) Sheet resistance (R_s) for AgNW networks with aligned and randomly oriented geometries as a function of NW linear density. (c) Optical transmittance T (solid lines) and haze factor (dashed lines) over the visible spectrum for aligned (blue) and random (red) AgNWs with similar R_s values. The substrate was used as a reference. (d) Change in the R_s of aligned AgNW networks as a function of the alignment degree, wherein FWHM values are calculated from the radial summation of the pixel intensity in FFT patterns. Comparison of (e) the R_s-T performance and (f) FoM values of different AgNW electrodes.

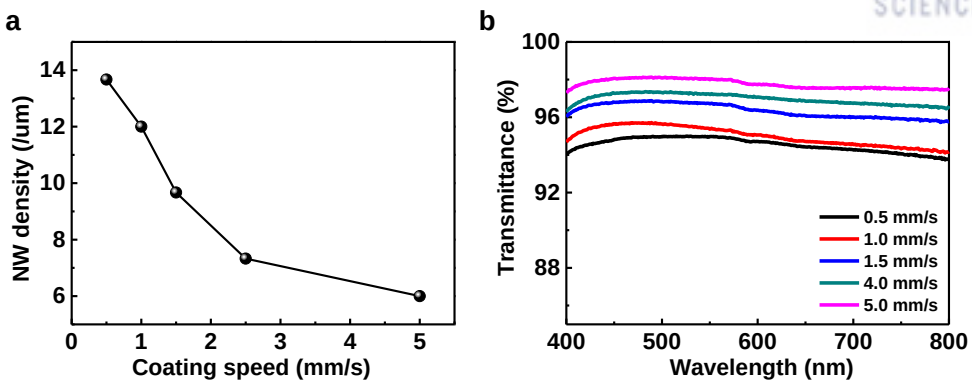

Figure 2.13 (a) Change in NW linear density and (b) T over the visible light range (400-800 nm wavelength) for aligned AgNW networks fabricated with different coating speeds. (c) The comparison of NW density of our work with the NW densities of other assembly techniques estimated from the reported results.

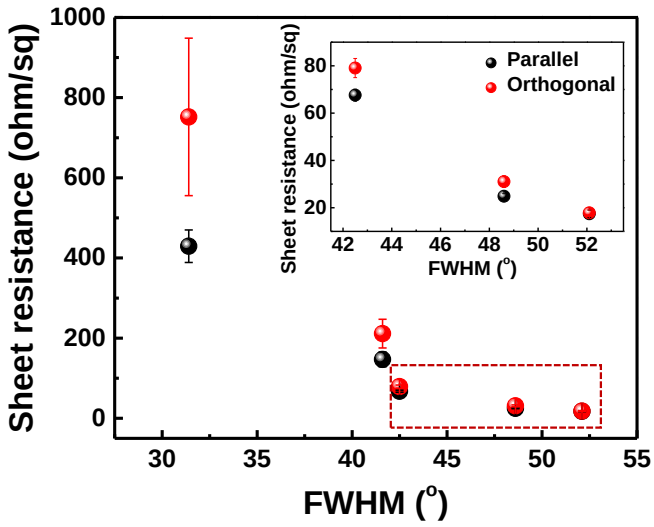

Figure 2.14 Sheet resistances of aligned AgNW networks for different measurement directions as a function of FWHM values. Aligned AgNW networks with various alignment degrees were fabricated with solution concentrations of 0.05-0.5 wt.%, coating speed of 1.5 mm/sec, and coating pressure of 1.57 kPa.

Figure 2.12e compares the R_s to T performance of various AgNW TCEs, including the aligned and

random AgNW networks fabricated in this study. The aligned AgNW networks exhibit superior transparencies of 95.0-96.7% and R_s values of 15.6-25.2 Ω/sq compared to other TCEs based on random AgNW networks. The best value of R_s-T performance of 19.5 Ω/sq at 96.7% transmittance for the aligned AgNW film compares favorably to the performances of previously reported AgNW TCEs, such as graphene-AgNWs hybrid film (33Ω/sq, 94%),[234] very long AgNWs (9-23Ω/sq, 89-95%),[214] spray-coated AgNWs (20Ω/sq, 92.1%),[200] dry-transferred AgNWs (10Ω/sq, 85%),[213] graphene oxide-soldered AgNWs (12-26Ω/sq, 86-92.1%),[206] and polymer-soldered AgNWs (25Ω/sq, 85%).[235]

In order to evaluate the trade-off in performance between R_s and T for TCEs, the electrical to optical conductivity ratio (σ_{dc}/σ_{opt}) is used as a figure of merit (FoM), defined as[181]

$$T = \left(1 + \frac{188.5}{R_s} \times \frac{\sigma_{opt}}{\sigma_{dc}}\right)^{-2}$$

where the values of R_s and T at 550 nm wavelength are used. The aligned AgNWs with T = 95.0-96.7% and R_s = 15.6-25.2 Ω/sq exhibited a FoM of σ_{dc}/σ_{opt} = 360-571.3 with an average value of 444.1. The FoM of the aligned AgNW films is significantly higher than that (218.6) of the random AgNW films as well as those of other solution-processed TCEs based on various NWs (σ_{dc}/σ_{opt} = 89-349) (Figure. 3f). The TCEs based on the aligned AgNWs also possess high flexibility. The aligned AgNW TCEs exhibit small variations in resistance (below 10%) under bending radii as small as 1.25 mm, whereas the resistance of ITO films sharply increases because of the brittle nature of ITO (**Figure 2.15a**). Moreover, the aligned AgNW films show high mechanical stabilities without significant changes in resistance, even after 1,000 bending cycles at the bending radius of 1.25 mm (**Figure 2.15b**).

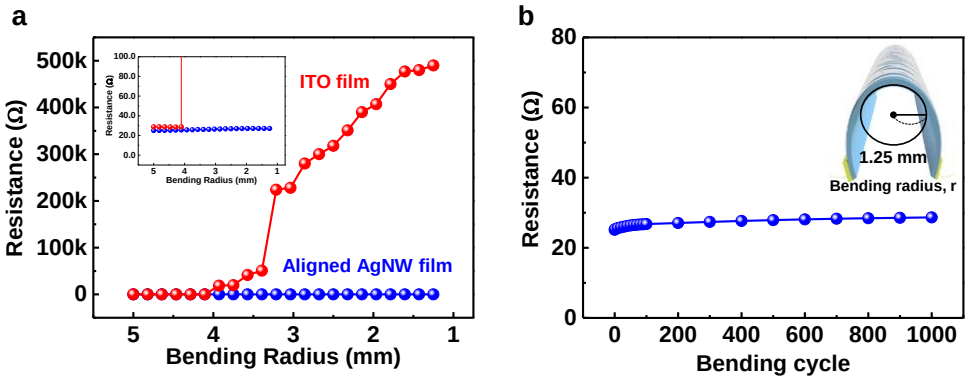

Figure 2.15 Mechanical properties of aligned AgNW films on PET substrates. (a) Variations in resistance of aligned AgNW film as a function of bending radius. (b) Resistance change over the course of 1000 bending cycles at the bending radius of 1.25 mm. Resistance was measured after the films were released and had resumed the lengths measured prior to bending.

In order to further evaluate the performances and compatibilities of the aligned AgNW TCEs for optoelectronic devices, we fabricated PLEDs using a device architecture of glass/Ag NWs/poly(3,4-ethylenedioxythiophene) polystyrene sulfonate (PEDOT:PSS)/emitting layer/LiF/Al (**Figure 2.16**). Super Yellow (SY-PPV) was used as the emitting layer material to create high-performance PLEDs.[236] Figure 4b shows the energy level diagram of the device. **Figure 2.16c-f** show the comparisons of current density, luminance, electroluminescence (EL), and power efficiencies of PLED devices based on ITO, random AgNW (R_s = 20 Ω/sq, T = 92.9%), and aligned AgNW electrodes (R_s = 21.4 Ω/sq, T = 95.8%), the results of which are summarized in **Table 2.1**. In traditional PLEDs with random AgNW networks, it has been reported that electrical charges were irregularly injected because of the protruding features and poor surface coverage of the AgNWs. This led to high leakage currents and irregular charge recombination inside the emissive layer, which caused unstable and low device efficiency.[203, 237] Meanwhile, as can be seen in Figure 4c, the device with an aligned AgNW network shows a lower leakage current with a turn-on voltage of 2.0 V than that of the device with a random AgNW network, which can be attributed to the smoother surface morphology of the aligned AgNW network (**Figure 2.17a,b**). In addition, the devices with aligned AgNW networks show enhanced light-emitting performances including maximum luminance, EL efficiency, and power efficiency of 33068 cd/m^2 (at 8.0V), 14.25 cd/A (at 5.8V), and 10.62 lm/W (3.6V), compared to devices with random AgNWs with performances of 25223 cd/m^2 (at 8.6V), 12.23 cd/A (at 7.0V), and 7.16 lm/W (4.8V), respectively (**Table 2.1**). The control devices with ITO electrodes exhibit the EL efficiency of 11.61 cd/A and power efficiency of 7.54 lm/W. In particular, the device with aligned AgNWs exhibits a 30% enhancement in maximum luminance compared to that with random AgNWs and also shows a high EL efficiency (14.25 cd/A), which is among the highest values reported so far using ITO-free TCEs for fluorescent PLEDs.[203, 236-240]

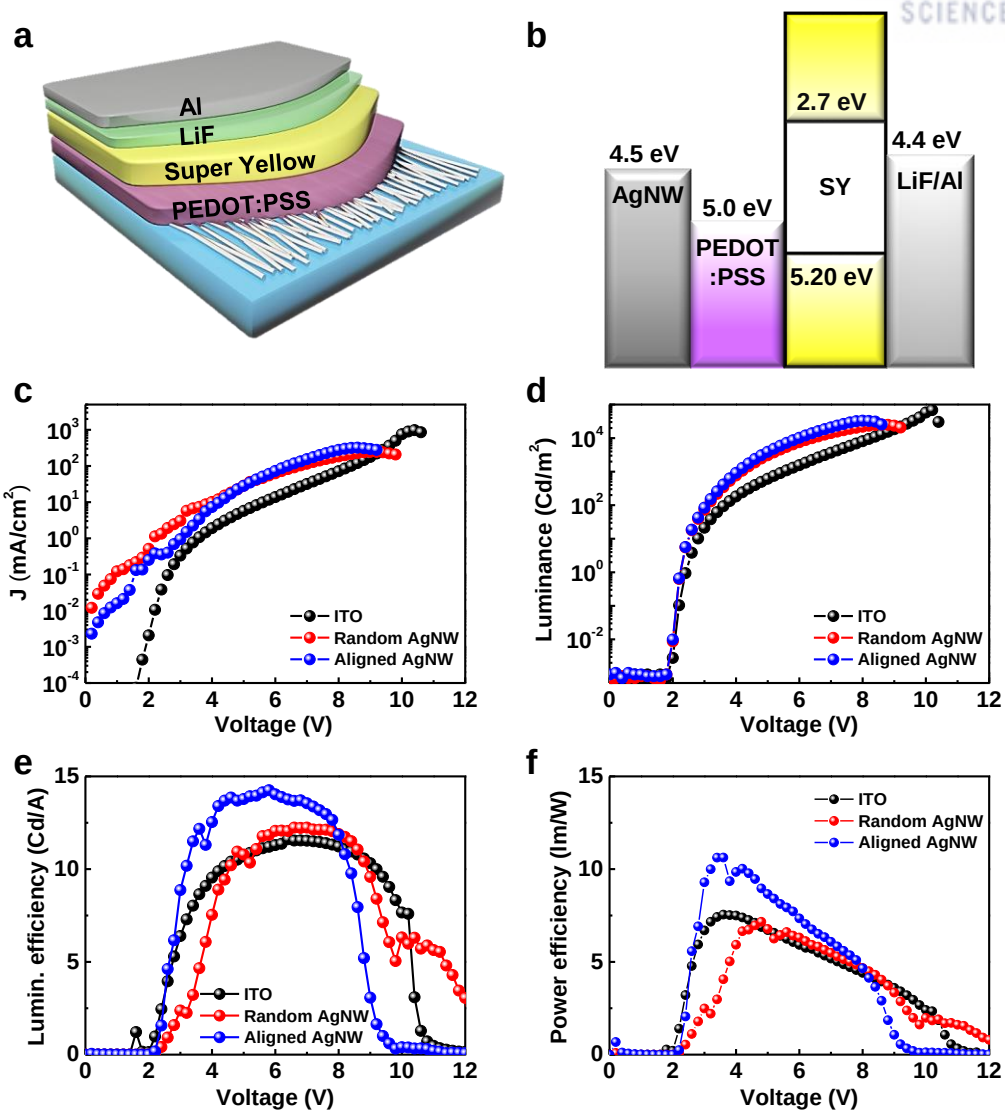

Figure 2.16 Device structure and characteristics of PLEDs using aligned AgNW electrodes. (a) Schematic PLED structure. (b) Schematic energy level diagrams under the flat-band condition for PLEDs with AgNW electrodes. (c) Current density, (d) luminance, (e) luminous efficiency, and (f) power efficiency with changes in the applied voltage for PLEDs with ITO, random, and aligned AgNW electrodes.

Table 2.1 Device characteristics of PTB7-Th:$PC_{71}BM$ PSCs and SY PLEDs with ITO or random and aligned AgNW electrodes.

PLED configuration	**Maximum luminance [cd/m^2] (at listed voltage)**	**Maximum EL efficiency [cd/A] (at listed voltage)**	**Maximum power efficiency [lm/W] (at listed voltage)**	**Turn-on Voltage**
ITO / PEDOT:PSS / SY / LiF / Al	68253 (10.2V) [62301 ±5952][a]	11.61 (6.4V) [10.16 ± 1.45][a]	7.54 (3.6V) [8.37 ± 0.83][a]	2.0 V
Random AgNW / PEDOT:PSS / SY / LiF / Al	25223 (8.6V) [22740 ±2483][a]	12.23 (7.0V) [11.89 ±0.34][a]	7.16 (4.8V) [7.83 ± 0.67][a]	2.0 V
Aligned AgNW / PEDOT:PSS / SY / LiF / Al	33068 (8.0V) [30523 ±2545][a]	14. 25 (5.8V) [12.49 ±1.76][a]	10.62 (3.6V) [9.51 ± 1.11][a]	2.0 V
PSC configuration	***J_{sc}*** **[mA/cm^2]**	***V_{oc}*** **[V]**	***FF***	**PCE [%]**
ITO / PEDOT:PSS / PTB7-Th:$PC_{71}BM$ / Al	17.17 [16.57±0.59][a]	0.80 [0.79±0.08][a]	0.61 [0.63±0.02][a]	8.56 [8.26±0.30][a]
Random AgNW / PEDOT:PSS / PTB7-Th:$PC_{71}BM$ / Al	16.37 [16.29±0.09][a]	0.76 [0.76±0.01][a]	0.61 [0.61±0.01] [a]	7.62 [7.46±0.01][a]
Aligned AgNW / PEDOT:PSS / PTB7-Th:$PC_{71}BM$ / Al	17.83 [17.20±0.62][a]	0.76 [0.76±0.01][a]	0.64 [0.64±0.01] [a]	8.57 [8.39±0.19][a]

[a] Average device performances among 10 devices

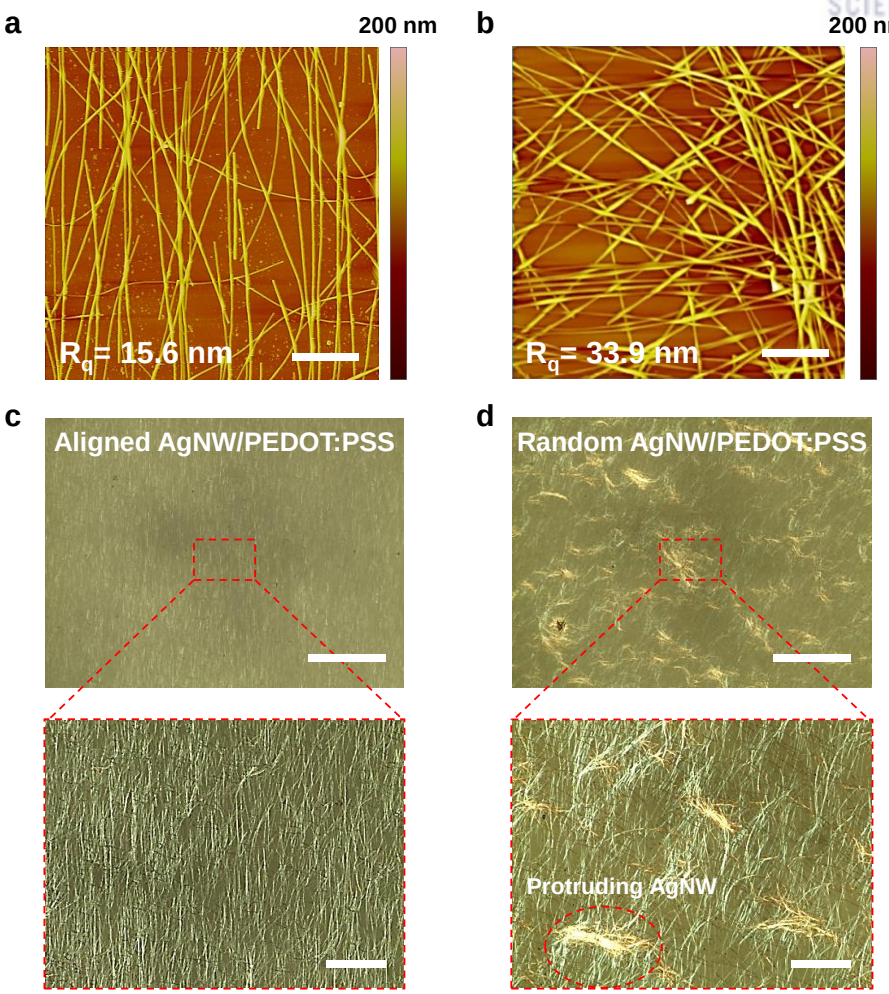

Figure 2.17 AFM images of (a) aligned AgNW networks and (b) random AgNW networks. The surface roughness of aligned AgNWs films is lower than that of random AgNWs films. The scale bars are 2 μm. Optical images for the surface of PEDOT:PSS coated onto (c) aligned and (d) random AgNW films. The scale bars are 100 μm. The surface of random AgNWs films shows the protrusion of NWs through the PEDOT:PSS layer. The scale bars of the magnifications are 20 μm.

The improved device performance with the aligned AgNW TCE can be attributed to the reduction in the optical loss of emitted light by the high *T* (**Figure 2.18**), low leakage current, and uniform charge injection by the smooth surface morphologies of the aligned AgNWs, resulting in the enhanced out-coupling efficiency. The low leakage current for the aligned AgNWs is beneficial in enhancing the stability and efficiency of the PLEDs. Atomic force microscope (AFM) and optical microscope images show that the aligned AgNW networks possesses a smoother surface (root mean square (RMS) roughness, R_q = 15.6 nm)

with no aggregated NWs, as compared to the random AgNW network with a large roughness (R_q = 33.9 nm) and clumps of NWs, which can cause irregular charge injection as well as high leakage currents and short circuits from the AgNWs protruding through the emissive layer (**Figure 2.19**). Although random AgNW networks have been known to enhance the light extraction efficiency of LED due to the light scattering effect,[241-243] this effect is not significant in our study because our random AgNWs have a relatively low haze factor (~2.8% at 550 nm wavelength) compared to the previous studies.

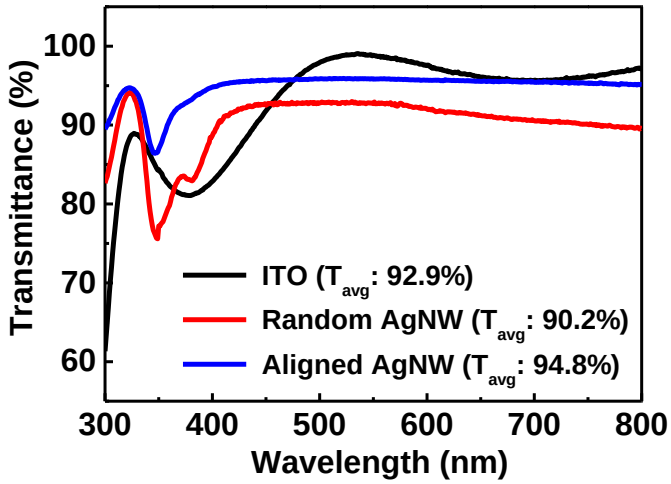

Figure 2.18 Transmittance spectra of ITO, random AgNW, and aligned AgNW films on glass substrates.

As another application in optoelectronic devices, we evaluated the device performance of PSCs using aligned AgNW TCEs. The device structure and energy level diagram are presented in **Figure 2.19a, b**. Blended poly[4,8-bis(5-(2-ethylhexyl) thiophen-2-yl)benzo[1,2-b:4,5-b']dithiophene-co-3-fluorothieno[3,4-b]thiophene-2-carboxylate] (PTB7-Th):[6,6]-phenyl-C_{71} butyric acid methyl ester (PC_{71}-BM) electron donor:electron acceptor was used as the active layer to ensure high-performance PSCs.[244] **Figure 2.19c** shows the current density–voltage (*J-V*) characteristics of the devices with ITO, random, and aligned AgNW TCEs. Detailed characteristics of the PSCs are reported in **Table 2.1**. Notably, an enhanced short-circuit current (J_{SC}) of 17.83 mA/cm^2 is observed for the case of aligned AgNWs. Meanwhile, random AgNW and ITO TCEs exhibited J_{SC} values of 16.37 mA/cm^2 and 17.17 mA/cm^2, respectively. The high J_{SC} value using aligned AgNW-based PSCs can be attributed to the effective charge-carrier collection from the smooth surface of the electrodes, as well as the high *T* of 95.8% at 550 nm wavelength of the aligned

AgNWs.

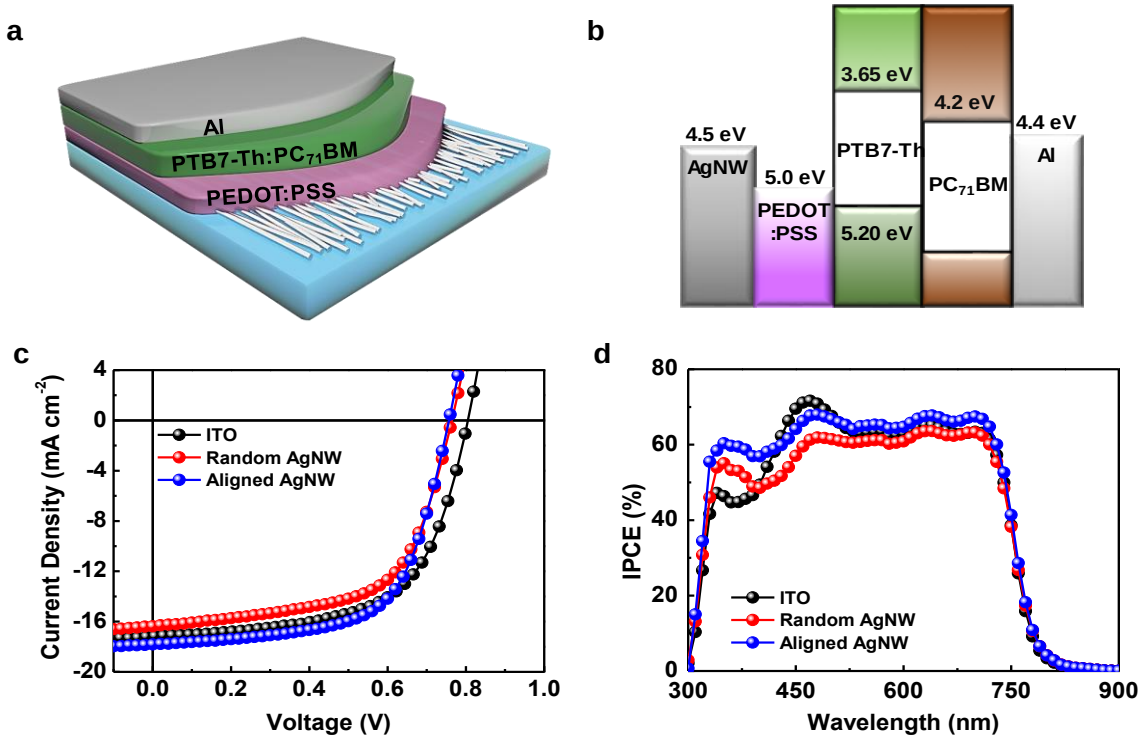

Figure 2.19 Device structure and characteristics of PSCs using aligned AgNW electrodes. (a) Schematic PSC structure. (b) Schematic energy level diagrams under the flat-band condition. (c) *J-V* characteristics under AM 1.5 illumination at 100 mW cm^{-2} and (d) IPCE of PSCs with ITO, random, and aligned AgNW electrodes.

The increase in J_{SC} using the aligned AgNW TCEs is evident in the incident photon-to-current efficiency (IPCE) data. **Figure 2.19d** compares the IPCE in the wavelength range of 300–900 nm for PSCs with different TCE materials. In particular, in the range of 350 to 500 nm, PSCs with aligned AgNWs show quantum efficiencies several percent higher than those with random AgNWs, as a result of the higher T of the aligned AgNWs (**Figure 2.18**). In addition, the series resistance of the aligned AgNW-based devices, measured at 5 Ω cm^2 was lower than those with random AgNW (8.20 Ω cm^2) and ITO (6.67 Ω cm^2) electrodes, which resulted in a higher fill factor of 0.64 for the PSCs with aligned AgNWs than for those with random AgNW (0.61) and ITO (0.61) electrodes. As the results of these features, the PSCs with aligned AgNWs yielded power conversion efficiency (PCE, η) of 8.57% which is superior to that of PSCs with random AgNWs (7.62%) and comparable to that of the control devices with ITO (8.56%). Notably, the

obtained η = 8.57% is the highest reported to date for PSCs using AgNW electrodes (**Table 2.2**).

Table 2.2 Comparison of results achieved here with performances of previously reported AgNW-based PSCs

PSCs configuration	Active layer materials	J_{sc} [mA/cm^2]	V_{oc} [V]	*FF*	PCE [%]	Reference
Inverted structure	PTB7:$PC_{71}BM$	16.77	0.75	0.62	7.57	*Nano Res.* 2014
conventional	PTB7:$PC_{71}BM$	20.73	0.67	0.55	7.38	*Small* 2014
conventional	PTB7-F20:$PC_{71}BM$	14.40	0.67	0.59	5.80	*Adv. Funct. Mater.* 2013
conventional	PBnDT-DTffBT:$PC_{71}BM$	9.64	0.59	0.48	2.80	*ACS Appl. Mater. Interfaces* 2011
conventional	**PTB7-Th:$PC_{71}BM$**	**17.83**	**0.76**	**0.64**	**8.57**	**Our work**

To further evaluate the potential use of aligned AgNW networks in flexible devices, flexible PLEDs and PSCs based on aligned AgNWs were prepared using flexible substrates. The characteristics of the flexible PLEDs and PSCs using aligned AgNW and ITO electrodes are shown in **Figure 2.20** and **Figure 2.21**, respectively, and summarized in Supporting Information **Table 2.3**. The performances of the flexible PLEDs and PSCs with aligned AgNW TCEs were comparable to those of the devices with ITO films. In particular, a PCE of 8% was achieved for flexible PSCs with aligned AgNWs, which constitutes the highest PCE to date among flexible PSCs based on AgNW TCEs.[227, 245-248] To investigate the mechanical stability of the flexible devices with aligned AgNWs, **Figure 2.22a** shows the change in luminance of flexible PLEDs using ITO and aligned AgNW TCEs over the course of 1,000 bending cycles at a bending radius of 5 mm. The flexible PLEDs using aligned AgNW TCEs retain 80% of the initial luminance over 300 bending cycles, whereas the ITO-based flexible PLEDs show rapid decreases in luminance. Likewise, the flexible PSCs using aligned AgNW TCEs retain over 80% of the original PCE value even after 1000 bending cycles, whereas the PCEs of devices using ITO rapidly decrease after only 100 cycles (**Figure 2.22b**). These results demonstrate the viability of using aligned AgNWs in flexible devices including OLEDs, PSCs and other optoelectronic devices.

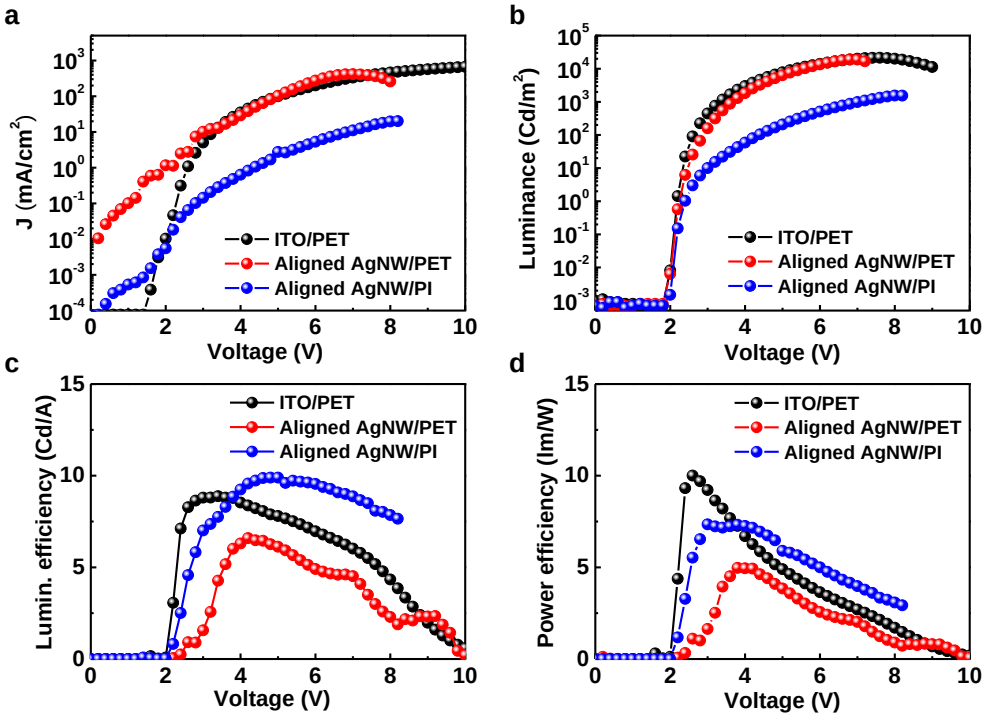

Figure 2.20 Light-emitting characteristics. Variations in (a) current density, (b) luminance, (c) EL efficiency, and (d) power efficiency with applied voltage using ITO-coated and random or aligned AgNW-based electrodes on flexible substrates.

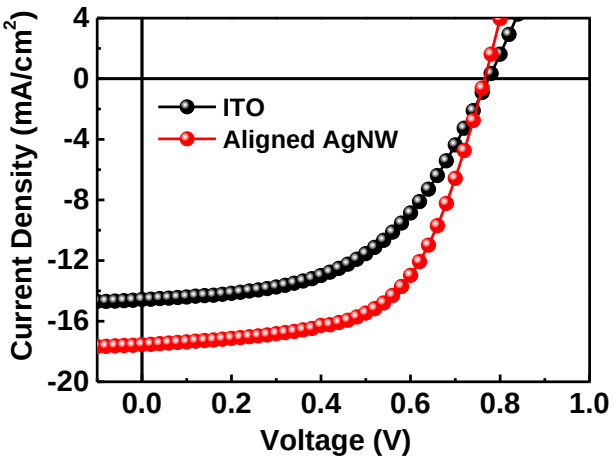

Figure 2.21 *J-V* characteristics under AM 1.5 illumination at 100 mW cm-2 with ITO and aligned AgNWs for flexible PSCs.

Table 2.3 Device characteristics of SY- based PLEDs and PTB7-Th:$PC_{71}BM$ PSCs using ITO coated and aligned AgNW electrodes on flexible substrates.

PLED configuration	**Maximum luminance [cd m^{-2}] (at listed voltage)**	**Maximum EL efficiency [cd A^{-1}] (at listed voltage)**	**Maximum power efficiency [lm W^{-1}] (at listed voltage)**	**Turn-on Voltage**
ITO / PEDOT:PSS / SY / LiF / Al (PET)	19130 (6.8V)	8.81 (3.6 V)	10.00 (2.6 V)	2.0 V
Aligned AgNW / PEDOT:PSS / SY / LiF / Al (PET)	19022 (10.8V)	6.59 (8.2 V)	4.97 (7.8 V)	2.0 V
Aligned AgNW / PEDOT:PSS / SY / LiF / Al (PI)	1554 (8.0V)	9.89 (4.8 V)	7.32 (3.8 V)	2.0 V
PSC configuration	**J_{sc} [mA cm^{-2}]**	**V_{oc} [V]**	***FF***	**PCE [%]**
ITO / PEDOT:PSS / PTB7-Th:$PC_{71}BM$ / Al (PET)	14.57	0.78	0.51	5.79
Aligned AgNW / PEDOT:PSS / PTB7-Th:$PC_{71}BM$ / Al (PET)	17.55	0.77	0.60	8.00

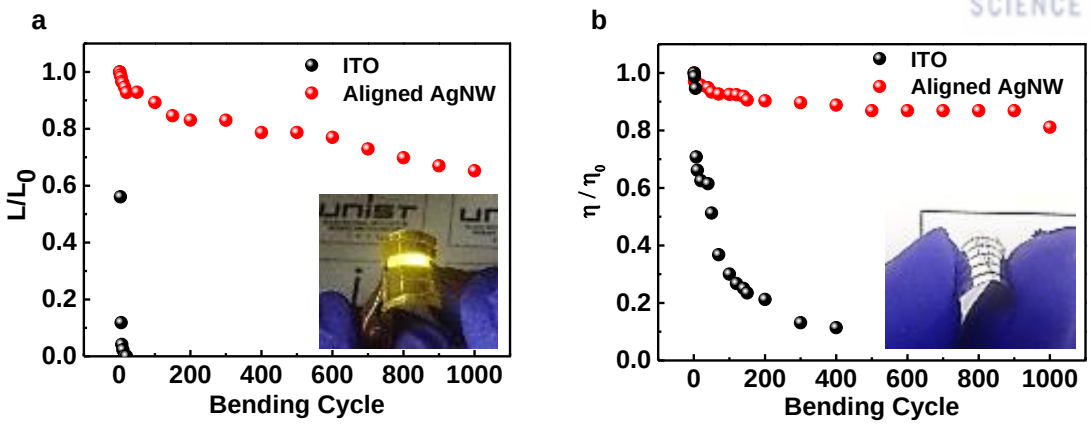

Figure 2.22 Performances of flexible PLEDs and PSCs. (a) Normalized luminance of flexible PLEDs and (b) power conversion efficiency (η) of PSCs using ITO and aligned AgNW on PET substrates over the course of 1000 bending cycles at 5 V with a bending radius of 5 mm. The insets show photographs of the flexible aligned AgNW-based PLED and PSC.

2.4 Conclusion

In conclusion, we have developed a high-throughput, one-step capillary printing strategy for the fabrication of TCEs based on aligned AgNWs. In the capillary printing process, the unidirectional dragging of AgNW solutions by a trigonal prismatic PDMS stamp with nano-patterned channels produced highly aligned AgNW arrays. The key technologies essential to the success of the capillary printing strategy include the pre-alignment of AgNWs in the PDMS nanochannels by physical confinement and the subsequent alignment of NW by the uniform meniscus line, which exerts solvent-evaporation-induced capillary forces on the meniscus-trapped AgNWs. The aligned AgNW networks showed lower electrical percolation thresholds than random AgNW networks, which led to higher T at similar R_s or lower R_s at similar T. Notably, partially misaligned NWs are necessary for the formation of the electrical percolation network. By tuning the degree of NW alignment, we demonstrated that the degree of NW alignment could be optimized for the fabrication of high-performance TCEs.

The TCEs based on aligned AgNW networks exhibited outstanding performances of 19.5 Ω/sq at 96.7% transmittance and a high FoM value of 571.3, which can be favorably compared to the performances of other NW-based TCEs. For the potential applications of aligned AgNW TCEs in optoelectronic devices, we demonstrated highly efficient, flexible PSCs and PLEDs. The observed PCE of 8.57% in PSCs, as well as the luminance efficiency of 14.25 cd/A and power efficiency of 10.62 lm/W in PLEDs, currently represent the highest efficiencies reported for AgNW-based devices. Moreover, the flexible PSC fabricated using aligned AgNWs had a PCE of 8.00%, 80% of which was maintained after 1,000 bending cycles. This work

demonstrates that aligned Ag NW networks are excellent candidates for low-cost ITO-free TCEs used in optoelectronic devices and future flexible electronics. While the AgNW entanglement issue for high aspect ratio AgNWs needs to be addressed in the future, this capillary printing strategy for the preparation of aligned AgNW films may be further explored and applied to the alignment and assembly of other NW types, and may be of great utility in the development and mass production of next-generation optoelectronic devices.

Chapter 3. Nanoparticle-Enhanced Silver Nanowire Plasmonic Electrodes for High-Performance Organic Optoelectronic Device

3.1 Research background

Organic optoelectronic devices (OODs) such as organic light-emitting diodes (OLEDs) and organic solar cells (OSCs) have attracted great attention due to their advantages such as cost-effective, light-weight, large scale solution processing and mechanical flexibility [249-252] . Although, significant progress has been made to enhance their device performance through the continued development of new materials and device configurations, further improvement of device efficiency is still necessary for their commercialization [253-257]. One strategy to maximize device efficiency is to increase the active layer thickness to improving light absorption. However, the thickness of active layer is severely limited by the low carrier mobilities of most organic materials[258, 259]. Therefore, it is necessary to find strategies to maximize light absorption within thin active layers.

Plasmonic, metal nanostructures such as nanoparticles (NPs), nanorods (NRs), and nanowires (NWs) have been introduced as an efficient way to improve device efficiency via scattering or trapping of light [22-28, 260-265]. Among various metal nanostructures, silver nanowires (AgNWs) are considered promising plasmonic materials with strong surface plasmon resonance (SPR) spanning the visible spectrum and near-IR region. Ag NWs offer the unique advantage of simultaneously serving as an excellent transparent electrode as well as a plasmonic nanostructure for high performance OODs [266]. Recently, plasmonic OSCs and OLEDs have been reported using random AgNW networks to enhance light scattering and trapping effects [237, 245, 267, 268]. However, these devices based on random AgNW networks still contain several drawbacks including rough surface morphology and NW aggregation, which results in electrical short-circuits or deteriorated device efficiency [203, 204]. In addition, despite their enormous potential for improving the efficiency of OSCs and OLEDs, the plasmonic effects of AgNW networks are still not fully understood and remain topics of intense investigation.

NP-NW plasmon coupling has been known to provide large E-field enhancements via the gap plasmon coupling effect[269-271]. In particular, NP-NW junctions can act as efficient nano-antennae for the coupling of incident light into surface plasmon propagations (SPPs) on metal NWs or to convert propagating SPPs into scattered light[269, 271]. The manipulation of complex plasmon effects in NP-NW plasmon systems constitutes a powerful platform for the design of new hybrid, plasmonic optoelectronic devices. However, there have not yet been concerted attempts to utilize NP-NW plasmon couplings to improve device performance in OLEDs and OSCs.

Here, we demonstrate plasmonic transparent electrodes based on aligned AgNW networks decorated

with core-shell Ag@SiO_2NPs (NP-enhanced plasmonic AgNW electrodes) for enhanced OOD performance. Ag@SiO_2NP-AgNW electrodes provide strong plasmon coupling of incident light into LSPs of NPs and SPPs of NW, resulting in outstanding E-field enhancement at NP-NW interfaces due to the NP-NW gap plasmon effect. Furthermore, compared to plasmonic OSCs and OLEDs based on random AgNW networks, the aligned AgNW networks in our devices provide excellent figures of merit (electrical to optical conductivity ratio) and smooth surface morphologies, providing good contact with the active area for efficient carrier injection and reduced series resistance [272]. Therefore, NP-enhanced plasmonic AgNW networks serve as high performance transparent electrodes, which can be synergistically combined with plasmonic properties via gap plasmon coupling effect to improve OOD device performance.

3.2 Experimental

Synthesis of core-shell Ag@SiO_2NP

For the preparation of core-shell Ag@SiO_2NPs, AgNPs were first synthesized by the polyol method. In detail, 0.1 g of silver nitrate was dissolved in a solution consisting of polyvinylpyrrolidone (PVP) (1.5 g) and ethylene glycol (6 mL). The PVP-capped Ag nanoparticles were collected after reaction at 120℃ for 1 hr. Next, silica shells were formed onto the surfaces of Ag NPs in the following way: A homogeneous Ag solution in ethanol (140 mL) was mixed with ammonium hydroxide (4 mL) with stirring, and then 0.75 mL of tetraethyl orthosilicate (TEOS) was injected. Another aliquot of TEOS (0.75 mL) was added in the resulting solution after 30 min. Finally, Ag@SiO2 NPs were collected after several centrifugations with ethanol.

Fabrication of aligned AgNW decorated by core-shell Ag@SiO_2NPs film

To prepare AgNP enhanced plasmonic AgNW electrodes, clean glass substrates were cleaned with acetone, isopropyl alcohol (IPA) and deionized (D.I.) water by sonication for 15 min. PLL layers attached amine functional groups were spin-coated on the substrates by a solution of 0.1% PLL in H2O at 4000 rpm for 60 s. Next, aligned AgNW networks were fabricated onto amine functional group terminated substrates by solution based capillary printing, where an 0.5 wt% AgNW dispersion in ethanol with an average length of 25 μm and diameter of 32 nm was used. To fabricate hybrid NW-NP structure, aligned AgNW films were immersed in an 1wt% Ag@SiO_2NPs dispersion in ethanol for 10 min.

Fabrication and characterization of OSCs using NP-enhanced plasmonic AgNW

PSCs were fabricated using Ag NWs and Ag@SiO_2NP-AgNW films on top of cleaned glass substrates. A poly[4,8-bis(5-(2-ethylhexyl) thiophen-2-yl)benzo[1,2-b:4,5-b']dithiophene-co-3-fluorothieno [3,4-b] thiophene-2-carboxylate] (PTB7-Th, 1-Material) and [6,6]-phenyl-C_{71} butyric acid methyl ester ($PC_{71}BM$,

Rieke Metal) blend system was used for the active layer of the PSCs. The device configurations used for the PSCs was AgNWs or Ag@SiO_2NP-AgNW / PEDOT:PSS / active layer / Al. A PEDOT:PSS(Al4083) solution was spin-cast on top of the Ag NWs and ITO films after UV-treatment for 15 min., then dried at 120 °C to remove moisture. The resulting substrates were transferred to a nitrogen-filled globe box and a PTB7-Th:$PC_{71}BM$ (12 mg:15 mg) mixture in chlorobenzene (1 mL) with 3% of diphenyl ether(DPE) as an additive was spin coated. Subsequently, the devices were transferred to a vacuum chamber (<10^{-6} torr) and Al electrodes (ca. 100 nm thick) were deposited by thermal evaporation. The area of the Al electrodes was 13 mm^2. The photovoltaic characteristics were measured inside a nitrogen filled glove box using a high quality optical fiber to guide light from a solar simulator. The current-voltage characteristics were measured using a Keithley 2635A source measurement unit under AM 1.5G illumination at 100 $mWcm^{-2}$. The external quantum efficiency was measured using an EQE system (Model QEX7) by PV measurement Inc (Boulder, Colorado).

Characterization

The synthesized core-shell Ag@SiO_2NPs were characterized using UV-visible spectrometry (Jasco V-670) and transmission electron microscope (TEM, JEOL). Optical properties of Ag@SiO_2NP-AgNW networks were measured using UV-visible spectrometry (Jasco V-670) equipped with a linear polarizer. The sheet resistance of hybrid Ag@SiO_2NP-AgNW films was obtained using the four-point probe technique (Kiethley 2400 equipment). For Raman mapping analysis, the Raman intensity was investigated using a confocal Raman microscope (Alpha 300, WITec) with 532 nm laser excitation.

3.3 Results and discussion

A schematic illustration of the NP-enhanced plasmonic AgNW electrode design is shown in **Figure 3.1a**, consisting of aligned AgNW networks decorated with core-shell Ag@SiO_2NPs where AgNPs are separated from the surface of AgNW by nanometer-scale gaps due to their SiO_2 shells. Here, we employed core-shell Ag@SiO_2NPs to provide dielectric gaps between NPs and NWs, thus preventing direct contact between AgNPs and AgNWs and generating gap plasmon couplings between LSPs of metal NPs and propagating SPPs of NWs. These gaps at the NP-NW interfaces can induce giant localized E-field enhancements. Specifically, AgNPs on the AgNWs can function as nano-antenna to couple the incident light into delocalized SPPs on the NW surfaces. This type of E-field enhancement is schematically shown in **Figure 3.1b** [269]. **Figure 3.1c** shows a transmission electron microscopy (TEM) image of core-shell Ag@SiO_2NPs, which comprise of the Ag@SiO_2NPs separated from the NWs by a nanoscale dielectric gap of ~ 5 nm provided by the the SiO_2 shells. The size of core-shell nanoparticles were controlled to prevent electric short-circuits through the active layer and to ensure a smooth surface morphology.

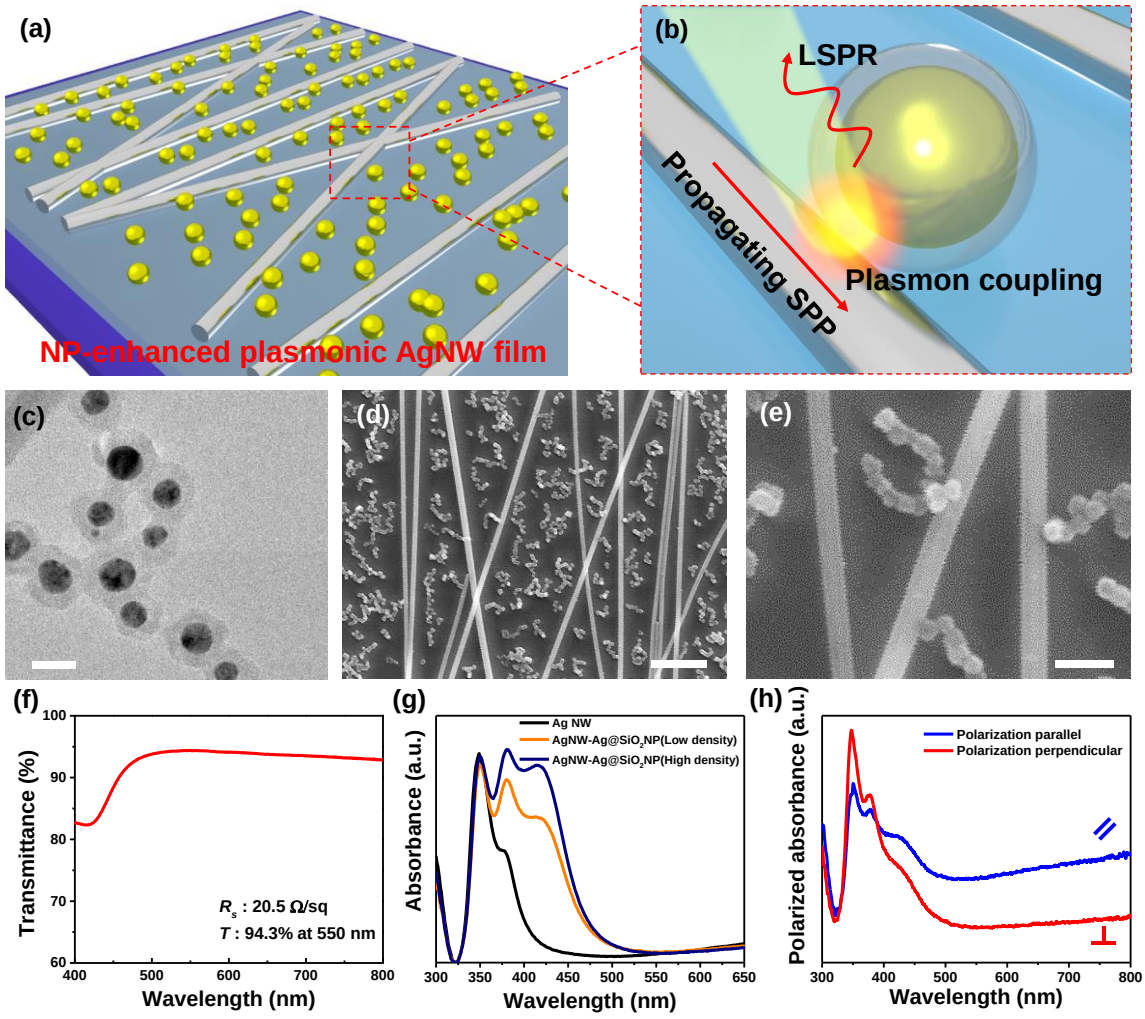

Figure 3.1 Hybrid NP-enhanced plasmonic AgNW network. (a) Representative illustration of a NP-enhanced plasmonic AgNW network. (b) Schematic illustration of plasmon coupling in a NW-NP hybrid plasmonic system showing the interaction between LSP of a metal NP and propagating SPP on a metal NW. (c) Transmission electron microscopy (TEM) image of core-shell Ag@SiO_2NPs. The scale bar indicates 20 nm. (d,e) SEM images of an aligned AgNW network decorated with core-shell Ag@SiO_2NPs. Scale bars indicate 500 nm and 100 nm, respectively. (f) Optical transmittance of an aligned AgNW decorated with Ag@SiO_2NPs film in the visible region. (g) Optical absorption spectra of aligned AgNW networks decorated with different densities of Ag@SiO_2NPs in the range of 300 – 650 nm. (h) Polarization dependent optical absorption spectra of aligned AgNW networks decorated with Ag@SiO_2NPs. Polarization angles are defined as parallel (0°of polarization) and perpendicular (90°of polarization) to the axis of the NWs.

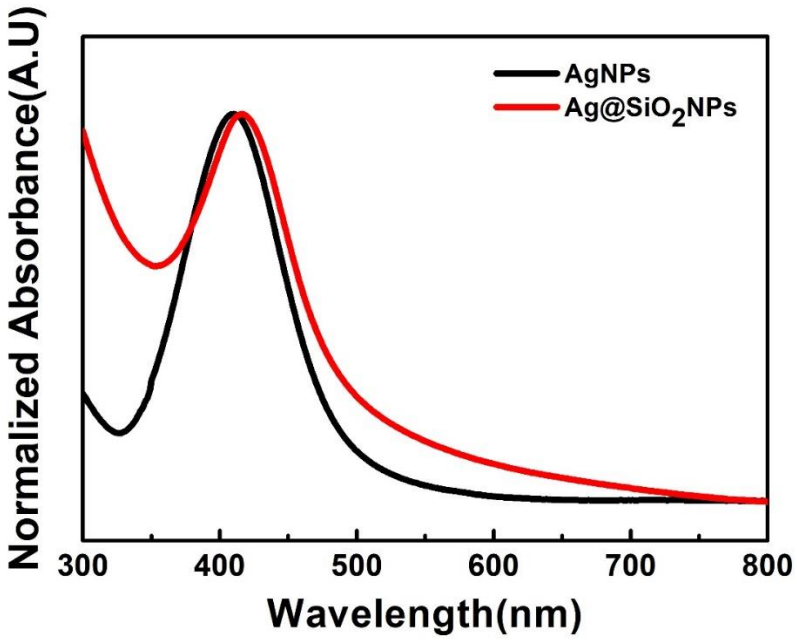

Figure 3.2 Optical absorption spectra of AgNPs and Ag@SiO_2NP in the range of 300 nm - 800 nm.

The optical absorption spectra of Ag@SiO_2NP films exhibit a broader and slightly red-shifted absorption band around 420 nm wavelength compared to AgNP films without shells (**Figure 3.2**), which is attributed to the dielectric environment change from air to SiO_2 which modulates the localized surface plasmon resonance (LSPR) frequency of AgNPs. The fabrication procedure of NP-enhanced plasmonic AgNW film is schematically illustrated in **Figure 3.3**.

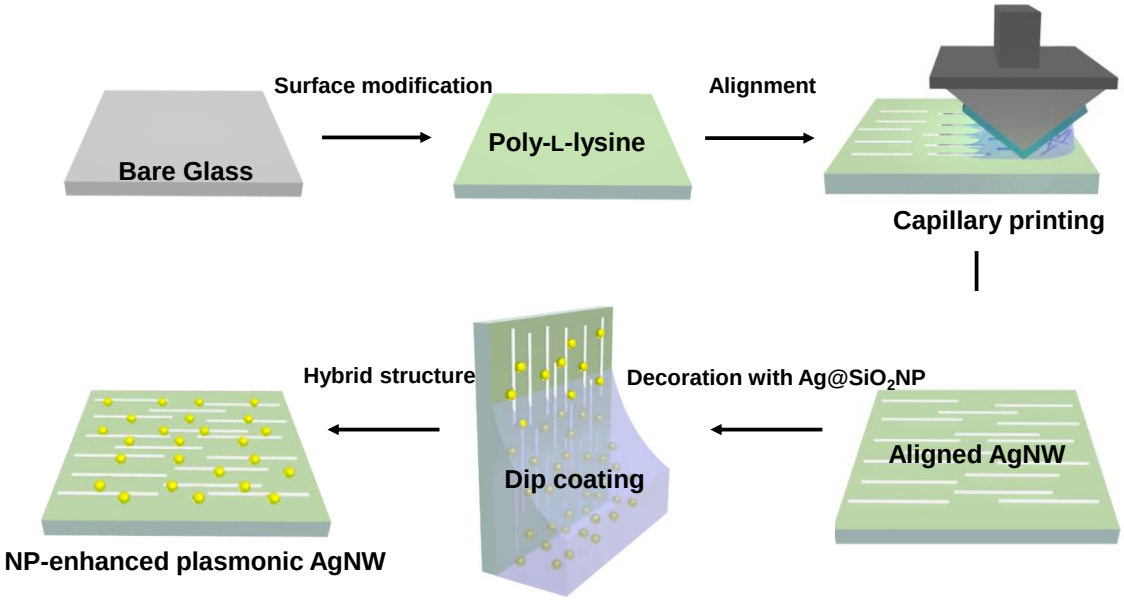

Figure 3.3 Schematic of fabrication process for NP-enhanced plasmonic AgNW electrodes on glass substrates.

The aligned AgNW networks are directly coated onto a glass substrate using a capillary printing technique after the modification of glass surface by amine-terminated poly-L-lysine (PLL) (**Figure 3.4**) [272].

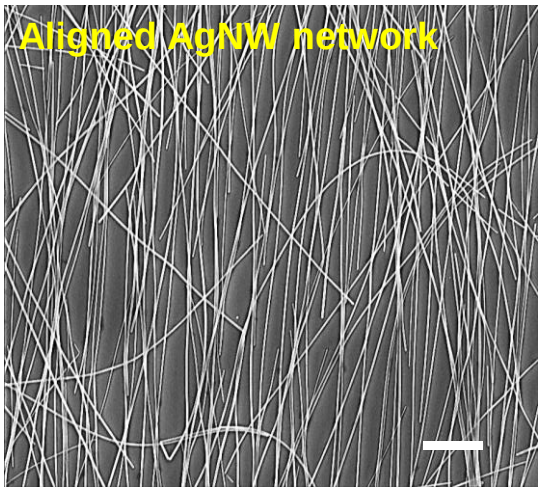

Figure 3.4 SEM images of aligned AgNW network. All scale bars indicate 1 μm.

Next, core-shell Ag@SiO_2NPs are uniformly coated onto the aligned AgNW networks using a dip coating method. **Figure 3.1d** shows a scanning electron microscope (SEM) image of the surface geometry of an NP-enhanced plasmonic AgNW film. It can be seen that Ag@SiO_2NPs are uniformly assembled onto and between the aligned AgNW networks. AgNPs adhered onto AgNWs provide NW-NP junctions which generate gap plasmon effects (**Figure 3.1e**). Moreover, the aligned AgNW networks have been demonstrated to exhibit a lower percolation threshold, resulting in significantly improved optical transmittance at a similar sheet resistance and smoother surface roughness compared to random AgNW networks[272]. Therefore, NP-enhanced plasmonic AgNW electrodes yield low sheet resistance (20.5 Ω/sq) and high transmittance (94.3% at 550 nm wavelength), allowing them to function as high performance transparent electrodes (**Figure 3.1f**).

The optical absorption spectra were collected with different densities of Ag@SiO_2NPs. NP-enhanced plasmonic AgNW films showed several absorption maxima, where 350 and 380 nm extinction peaks arise from the transverse SPR modes of AgNWs and the 420 nm extinction peak represents LSPR of AgNPs, respectively [266] (**Figure 3.1g**). The spectral intensities at 380 nm and 420 nm gradually increase with increasing surface density of Ag@SiO_2NPs, which can be attributed to a combination of absorption produced by plasmon excitations from the nano-antenna as well as the resonance couplings between SPRs of AgNPs and AgNWs[273]. To further investigate the plasmon coupling of NP-enhanced plasmonic AgNW films, we collected absorption spectra of aligned AgNW networks without AgNPs using light with different polarization directions. As shown in **Figure. 3.5**, the aligned AgNW networks clearly show polarization dependent absorption spectra according to the polarization direction of incident light relative to the NW orientantion. In contrast, random AgNW networks do not show polarization dependence. For the aligned AgNW networks, the intensities of two absorption maxima at ~350 and ~380 nm are strongly enhanced for incident light polarized perpendicular to the NWs due to two distinct transverse SPR modes. In contrast, the broad absorption at longer wavelengths (500 – 800 nm), arising from the longitudinal SPR modes of AgNWs, is enhanced when the incident light is polarized parallel to the NWs. This polarization dependent optical behavior is mainly attributed to optical anisotropy of the aligned AgNW networks [221, 274].

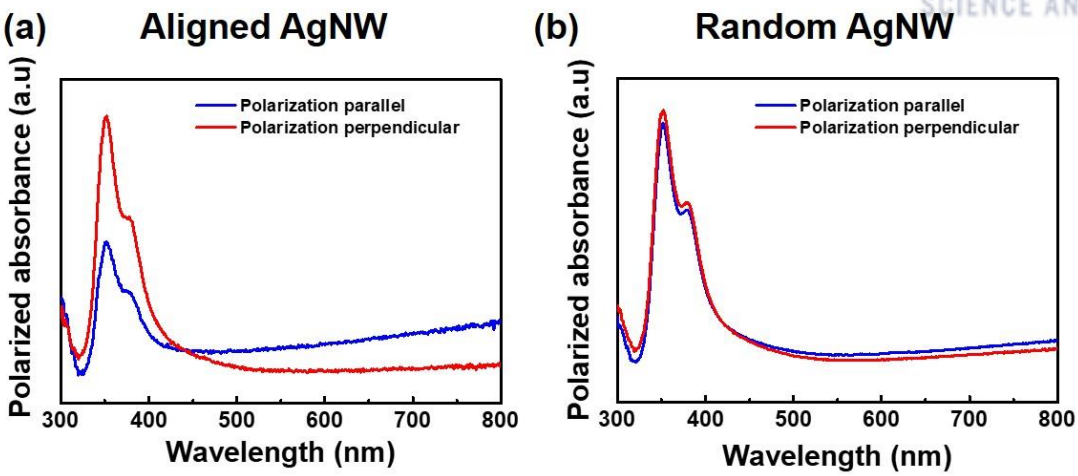

Figure 3.5 Simulated extinction spectra of a single AgNW and an AgNW-Ag@SiO_2NP junction.

Plasmonic behavior of NP-enhanced plasmonic AgNW films differs somewhat from aligned AgNW films. Previously, it has been reported that SPPs can be excited by incident light through the NP antenna on NWs and propagate along the NWs over tens of microns (with gradual energy loss by Ohmic damping) and can be scattered back into free-space photons by the NP antennas on the NWs [269, 275, 276]. **Figure 3.1h** shows polarized absorption spectra of NP-enhanced aligned plasmonic AgNW films with different polarization directions of incident light. Interestingly, when the incident light is polarized perpendicular to the NW axis, the intensities of transverse SPR peaks (350 and 380 nm peaks) of AgNWs are higher than those of parallel polarization, indicating the higher probability of excitation of transverse SPR modes of AgNWs at perpendicular polarization. In the meantime, the intensity of the LSPR peak (420 nm) of AgNPs for perpendicular polarization is lower than that of parallel polarization, suggesting that the LSPR mode of AgNPs is partially deactivated through the hybridization between LSPs of AgNPs and propagating SPPs on AgNWs. This result indicates that the coupling efficiency of NP-NW gap plasmons is higher at perpendicular than parallel polarization, in agreement with previous reports [277]. We also observe that the broad absorption at long wavelengths (500 to 800 nm) is higher for parallel polarization than for perpendicular polarization, implying that the longitudinal SPP modes on AgNWs are highly excited by parallel polarization (**Figure 3.1h**).

To elucidate NP-NW plasmon couplings, extinction spectra of NP-enhanced plasmonic AgNWs were simulated by the discrete dipole approximation (DDA) algorithm to calculate the E-field enhancement by NP-NW plasmon couplings. Simulated extinction spectra of both AgNW and Ag@SiO_2NP-AgNW systems were obtained where two distinct peaks at 372 and 402 nm are commonly observed due to transverse SPRs of AgNWs (**Figure 3.6**).

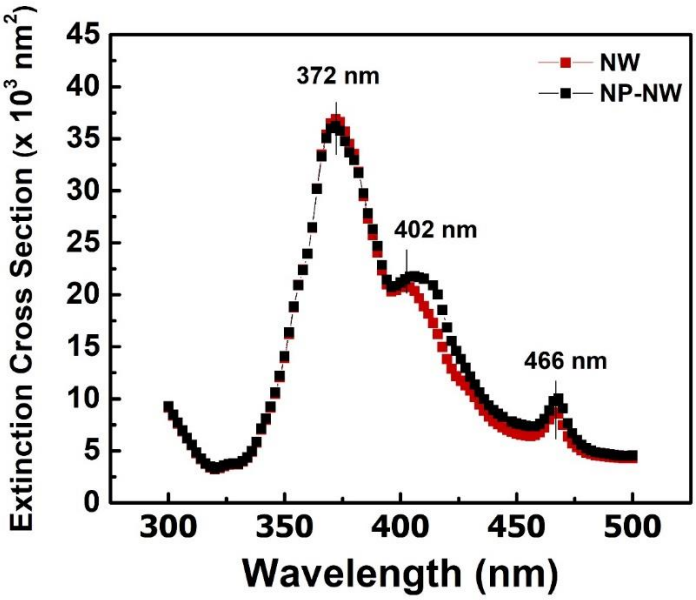

Figure 3.6 Simulated extinction spectra of a single AgNW and an AgNW-Ag@SiO_2NP junction.

One weak excitation mode at 466 nm was also observed due to the longitudinal SPR excitation along the axis parallel to the wire[278]. In addition, a significant extinction enhancement was observed at 416 nm with the addition of Ag@SiO_2NP in the NP-NW plasmonic system (**Figure 3.7**).

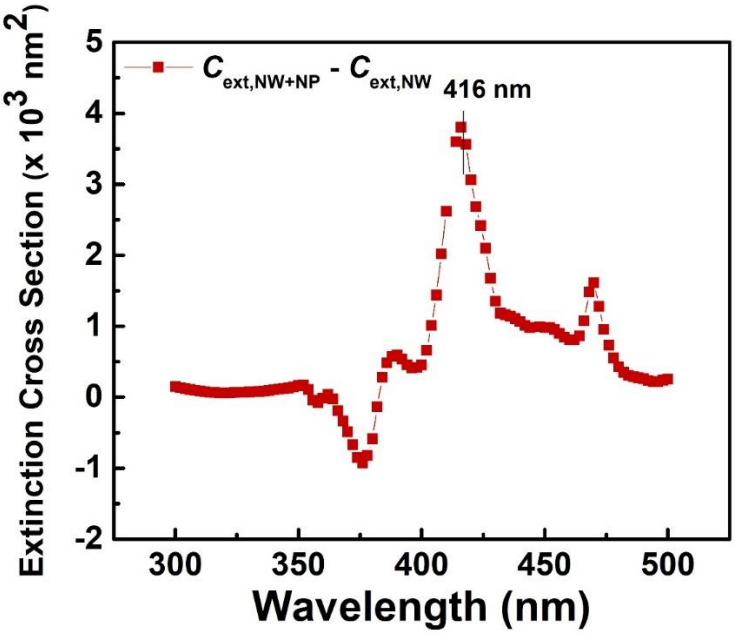

Figure 3.7 Enhancement in extinction spectrum of NP-enhanced plasmonic AgNWs.

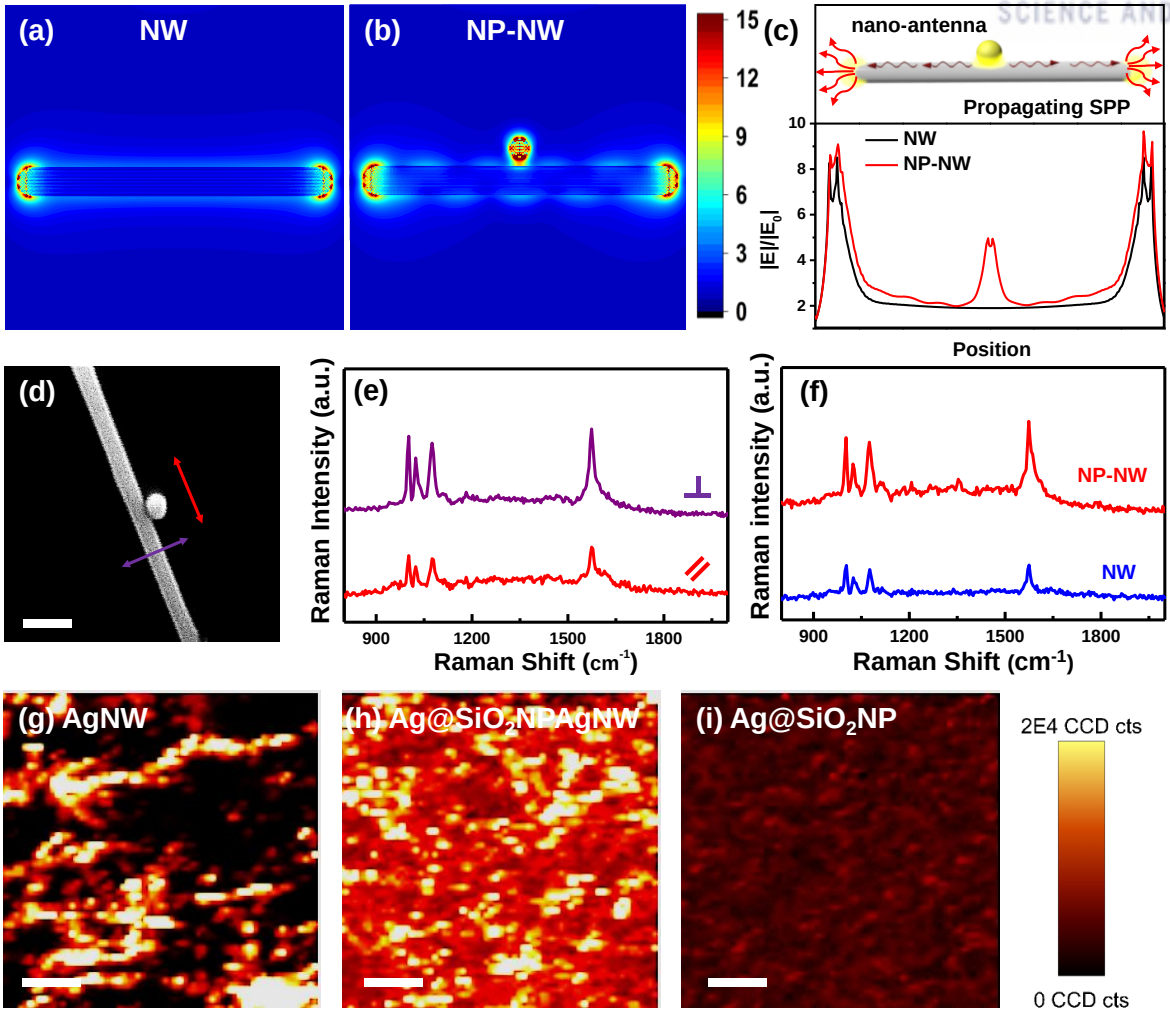

Figure 3.8 Plasmonic behavior of NP-enhanced plasmonic AgNW electrodes. E-field distribution of (a) an AgNW and (b) an AgNW decorated with an Ag@SiO_2NP. Incident light of 416 nm wavelength is polarized perpendicular to the long axis of the NW. (c) Schematic of plasmonic behavior of an AgNW decorated with an Ag@SiO_2NP. The AgNP on the AgNW acts as nano-antenna to couple incident light into SPPs propagating along the NW (upper). Calculated electric field intensity for NW and NP-NW along the NW length (bottom). (d,e) Raman analysis of a NP-NW system with different polarization angles of incident light. (d) SEM image of a single AgNW decorated with an AgNP for Raman analysis. The arrows indicate incident light with perpendicular (purple) and parallel (red) polarization along the NW direction, respectively. The scale bar is 100nm. (e) Raman spectra of poly-L-lysine (PLL) adsorbed on NP-NW junction by using incident laser with 532 nm wavelength, polarized perpendicular (purple) and parallel (red) along the NW direction. (f) Raman spectra of PLL adsorbed onto NW and NP-NW junction networks. (g-i) Surface-enhanced Raman spectroscopy (SERS) images. Raman mapping images of PLL adsorbed on AgNW, Ag@SiO_2NPs-AgNWs and Ag@SiO_2NPs on glass substrates.

Figure 3.8a,b show local electric-field enhancement images of NW and NP-NW systems, respectively, under 416 nm excitation for polarization perpendicular to the nanowire. E-field enhancement images for the NP-NW system show a giant enhancement of localized E-field at the NP-NW junction due to the strong gap plasmon couplings at the nanoscale gap of the NP-NW interface. **Figure 3.8c** shows normalized E-field intensities for NW and NP-NW systems along the NW length. In the NP-NW system, the gap plasmon effect between NW and NP provides significant E-field enhancement at NP-NW junction as well as additional E-field enhancement at both ends of the AgNW. The modeled E-field enhancements provide a conceptual basis to confirm the mechanism by which AgNPs adhered on AgNWs can act as nano-antennae which couple incident light into SPP modes in the AgNWs which propagate to both ends of the NW [276]. In addition, it has been reported that NP-NW coupling strongly depends on polarization direction where E-field enhancements are much larger for polarization perpendicular to NWs than for polarization parallel to NWs[269, 277]. In our simulation, for light polarization parallel to the NW, E-field enhancement at the NP-NW interface is relatively low compared to polarization perpendicular to the NW which demonstrates the existence of polarization dependent plasmon coupling (**Figure 3.8a,b** and **3.9**).

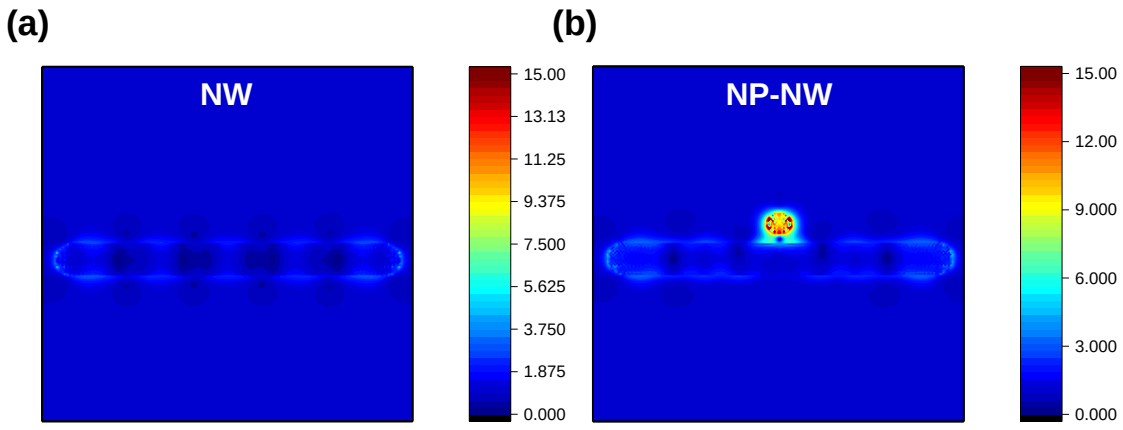

Figure 3.9 E-field distribution for single AgNW and AgNW decorated with Ag@SiO2NP when the incident light at 416 nm, polarized in parallel direction to NW.

To verify the plasmon coupling at NP-NW junctions, surface enhanced Raman scattering (SERS) spectra of NP-NW junctions absorbed on PLL were investigated under different polarizations in single NP-NW system as shown in **Figure 3.8d**. The Raman spectra of PLL at NP-NW junctions exhibits higher intensity when the incident light is polarized perpendicular to the NWs, which shows good agreement with the

simulation results (**Figure 3.8e**). In addition, the Raman intensity for NP-NW junctions is considerably larger than that for the NWs alone, indicating a giant enhancement due to the NP-NW plasmon coupling effect (**Figure 3.8f**). To compare plasmonic behavior of three different plasmonic systems including AgNW films, NP-enhanced plasmonic AgNW films, and Ag@SiO_2NP films, Raman mapping analysis images were obtained as shown in **Figure 3.8g-i**. SEM images of the three different systems showing their surface geometries are shown in **Figure 3.10**.

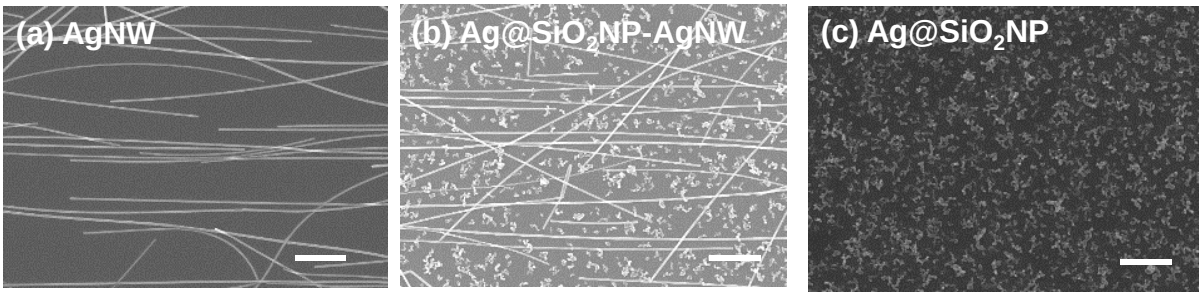

Figure 3.10 (a-c) SEM images for three different structures of (a) AgNW, (b) AgNW-Ag@SiO_2NPs, and (c) Ag@SiO_2NPs. All scale bars indicate 1 μm.

Notably, NP-enhanced plasmonic AgNW films showed the brightest regions with many intense spots, indicating that the strong NP-NW plasmon couplings resulted in overall increases in Raman intensity. On the other hand, AgNW films without NPs exhibited only local bright spots due to strong plasmon couplings at the junctions between AgNWs. In contrast, the Raman mapping image of an Ag@SiO_2NP film shows an entirely dark region with extremely low Raman signals, suggesting that NP-NP plasmon interactions in Ag@SiO_2NP assemblies are not the main factor in our NP-NW plasmonic system due to the larger gap distance formed by two SiO_2 shells at NP-NP contacts, which reduces the SERS intensities. The large improvement of Raman intensity distribution for NP-enhanced plasmonic AgNW films can be attributed to giant E-field enhancement due to NP-NW gap plasmon couplings.

To elucidate the effect of NP-NW plasmon coupling on OPV devices, we performed confocal laser scanning microscopy (CLSM) using Super Yellow (SY) as the fluorescence emissive layer coated on AgNWs and NP-enhanced plasmonic AgNW films, respectively (**Figures 3.11a,b**). For NP-enhanced plasmonic AgNW films, emission enhancement is clearly observed with a significant number of bright spots, corresponding points where Ag@SiO_2NPs couple to AgNWs, while weaker fluorescence emission is observed in the Ag NW only films, caused by a few NW-NW junctions. These results are consistent with enhanced fluorescence generated by SY within the near-field of NP-NW plasmon coupling points.

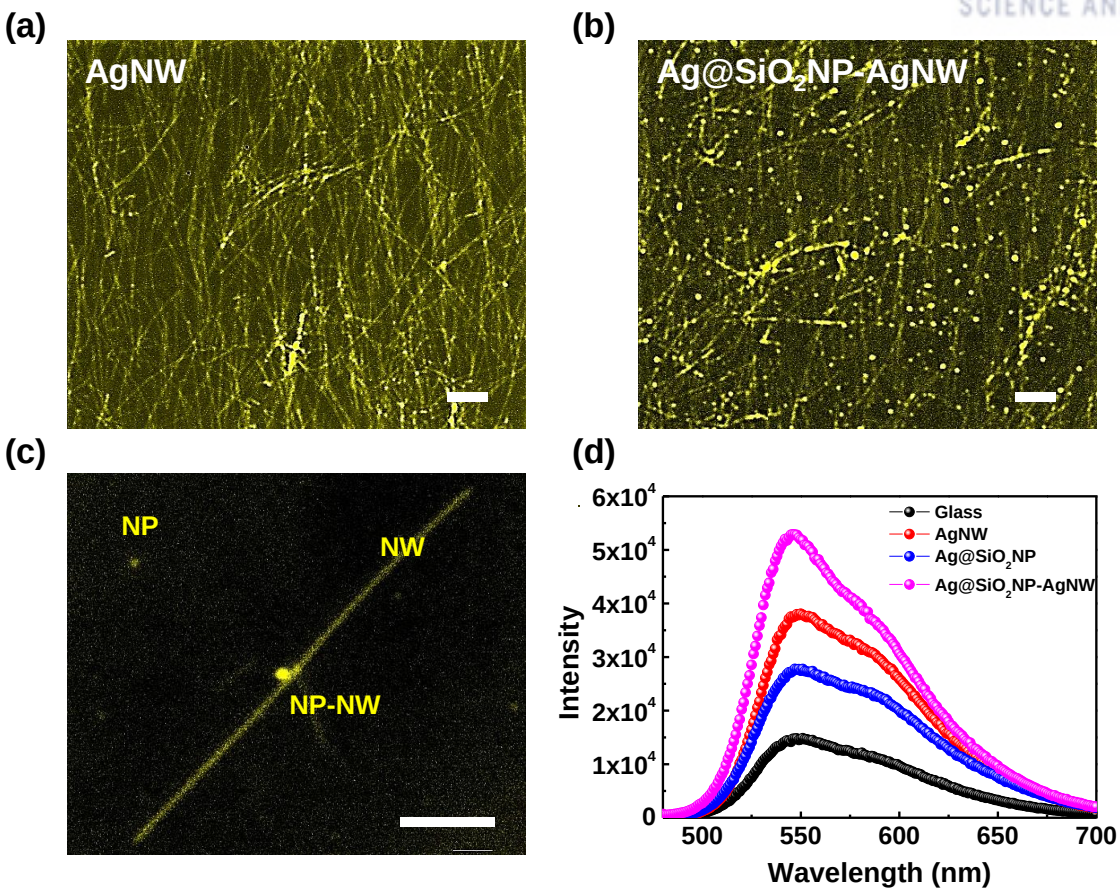

Figure 3.11 Photoluminescence behavior of fluorescent SY films on NP-enhanced plasmonic AgNW electrodes. Confocal images of (a) an aligned AgNW network and (b) an aligned AgNW network decorated by Ag@SiO_2NPs coated by SY. The scale bars indicate 5 μm. (c) Confocal image with high resolution of a single AgNW decorated by Ag@SiO_2NP, coated by SY where significant enhancement of fluorescence emission is observed at the NW-NP junction. The scale bar is 4 μm. (d) Steady-state photoluminescence spectra of the SY film with aligned an aligned AgNW network and an aligned AgNW network decorated by Ag@SiO_2NPs.

To further investigate emission enhancement due to NP-NW plasmon coupling, confocal images with high resolution were obtained for a single Ag@SiO_2NP decorated NW system as shown in **Figure 3.11c**. We observed photoluminescence (PL) enhancement for all three plasmonic systems including NW, NP, and NP-NW junction. Notably, NP-NW junctions show significantly enhanced emission compared to NWs or NPs alone, due to the giant near-field effect of the NP-NW plasmonic system, which is in good agreement with theoretical DDA simulations of the near-field enhancement.

Steady-state PL spectra of SY are plotted in **Figure 3.11d**, using different substrates including SY,

poly(3,4-ethylenedioxythiophene):polystyrene sulphonic acid (PEDOT:PSS/SY), AgNW/PEDOT:PSS/ SY, AgNP/PEDOT:PSS/SY and Ag@SiO_2NP-AgNW/PEDOT:PSS/SY films coated on quartz substrates. As a control, we tested SY films on top of PEDOT:PSS. Among these spectra, the PEDOT:PSS/SY film showed the lowest photoluminescence due to exciton quenching at the PEDOT:PSS/SY interface. Ag@SiO_2NP-AgNW/PEDOT:PSS/SY films showed the highest PL intensity due to the NP-NW plasmon coupling effect, compared to films with AgNPs or AgNWs alone. The results of photoluminescence are consistent with confocal microscopy results which support fluorescence emission enhancement due to NP-enhanced plasmonic AgNW networks.

To investigate the effect of plasmon coupling on the improvement of device performance in OSCs and OLEDs, first, we fabricated fluorescent OLEDs with NP-enhanced plasmonic AgNW electrodes to improve the light emitting properties of the OLEDs. The device structure and energy diagram are schematically illustrated in **Figures 3.12a,b**. SY was used as the emissive layer to ensure high-performance OLEDs [236, 260]. **Figures 3.12c-f** show OLED characteristics of devices using ITO, aligned AgNWs and NP-enhanced plasmonic AgNW electrodes.

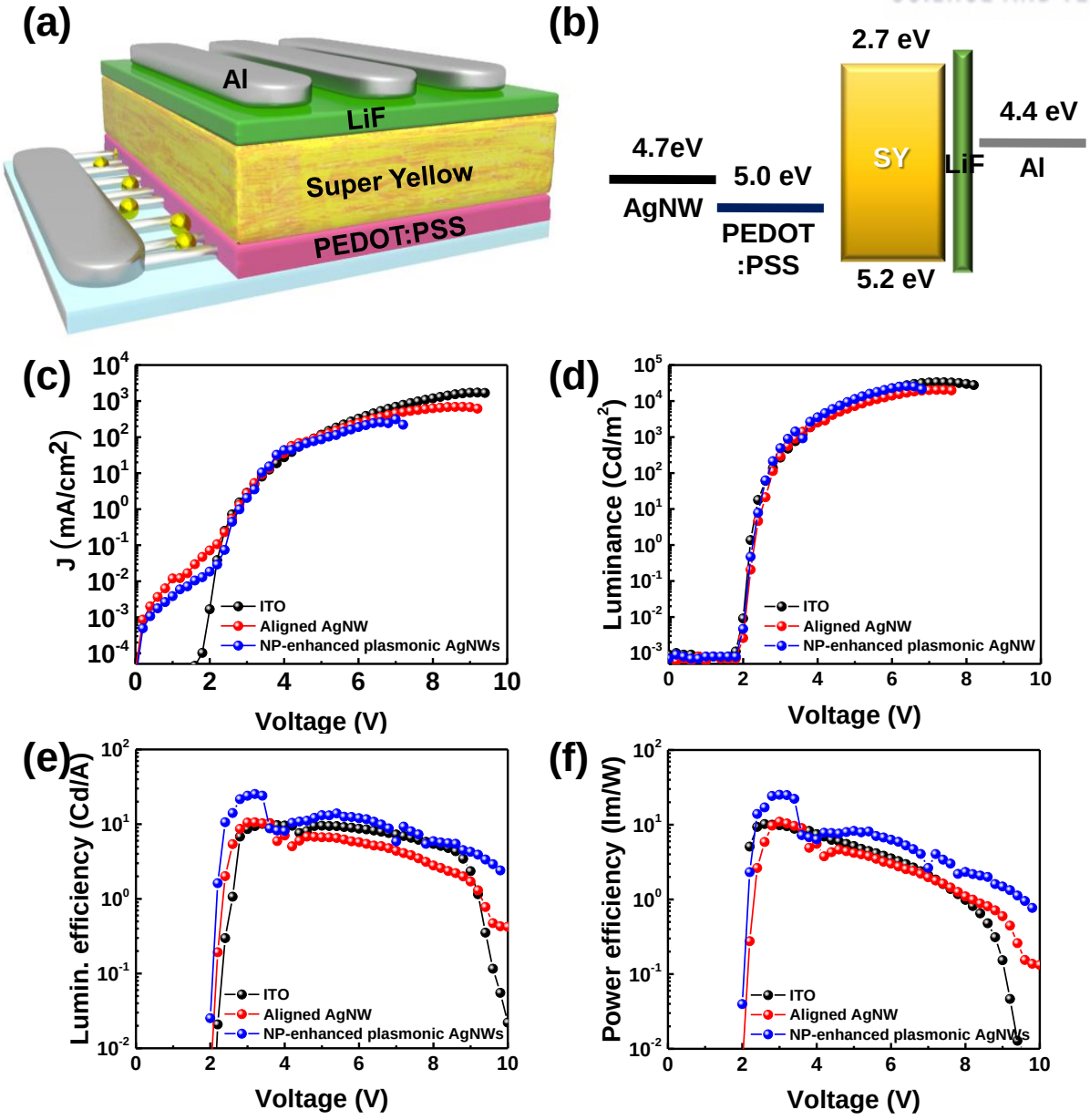

Figure 3.12 Device structure and characteristics of OLEDs using NP-enhanced plasmonic AgNW electrodes. (a) Schematic device structure of OLEDs with NP-enhanced plasmonic AgNW electrodes. (b) Schematic energy level diagram under the flat-band condition. (c) Current density, (d) luminance, (e) luminous efficiency and (f) power efficiency versus applied voltage for OLEDs with ITO, aligned AgNW, and NP-enhanced plasmonic AgNW electrodes.

In our previous work, we reported an improvement of device performance in OSCs and OLEDs using aligned AgNWs due to coverage of protruding features and poor surface coverage [272]. As shown in **Figure**

3.12c, both devices with NP-enhanced plasmonic AgNW and aligned AgNW electrodes showed low leakage currents with a turn on voltage of 2.0 V due to the smooth surface morphology of aligned AgNW networks. The devices with NP-enhanced plasmonic AgNW electrodes showed similar current density and reduced voltage for maximum luminance compared to devices with aligned AgNW only electrodes. The device with NP-enhanced plasmonic AgNW electrodes showed substantially improved light-emitting properties with the highest luminance (29991 cd/m2 at 7.2 V for the device with NP-enhanced plasmonic AgNW electrode and 20436 cd/m2 at 7.4 V for the device with aligned AgNW electrode) as shown in **Figure 3.12d**. In particular, the EL efficiency and power efficiency were found to be 25.33 cd/A, and 25.14 lm/W, respectively, for the device with NP-enhanced plasmonic AgNW electrodes, which are more than twice as large compared to aligned AgNW only electrodes (EL efficiency and power efficiency is 10.57 cd/A, and 10.98 lm/W). Control devices with ITO electrodes exhibited an EL efficiency of 10.28 cd/A and power efficiency of 9.31 lm/W. In particular, the device with NP-enhanced plasmonic AgNW electrodes exhibited by far the highest power efficiency of 25.14 lm/W. These values of EL efficiency and power efficiency are the highest values reported so far using ITO-free TCEs for fluorescent OLEDs [203 238 239]. The improved device performance with NP-enhanced plasmonic AgNW electrodes can be attributed to strong plasmon coupling light into LSPs of NPs and SPPs of NWs, resulting in outstanding E-field enhancement at NP-NW interfaces due to the NP-NW gap plasmon effect. Fluorescence emission enhancement of the SY film with NP-enhanced plasmonic AgNW electrodes also supports the improved device performance in OLEDs, which was further confirmed by solid state PL measurements and CLSM.

To investigate OSC characteristics with NP-enhanced plasmonic AgNW electrodes, we employed various approaches to demonstrate the effect of plasmon coupling. The device structure and energy diagram are schematically illustrated in **Figure 3.13a** and **b**. Blended poly[4,8-bis(5-(2-ethylhexyl) thiophen-2-yl)benzo[1,2-b:4,5-b′]dithiophene-co-3-fluorothieno[3,4-b]thiophene-2-carboxylate] (PTB7-Th):[6,6]-phenyl-C71 butyric acid methyl ester ($PC_{71}BM$) electron donor/electron acceptor bulk heterojunctions were used as the active layers to ensure high-performance OSCs [244].

Figure 3.13c shows the *J-V* characteristics of OSC devices using ITO, aligned AgNW and NP-enhanced plasmonic AgNW electrodes. Both OSCs using two different electrodes showed higher fill factors of 0.70 and 0.71 due to the smooth surface morphology of aligned AgNW networks[274]. The J_{sc} value of 16.25 mA/cm^2 for the device with NP-enhanced AgNW electrode was improved compared to the J_{sc} values of 14.58 mA/cm^2 and 15.20 mA/cm^2 observed for aligned AgNW and ITO electrodes, respectively, whereas values of V_{oc} and *FF* remained similar. The increase in J_{sc} with NP-enhanced plasmonic AgNW electrode was verified by external quantum efficiency (EQE) enhancement in the range of 300-800 nm, as shown in **Figure 3.13d** and **Figure 3.14**.

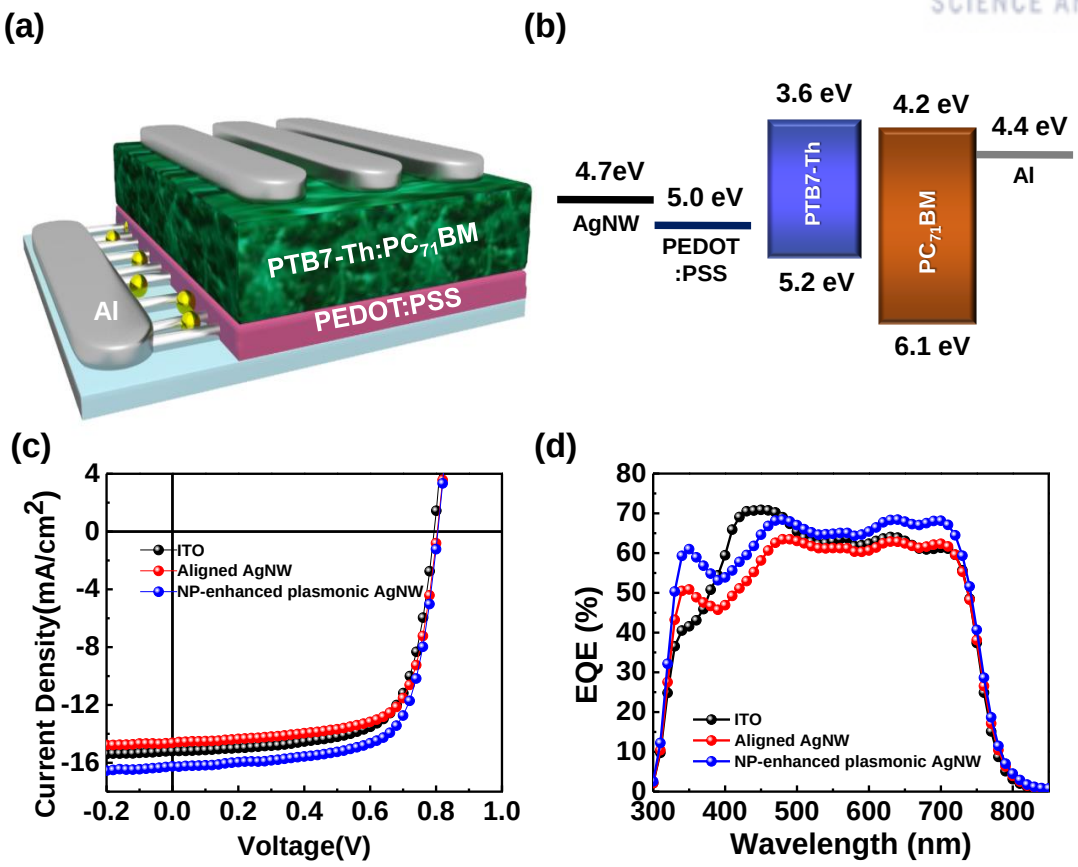

Figure 3.13 Device structure and characteristics of OSCs using NP-enhanced plasmonic AgNW electrodes. (a) Schematic device structure of OSCs with NP-enhanced plasmonic AgNW electrodes. (b) Schematic energy level diagram under the flat-band condition. (c) *J-V* characteristics of under AM 1.5G illumination at 100mW cm^{-2}. (d) IPCE spectra of OSCs using ITO, aligned AgNW and NP-enhanced plasmonic AgNW electrodes.

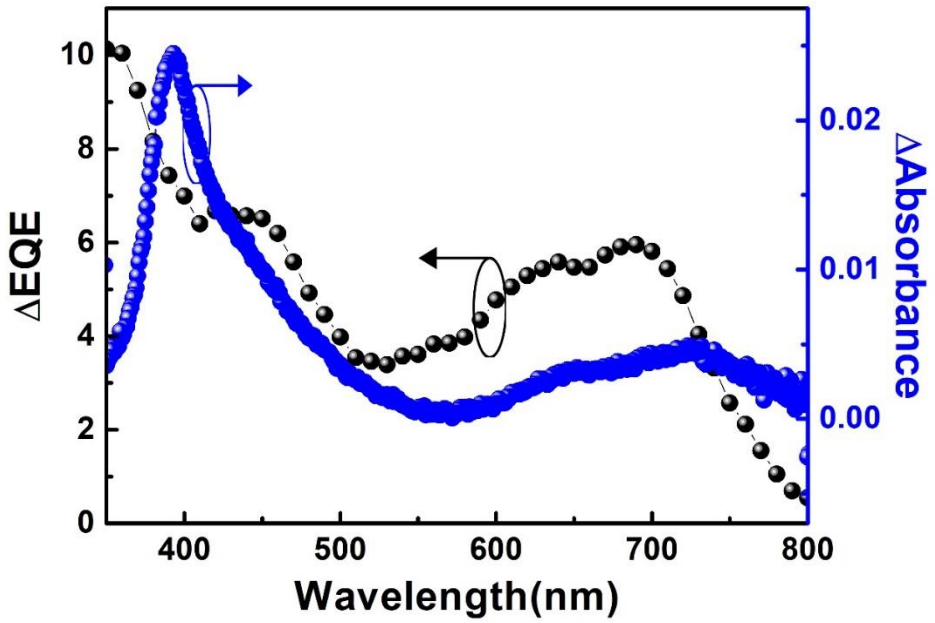

Figure 3.14 Comparison of EQE enhancement with absorption changes caused by AgNW-Ag@SiO_2NPs.

To clarify the plasmon coupling effect of NP-enhanced plasmonic AgNW electrodes on the photogeneration of charge carriers, we calculated the changes in absorption (Δabsorbance) and EQE (ΔEQE) of the NP-enhanced plasmonic AgNW devices. **Figure 3.14** shows that the enhancement of EQE is consistent with increases in absorption, showing similar enhancement peaks at wavelengths of 400 nm and 700 nm. As a result of these features, we achieved excellent PCEs of up to 9.19% for the OSCs with NP-enhanced plasmonic AgNW electrodes, constituting a ~10% enhancement compared to 8.28% observed for aligned AgNW electrodes (**Table 3.1**). Note that the PCE value of 9.19% represents the highest device efficiency reported for OSC devices using AgNW electrodes (**Table 3.1**).

Table 3.1 Comparison of results achieved in this work with the performance of perviously reported AgNW-based PSCs.

PSC configuration	Active layer materials	J_{sc} [mA cm^{-2}]	V_{oc} [V]	*FF*	PCE [%]	Reference
Inverted	PTB7:$PC_{71}BM$	16.77	0.75	0.62	7.88	*Nano Res. 2014*[227]
Conventional	PTB7:$PC_{71}BM$	20.73	0.67	0.55	7.38	*Small 2014*[268]
Conventional	PTB7-F20:$PC_{71}BM$	14.40	0.67	0.59	5.80	*Adv. Funct. Mater. 2013*[245]
Conventional	PBnDT-DTffBT:$PC_{71}BM$	9.64	0.59	0.48	2.80	*ACS Appl. Mater. Interfaces 2011*[279]
Conventional	PTB7-Th:$PC_{71}BM$	17.00	0.76	0.65	8.40	*Nano lett.2015*[272]
Inverted	PTB7-Th:$PC_{71}BM$	17.8	0.76	0.64	8.94	*Adv. Mater. 2017*[280]
Conventional	PTB7-Th:$PC_{71}BM$	16.25	0.81	0.70	9.19	Our work

To investigate the charge generation and extraction processes using NP-enhanced plasmonic AgNW electrodes, photocurrent (J_{ph}) versus effective voltage (V_{eff}) is plotted for OSCs under illuminated and in the dark (**Figure 3.15**). J_{ph} is given by $J_{ph} = J_L - J_D$, where J_L is illuminated current density and J_D is dark current density. V_{eff} is given by $V_{eff} = V_0 - V$, where V_0 is the compensation voltage at $J_{ph} = 0$ and V is the applied bias voltage. Log–log plots of J_{ph}–V_{eff} show a transition to saturation regime at certain V_{eff}, where it bedomes limited by the field and G using the following equation (1);

$$J_{sat} = qLG_{max} \quad (1)$$

where q is the elementary charge, L is the thickness of the active layer, and G_{max} is the maximum photo-induced carrier generation rate per unit volume. The OSCs with NP-enhanced plasmonic AgNW electrodes reached the saturation region at lower field compared to OSCs with aligned AgNW electrodes (**Fig 3.15**).

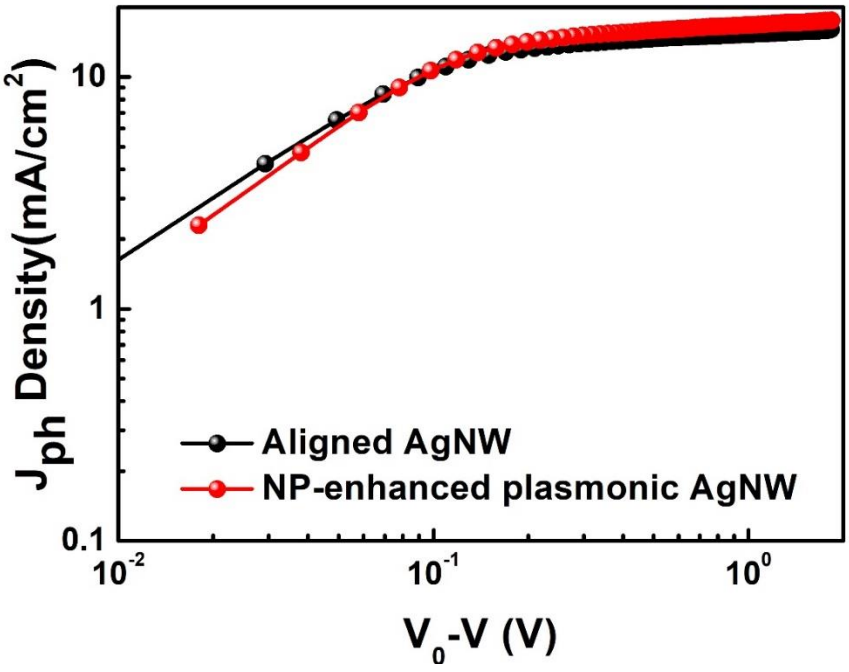

Figure 3.15 Photocurrent density versus effective voltage for devices with AgNW and Ag@SiO2NPs-AgNW electrodes.

This result is evidence that the excitation of LSP modes generated excitons which dissociated to free charge carriers. Consequentially, it is inferred that the photocurrent generated by LSP not only improved the exciton generation rate but also exciton dissociation [281].

3.4 Conclusion

We have demonstrated the use of NP-enhanced plasmonic AgNW electrodes, consisting of aligned AgNW networks decorated by core-shell Ag@SiO_2NPs, for the improvement of device efficiency in both OLEDs and OSCs. The NP-enhanced plasmonic AgNW electrodes functioned as outstanding transparent electrodes as well as performing as hybrid plasmonic structures. In the NP-NW hybrid plasmonic system, AgNPs played an important role as nanoantennae, serving to couple incoming light into NW plasmons propagating along the NW, resulting in large near-field enhancement, which affected light absorption efficiency in OSCs. In addition, simulated near-field distributions of the NP-NW system exhibited giant local E-field enhancement at NP-NW junctions due to strong gap plasmon coupling between LSPs of AgNPs and propagating SPPs of AgNWs. Raman mapping results revealed that strong plasmon coupling

in the NW-NP system provides large E-field enhancement at NP-NW junctions. Additionally, we achieved high EL efficiencies of up to 25.33 cd/A (at 3.2 V) and power efficiency of 25.14 lm/W (3.0 V) in fluorescent LEDs as well as a PCE of 9.19% in OSCs using Ag@SiO_2NP-AgNW electrodes. These significant results represent the highest efficiency reported for OLEDs and OSCs based on AgNW electrodes. Furthermore, NP-enhanced plasmonic AgNW films may be further explored for use in a variety of optoelectronic devices and other plasmonic applications.

Chapter 4. Considerations on The Optical and Morphological Behavior for High-Performance Ternary Blend Polymer Solar Cells Combining Two Acceptors.

4.1 Research background

Light-weight, mechanical flexibility, and large-area processibility with low-cost have allowed polymer solar cell to be a promising candidate for next generation solar cells.[254, 257, 282, 283] Low power conversion efficiency (PCE) of polymer solar cells, however, is still catching up with them being a major player in current photovoltaic market. Strenuous efforts of developing new materials by chemists and identifying device physics and charge carrier dynamics by physicists in solar cell research community have paid off by reaching 11.5% of record efficiency by Zhao et al. in 2016,[284] which was certified by Newport.

As an efficient strategy to boost PCE of the solar cells, intensive studies on ternary blend polymer solar cells (TPSCs),[165, 166, 285] which embeds third component into the active layer, have been reported due to their innocuous and synergistic collaboration with preexisting donor and acceptor materials without additional fabrication process. Because of the difficulty of synthesizing new acceptor outperforming [6,6]-phenyl C_{71} butyric acid methyl ester ($PC_{71}BM$), most researches have focused on the two donors system,[285-290] in which two electron donor materials and one acceptor material are adopted as active materials. Broad applications of TPSC have been intensively reported; applying third component as light sensitizer,[291, 292] a charge relay,[293, 294] or a phase modulation agent[295] for optimized morphology of bulk heterojunction (BHJ) blend.

Although a major portion of recent studies on TPSCs have concentrated on two donor systems, a few reports on two acceptor system have also demonstrated their significant potentials by enhancing spectral response in near infrared (NIR) region[296] or optimizing morphology[297] and energy levels of organic blends.[173] Nevertheless, it has still lacked in understanding charge carrier dynamics of two acceptors system, the studies on morphology, and even in absolute amount of studies on the system compared to two donors system.

We fabricated bulkheterojunction (BHJ) polymer solar cells using 1,4-bis(5-(trimethylstannyl)thiophene-2,5-diflurobenzene and (4,8-bis(5-(2-ethylhexyl)thiophen-2-yl)benzo[1,2-b:4,5-b']dithiophene-2,6-diyl)bis(trimethylstannane) (PBTTFB) as donor and $PC_{71}BM$ as acceptor.[2] Outstanding open circuit voltage (V_{OC}) of 0.99 V was achieved due to wide bandgap (1.89 eV) of PBTTFB. But its narrow spectral response up to 660 nm limited short circuit current density (J_{SC}) less than 11 mA/cm^2. In order to extend light sensitization to near infrared, one of the widely used non-fullerene acceptor, 3,9-bis(2methylene-(3-(1,1-dicyanomethylene)-indanone))-5,5,11,11-tetrakis(4-hexylphenyl)-dithieno[2,3-d:2’3’-d’]-s-indaceno[1,2-b:5,6-b’]dithiophene) (ITIC) was introduced in active layer as a third component.

Detailed molecular structures are shown in **Figure 4.1a**. During the device optimization process, we confirmed that introducing ITIC exhibited significant improvement in the absorption of photon with longer wavelengths, as we expected. Unfortunately, unexpected problems followed on it. Mixing $PC_{71}BM$ with more than adequate amount of ITIC caused the formation of large agglomerates, which was confirmed by grazing incidence wide angle X-ray spectroscopy (GIWAXS) and atomic force microscope (AFM).

In this study, we thoroughly characterize photovoltaic parameters of the TPSCs with different acceptor weight ratio, morphologies of the ternary blends, and optical alternations after introducing ITIC into the binary BHJ via transfer matrix formalism (TMF). Along with the characterization, we address the issue arising from the system, which has not been reported so far, but must be considered before trying TPSC strategy using two famous electron acceptors simultaneously. Nevertheless, it is proved that ITIC is still a great option for NIR photon harvest, according to the results of optical simulation.

4.2 Experimental

General

Poly(3,4-ethylenedioxythiophene):poly(4-styrenesulfonate) (PEDOT:PSS) (Baytron AI 4083 and PH500) were purchased from H. C. Starck (Germany). PTFFTB was synthesized according to the literature. [6,6]-phenyl-C_{71}-butyric acid methyl ester ($PC_{71}BM$) and 3,9-bis(2-methylene-(3-(1,1-dicyanomethylene)-indanone))-5,5,11,11-tetrakis(4-hexylphenyl)-dithieno[2,3-d:2',3'-d']-s-indaceno[1,2-b:5,6-b']dithiophene (ITIC) were purchased from Organic Semiconductor Materials (OSM) and 1-materials Index Co., Ltd. The optical properties of composite films were analyzed using a UV-vis spectrophotometer (Varian Carry 5000). The atomic force microscopy (AFM) images (2 μm × 2 μm) were obtained using a Veeco AFM microscope in a tapping mode.

2D-GIXRD measurement

GIXRD measurements were carried out at PLS-II 9A U-SAXS beam line of Pohang Accelerator Laboratory, Korea. The X-ray coming from the in-vacuum undulator (IVU) was monochromated (Ek = 11.06 keV, λ = 1.103 Å) using a Si(111) double crystal monochromator and focused horizontally and vertically at the sample position (450 (H) x 60 (V) μm2 in FWHM) using KB type focusing mirror system. The GIXRD sample stage was equipped with a 7-axis motorized stage for the fine alignment of the thin sample and the incidence angle of X-ray was adjusted to 0.12º~0.14º. GIXRD patterns were recorded with a 2D CCD detector (Rayonix SX165, USA) and X-ray irradiation time was 0.5 ~ 5 s dependent on the saturation level of the detector. The diffraction angle was calibrated by a pre-calibrated sucrose (Monoclinic, P21, a = 10.8631 Å, b = 8.7044 Å, c = 7.7624 Å, β = 102.938o) and the sample-to-detector distance was about 232 mm.

Fabrication and characterization of PSCs

The PSC device was fabricated with a configuration of ITO/PEDOT:PSS/PTFFTB:$PC_{71}BM$:ITIC/Al. The devices were fabricated according to the following procedures: First, ITO-coated glass substrates were cleaned with detergent, then sequentially ultrasonicated in acetone and isopropyl alcohol and dried in an oven overnight at 100 °C. The PEDOT:PSS layer was spin-coated (after filtration through a 0.45 μm filter) at 5000 rpm for 40 s, baked at 140 °C for 10 min in air and then moved into a nitrogen filled glove box. A mixed solution (12mg/ml) of PTFFTB:$PC_{71}BM$ (or PTFFTB:ITIC or PTFFTB:($PC_{71}BM$+ITIC)) (blend ratio = 1:1.5 by weight) in chlorobenzene: diphenylether (DPE) (97:3 vol%) was spin-coated at 1300 rpm for 60 s on top of the PEDOT:PSS layers. Devices were then brought under vacuum (< 10–6 torr), and a 100 nm thick Al electrode was deposited on top of the active layer by thermal evaporation. The deposited Al electrode area defined the active area of the devices as 13 mm^2. Measurements were carried out inside a glove box using a high quality optical fiber to guide the light from the solar simulator. *J-V* characteristics were measured under AM 1.5G illumination (100 mWcm-2) with a Keithley 2635A source measurement unit. EQE measurements were conducted in air using an EQE system (Model QEX7) by PV measurements Inc. (Boulder, Colorado).

4.3 Results and discussion

Ternary blend comprises a wide band gap polymer PBTTFB with a strong absorption from 400 to 660 nm (See **Figure 4.1b**) as donor and two acceptors with a complementary absorption below 450 nm for $PC_{71}BM$ and the additional absorption from 650 to 780 nm for ITIC, which allows broad light absorption coverage from 300 to 780 nm.

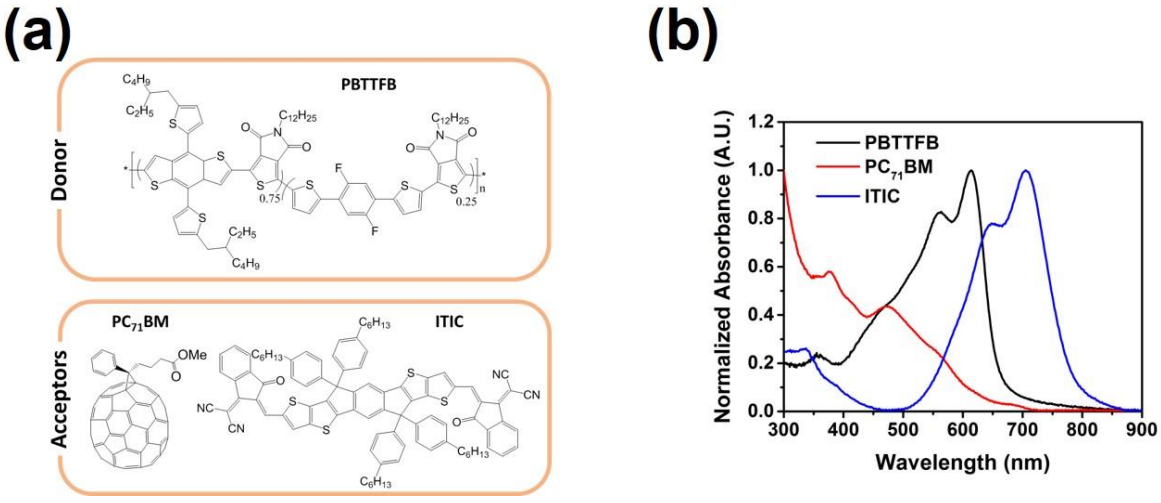

Figure 4.1 (a) Molecular structure of PBTTFB, ITIC and $PC_{71}BM$. (b) UV-vis-NIR absorption spectra of pristine organic thin films.

Absorption spectrum of ternary blends are shown in **Figure 4 2a**. All spectra were normalized by 0-0 vibronic transition of PBTTFB. As we expected in the absorption spectrum of each material, spectral response of the ternary blends was intentionally tuned by varying the ratio between two acceptors, e.g. measured absorbance was enhanced in the wavelengths below (above) 600 nm as the amount of $PC_{71}BM$ (ITIC) became dominant in the ternary blend.

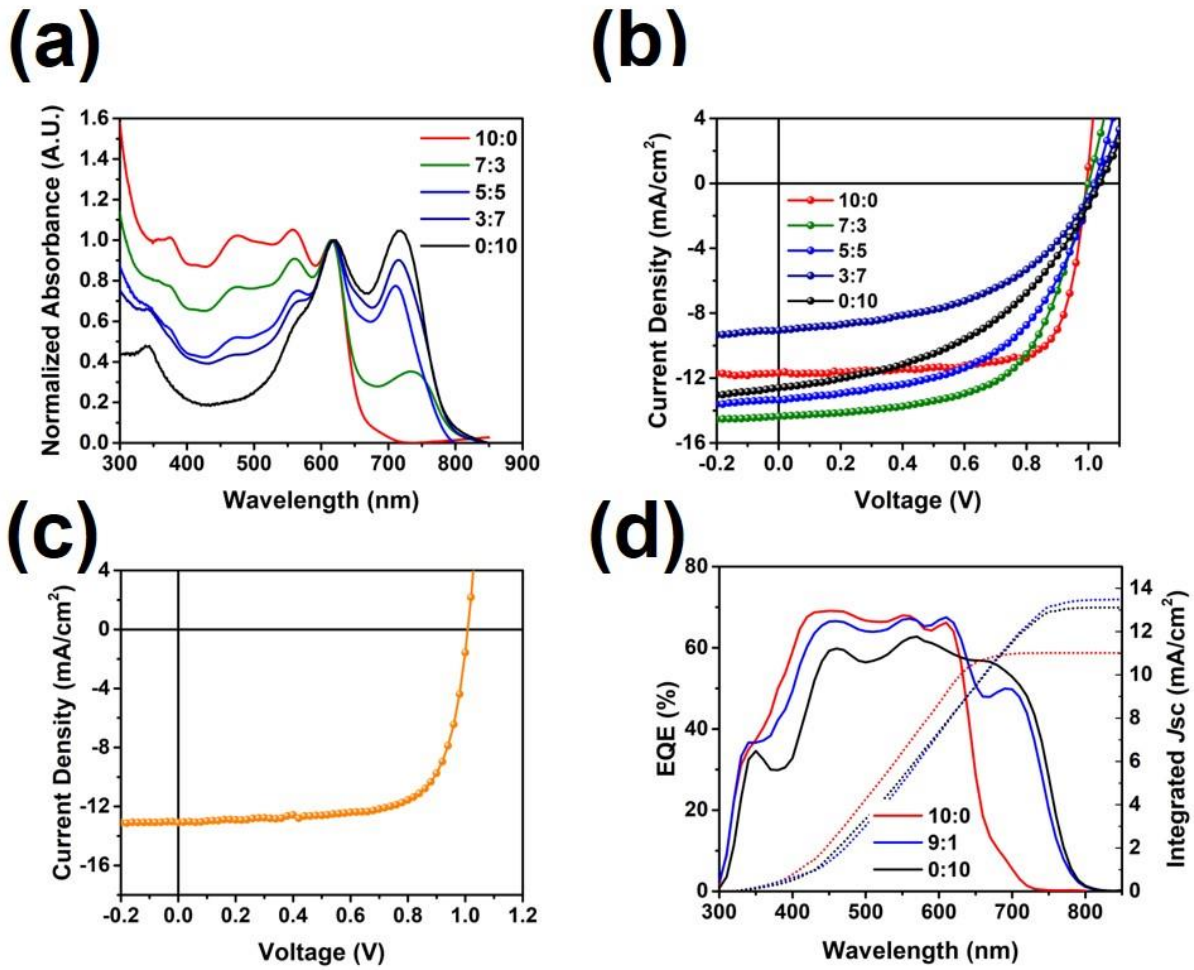

Figure 4.2 (a) UV-vis-NIR absorption spectra of polymer blend films. (b) J-V characteristics of TPCSs with various blend ratio and (c) the characteristics at the optimum condition (9:1). (d) Measured and simulated external quantum efficiency and corresponding integrated *J*sc curve of TPSCs with 10:0, 9:1 and 0:10 blend ratio (X:Y = $PC_{71}BM$:ITIC).

TPSCs were fabricated using the ternary blend with a device configuration of ITO/PEDOT:PSS/ternary blend/Al, where PEDOT:PSS (poly (3, 4-ethylenedioxythiophene): poly (styrene-sulfonate)) was utilized as hole transport layer. *J-V* characteristics of the fabricated TPSCs are shown in **Figure 4 2b** and

photovoltaic parameters are summarized in **Table 4 1**. PBTTFB:$PC_{71}BM$ binary solar cells (denoted as 10:0 in the figure) exhibited outstanding V_{OC} and *FF* of 0.99 V and 0.74, respectively. But its relatively low J_{SC} limited PCE to less than 8%. The device with 7:3 of acceptor weight ratio revealed significantly enhanced J_{SC} up to 14.4 mA/cm^2. This enhancement is attributed to the broaden light absorption up to 780 nm by ITIC addition. However, further increasing the amount of ITIC in the ternary blend resulted in significantly reduced J_{SC} and *FF*; 9.10 mA/cm^2 and 0.49 in the device with 3:7 weight ratio, while V_{OC} was almost unchanged in all conditions. PBTTFB:ITIC binary device showed recovered J_{SC} of 12.59 mA/cm^2, but further decreases in *FF* of 0.45. Device performance was optimized at 9:1 $PC_{71}BM$ to ITIC weight ratio. *J-V* characteristics of optimized device conditions are represented in **Figure 2c**. 10% of ITIC in the ternary blend allowed negligible change in V_{OC} and *FF*, relative to PBTTFB:$PC_{71}BM$ binary solar cell, but significantly boosted J_{SC} to 13.48 mA/cm^2. According to integrated J_{SC} plot in **Figure 2d**, the increase in J_{SC} of the device with 9:1 ratio corresponds to high external quantum efficiency (EQE) at longer wavelengths even with 10% of ITIC in the ternary blend. Interestingly, the difference of EQE spectrum between 9:1 and 0: 10 device (PBTTFB:ITIC binary solar cell) in the wavelengths from 650 to 780 nm was not dramatic even if the difference in the amount of ITIC in the active blend is huge.

Table 4.1 Summary of photovoltaic parameters

Acceptor ratio (X:Y)	J_{sc} (mA/cm^2)	V_{oc} (V)	*FF*	η (%)
10:0	10.79	0.99	0.74	7.98
7:3	14.4	1.01	0.60	8.66
5:5	13.4	1.02	0.54	7.29
3:7	9.10	1.02	0.49	4.51
0:10	12.59	1.04	0.45	5.91
9:1 (Opt.)	**13.48**	**1.01**	**0.71**	**9.73**

In order to characterize the morphology of blend film, AFM was carried out (**Figure 4.3**). 10:0 binary blend showed the smoothest surface roughness (1.17 nm) with homogeneous phase mixing, which indicates that ideal mixing between PBTTFB and $PC_{71}BM$ produces photoinduced current with the least carrier recombination before charge collection at the electrode, resulting in the device with high *FF* as shown in Figure 2b. As increasing the contents of ITIC, however, the size of phase become bigger with rougher root-mean-square (rms) roughness; 16.9 nm of rms roughness was observed in the blend with 3:7 acceptor weight ratio. However, slightly rough but the phase mixing without noticeable aggregation in 0:10 binary

blend reveals that the aggregation observed in the ternary blends arises from the strong intermolecular interaction between $PC_{71}BM$ and ITIC, not between PBTTFB and ITIC. These unintended agglomerates would cause inefficient charge transfer between active materials and, as a result, the performance of devices would decrease. At optimum condition, 9:1 blend ratio, smooth and homogeneous morphology, similar to 10:0 binary blend, implies that 10% of ITIC in the blend is safe to maintain the ideal morphology formed by PBTTFB and $PC_{71}BM$.

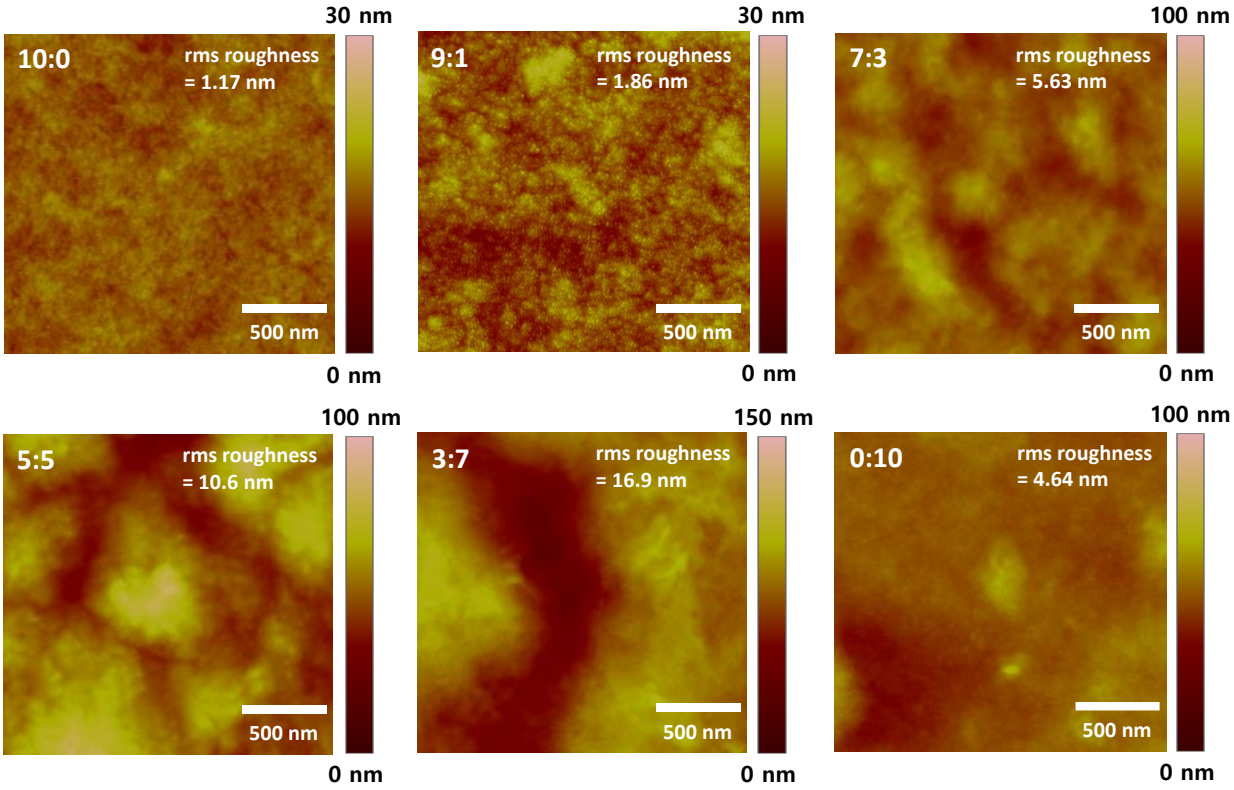

Figure 4.3 AFM topological images (2 μm by 2 μm) for ternary blend films prepared on ITO/PEDOT:PSS pre-coated glass substrate. (X:Y = $PC_{71}BM$:ITIC).

The performance trend shown in **Figure 4.2b** is well consistent with the morphology study. Spectral lincuts and images acquired via GIWAXS (**Figure 4.4**) further supports our interpretations above. Even with 10% ITIC in the blend, molecular packing of the blend is nearly identical to 10:0 binary blend. However, more than 10% of ITIC content in the blend causes unexpected molecular packing, which is not observed in 0:10 binary blend.

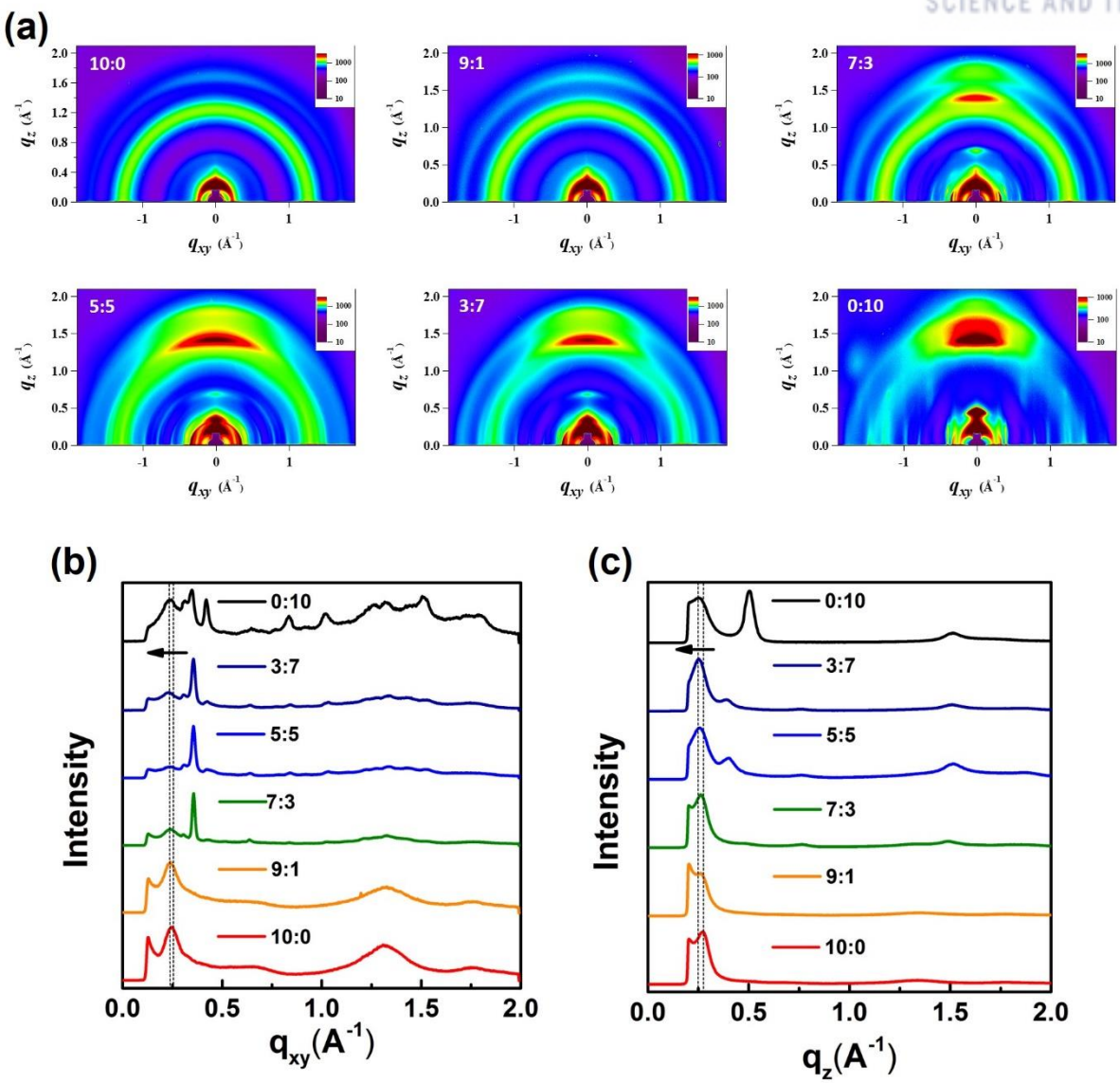

Figure S2. 2D-GIWAXS images for ternary blend films on Si substrate with controlled ratio (X:Y = $PC_{71}BM$:ITIC).

Figure 4.4 2D-GIWAXS images for ternary blend films on Si substrate with controlled ratio (X:Y = $PC_{71}BM$:ITIC).

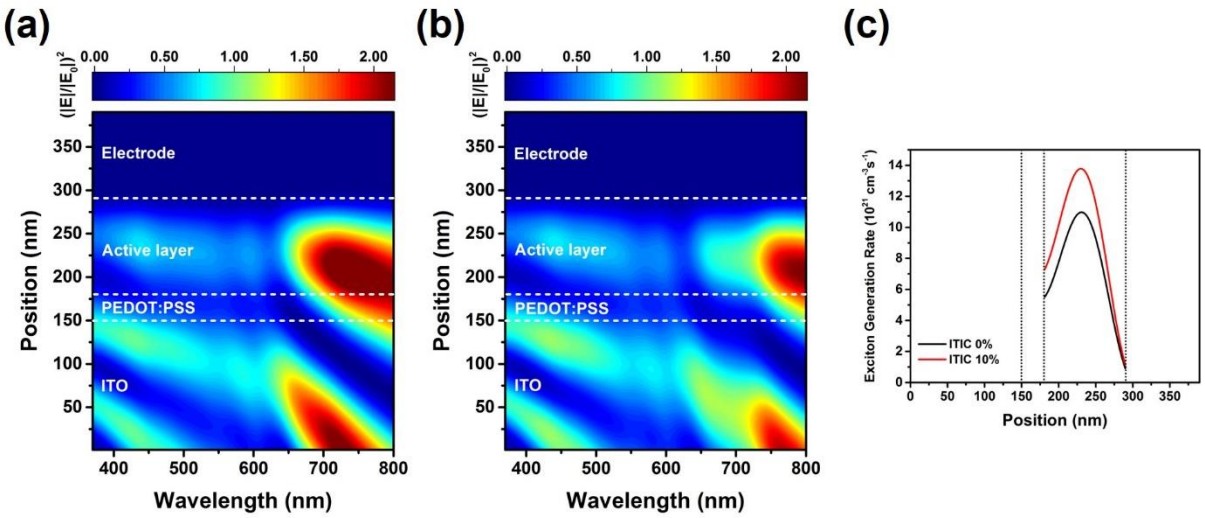

Figure 4.5. Simulated spatial distribution of squared electric field intensity inside TPSCs with (a) 10:0 acceptor ratio and (b) 9:1 ratio. Electric field intensity was normalized by incident field intensity. (c) Simulated exciton generation rate in the active layer of TPSCs.

Figure 4.5 shows the change of electric field distribution inside the device calculated by TMF. TMF calculates spatial distribution of electric field inside the device under illumination by calculating transfer matrix at each interface. We calculated the electric field distribution of the devices with 10:0 and 9:1 acceptor weight ratio. In the 10:0 device (**Figure 4.5a**), undissipated electric field in the wavelengths from 650 nm to 800 nm is strongly localized in the active layer, while the field in the wavelengths below 650 nm are localized at same position but dissipated considerably by PBTTFB and $PC_{71}BM$. However, when the amount of ITIC is 10% (**Figure 4.5b**), it was found that the electric field intensity in the wavelengths from 650 nm to 800 nm, which was not absorbed by PBTTFB and $PC_{71}BM$, was drastically decreased. It is probably due to the exceptionally strong light absorption ability of ITIC in the NIR region. Based on the information of residual electric field in the active layer, exciton generation rate was derived. (**Figure 4.5c**). Assuming that the area under the exciton generation rate curve is proportional to the maximum value of each curve, 25.6% improvement of exciton generation rate at maximum (from 10.97 x 10^{21} cm^{-3} s^{-1} to 13.78 x 10^{21} cm^{-3} s^{-1} for 10:0 and 9:1 devices, respectively.) is exactly consistent with our previous observation that the J_{SC} of the 9:1 ternary device is 24.9% improved compared to that of the 10:0 binary device. From this result, it is almost certain that the increase of J_{SC} in 9:1 ternary device is solely from the improved

exciton generation rate due to extended light harvesting ability to NIR by ITIC.

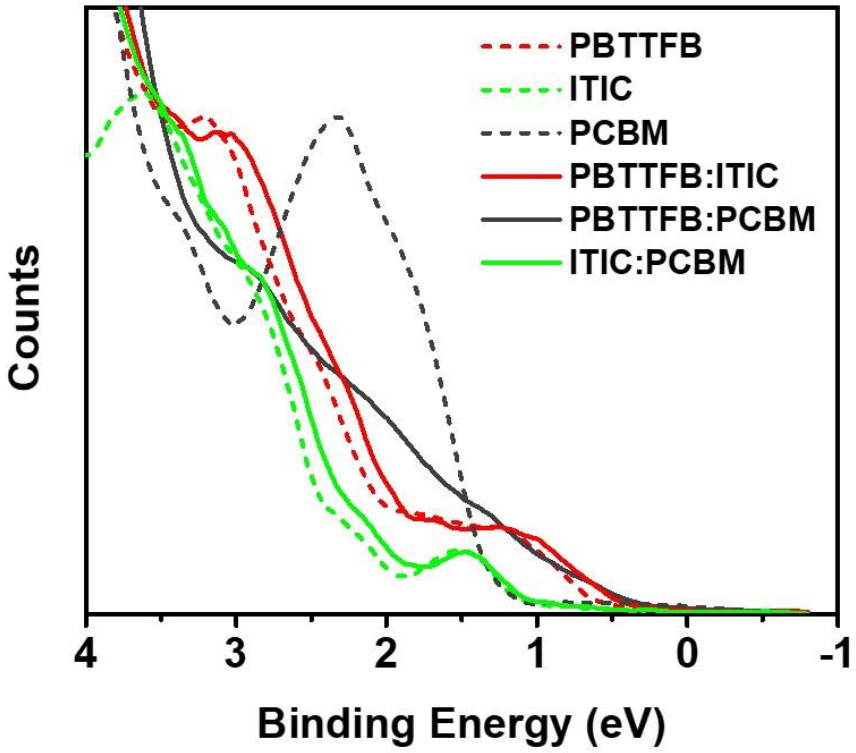

Figure 4.6. UPS spectra of pure PBTTFB, ITIC and $PC_{71}BM$ and blend film of PBTTFB:ITIC, PBTTFB:$PC_{71}BM$ and ITIC:$PC_{71}BM$.

For the detailed study on the charge carrier dynamics of TPSCs, ultraviolet photoelectron spectroscopy (UPS) was conducted for each material and binary blends. In **Figure 4.6,** PBTTFB:$PC_{71}BM$ blend exhibit its spectral shape somewhere between that of PBTTFB and $PC_{71}BM$. Considering the fact that UPS characterizes the surface electronic state of the sample, the mixed spectrum suggests that PBTTFB:$PC_{71}BM$ binary blend is finely mixed forming homogeneous morphology over the entire film. On the contrary, other two binary blends, PBTTFB:ITIC and ITIC:$PC_{71}BM$ showed different behavior. In the case of PBTTFB:ITIC, the spectral shape is nearly identical to the shape of PBTTFB. In similar, the spectrum of ITIC:$PC_{71}BM$ resembles that of ITIC. Again, because UPS reveals the surface energy state, these results imply that PBTTFB dominates the surface of PBTTFB:ITIC blend and ITIC dominates the surface of ITIC:$PC_{71}BM$. Thus, it is reasonable to estimate that successive phase separation is thermodynamically favorable in this order, $PC_{71}BM$ < ITIC < PBTTFB (< air). Similar phenomenon was previously reported elsewhere,[298] concluding that ITIC is located at the interface between donor and acceptor.

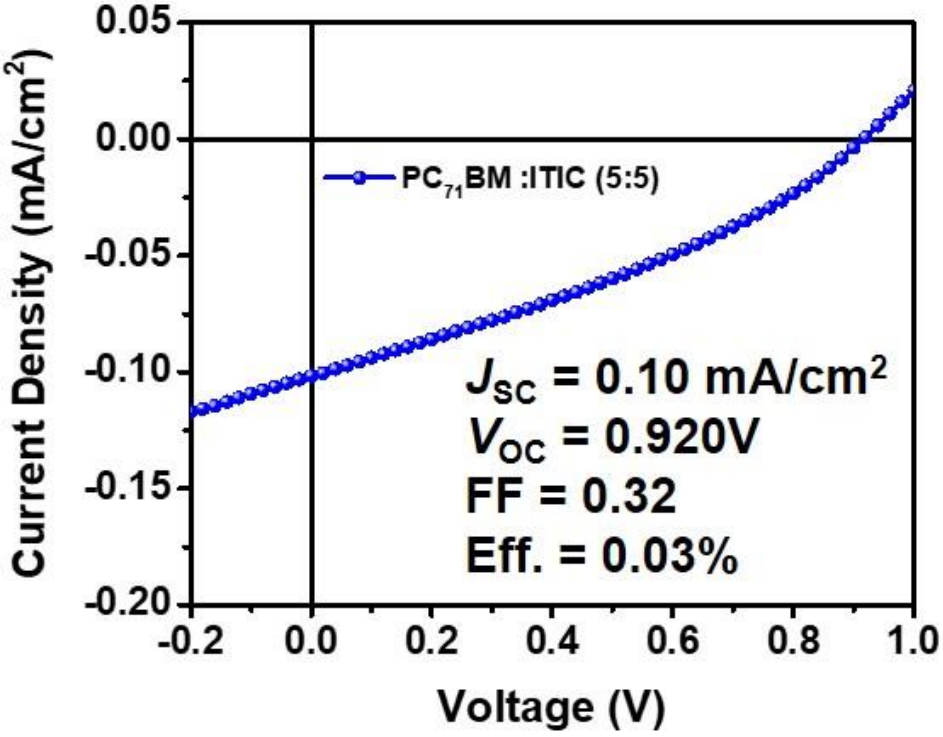

Figure 4.7. *J-V* characteristics of $PC_{71}BM$:ITIC binary solar cells.

Considering the HOMO level differences between $PC_{71}BM$ and ITIC and optical band gap derived from UV-vis-NIR absorption spectra, LUMO of two acceptors showed negligible differences. **Figure 4.7** shows *J-V* characteristics of $PC_{71}BM$:ITIC binary solar cells. Marginal current generation in this device supports that electron transfer between two acceptors is not favorable. Furthermore, **Figure 4.8a** shows negligible quenching of ITIC PL even after mixing with PCBM. This observation explains why V_{OC} of the devices is not dependent on the relative content of acceptors. From the calculated HOMO level, negligible differences in HOMO between PBTTFB and ITIC was observed, which causes inefficient hole transfer between two materials. This was further confirmed by residual photoluminescence (PL) of ITIC in PBTTFB:ITIC binary blend, shown in **Figure 4.8b**. The residual PL was fully quenched at 9:1 of optimum condition (**Figure 4.8c**).

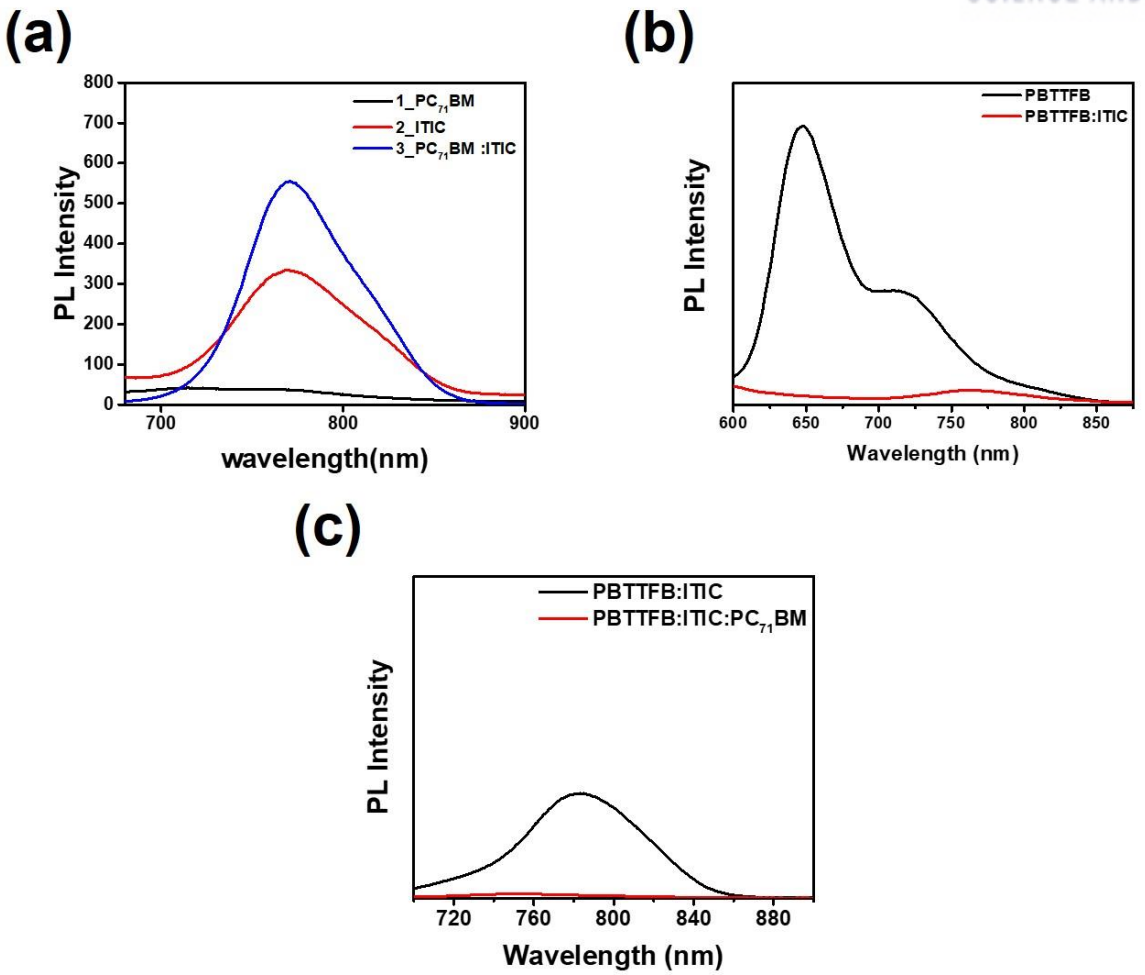

Figure 4.8. Photoluminescence spectra of (a) each acceptors and the blend with 5:5 ratio, (b) PBTTFB, binary blend with ITIC, and (c) PBTTFB, binary and ternary blend with ITIC and $PC_{71}BM$ in TPSCs.

4.4 Conclusion

In summary, we characterized TPSCs using two universal acceptors, $PC_{71}BM$ and ITIC, simultaneously. TPSCs with various acceptor ratio were examined and found that adding more than adequate amount of ITIC degrades device performance considerably, especially in J_{SC} and *FF*. Considering the fact that PBTTFB:ITIC binary blend maintains its high J_{SC}, it is likely that the issue stems from the unintended intermolecular interaction between two accepting molecules. As we expected, strong aggregation and molecular packing between ITIC and $PC_{71}BM$ were observed via AFM and GIWAXS measurement. At optimum condition, however, 10 weight% of ITIC didn't perturbed ideal BHJ morphology formed by PBTTFB and ITIC and enabled to maintain high V_{OC} and *FF*. Its strong light absorption ability in NIR enabled 25.6% enhancement of exciton generation in the ternary blend, resulting in significantly improved J_{SC} of 13.48 mA/cm^2, which is comparable to the that of PBTTFB:ITIC binary solar cell. Common and

easily accessible two famous acceptors, $PC_{71}BM$ and ITIC, shows efficient light deficiency compensation at both short and long wavelengths and thus many researchers would try this ternary system. But must be consider the strong and unintended intermolecular interaction between two molecules, which degrades the device performance. Nevertheless, our thorough studies on BHJ morphology and optical alternation in the devices suggests that ITIC is still a good candidate for third component in the polymer solar cells.

Chapter 5. 2,1,3-Benzothiadiazole-5,6-dicarboxylicimide Based Semi-crystalline Polymers for Photovoltaic Cells

5.1 Research background

Polymer solar cells (PSCs) have attracted much attention as one of future energy resources due to their low cost, light weight, mechanical flexibility and ability to produce large-area devices via the solution process at room temperature.[282, 283, 299-301] Recently, bulk heterojunction (BHJ) type PSCs comprising of conjugated organic semiconductors as donor (D) and the fullerene derivatives ([6,6]-phenyl-C_{61}-butyric acid methyl ester ($PC_{61}BM$) or [6,6]-phenyl-C_{71}-butyric acid methyl ester ($PC_{71}BM$)) as acceptor (A) have led to a dramatic improvement of power conversion efficiency (PCE) in the range of 8~11% for single cells.[302-308] By optimization of molecular structures of D and A, film morphology and device fabrication conditions, remarkable progresses have been made in BHJ PSCs,[145, 309-312] demonstrating a great potential as a flexible and portable power source.

D-A type alternating copolymers[313-316] have been considered as an ideal model system for realizing low band gap (LBG) photovoltaic materials by inducing intramolecular charge transfer (ICT) interaction. 2,1,3-Benzothiadiazole (BT)[317] and 5,6-difluorinated benzothiadiazole (2FBT) have been extensively studied as an electron-deficient moiety to construct the D-A push-pull conjugated LBG copolymers.[302, 318, 319] However, the polymers based on thiophene-BT derivatives often show a band gap of ~1.7 eV. To further optimize the light harvesting, the band gap of photovoltaic polymers needs to be decreased to 1.4~1.5 eV.[320] It is necessary to design new strong ICT structures by incorporating stronger D and A moieties in the polymeric backbone. Recently, a new strong electron-withdrawing unit was reported by introducing a cyclic imide into the 5- and 6-positions of the BT moiety to afford 2,1,3-benzothiadiazole-5,6-dicarboxylicimide (BTI) with stronger electron-withdrawing ability than 2FBT. Moreover, the solubility of resulting D-A polymers can be improved by incorporating an alkyl solubilizing group onto the BTI unit.[321-324] By incorporating the BTI unit in the D-A type copolymers, the narrow band gap and deeper highest occupied molecular orbital (HOMO) and lowest unoccupied molecular orbital (LUMO) energy levels could provide a way to construct ideal LBG photovoltaic polymers for further improving both the short-circuit current density (J_{SC}) and open-circuit voltage (V_{OC}).

Recently, intrachain (and/or interchain) noncovalent coulombic interactions (via $S^{\delta+}$---$O^{\delta-}$, etc.) have been successfully utilized to minimize torsional angles within the polymer chain,[325-327] thus leading to the chain planarity with tight solid-state π-π stacking.[328-330] We reported previously a series of semi-crystalline photovoltaic polymers with noncovalent coulombic attractions, showing highly ordered film morphology and high/balanced electron-hole mobilities with the PCE over 9%.[24] Extended design approaches were

also tried by controlling the chain curvature in which the interchain packing structure (edge on or face on orientation) was modulated, suggesting that the chain linearity plays a critical role for controlling the intermolecular orientation and interaction with fullerene derivatives.[331, 332]

Inspired from the above previous studies, we designed and synthesized two LBG D-A type copolymers, PPDTBTI and PPDTTBTI based on the strongly electron-deficient BTI unit, where the intrachain noncovalent coulombic interactions (such as dipole-dipole attraction and hydrogen bonding) are incorporated in a polymeric backbone. The polymers show an ideal band gap of ~1.5 eV, harvesting a broad range of solar spectrum up to 850 nm. The relationships of molecular structure, optical, electrochemical, morphological and photo-response characteristics were investigated in detail. The PSCs of PPDTBTI and PPDTTBTI showed the PCE of 5.47% and 6.78%, respectively. The higher PCE of the PPDTTBTI device can be interpreted in terms of proper film morphology with predominant face on orientation, the resulting higher vertical hole mobility and J_{SC}. The light intensity dependent J_{SC} and photocurrent-effective voltage characteristics are in good agreement with the measured device photovoltaic characteristics.

5.2 Experimental

General

A microwave reactor (Biotage Initiator™) was used to synthesize the polymers. ^{1}H and ^{13}C NMR spectra were recorded on an Oxford NMR AS400 system operating at 400 MHz and 100 MHz, respectively. UV-vis spectra were obtained with a JASCO V-730 spectrophotometer. The number- and weight-average molecular weights of the polymers were determined by gel permeation chromatography (GPC) with *o*-dichlorobenzene (*o*-DCB) as an eluent at 80 °C on an Agilent GPC 1200 series, relative to polystyrene standards. Cyclic voltammetry (CV) experiments were performed with a Versa STAT 3 analyzer. All CV measurements were carried out in 0.1 M tetrabutylammonium tetrafluoroborate (Bu_4NBF_4) in acetonitrile with a conventional three-electrode configuration employing a platinum wire as a counter electrode, platinum electrode coated with a thin polymer film as a working electrode, and Ag/Ag^+ electrode as a reference electrode (scan rate: 50 mV/s). Thermogravimetric analysis (TGA, 2050 TGA V5.4A) and differential scanning calorimetry (DSC, DSC Q200 V24.4) measurements were performed at a heating and cooling rate of 10 °C/min under nitrogen (purity, 99.999%).

AFM measurement

Atomic force microscopy (AFM) images were recorded in high-resolution tapping mode using an Agilent 5500 scanning probe microscope (SPM) running with a Nanoscope V controller. AFM images were obtained using high-resolution tapping mode under ambient conditions. Premium silicon cantilevers (TESP-V2, T: 3.8 μm, L: 127 μm, W: 35 μm) were used with a rotated tip to provide more symmetric

representation of features over 200 nm.

2D-GIXRD measurement

Grazing incidence wide angle X-ray scattering (GIWAXS) measurements were accomplished at PLS-II 9A U-SAXS beamline of the Pohang Accelerator Laboratory in Korea.

Photovoltaic Cell Fabrication

Indium tin oxide (ITO)-coated glasses were cleaned with detergent and ultra-sonicated in deionized water, acetone and isopropyl alcohol sequentially and dried in an oven for 12 h. The substrates were subjected to UV-ozone treatments for 15 min and then poly(3,4-ethylenedioxythiophene):polystyrene sulfonate (PEDOT:PSS) (Baytron Al4083) was spin-coated onto ITO and dried at 140 ºC for 10 min. The substrates were transferred to a N_2 filled glove box and the active layer was spin-casted on top of the PEDOT:PSS layer from a polymer:$PC_{71}BM$ solution (18 mg/mL) in chlorobenzene with changing a blend ratio. The device was pumped down under vacuum (< 10^{-6} Torr), and Al (100 nm) was deposited. The area of the Al electrode defines an active area of the device as 13.0 mm^2. The photovoltaic characteristics were measured inside a glove box by using a high quality optical fiber to guide the light from the solar simulator. The current density-voltage (*J-V*) characteristics were measured using a Keithley 2635A source measurement unit under AM 1.5G illumination at 100 mW/cm^2. The incident photon to current efficiency (IPCE) was measured by using a QEX7 from PV measurement Inc. The space-charge-limited-current (SCLC) mobilities were measured by fabricating hole-only (ITO/PEDOT:PSS/active layer/Au) and electron-only (FTO/active layer/Al, FTO: fluorine-doped tin oxide) diodes based on the Mott-Gurney relationship.

Fabrication of Organic Field Effect Transistors (OFETs)

Top contact OFETs were fabricated on a heavily n-doped silicon wafer coated with thick SiO_2 layer as a gate electrode and dielectric. The cleaned wafers were pretreated with a solution of 1.0 mM octadecyltrichlorosilane (ODTS) in toluene under N_2, and the polymers were spin-cast at 1700 rpm from a 0.4 wt% chlorobenzene solution. On top of the active layer, gold was deposited by thermal evaporation as both of source and drain electrodes. The thickness of top electrode (source and drain) was 80 nm. Electrical characterization was tested using a Keithley semiconductor parametric equipment (Keithley 4200) under a N_2 atmosphere. The charge mobilities were calculated by using the following equation: $I_{DS} = (W/2L)C_i\mu(V_G-V_T)^2$, where I_{DS} is the drain-source current, μ is the field effect mobility, C_i is the capacitance per unit area of the gate, the channel's width to length ratio (W/L) of the devices was 59/1.

5.3 Results and discussion

The synthetic routes to the polymers, PPDTBTI and PPDTTBTI are shown in **Figure 5.1.** The resulting two polymers were prepared by the Stille coupling polymerization of the brominated monomer M1 and stannylated M2 or M3 to afford PPDTBTI in 80% yield and PPDTTBTI in 75% yield in the presence of $Pd_2(dba)_3$ as a catalyst in anhydrous toluene.

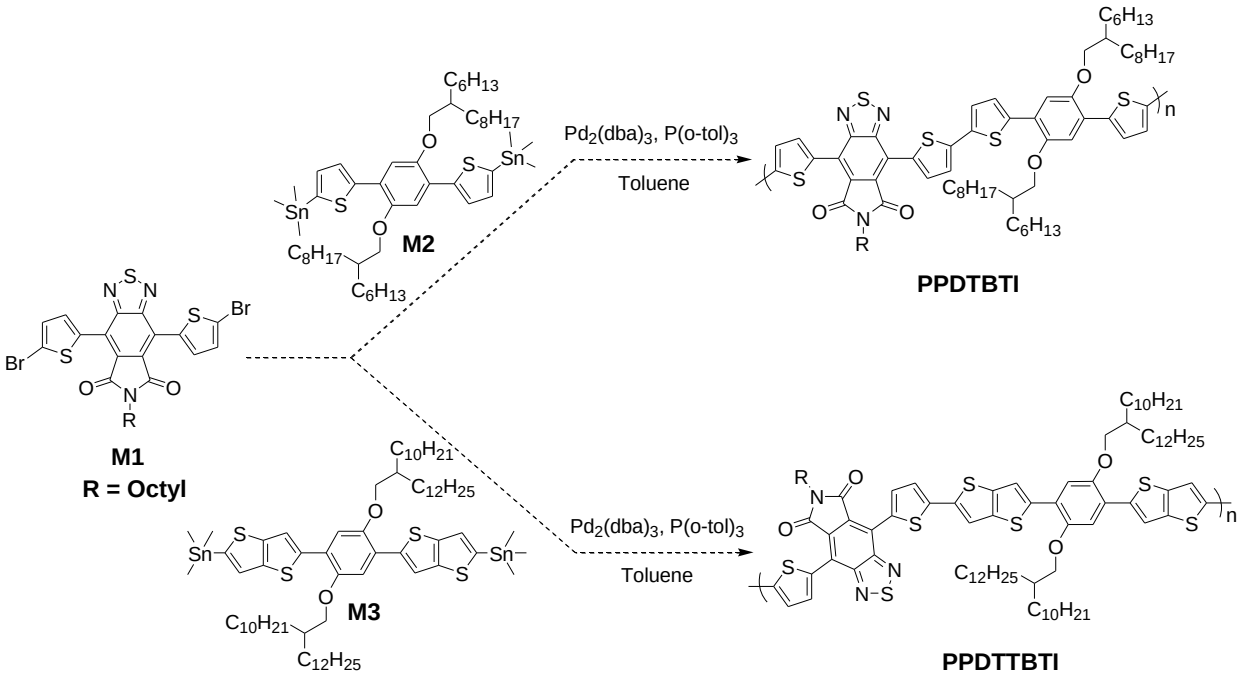

Figure 5.1 Synthesis of PPDTBTI and PPDTTBTI.

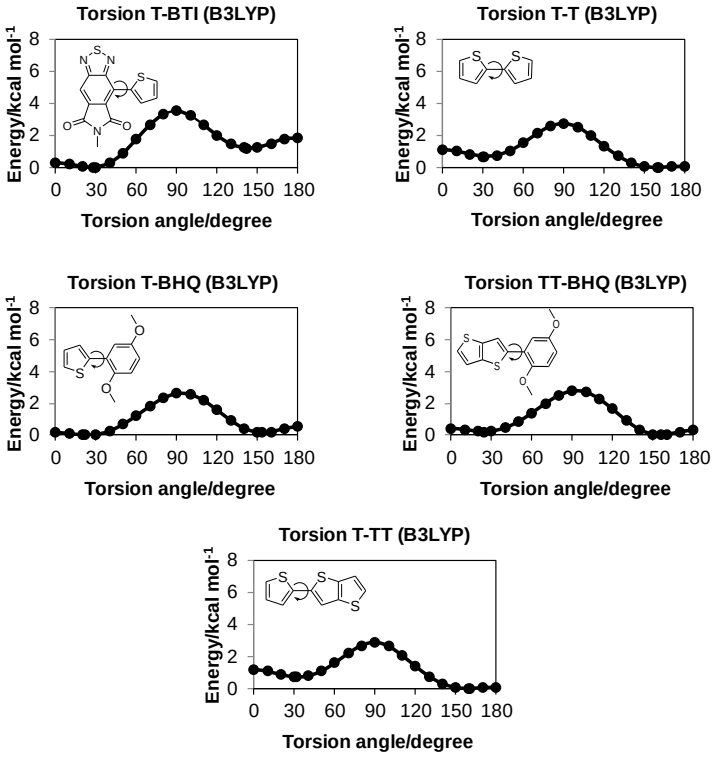

Figure 5.2 Torsional Profiles.

Both polymers are readily soluble in common organic solvents such as chloroform, chlorobenzene, and *o*-DCB. To estimate the torsional angles and the resulting minimum energy conformations, computational studies using density functional theory (DFT, Jaguar quantum chemistry software, B3LYP/6-31G** level) were performed on one repeating polymer unit with methyl substituents. The calculated torsional profiles are presented in **Figure 5.2**. The energy minimum torsional angles were calculated to be 25° for BTI-thiophene and 20~27° for thiophene (or thienothiophene)-dimethoxyphenylene linkages, respectively. The noncovalent coulombic interactions were applied along the conjugated backbone to minimize the torsional angles, leading to chain planarity and ordering of polymer chains in a solid film. The number-average molecular weight was determined to be 26 (PDI = 1.9) and 46 kDa (2.1) for PPDTBTI and PPDTTBTI, respectively, by high-temperature GPC using *o*-DCB as the eluent at 80 °C (**Table 5.1**). Thermal properties of the polymers were investigated by TGA and DSC measurements (**Figure 5.3**). Two polymers show high decomposition temperatures (T_d) at 394 and 386 °C for PPDTBTI and PPDTTBTI with 5% weight loss under nitrogen. There are no discernible thermal transitions in the temperature range of 25-350 °C in the DSC thermograms.

Table 5.1 Summary of optical, electrochemical and thermal properties.

Polymers	M_n (kDa) [a]	PDI[a]	Film λ_{onset} [b]	E_g^{opt} (eV) [b]	HOMO (eV)[c]	LUMO (eV)[d]	T_d (°C)[e]
PPDTBTI	26	1.9	850	1.46	-5.36	-3.90	394
PPDTTBTI	46	2.2	850	1.46	-5.30	-3.84	386

[a]Number-average molecular weight (M_n) and polydispersity index were determined by GPC in *o*-DCB at 80 °C. [b]Optical band gap was obtained from the absorption onset in film. [c]HOMO level was estimated from the onset of oxidation (E_{ox}^{onset}) by cyclic voltammetry. [d]LUMO level was estimated from the HOMO value and corresponding optical band gap in film. [e]Decomposition temperature (T_d) was determined by TGA under nitrogen (with 5% weight-loss).

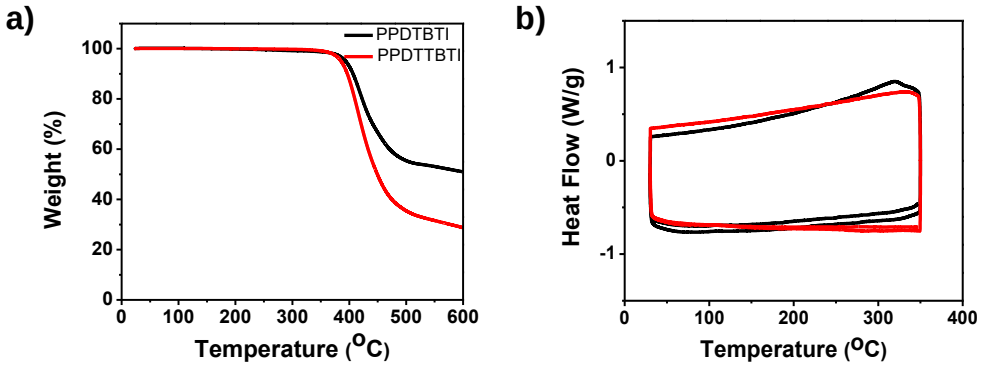

Figure 5.3 a) TGA and b) DSC thermograms of PPDTBTI and PPDTTBTI.

The normalized UV-vis spectra of PPDTBTI and PPDTTBTI in chloroform and in film are shown in **Figure 5.4a**. Absorption spectra of both polymers exhibit two separate peaks, low energy and high energy transitions originating from π-π* transition and ICT interactions. In solution, the absorption maxima were measured at 426 and 600 nm for PPDTBTI and 451 and 654 nm for PPDTTBTI. PPDTTBTI shows a mor e red-shifted absorption compared to PPDTBTI via the stronger ICT (due to enhanced electron-donating ability of thienothiophene than thiophene) and/or intermolecular aggregation originating from enhanced chain rigidity. The large red-shift in the spectra from solution to film indicates the enhanced interchain interaction and/or aggregation in film. The optical band gap from the absorption onset in film was estimated to be 1.46 eV for both polymers. Moreover, we note that the optical band gap of the polymers is near the optimum value for organic photovoltaic devices.[117, 333, 334] The molar absorption coefficient (ε_{max}) of PPDTBTI and PPDTTBTI was measured to be 2.1 x 10^5 M^{-1} cm^{-1} and 1.7 x 10^5 M^{-1} cm^{-1}, respectively (**Figure 5.5a**).

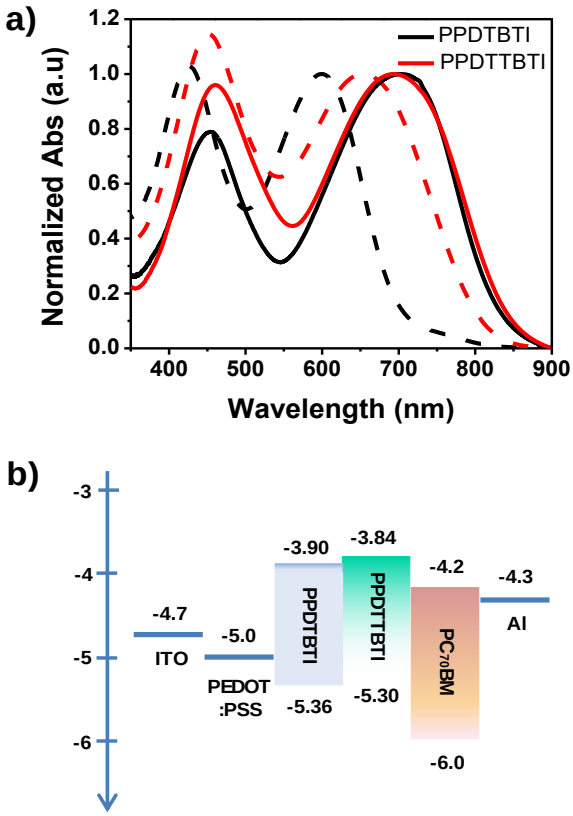

Figure 5.4 a) Normalized UV-vis absorption spectra in chloroform (dashed line) and in film (solid line) and b) energy level diagram.

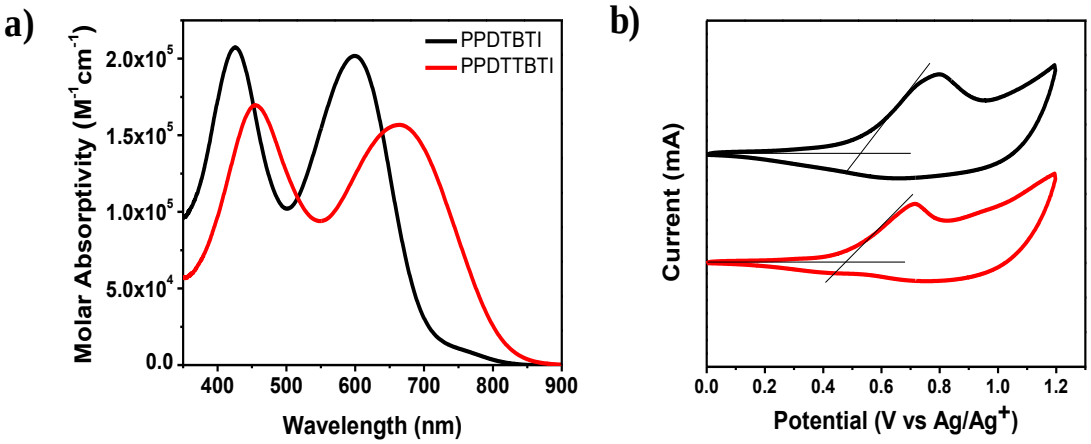

Figure 5.5 a) Molar absorptivity in chloroform and b) cyclic voltammograms of PPDTBTI and PPDTTBTI.

Frontier energy levels of PPDTBTI and PPDTTBTI were also investigated by CV (**Figure 5.5b**). The HOMO energy levels were estimated to be -5.36 eV and -5.30 eV for PPDTBTI and PPDTTBTI,

respectively, by the following equation: HOMO = -(E_{ox}^{onset} -$E_{1/2}^{ferrocene}$ +4.8) eV.[335] The LUMO energy levels were calculated to be -3.90 and -3.84 eV for PPDTBTI and PPDTTBTI, based on the optical band gap and HOMO energy level (Table 1). The stronger donating-ability of thienothiophene shifts up both HOMO and LUMO energy levels of PPDTTBTI compared to those of PPDTBTI.

To investigate the photovoltaic properties, the BHJ PSCs were fabricated with a conventional device structure of ITO/PEDOT:PSS/polymer:$PC_{71}BM$/Al. The detailed device fabrication was described in the Experimental Section. To optimize the PSC devices, a series of devices was tested by changing polymer:$PC_{71}BM$ blend ratio, processing additives (diphenylether (DPE), 1,8-diiodooctane (DIO), 1-chloronaphthalene (CN) and 1,8-octanedithiol (ODT)) and incorporating a buffer layer. The BHJ blend films were fabricated using chlorobenzene (CB) as a solvent. The optimum devices were obtained with donor:acceptor (D:A) ratio of 1:1.5 and 1:2 (w/w) for PPDTBTI and PPDTTBTI BHJ films using a solvent mixture of chlorobenzene and DPE (97:3 vol%). The incorporation of ZnO buffer layer showed no positive effect on the device performance. **Figure 5.6** shows the *J-V* characteristics of each optimized device under illumination of simulated 1.5G condition (100 mW/cm^2) and the photovoltaic parameters are summarized in **Table 5.2**.

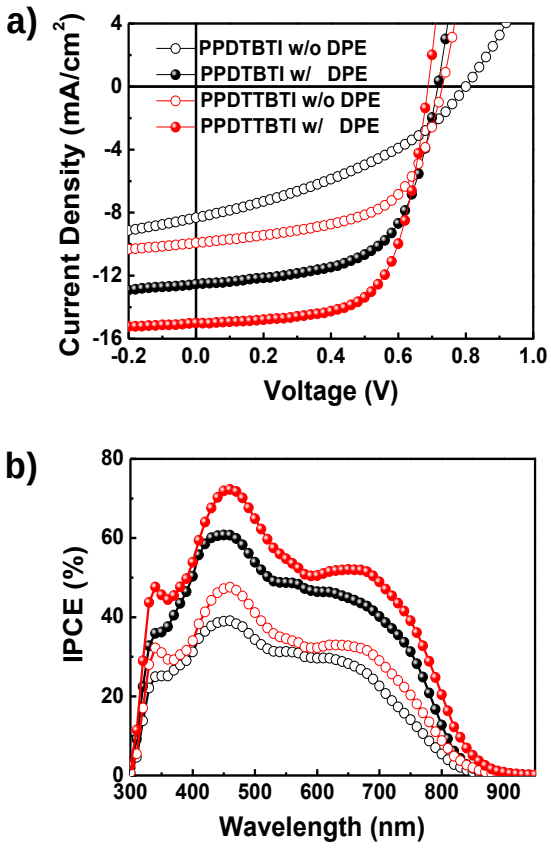

Figure 5.6 a) *J-V* characteristics and b) IPCE spectra of polymer:$PC_{71}BM$ blends.

Table 5.2 Summary of photovoltaic characteristics.

Polymer:$PC_{71}BM$	D/A Ratio	Additive	J_{SC} (mA/cm^2)	J_{SC} [*Cal*] [a] (mA/cm^2).	V_{OC} (V)	FF	PCE[b] (%)
PPDTBTI	1:1.5	None	8.33	7.39	0.80	0.37	2.49 (2.36 ± 0.13)
		DPE	12.53	12.19	0.72	0.61	5.47 (5.20 ± 0.26)
PPDTTBTI	1:2	None	9.92	8.82	0.73	0.58	4.22 (4.08 ± 0.14)
		DPE	15.0	14.47	0.69	0.66	6.78 (6.55 ± 0.23)

[a] J_{SC} [*Cal*], calculated J_{SC} from a IPCE curve. [b] The average values and standard deviations based on 10 devices.

Without addition of the processing additive, DPE, the PPDTTBTI:$PC_{71}BM$ device exhibited the higher PCE of 4.22% with J_{SC} of 9.92 mA/cm^2, V_{OC} of 0.73 V and FF of 0.58, compared to PP DTBTI:$PC_{71}BM$ (PCE: 2.49% with J_{SC} of 8.33 mA/cm^2, V_{OC} of 0.80 V and FF of 0.37). The PPDTBTI:$PC_{71}BM$ and PPDTTBTI:$PC_{71}BM$ devices showed the best PCE with a film thickness of 100~115 nm. It is well-known that the processing additives often enhance the device performance significantly via fine-modulation of BHJ morphology.[319, 336] Especially, the PPDTTBTI:$PC_{71}BM$ based PSC exhibited the highest PCE of 6.78% by addition of DPE, mainly due to improved J_{SC} from 9.92 to 15.0 mA/cm^2.

This remarkable improvement is expected to be caused by the proper film morphology which will be discussed in the following section. The corresponding IPCE spectra of the optimized devices are shown in **Figure 5.6b**, showing broad response from 300 nm to 850 nm. Especially, the maximum IPCE of 72.6% was measured at 460 nm for PPDTTBTI:$PC_{71}BM$. The calculated J_{SC} values were obtained by integrating the IPCE spectra with respect to wavelength, being consistent with the measured ones within 10% error are listed in **Table 5.2**.

To correlate the morphology of active layer with device properties, the nanoscale morphology of blend films was examined by tapping mode AFM and two dimensional GIWAXS. The AFM topography and phase images of both BHJ films show a clearly different morphology with and without DPE. As shown in **Figure 5.7**, the blend film of PPDTBTI:$PC_{71}BM$ fabricated without DPE shows a smooth surface with root mean square (rms) roughness of 1.5 nm whereas the PPDTTBTI:$PC_{71}BM$ blend film shows a rough surface (rms roughness of 4.2 nm) with large phase separation (diameter of ~100 nm). This large phase separation may induce a limited probability for exciton dissociation by reducing interfacial areas between donor and acceptor. However, upon addition of DPE, the blend films show a smooth surface (rms roughness of ~2 nm) with finely-distributed nano morphology. The improved J_{SC} and PCE of both polymer blends with DPE show a good agreement with the morphological changes with and without DPE.

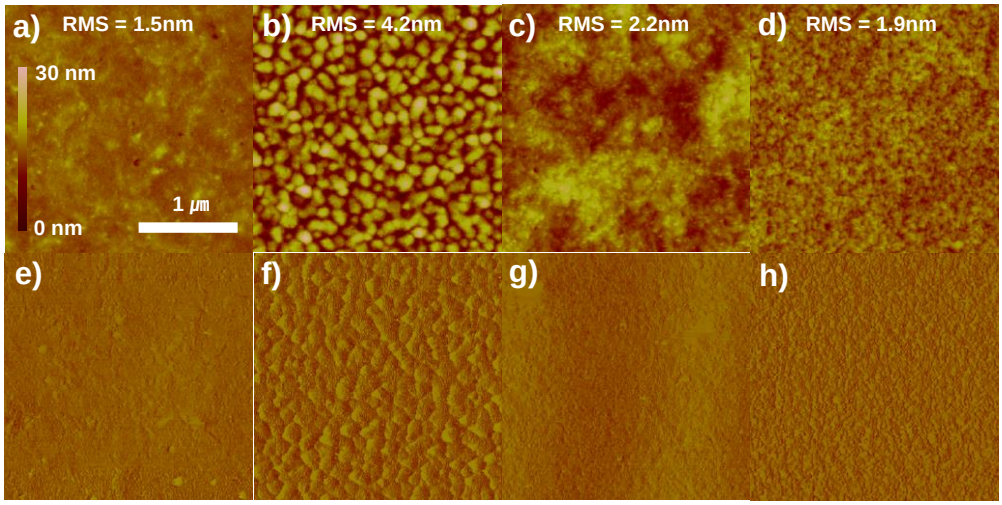

Figure 5.7 Surface morphology of polymer:$PC_{71}BM$ BHJ films. AFM topographical (a-d) and phase (e-h) images. PPDTBTI:$PC_{71}BM$ without (a, e) and with DPE (c, g). PPDTTBTI:$PC_{71}BM$ without (b, f) and with DPE (d, h). The BHJ films were deposited on ITO/PEDOT:PSS under the same condition with the optimal BHJ PSCs.

To investigate the interchain packing structures of pristine and blend films, we also carried out GIWAXS measurements. **Figure 5.8** shows the 2D-GIWAXS patterns and **Table 5.3** summarizes the extracted packing parameters.

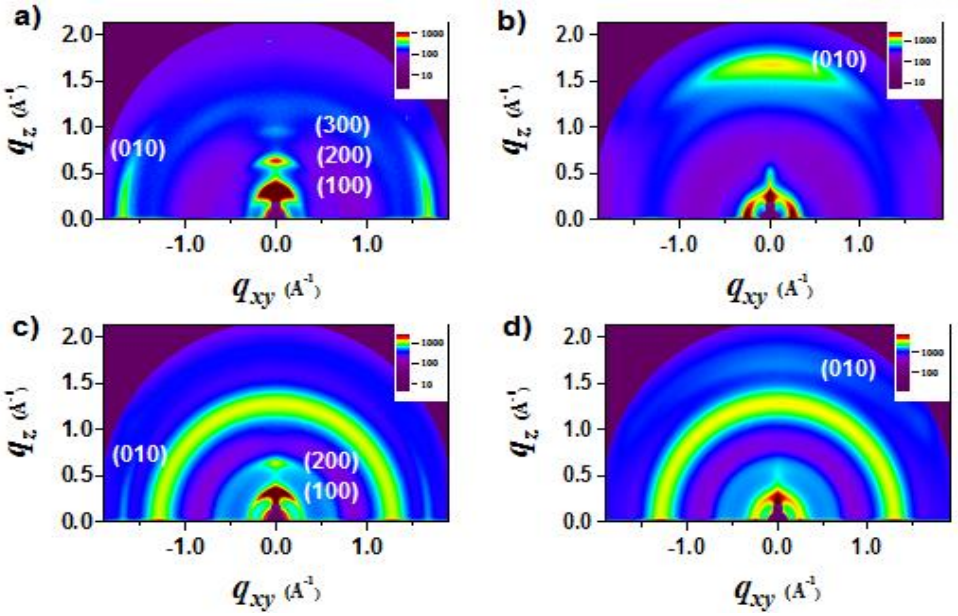

Figure 5.8 GIWAXS morphological data of pristine polymers (a, b) and polymer:$PC_{71}BM$ blen ded films (c, d) for PPDTBTI a), c) and PPDTTBTI b), d). BHJ films were prepared at the s ame condition for the optimized photovoltaic devices.

Table 5.3 Summary of GIWAXS packing paramerters

Films	Plane	Packing parameters			
		Lamellar spacing		π-π stacking	
		q (Å^{-1})	d-spacing (Å)	q (Å^{-1})	d-spacing (Å)
PPDTBTI	In	0.310	20.3	1.70	3.69
	Out	0.331	19	1.72	3.65
PPDTBTI :$PC_{71}BM$	In	0.314	20	1.71	3.67
	Out	-	-	1.75	3.59
PPDTTBTI	In	0.256	24.5	-	-
	Out	-	-	1.73	3.63
PPDTTBTI :$PC_{71}BM$	In	0.258	24.3	-	-
	Out	0.337	18.6	1.79	3.51

The pristine film of PPDTBTI displays a well resolved interlamellar scattering up to (300) in the out-of-plane direction with a strong in-plane (010) π-π stacking, showing a preferential edge on orientation. On the contrary, the pristine PPDTTBTI film contains a fused-thienothiophene unit on the polymeric backbone exhibits a strong (100) scattering in the in-plane direction and a (010) π-π stacking peak in the out-of-plane direction, suggesting a preferable face on orientation. From the in-plane (100) peaks, the lamellar d-spacing was estimated to be 20.3 Å and 24.5 Å for pristine PPDTBTI and PPDTTBTI, respectively. The larger interlamellar distance in PPDTTBTI is due to the longer

decyltetradecyl side-chains compared to hexyldecyl substituents in PPDTBTI. The π-π stacking distance was also measured to be 3.69 Å for PPDTBTI and 3.63 Å for PPDTTBTI. The BHJ blend films also show a similar tendency where the blend film of PPDTBTI:$PC_{71}BM$ shows the interlamellar peaks up to (200) in the out-of-plane direction with the (010) peak in the in-plane direction. The edge on and face on orientation was clearly observed for PPDTBTI:$PC_{71}BM$ and PPDTTBTI:$PC_{71}BM$, respectively. Although the molecular structure strongly influences the packing orientation, the relationship between them is not clear and hard to predict at a present stage. The thorough investigation on the molecular structure-interchain packing is necessary for large numbers of different polymers to reveal the exact correlation of them. The face on intermolecular orientation in PPDTTBTI:$PC_{71}BM$ is beneficial for charge transport and extraction in a vertical direction.[337] The morphological data clearly support the higher photovoltaic properties of PPDTTBTI:$PC_{71}BM$ relative to PPDTBTI:$PC_{71}BM$.

To investigate the charge transport characteristics in a vertical direction, we measured the SCLC mobility Hole-only (ITO/PEDOT:PSS/polymer:$PC_{71}BM$/Au) and electron-only (FTO/polymer:$PC_{71}BM$/Al) devices were fabricated under the same conditions for the optimized BHJ devices. The potential loss due to the series resistance of ITO and the built-in potential were considered carefully to ensure the accuracy in the measurements. As shown in **Figure 5.8a** and **5.8b**, the *J-V* characteristics showed a quadratic dependence on the applied voltage over a range of several volts by following the Mott-Gurney relationship (1):[338]

$$J_{SCLC} = \frac{9\varepsilon_0\varepsilon_r\mu V^2}{8L^3} \qquad (1)$$

where ε_0 is the free-space permittivity, ε_r is the dielectric constant of semiconductor, μ is the charge mobility, V is the applied voltage and L is the thickness of BHJ films. The PPDTTBTI:$PC_{71}BM$ blend showed the higher hole mobility ($\mu_h = 1.44 \times 10^{-4}$ cm^2/V.s) than PPDTBTI:$PC_{71}BM$ ($\mu_h = 3.76 \times 10^{-5}$ cm^2/V.s) with the balanced μ_h/μ_e ratio of 0.84. The similar electron mobility was measured to be $\mu_e = 2.01 \times 10^{-4}$ and 1.71×10^{-4} cm^2/V.s for PPDTBTI:$PC_{71}BM$ and PPDTTBTI:$PC_{71}BM$, respectively. The higher μ_h for PPDTTBTI:$PC_{71}BM$ with balanced hole and electron mobility ratio is well consistent with the face on interchain packing confirmed by GIWAXS.

To quantify charge recombination and extraction for the two BHJ PSCs, we measured the light intensity dependent *J-V* characteristics under short-circuit condition. **Figure 5.8c** shows a log-log plot of J_{SC} as a function of light intensity. The curve was fitted according to the power-law dependence of J_{SC} on the light intensity. The light intensity dependence of J_{SC} can be used to determine if the J_{SC} is limited by bimolecular recombination. By fitting the photocurrent plots using equation (2):[285, 339]

$$J_{sc} \propto I^{\alpha} \qquad (2)$$

where I is the light intensity, α is exponent constant for BHJ PSCs. The value of α was determined to

be 0.999 for PPDTTBTI:$PC_{71}BM$, indicating weak bimolecular recombination at short circuit.

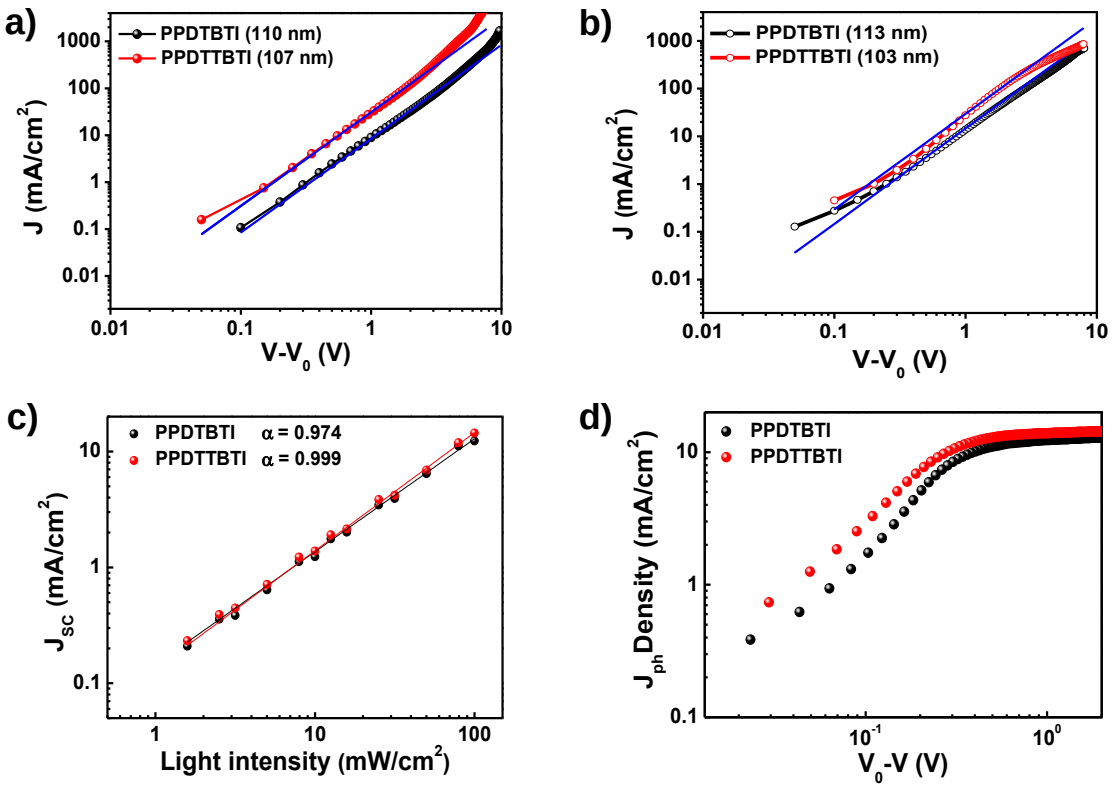

Figure 5.8 Measured *J-V* characteristics of polymer:$PC_{71}BM$ BHJ films by the SCLC method under dark condition for a) hole-only devices and b) electron-only devices. c) J_{SC} as a function of light intensity and d) photocurrent versus effective voltage.

On the contrary, PPDTBTI:$PC_{71}BM$ shows the α value of 0.974 which suggests the substantially higher bimolecular recombination than PPDTTBTI:$PC_{71}BM$, probably due to unfavorable edge on packing. We also studied the photocurrent (J_{ph}) versus effective voltage (V_{eff}) characteristics (**Figure 5.8d**). J_{ph} is defined as the difference between the current density under illumination (J_L) and dark (J_D) conditions ($J_{ph} = J_L - J_D$). V_{eff} is the voltage difference between compensation voltage (V_0) at $J_{ph} = 0$ and applied voltage, V ($V_{eff} = V_0 - V$). Both PSCs show the linear and saturation regimes of J_{ph}. The saturation of J_{ph} suggests the effective charge sweep out and extraction of photo-generated charge carriers with negligible recombination. PPDTTBTI:$PC_{71}BM$ shows a higher J_{ph} and saturation of J_{ph} at the lower V_{eff} = ~0.4 V. These results are in good agreement with the film morphology and photovoltaic device properties.

In order to investigate the charge carrier mobility of two polymers in a horizontal direction, OFETs were also fabricated with a top contact and bottom gate configuration. Transfer characteristics and output curves are shown in **Figure 5.9**. An overall summary of OFET characteristcs are presented in

Table 3. From the slope of the curve of $I_D^{1/2}$ *vs* V_G, the best OFET hole mobility was determined to be 4.39 × 10^{-3} $cm^2V^{-1}s^{-1}$ for PPDTBTI (annealed at 150 ℃) and 2.97 × 10^{-4} $cm^2V^{-1}s^{-1}$ for PPDTTBTI (annealed at 100 ℃), respectively. In addition, High I_{on}/I_{off} ratio was measured to be 7.6 × 10^4 and 1.26 × 10^4 for PPDTBTI and PPDTTBTI devices at the optimal annealing temperature. The thiophene-based PPDTBTI shows the higher OFET hole mobility by an order of magnitude, which is closely related to the edge on orientation of PPDTBTI in film. The horizontal hole transport behavior is also well consistant with the GIWAXS results.

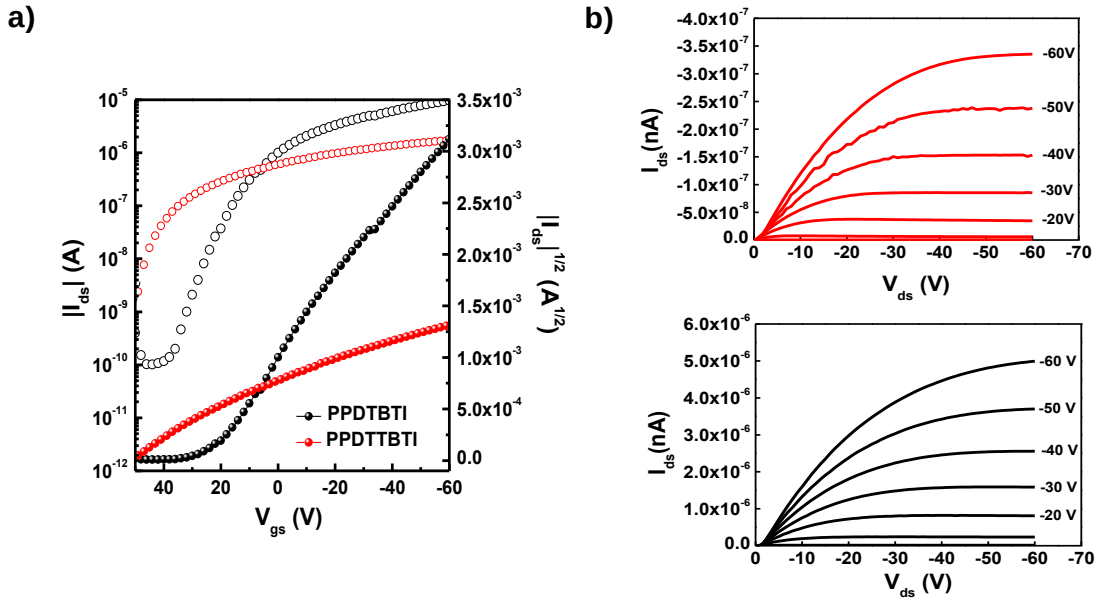

Figure 5.9 a) Transfer characteristics and b) output characteristics of PPDTBTI- and PPDTTBTI-based OFET devices .

Table 5.4 Hole mobilities of PPDTBTI and PPDTTBTI by OFET fabrication.

Polymer	Thermal Annealing (℃)	Mobility ($cm^2s^{-1}V^{-1}$)	I_{off} (A)	I_{on} (A)	I_{on}/I_{off}	V_T (V)
PPDTBTI	150	4.39×10^{-3}	1.25×10^{-10}	9.56×10^{-6}	7.6×10^4	22.5
PPDTTBTI	100	2.97×10^{-4}	1.43×10^{-10}	1.72×10^{-6}	1.2×10^4	69.2

5.4 Conclusion

Two kinds of semi-crystalline photovoltaic polymers (PPDTBTI and PPDTTBTI) based on 2,1,3-benzothiadiazole-5,6-dicarboxylicimide were synthesized and their optical, morphological, electrical and photovoltaic characteristics were investigated. By combining electron-rich thiophene (or thienothiophene) and the strongly electron-withdrawing BTI moieties in a polymeric backbone, a low band gap of ~1.5 eV was obtained via intramolecular charge transfer interaction. Both polymers show a broad light absorption in the range of 300~850 nm and semi-crystalline film morphology was observed in the GIWAXS measurements via intrachain (and/or interchain) noncovalent coulombic interactions. Interestingly, the thiophene-BTI based PPDTBTI showed a strong edge on interchain packing but the thienothiophene-BTI based PPDTTBTI had a face on packing structure in both pristine and blend films. By replacing thiophene with thienothiophene, the PPDTTBTI based PSC showed the lower V_{OC} (due to higher HOMO), but the J_{SC} was substantially higher than the PPDTBTI device. The enhanced J_{SC} of PPDTTBTI:$PC_{71}BM$ shows a good agreement with the face on interchain orientation and higher hole mobility in a vertical direction. The best PCE of 6.78% was measured for the PPDTTBTI:$PC_{71}BM$ device.

Chapter 6. Medium Bandgap Copolymers Based on Carbazole and Quinoxaline Exceeding 1.0 V Open Circuit Voltages

6.1 Research background

In the research community of bulk-heterojunction (BHJ)-based polymer solar cells (PSCs), the majority of synthetic efforts and structure-property studies have been devoted to "low bandgap" donor–acceptor (D–A) copolymers with increased light-harvesting capability to improve short-circuit current density (J_{SC}), which essentially enables high power-conversion efficiencies (PCEs) over 9% in certain systems.[340-345] However, the low bandgap D–A copolymers possess usually higher-than-optimal highest occupied molecular orbital (HOMO) energy levels, which consequently limits the open-circuit voltage (V_{OC}) of the resulting PSCs. Therefore, some recent studies have begun to focus on 'medium bandgap' D–A copolymers, due to their deep-lying HOMO levels and potential application in tandem PSCs,[344, 346-348] though they relatively suffer from light absorptions in visible wavelength range.[349, 350]

Since the impressive performance of PSCs based on a quinoxaline (Qx) unit reported by Andersson *et al.*,[351] a series of conjugated materials that belong to the family of D–A copolymers based on Qx have been investigated, which showed their obvious potential for achieving high PCEs in PSCs.[352, 353] Independently, we also studied a family of Qx-containing D–A copolymers and found that they had very deep-lying HOMO levels, providing a significantly larger V_{OC} of up to 1.00 V[354-356]

Seeking to further enhance the V_{OC} values in PSCs, here we attempt to extend the molecular design approach to D–A platform associated with Qx unit; to date, thiophene-based moieties as the natural choice for strong donor portions within the main backbone have been predominantly implementedin constructing Qx-based D–A copolymers for applications in PSCs.[357-360]

To this end, we have designed and synthesized three medium bandgap D–A copolymers, **PCzDT-Qx**, **PCzDT-fQx**, and **PCzDT-ffQx** (**Figure 6.1**), by copolymerizing tricyclic 2,7-carbazole (Cz) as the donor moiety with either Qx or its fluorinated analogs (fQx (1F) and ffQx (2F)) as the acceptor for the following reasons: (i) Taking into account the verified high V_{OC} values generated from D–A copolymers based on Cz donor unit,[361-363] we surmise that outgrowth via a synergistic effect of combining Cz and Qx moieties in the main backbone can contribute to the realization of superior V_{OC}. (ii) It is also expected to further improve V_{OC} in the devices of F-containing copolymers, as a results of the more lowered HOMO levels induced by the electron-withdrawing effect of the F substituents. (iii) In addition, the two flanking thienyl spacers can relieve the steric hindrance between the conjugated units, thereby enhancing co-planarity of the backbone, which would in turn help charge transport property by hopping.[364, 365]

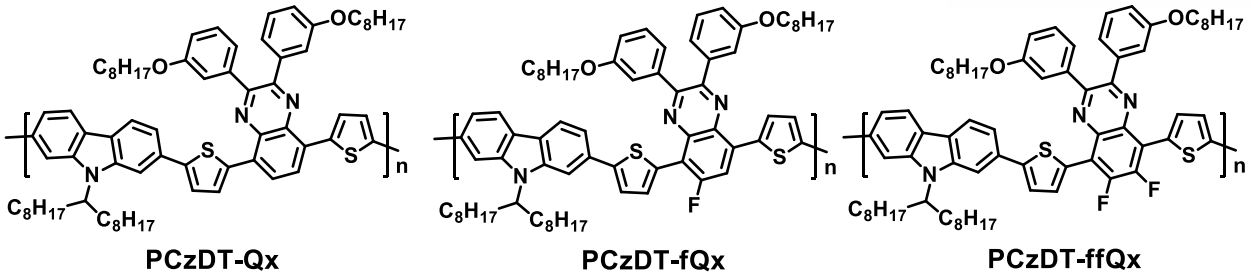

Figure 6.1 Three kinds of carbazole- quinolzaline based polymer structures.

Herein, detailed optical, electrochemical, and BHJ morphology, as well as PSC characteristics derived from this series of copolymers are studied and analyzed. To our delight, we find that the PSCs based on fluorinated copolymers (**PCzDT-fQx**, and **PCzDT-ffQx**) show very high V_{OC} values exceeding 1.0 V, which, to the best of our knowledge, are among the highest values, though they suffer somewhat from poor J_{SC} and fill factor (*FF*). Compared with **PCzDT-Qx** and **PCzDT-ffQx**, a better PCE is realized in PSCs based on **PCzDT-fQx**, which is clarified as the collective effects of deep-lying HOMO, more balanced charge transport, as well as suppression of recombination losses, as evidenced by measuring the dependence of J_{SC} on light intensity as well as photocurrent.

6.2 Experimental

PSC fabrication

The ITO–coated glasses were cleaned with detergent and ultra-sonicated in deionized water, acetone and isopropyl alcohol sequentially and dried in an oven for 12 h. The substrates were subjected to UV-ozone treatment for 15 min and then PEDOT:PSS (Al4083) was spin-coated on ITO and were dried at 140 °C to remove moisture. The substrates were transferred to globe box that is filled in N_2 and spin-casted with active layer in *o*-dichlorobenzene. 100 nm of Al was evaporated on top of the active layer under high vacuum ($<10^{-6}$ torr). The area of Al electrode is 13 mm^2. The photovoltaic characteristics were measured in glove box by using a high quality optical fiber to guide light from the solar simulator. The *J-V* characteristics of the PSC were measured using a Keithley 2635A source measurement unit under AM 1.5G illumination at 100 mW/cm^2. The incident photon-to-current efficiency (IPCE) was measured by using a QEX7 from PV measurement Inc. The space-charge-limited-current (SCLC) mobilities were calculated by using Mott-Gurney relationship.

AFM measurement

An Agilent 5500 scanning probe microscope (SPM) running with a Nanoscope V controller was used to obtain AFM images of polymer thin films. AFM images were recorded in high-resolution tapping mode under ambient conditions. Premium silicon cantilevers (TESP-V2) were used with a rotated tip

to provide more symmetric representation of features over 200 nm.

2D-GIXRD measurement

Grazing-incidence wide-angle X-ray scattering (GIWAXS) measurements were conducted at PLS-II 9A U-SAXS beamline of the Pohang Accelerator Laboratory in Korea. X-rays coming from the in-vacuum undulator (IVU) were monochromated (wavelength λ = 1.10994 Å) using a double crystal monochromator and focused both horizontally and vertically (450 (H) × 60 (V) μm^2 in FWHM @ sample position) using K-B type mirrors. The GIWAXS sample stage was equipped with a 7-axis motorized stage for the fine alignment of sample, and the incidence angle of X-ray beam was set to be 0.13° to 0.135° for IIGDT-based polymer films and blended films. GIWAXS patterns were recorded with a 2D CCD detector (Rayonix SX165) and X-ray irradiation time was 6–9 s, dependent on the saturation level of the detector. Diffraction angles were calibrated using a sucrose standard (Monoclinic, P21, a = 10.8631 Å, b = 8.7044 Å, c = 7.7624 Å, β = 102.938°) and the sample-to-detector distance was ~231 mm.

6.3 Results and discussion

Diboronic ester monomer (M1) and dibromide co-monomers (M2, M3, and M4) were synthesized according to previously reported procedures.[366] **Figure 6.1** shows the synthetic routes for the copolymers. The copolymerizations were accomplished via $Pd_2(dba)_3$-catalyzed Suzuki coupling of the monomer M1 with the corresponding co-monomers M2, M3, and M4, respectively. The resulting copolymers were precipitated in methanol: ammonia solution (9:1), collected by filtration, and purified by Soxhlet extraction, using different organic solvents, to remove impurities and/or low molecular weight fractions.

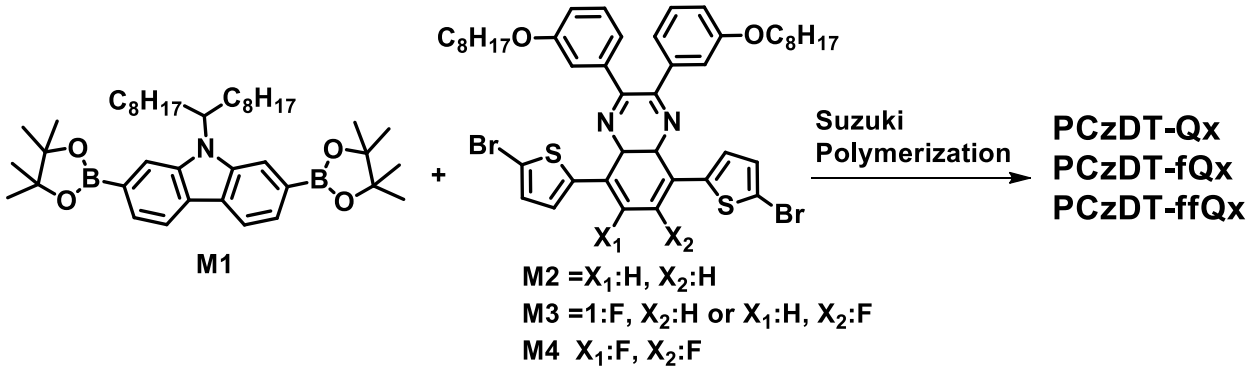

Figure 6.1 Synthetic routes of **PCzDT-Qx, PCzDT-fQx and PCzDT-ffQx**.

The remaining part was extracted with chloroform. The purified copolymers exhibit comparable molar masses (M_n) with polydispersity indexes (PDI), determined by gel permeation chromatography

(GPC) with THF as an eluent against polystyrene standards, as summarized in **Table 6.1**. All copolymers have good solubility in common organic solvents such as chloroform, THF, and chlorobenzene at room temperature. The thermogravimetric analysis measurements (TGA) showed that the onset temperatures with 5% weight-loss (T_d) of the copolymers are all over 415 °C, which indicates their excellent thermal stability (see **Figure 6.2**).

Table 6.1 Molecular weights, optical and electrochemical properties

Polymer	λ_{max}^{sol} (nm)[b]	λ_{max}^{film} (nm)	E_g^{opt} (eV)[c]	E_{LUMO} (eV)[d]	E_{HOMO} (eV)[d]	E_g^{CV} (eV)[e]
PCzDT-Qx	525	555	1.67	-3.61	-5.45	1.83
PCzDT-fQx	519	548	1.67	-3.53	-5.49	1.95
PCzDTQ-ffQx	510	543	1.64	-3.62	-5.61	1.98

[a]The temperature of 5% weight-loss under nitrogen; [b]Chloroform solution; [c]Determined from the onset of the electronic absorption spectra; [d]Cyclic voltammetry determined with Fc/Fc+ (E_{HOMO} = - 4.80 eV) as the external reference; [e]E_g^{CV}= E_{LUMO}- E_{HOMO} .

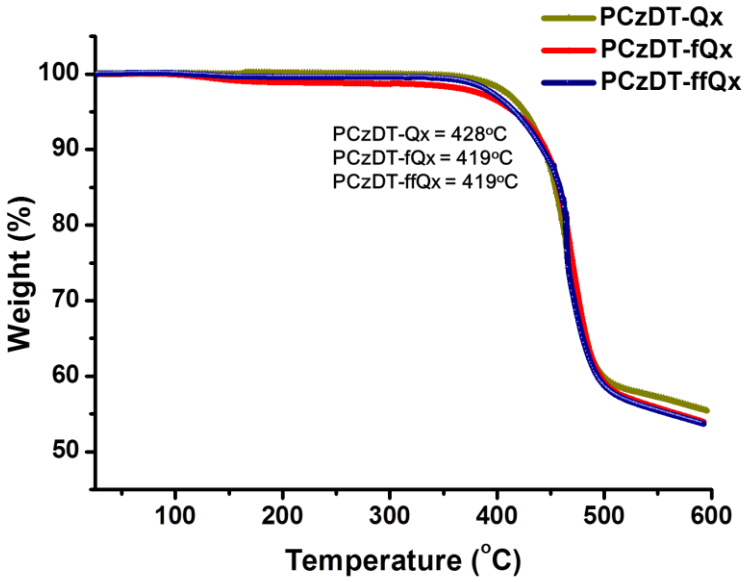

Figure 6.2 TGA for a series of the of the Cz- Qx-based copolymers

The UV-vis absorption spectra of three copolymers in chloroform solution and thin film are shown in **Figure 6.3**, and the detailed data obtained from these absorption spectra are summarized in **Table 6.1**.

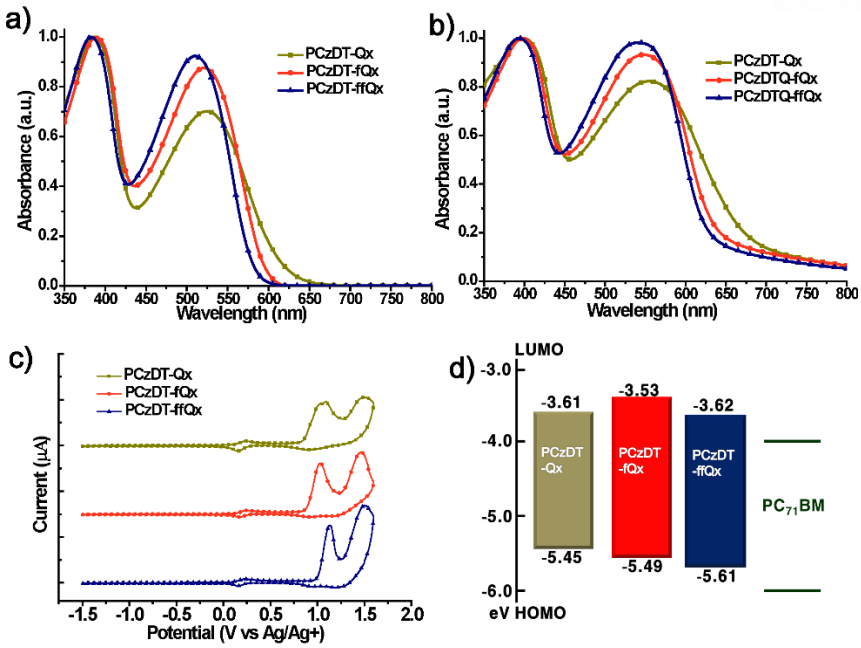

Figure 6.3. UV/Vis absorption spectra of **PCzDT-Qx**, **PCzDT-fQx**, **PCzDT-ffQx** a) in chloroform solution and b) as thin solid films spin-cast from chloroform. c) cyclic voltammograms of **PCzDT-Qx**, **PCzDT-fQx**, **PCzDT-ffQx** thin films. d) Energy level diagrams for **PCzDT-Qx**, **PCzDT-fQx**, **PCzDT-ffQx** and $PC_{71}BM$.

All three copolymers exhibit dual characteristic absorption bands, where the short-wavelength absorbance (350–400 nm) originated from the π-π* transition of the main backbone, while the long-wavelength (450–650 nm) absorbance could be ascribed to the intramolecular charge transfer (ICT) between the donor to acceptor segments. With respect to the absorption characteristics in solution, the lower-energy bands of the three copolymers slightly broaden in thin films, indicating that strong intermolecular interaction exists in the film. Note that increasing the number of F substituents from 0 to 2 led to blue shift in the ICT transitions of the copolymers. These phenomena should be related to strong electronegativity of F atom, which matches previously reported results based on copolymers with F substituents,[29] Consequently, the optical bandgaps of **PCzDT-Qx**, **PCzDT-fQx**, and **PCzDT-ffQx** are -1.83, -1.95, and -1.98 eV, respectively, as estimated from the absorption onsets in the film. Interestingly, we also observed that the ICT absorption coefficients of the fluorinated copolymers in both solution and thin film are higher than those of the non-fluorinated analogue,implying the increased intra/inter-chain interacts, as a result of the effects of C-F···H and F···S.[367, 368]

The electrochemical study of these three copolymers was conducted by using cyclic voltammetry (CV) to measure their energy levels; the corresponding redox curves are shown in **Figure 6.3** and the relevant data are summarized in **Table 6.1**. The onset of oxidation potentials (E_{ox}) of **PCzDT-Qx**, **PCzDT-fQx**, and **PCzDT-ffQx** referred to ferrocene/ferrocenium (Fc/Fc+) were 0.197, 0.202, and

0.207 V, respectively, with corresponding calculated HOMO energy levels of -5.45, -5.49, and -5.61 eV, respectively, according to the equation of HOMO = -*e*(E_{ox} + 4.80) (eV). The LUMO energy levels were calculated from the difference of the HOMO energy levels and optical bandgaps according to the equation of LUMO = (HOMO + E_g^{opt}) eV, which lies in the range of -3.53 to -3.62 eV. It is realized that Cz-Qx-containing copolymers offer significant deep-lying HOMO levels (below -5.45 eV). Furthermore, the HOMO levels scale with increasing the number of F substituents, which correlates well with the observed increase in the optical bandgaps above, as a function of the number of F substituents. Therefore, we can anticipate high V_{OC} in the PSCs with the copolymers as our proposed strategy in the introduction.

To elucidate the molecular orbital geometry and electrical property of these copolymers, the dimer models were computerized by using density functional theory (DFT) at the B3LYP/6-31G* level. For all copolymers, the LUMOs are mainly located around the Qx derivative units,while the HOMOs are delocalized over the backbones. The torsional angles (θ) between the Qx and neighboring thienyl units in **PCzDT-Qx**, **PCzDT-fQx**, and **PCzDT-ffQx** models are calculated to be 12.37, 8.06, and 8.03°, respectively (**Figure 6.4**), supporting that the fluorinated copolymers have better co-planarity for π-π stacking than the non-fluorinated copolymer does. Therefore, it is expected that both **PCzDT-fQx**, and **PCzDT-ffQx** show the relatively enhanced charge transport.

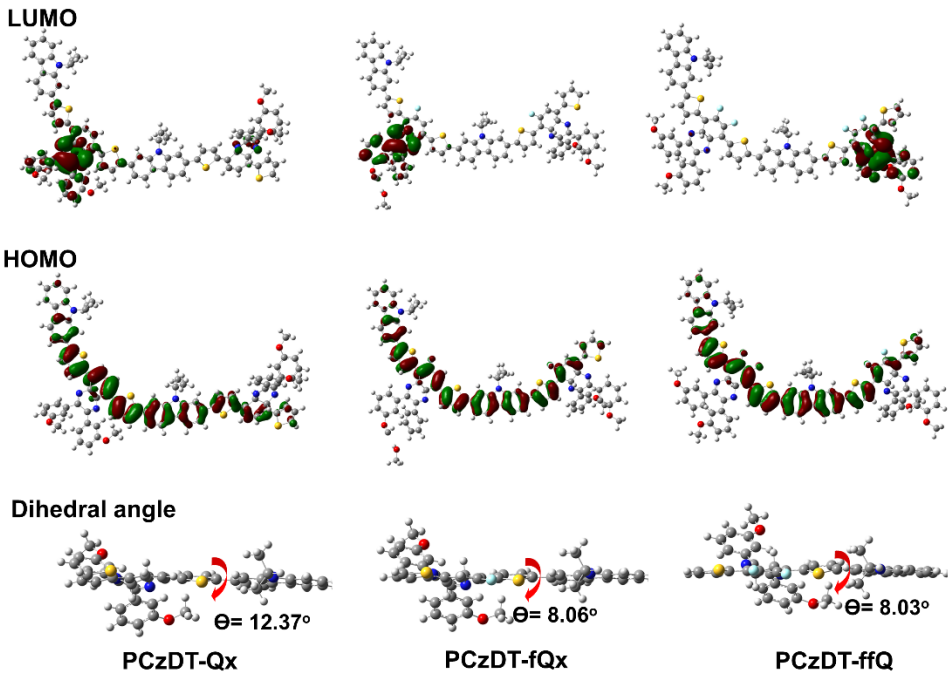

Figure 6.4 DFT calculation for a series of copolymers with each dimer model at the B3LYP/6-31G* level.

BHJ PSCs were fabricated with a device structure of ITO/PEDOT:PSS/copolymer:$PC_{71}BM$/Al. The active layers of these devices were spin-coated from *o*-dichlorobenzene (*o*-DCB) solutions of these copolymers, wherein the weight ratios of polymer:$PC_{71}BM$ varied from 1:1 to 1:3. The optimized ratios were found to be 1:3, 1:2.5, and 1:2 (w/w) for **PCzDT-Qx**, **PCzDT-fQx**, and **PCzDT-ffQx**, respectively. The representative current–voltage characteristics (*J–V*) of the each optimized device under illumination of simulated 1.5G condition (100 mW/cm^2) are shown in **Figure 6.5a,** and the device parameters are summarized in **Table 6.2**.

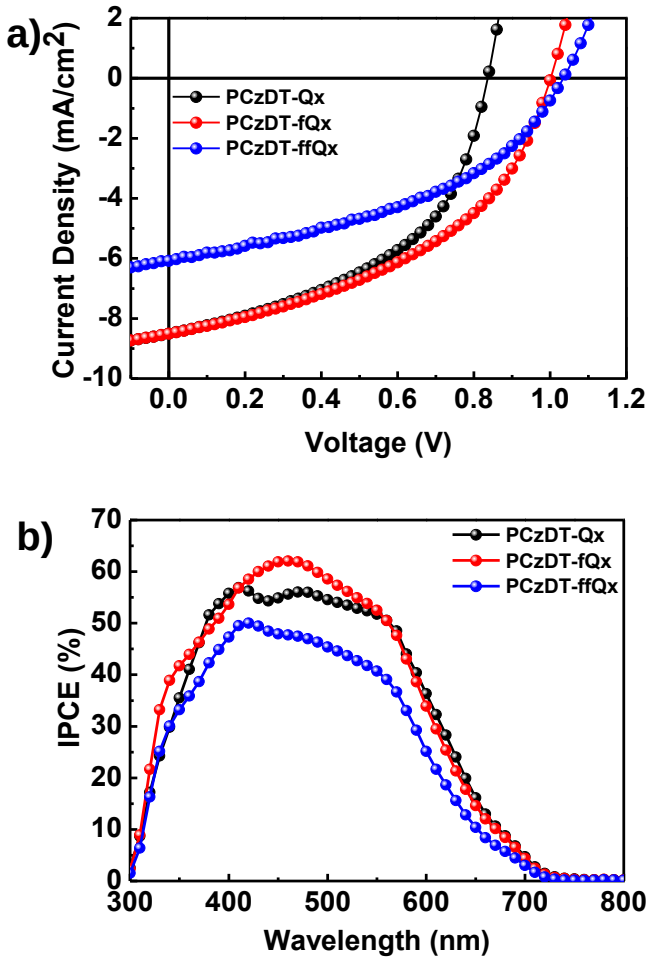

Figure 6.5. Photovoltaic characteristics of copolymer:$PC_{71}BM$-based devices; a) Current density versus voltage (*J–V*) characteristics and b) incident photon-to-current efficiency (IPCE) after thermal annealing (110℃,10min).

Table 6.2 Summary of photovoltaic characteristics

Polymer : $PC_{71}BM$ (ratio)	D/A Ratio	Thermal Annealing[a]	J_{sc} (mA/cm^2)	V_{oc} (V)	*FF*	η (%)
PCzDT-Qx	1:3	X	8.58	0.80	0.41	2.83
		O	8.50	0.84	0.49	3.44
PCzDTQ-fQx	1:2.5	X	7.41	0.87	0.40	2.54
		O	8.51	1.00	0.45	3.80
PCzDT-ffQx	1:2	X	5.82	0.91	0.38	2.01
		O	6.08	1.04	0.42	2.67

a) thermal annealing at 110℃,10min.

The detailed photovoltaic data of the optimization process for the PSCs are listed in **Figure 6.6** and **Table 6.3**. Under the optimal conditions without thermal annealing, PCEs of the copolymer devices ranged from 2.01 to 2.83%. The photovoltaic parameters of all the devices were improved as a result of thermal annealing (110 ºC, 10 min). Particularly in the cases of fluorinated copolymers, the V_{OC} values tended to be more sensitive with respect to the thermal treatment. Best device performance was achieved based on **PCzDT-fQx**:$PC_{71}BM$ with thermal annealing, which showed a V_{OC} of 1.00 V, a J_{SC} of 8.51 mA/cm^2, an *FF* of 45%, and a PCE of 3.80%. Although the PCE of **PCzDT-ffQx**-based devices was inferior to those of the devices with other copolymers due to the loss in J_{SC} and *FF*, it is intriguing to note that **PCzDT-ffQx** achieved a highest V_{OC} of 1.04 V, which is mainly attributed to its relatively deeper-lying HOMO level.

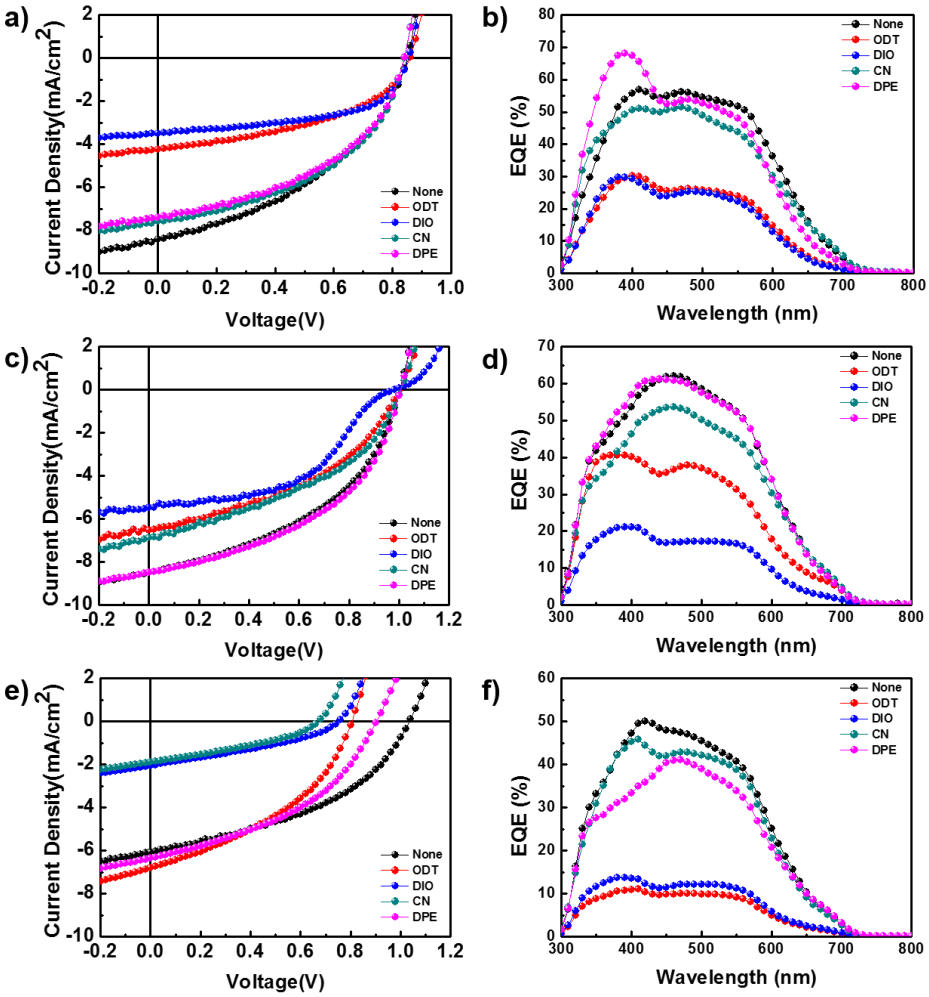

Figure 6.6 Photovoltaic characteristics of polymer:$PC_{71}BM$-based devices fabricated using a CB solvent with various additives. (a, c, e) Current density versus voltage (J–V) characteristics and (b, d, f) external quantum efficiency (EQE) for (a,b) **PCzDT-Qx**, (b,c) **PCzDT-fQx**, (e,f) **PCzDT-ffQx**, respectively.

Table 6.3 Summary of photovoltaic characteristics

Polymer : $PC_{71}BM$ (ratio)	D/A Ratio	additives	J_{sc} (mA/cm^2)	V_{oc} (V)	*FF*	η (%)
PCzDT-Qx	1:3	X	8.42	0.85	0.42	3.24
		ODT	4.24	0.86	0.45	1.77
		DIO	3.50	0.85	0.55	1.78
		CN	7.58	0.84	0.47	3.23
		DPE	7.39	0.84	0.46	3.08
PCzDTQ-fQx	1:2.5	X	8.51	1.00	0.45	3.80
		ODT	5.47	0.98	0.47	2.54
		DIO	6.54	1.00	0.42	2.76
		CN	6.89	1.00	0.42	2.88
		DPE	8.63	0.96	0.49	4.03
PCzDT-ffQx	1:2	X	6.08	1.04	0.42	2.67
		ODT	2.51	0.81	0.39	0.79
		DIO	1.93	0.70	0.35	0.47
		CN	6.81	0.81	0.40	2.21
		DPE	6.35	0.90	0.42	2.40

To the best of our knowledge, this is among the best V_{OC} values obtained from single junction BHJ PSCs. The corresponding incident photon-to-current efficiency (IPCE) spectra of the best devices are shown in **Figure 6.5b**. The intensity distributions of IPCE spectra are well-matched with their absorption spectra. The J_{SC} values calculated from IPCE data are consistent with *J*–*V* characteristics within 5% error limit.

To verify changes on V_{OC} upon thermal annealing, we also measured the dark *J*–*V* curves of PSCs and the resulting dark current density versus bias voltage curves of each optimized copolymer:$PC_{71}BM$ blend film with and without the thermal treatment are shown in **Figure 6.7**. The V_{OC} depends on the saturation current density (J_0), and J_{SC} can be calculated by using the following the eq. (1),[369, 370]

$$\mathrm{Voc} = \frac{nkT}{q}\ln\left(\frac{J_{SC}}{J_0} + 1\right) \quad (1)$$

where *q* is the charge of an electron, *n* is the ideality factor, *k* is the Boltzmann constant, and T is temperature. While J_{SC} typically has a small variation, the saturation current plays a key role in the V_{OC} since it is varied by orders of magnitude. In order to obtain a high V_{OC}, the J_0 needs

to be very low because the leakage current leads to a reduced V_{OC}. In contrast with similarity of the ratification ratios from **PCzDT-Qx**-based blend films processed with and without thermal treatment, both **PCzDT-fQx**, and **PCzDT-ffQx** ones showed reduced saturation dark currents after the thermal annealing which, in conjunction with their deep-lying HOMOs, contributes to the increase in V_{OC}.

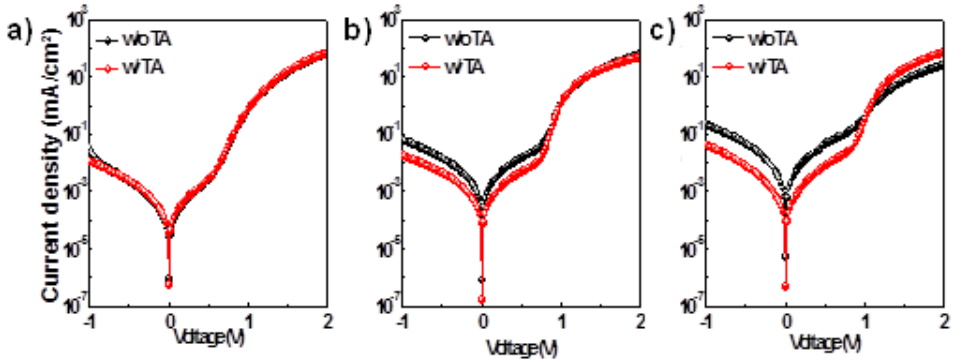

Figure 6.7 Current density-voltage (*J*-V) characteristics of copolymer:$PC_{71}BM$-based devices for a)**PCzDT-Qx** b) **PCzDT-fQx** c) **PCzDT-ffQx** fabricated using a CB solvent with and without thermal treatment in the dark condition.

It is well known that processing additives can significantly enhance device performance.[19] Thus, we have also studied the effect of several additives (1,8-octanedithiol (ODT), 1,8-diiodooctane (DIO), diphenylether (DPE), and 1-chloronaphthalene (CN)) on the optimized blend films annealed at 110 °C. All the device data with various additives are summarized in **Table 6.3**.

Disappointingly, the introduction of various additives (2%, v/v) has no positive effect on the device performance of the three copolymers. The PCEs of the relevant devices exhibited a reduction mainly due to the decrease of J_{SC} (**Table 6.3**). However, there was an exceptional case of **PCzDT-fQx**-based PSCs with DPE; the highest PCE of 4.03% was achieved with J_{SC} of 8.63 mA/cm^2, V_{OC} of 0.96 V, and *FF* of 49%.

The nanoscale morphology of polymer:$PC_{71}BM$ blend films was studied by tapping mode atomic force microscopy (AFM). **In Figure 6.8**, AFM images of all BHJ films showed uniform and smooth films with a small root-mean-squared (RMS) of 0.29–0.33 nm, indicating homogeneous mixing of copolymers and $PC_{71}BM$. Only a minor increase (0.41–0.47 nm) in RMS values was observed in the annealed films, which could account for the observed similar J_{SC} and *FF* in the PSCs processed with and without thermal treatments. In addition, we also recorded gazing-incidence wide-angle X-ray scattering (GIWAXS) measurement to gain additional structural insight into crystallites of the blend films (**Figure 6.8**). In all cases, only the integrated intensities associated with $PC_{71}BM$ were visible, indicating their amorphous nature, in agreement with what is observed in the AFM images.

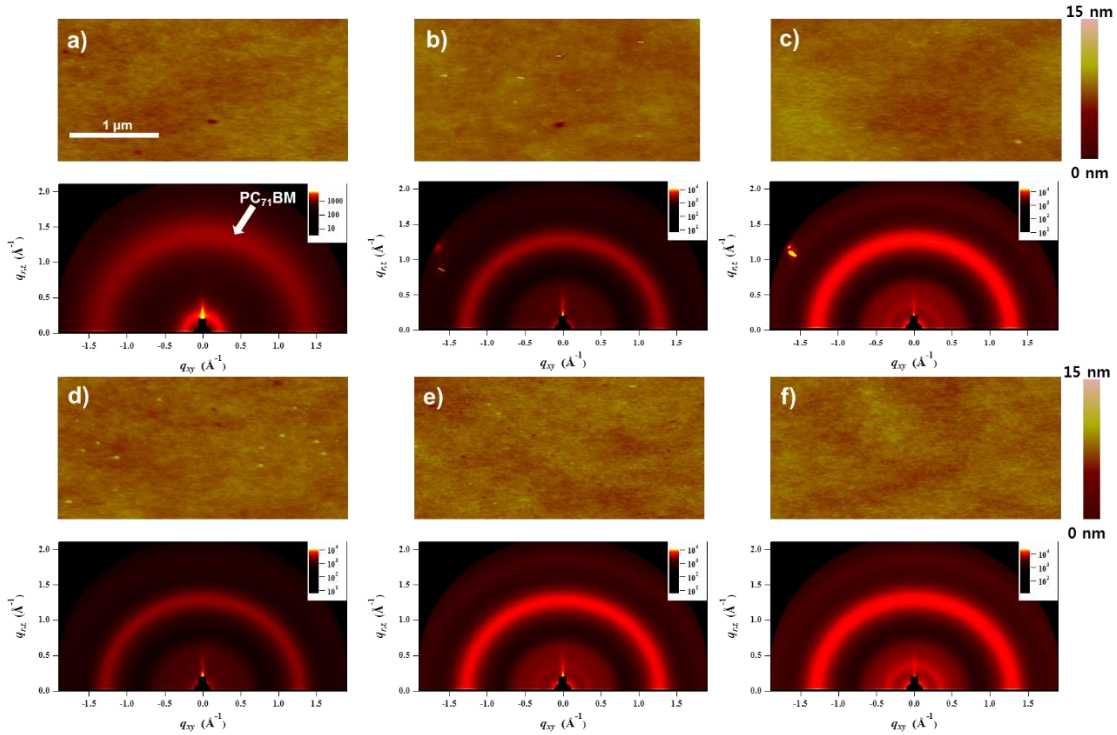

Figure 6.8 AFM topological images (top) of the best PSCs with (a-c) and without (d-f) thermal treatment for **PCzDT-Qx** (a,d), **PCzDT-fQx** (b,e), **PCzDT-ffQx** (c,f). The corresponding GIWAXS patterns are shown in the bottom of each AFM images.

The space-charge-limited-current (SCLC, J_{SCL}) measurement is used to investigate hole (μ_h) and electron (μ_e) mobilities perpendicular to substrates since they can explain the direct relationship between charge-carrier mobilities and photovoltaic device characteristics. The hole-only (ITO/PEDOT:PSS/copolymer:$PC_{71}BM$/Al) and electron-only (FTO/copolymer:$PC_{71}BM$/Al) devices were prepared by using the optimized BHJ films with thermal annealing (**Figure 6.9**). The potential loss due to the series resistance of the ITO and the built-in potential were carefully considered in order to ensure accuracy in the measurement. The *J–V* characteristics showed a quadratic dependence on voltage over a range of several volts and an inverse cubic dependence on the film thickness, consistent with the Mott–Gurney relationship, shown in eq. (2),

$$J_{SCL} = \frac{9\varepsilon_0\varepsilon_r\mu V^2}{8L^3} \quad (2)$$

where ε_0 is the free-space permittivity, ε_r is the dielectric constant of semiconductor, μ is the mobility, V is the applied voltage, and L is the thickness of BHJ films. The average hole and electron mobilities were determined to be μ_h = 6.86 ×10^{-6}, 2.15 ×10^{-5}, and 1.25 ×10^{-5} $cm^2/V{\cdot}s$ and μ_e = 2.44 ×10^{-5}, 7.21 ×10^{-5}, and 3.62 ×$10^{-5}$$cm^2/V{\cdot}s$ for **PCzDT-Qx**, **PCzDT-fQx**, and

PCzDT-ffQx, respectively (**Table 6.4**). These results showed that both fluorinated copolymers have more balanced charge mobilities than the non-fluorinated copolymer in the BHJ films. A relatively more balanced charge transport can reduce the space-charge effect that is one of the reasons for charge recombination.

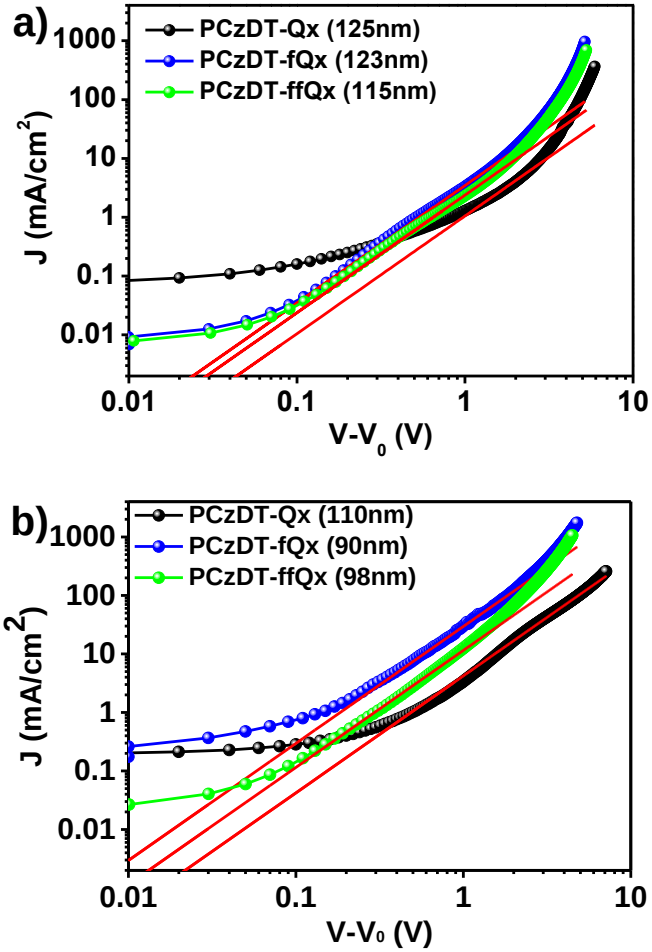

Figure 6.9 Measured *J-V* characteristics by the space-charge-limited current (SCLC) method with copolymer:$PC_{71}BM$ films under dark condition for a) hole-only devices and b) electron-only devices.

Table 6.4 Hole and electron mobilities of blend films of PCzDT-Qx, PCzDT-fQx, and PCzDT-ffQx with $PC_{71}BM$ derived using the SCLC method.

BHJ layer	μ_h [$cm^2/V{\cdot}s$]	Thickness (hole)	μ_e [$cm^2/V{\cdot}s$]	Thickness (electron)	μ_h/μ_e
PCzDT-Qx:$PC_{71}BM$	6.86×10^{-6}	125	1.03×10^{-4}	110	0.06
PCzDT-fQx:$PC_{71}BM$	2.15×10^{-5}	123	7.21×10^{-5}	90	0.298
PCzDT-ffQx:$PC_{71}BM$	1.25×10^{-5}	115	3.62×10^{-5}	98	0.345

We analysed the light intensity dependence of the *J-V* characteristics in order to quantify recombination and charge extraction within the devices. PSCs based on copolymers were characterized under various illumination intensities in the range of 10–100 mW/cm^2. The dependence of J_{SC} on light intensity can be used to determine whether J_{SC} is limited by bimolecular recombination and/or trap-assisted recombination. **Figure 6.10a** shows a log–log plot of J_{SC} as a function of light intensity. By fitting the curve to the power-law dependence of J_{SC} on light intensity, expressed as the following eq.[285, 339]

$$J_{sc} \propto I^{\alpha} \tag{3}$$

where I is intensity of incident light and α is exponent constant for BHJ PSCs. We determined the value of α to be 0.953 and 0.954 for **PCzDT-fQx**, and **PCzDT-ffQx**, respectively. In both cases of the fluorinated copolymers, the carriers are swept out without substantial recombination, whereas the non-fluorinated copolymer exhibited somewhat a lower α value, such as 0.937, implying that there exists a relatively greater possibility for bimolecular recombination in **PCzDT-Qx** blend films.

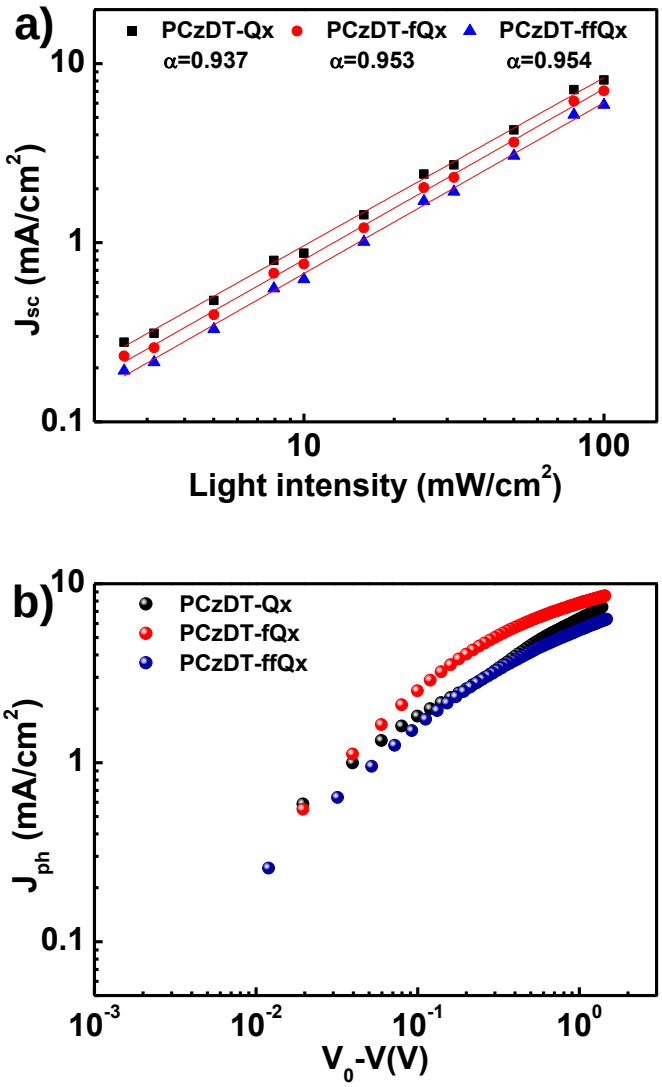

Figure 6.10 Charge recombination and transport a) double-logarithmic scale of the short circuit current density as a function of light intensity and b) photocurrent versus effective voltage of optimal PSCs.

To investigate the charge generation and extraction process, photocurrent (J_{ph}) versus effective voltage (V_{eff}) is plotted for BHJ PSCs based on illuminated and dark *J*–*V* curves (**Figure 6.10b**). J_{ph} is given by $J_{ph} = J_L - J_D$, where J_L is illuminated current density and J_D is dark current density of BHJ PSCs. V_{eff} is given by $V_{eff} = V_0 - V$, where V_0 is compensation voltage at $J_{ph} = 0$ and V is applied bias voltage. Log–log plot of J_{ph}–V_{eff} shows a transition to saturation region at certain V_{eff}, where it is getting limited by the field and *G*. The BHJ PSCs of both fluorinated copolymers reached a saturated region around 1.0 V, while the non-fluorinated system exhibited no clear saturation with over 1.1 V, where J_{ph} is still increased. Note that the value of the saturated photocurrent for **PCzDT-fQx** is higher than those of others, which is directly related with *G*. In other words, not only is the free charges extraction to the electrodes more efficient, but also the charge generation rate is better in BHJ PSCs with **PCzDT-fQx**

compared with others.[371, 372] This result is consistent with the charge transport and recombination studies above.

6.4 Conclusion

In summary, three medium bandgap D–A copolymers based on Cz and Qx (**PCzDT-Qx**, **PCzDT-fQ**x, and **PCzDT-ffQx**) have been designed and synthesized by Suzuki polymerization, seeking to achieve outstanding V_{OC} values in PSCs. All copolymers show deep-lying HOMO levels (-5.45 to -5.61 eV) that consequently can translate into high V_{OC} values in optimized BHJ PSCs with the copolymers. In particular, a pleasant surprise comes from the **PCzDT-ffQx** with a peak V_{OC} as high as 1.04 V observed, though the J_{SC} and *FF* are relatively reduced. The best PCSs derived from **PCzDT-fQx** show a PCE of 3.80% while maintaining high V_{OC} of 1.0 V, in which, moreover, PCE of up to 4.03% with DPE additive is achieved. By using dark *J*–*V* curves and SCLC in combination with detailed light-intensity-dependent J_{SC} and photocurrent measurements, we are able to disclose a precise picture of structure–property relationships in this system. We anticipate that in-depth studies (on the mechanism of charge recombination and transport characteristics) combined with further adopting molecular design strategies will be the key to obtain maximum V_{OC} and PCE simultaneously.

Chapter 7. 2,7-Carbazole and Thieno[3,4-c]pyrrole-4,6-dione Based Copolymers with Deep Highest Occupied Molecular Orbital for Photovoltaic Cells

7.1 Research background

Over the past few decades, organic solar cells comprising a conjugated polymer (as an electron donor) and fullerene derivative (as an electron acceptor) have witnessed rapid development through optimization of the material structure, device architecture and fabrication condition.[373-375] Power conversion efficiencies (PCEs) as high as ~9% have been reported recently for conventional- and inverted-type single cells.[376] To increase the short-circuit current density (J_{SC}), broad light absorption covering from the visible to near infrared regions is desirable, which has been demonstrated by designing low bandgap (LBG) conjugated donor materials.[5-7] On the other hand, the use of LBG donor materials often results in a low open-circuit voltage (V_{OC}) when donor:acceptor bulk heterojunction (BHJ) systems are prepared with fullerene derivatives as acceptors.

The V_{OC} can be estimated roughly from the energy offset between the highest occupied molecular orbital (HOMO) of conjugated polymers and lowest unoccupied molecular orbital (LUMO) of fullerene derivatives.[377] Therefore, the design strategy to maximize the offset was investigated by fine-tuning the energy level of the conjugated polymer or fullerene derivative to obtain high V_{OC}.[378, 379] A range of electron rich and deficient moieties were incorporated into a conjugated backbone in an alternating manner (donor-acceptor (D-A) type conjugated polymer).[380, 381] 2,7-Carbazole, as a weak donor in the D-A conjugated polymer backbone, showed promising photovoltaic properties.[382, 383] Poly[N-9”-heptadecanyl-2,7-carbazole-alt-5,5-(4’,7’-di-2-thienyl-2’,1’,3’-benzothiadiazole)] (PCDTBT) reported by Leclerc et al. exhibited a deep HOMO level (-5.5 eV), affording significantly high V_{OC} (~0.9 V) with [6,6]-phenyl-C_{61} butyric acid methyl ester ($PC_{61}BM$).[9] The copolymerization of carbazole with various electron accepting moieties, such as benzothiadiazole (BT)[9,11,13] and 1,4-diketopyrrolopyrrole (DPP),[15,16] afforded a HOMO level of -5.3 ~ -5.5 eV, indicating that the carbazole unit is a versatile weak electron donating moiety to obtain a high V_{OC}. In addition, a thieno[3,4-c]pyrrole-4,6-dione (TPD) unit has found wide utility in photovoltaic cells as a building block for the synthesis of conjugated polymers with rigid and electron-deficient character, rendering a deep HOMO level. Copolymerization with benzo[1,2-b:3,4-b]dithiophene (BDT),[17,18] dithienosilole (DTS),[19] dithienogermole (DTG),[20] or bithiophene showed the HOMO level of -5.5 ~ -5.7 eV with V_{OC} of 0.85 ~ 0.95 V. While maintaining the deep HOMO level of a polymer for a high V_{OC}, the HOMO level offset between a conjugated polymer and fullerene derivative should be sufficiently large to ensure efficient hole transfer.[21,22] McGehee et al.[21] reported a photovoltaic cell based on poly[bis(2-ethylhexyloxy)benzo[1,2-b:4,5-

b']dithiophene-*co*-octylthieno[3,4-c]pyrrole-4,6-dione] (PBDTTPD) and indene-C60 bisadduct (ICBA, HOMO: -5.59 eV, LUMO: -3.90 eV), which has higher HOMO and LUMO levels than $PC_{61}BM$ (HOMO: -5.79 eV, LUMO: -4.07 eV), showing a very high V_{OC} of ~1.09 V. On the other hand, hole transfer from ICBA to PBDTTPD was found to be inefficient, resulting in a reduced J_{SC} and fill factor (*FF*).

In the present study, three types of deep HOMO conjugated polymers were reported based on 2,7-carbazole and TPD moieties. Previously, Leclerc et al.[23] reported poly[N-9'-heptadecanyl-2,7-carbazole-alt-5-octylthieno[3,4-c]pyrrole-4,6-dione] (PCTPD) with a very deep HOMO level of -5.88 eV and an optical bandgap of 2.36 eV but it was not further investigated for photovoltaic application. The molecular structures were modified by incorporating 3 different thiophene-based π-bridges (thiophene, thieno[3,2-b]thiophene, bithiophene) to yield three D-A conjugated polymers, **PCTTPD**, **PCTTTPD** and **PCBTTPD**, by fine-controlling the HOMO levels. The HOMO levels were up-shifted gradually by extending the π-conjugation, showing -5.72, -5.67 and -5.57 eV for **PCTTPD**, **PCTTTPD** and **PCBTTPD**, respectively. Polymer:[6,6]-phenyl-C_{71} butyric acid methyl ester ($PC_{71}BM$) based photovoltaic cells resulted in high V_{OC} (0.86~0.94 V), which matches the energy offset of the LUMO of $PC_{71}BM$ and the HOMO of the polymer. On the other hand, **PCTTPD** and **PCTTTPD** with a deeper HOMO (relative to **PCBTTPD**) suffered from low J_{SC} (2.70 ~ 3.86 mA/cm^2), resulting in an overall PCE of approximately 1%. The measured voltage-dependent photocurrent and PL quenching data by blending with $PC_{71}BM$ suggests that an excessively deep HOMO of polymer may yield inefficient hole transfer from $PC_{71}BM$ to the polymer, suggesting significant electron-hole (e-h) recombination at the polymer/$PC_{71}BM$ interfaces.

7.2 Experimental

Polymer solar cell fabrication

Photovoltaic devices were fabricated on an indium tin oxide (ITO)-coated glass substrate with a conventional (ITO/poly(3,4-ethylenedioxythiophene):polystyrene sulfonate (PEDOT:PSS)/polymer:$PC_{71}BM$/Al) device configuration. The ITO-coated glasses were cleaned with detergent and ultrasonicated in deionized water, acetone and isopropyl alcohol and dried in an oven for a day. The PEDOT:PSS (Al4083) solution was spin-coated on ITO substrates (after UV-ozone treatments for 15 min) and dried at 140 °C. The resulting substrates were transferred to a nitrogen-filled globe box and spin-casted with polymer (0.76 wt%)/$PC_{71}BM$ (1.51 wt%) mixtures in *o*-dichlorobenzene. Subsequently, the device was pumped down under vacuum (<10^{-6} torr) and Al electrode (ca. 100 nm thick) was deposited. The area of Al electrode is 13 mm^2. The photovoltaic characteristics were measured inside the glove box using a high quality optical fiber to guide light from a solar simulator. The current-voltage characteristics were measured using a Keithley 2635A source measurement unit

under AM 1.5G illumination at 100 mWcm^{-2}. The external quantum efficiency was measured using an EQE system (Model QEX7) by PV measurement Inc (Boulder, Colorado).

7.3 Results and discussion

Figure 7.1 presents the synthetic routes to the monomers and corresponding copolymers. The monomers (M1-M3) were synthesized using a slight modification of the procedures reported

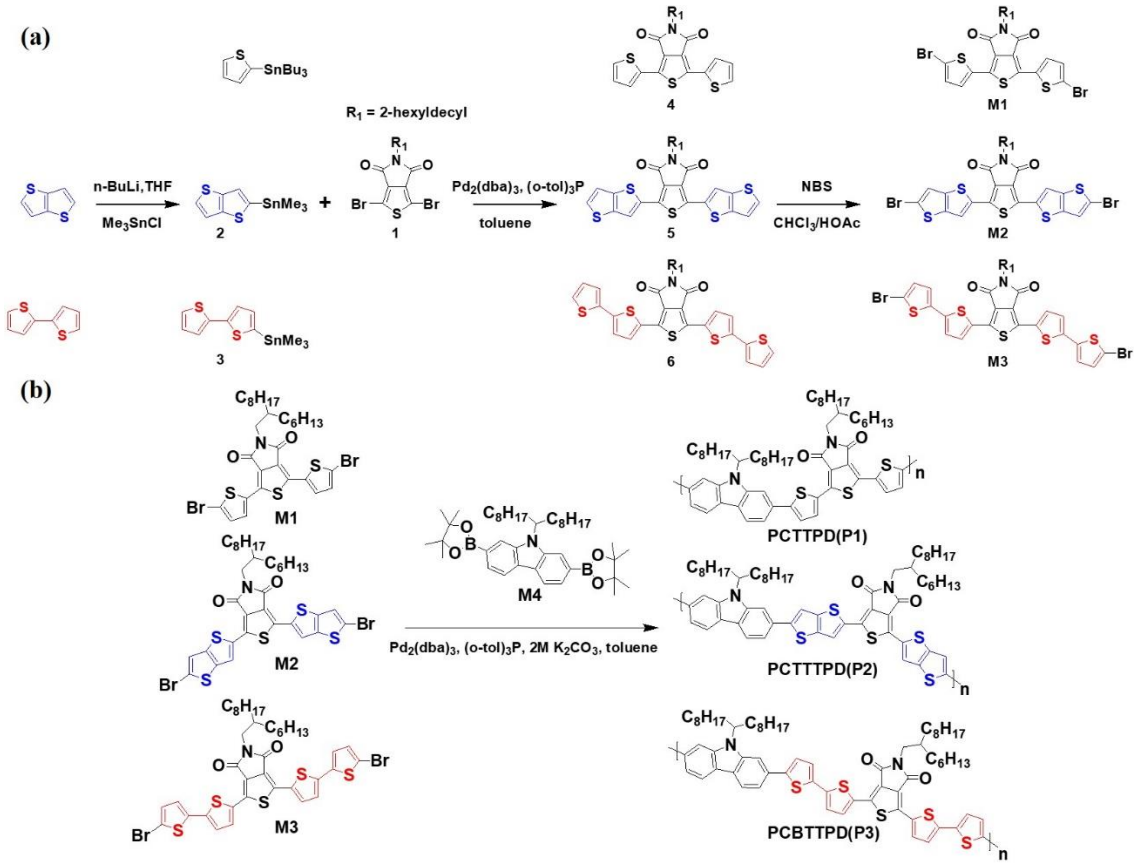

Figure 7.1 Synthetic scheme for (a) monomers and (b) polymers.

elsewhere.[23] Briefly, Stille coupling between 2-(trimethylstannyl)thieno[3,2-b]thiophene (2) and 1,3-dibromo-5-(2-hexyldecyl)thieno[3,4-c]pyrrole-4,6-dione produced compound 6 in 68% yield, and successive bromination with N-bromosuccinimide in a mixture of acetic acid and chloroform yielded M2 (64%). The other monomers, M1 and M3, were also prepared using a similar procedure.[23,25] The three types of copolymers (**PCTTPD**, **PCTTTPD**, **PCBTTPD**) were synthesized in 49~73% yield via the Suzuki cross coupling of 2,7-bis(4',4',5',5'-tetramethyl-1',3',2'-dioxaborolan-2'-yl)-N-9''-heptadecanylcarbazole (M4) and dibromo monomers (M1~M3) using $Pd_2(dba)_3$/P(*o*-tol)$_3$ as a catalyst in a mixture of toluene and aqueous K_2CO_3 solutions.

PCTTPD was readily soluble in chlorinated organic solvents (such as chloroform, chlorobenzene,

1,2-dichlorobenzene, etc.). **PCTTTPD** and **PCBTTPD** have limited solubility in chlorinated benzene solvents because of the more extended conjugation by incorporation of thienothiophene or bithiophene. The number- and weight- average molecular weights of the polymers were determined to be 20 (polydispersity index, PDI = 1.81), 13 (3.27) and 20 (3.23) Kg/mol for **PCTTPD**, **PCTTTPD** and **PCBTTPD**, respectively. All polymers showed high thermal stability with decomposition temperatures (with 5 wt.% weight loss) in a range of 350 ~ 444 °C (**Figure 7.2**). Neither melting nor recrystallization peaks were observed in the DSC measurements, suggesting the amorphous nature of the polymers caused by branched bulky alkyl chains on both the carbazole and TPD units.

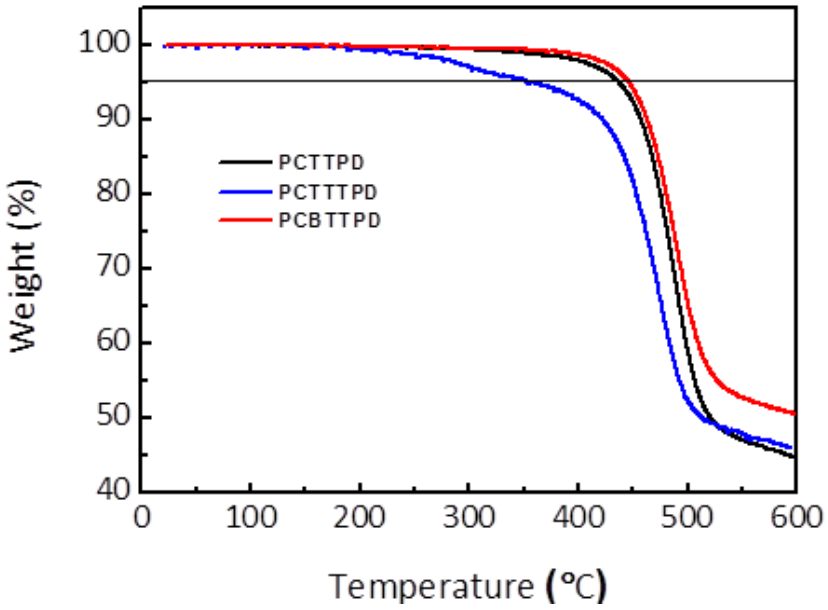

Figure 7.2 TGA thermograms for polymers.

Table 7.3 Summary of physical, optical, electrochemical and thermal properties.

Polymer	M_n[a] (g mol^{-1})	PDI	Solution		Film		E_{HOMO}[c] (eV)	E_{LUMO}[d] (eV)	T_d (°C)[e]
			λ_{abs} (nm)	ε_{max} (cm^{-1}M^{-})	λ_{abs} (nm)	E_g^{opt}[b] (eV)			
PCTTPD	20,000	1.81	487	41,600	498	2.03	-5.72	-3.69	436
PCTTTPD	12,500	3.27	517	42,500	521	2.02	-5.67	-3.65	350
PCBTTPD	20,200	3.23	528,558	52,600	528,563	1.91	-5.57	-3.66	444

[a]Number-average molecular weight determined by GPC with chloroform or trichlorobenzene eluent. [b]Optical band gap in film. [c]HOMO level was estimated from the tangential onset of oxidation (E_{ox}^{onset}) by cyclic voltammetry. HOMO (eV) = -(E_{ox}^{onset} - $E_{ferrocene}^{onset}$ + 4.8). [d]LUMO level was estimated from the HOMO value and optical band gap in film. [e]Decomposition temperature (T_d) was determined by TGA (with 5% weight-loss)

Figure 7.3 shows the UV-Vis absorption spectra of the polymers in a dilute solution (*o*-dichlorobenzene) and in thin film. The polymers showed absorption spectra in the range of 350 ~ 650 nm. The optical bandgap of **PCTTPD**, **PCTTTPD** and **PCBTTPD** was estimated to be 2.03, 2.02 and 1.91 eV, respectively, from the onset point of the absorption spectra in the thin film. With increasing conjugation length by the incorporation of thieno[3,2-b]thiophene (**PCTTTPD**) or bithiophene (**PCBTTPD**), the absorption was red-shifted in both solution and film form, relative to the thiophene-containing **PCTTPD**. **PCTTPD** and **PCTTTPD** showed featureless absorption spectra in solution but the spectra in the film were red-shifted by ~10 nm with a vibronic shoulder peak at 544 nm or 556 nm, respectively, indicating enhanced π-π stacking with the neighboring polymer chains.

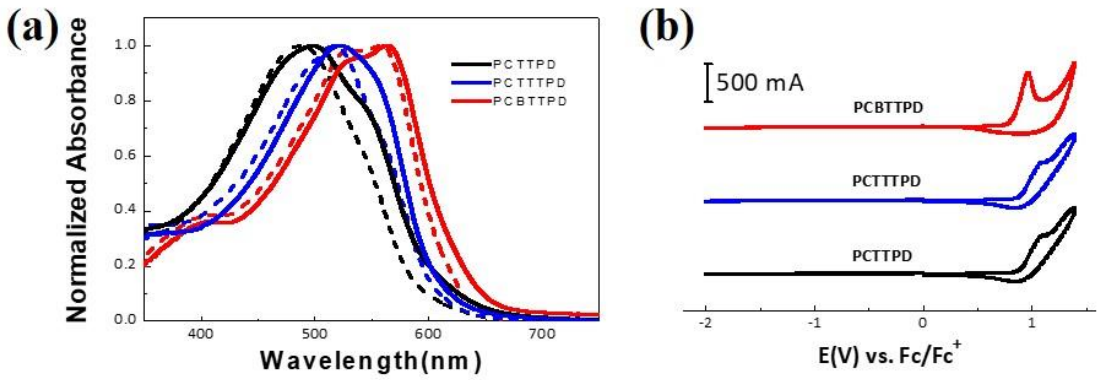

Figure 7.3 (a) UV-Vis absorption spectra in *o*-dichlorobenzene (dotted) and in film (solid) and (b) cyclic voltammogram for **PCTTPD**, **PCTTTPD** and **PCBTTPD**.

In the case of **PCBTTPD**, an inter-chain packing-related shoulder peak was observed, even in solution. The similar absorption profiles in solution and film with a clear shoulder peak suggest that **PCBTTPD** adopts pronounced intermolecular interactions, which might originate from the elongated conjugation length and reduced steric hindrance between the two bulky alkyl chains (on the carbazole and TPD units) due to the presence of a bithiophene bridge (or spacer) in between.[26] As shown in Table 1, **PCBTTPD** showed a larger extinction coefficient than **PCTTPD** and **PCTTTPD**, which is suitable for harvesting more solar energy.[384]

The electrochemical properties of three polymers were evaluated by cyclic voltammetry (CV) in the thin film to estimate the electronic energy levels relative to the standard Fc/Fc^+ redox system.[27] All polymers showed clear oxidation but no reductive current. The HOMO levels were determined to be -5.72, -5.67 and -5.57 eV for **PCTTPD**, **PCTTTPD** and **PCBTTPD**, respectively. The LUMO levels calculated from the HOMO level and the corresponding optical bandgap were -3.69 (**PCTTPD**), -3.65 (**PCTTTPD**) and -3.66 eV (**PCBTTPD**). **Table 7.1** lists the physical, optical, electrochemical and

thermal characteristics of three polymers.

The energy minimum conformation and frontier orbital structures were calculated by density functional theory (DFT; Jaguar quantum chemistry software, B3LYP/6-31G** level) (Figure 2, S2). For simplicity, methyl substituents were considered for calculations in the place of the heptadecanyl or hexyldecyl side-chains. According to the torsional profiles of TPD and thiophene (or thienothiophene), a coplanar geometry is expected for three polymers with intramolecular hydrogen bonding between the carbonyl oxygen (in TPD) and hydrogen (in the neighboring thiophene or thinethiophene). The thiophene and carbazole linkage was calculated to have a torsional angle of ~25°. The deep HOMO levels (-5.57 ~ -5.72 eV) of the polymers were achieved by a combination of the carbazole (weak e-donor) and strongly electron-accepting TPD moieties, where a high V_{OC} and oxidation stability are expected. With increasing conjugation length, the HOMO level was up-shifted gradually while the LUMO level remained similar. This is consistent with the extended conjugation affording a destabilized HOMO, which is subjected mainly to the electron-rich units, suggesting its negligible influence on the LUMO. The LUMO is localized mainly on the e-poor TPD moiety (**Figure 7.4**). The LUMO level offset for photo-induced electron transfer from the polymers to $PC_{71}BM$ (LUMO -3.9 eV) is expected to be sufficiently large.[377]

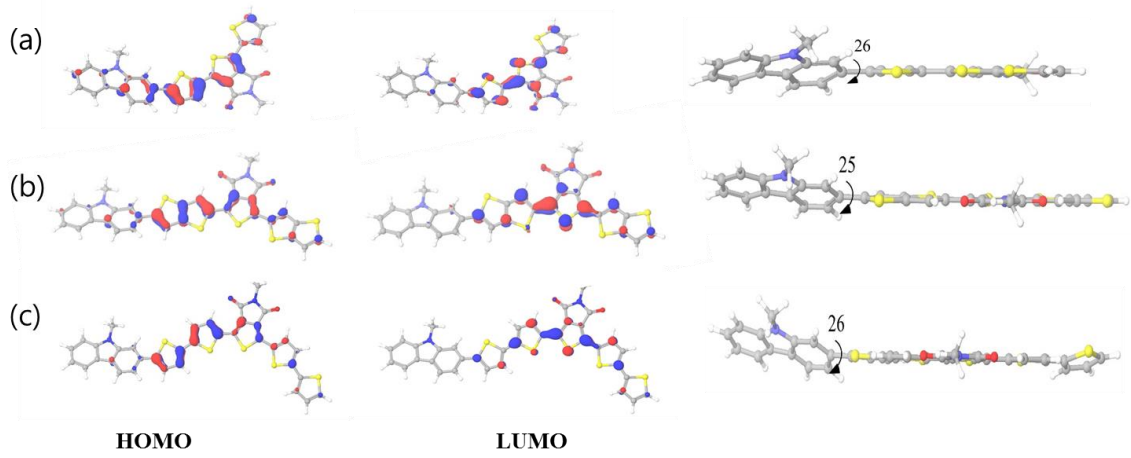

Figure 7.4 Calculated HOMO, LUMO and side-view for (a) **PCTTPD**, (b) **PCTTTPD** and (c) **PCBTTPD**. (In side-view, yellow: sulfur, red: oxygen, blue: nitrogen)

To examine photovoltaic properties, the BHJ-type PSC was fabricated with a conventional device configuration of ITO/PEDOT:PSS/polymer:$PC_{71}BM$/Al. The device fabrication details are described in the Experimental Section. To optimize the device fabrication conditions, the PSC devices were tested under a range of conditions, such as the different blend ratio, thermal treatments and processing

additives. The best performing device was obtained using the blend, polymer:$PC_{71}BM$= 1:2 (by weight) in *o*-dichlorobenzene (10 mg/mL). The current density (*J*)-voltage (*V*) curves for the optimized devices are shown in **Figure 7.5** and the detailed photovoltaic characteristics are summarized in **Table 7.2**. The V_{OC} for the blended **PCTTPD**, **PCTTTPD** and **PCBTTPD** devices was measured to be 0.94, 0.90 and 0.86 V, respectively. With increasing the conjugation length (**PCTTPD -> PCBTTPD**), the V_{OC} gradually decreased due to the increased HOMO level. The J_{SC} was measured to be 2.70, 3.86 and 7.79 mA cm^{-2} and the overall PCE was determined to be 1.14, 1.25 and 3.42% for **PCTTPD**, **PCTTTPD** and **PCBTTPD** devices.

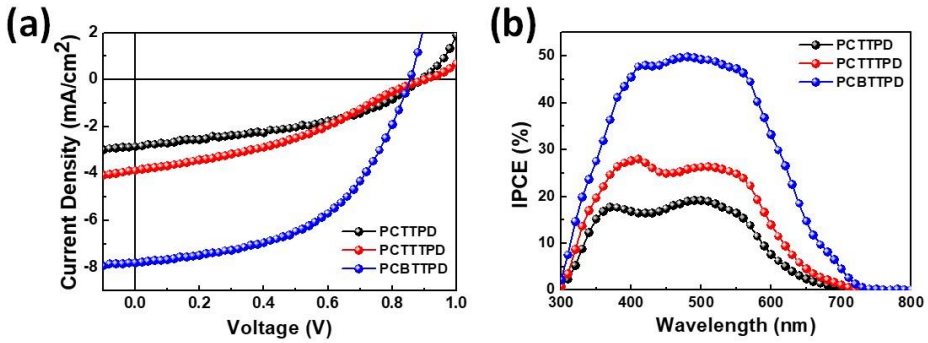

Figure 7.5 (a) Current density-voltage (*J*-*V*) charcteristics and (b) incident photon to current efficiency (IPCE) spectra.

Table 7.4 Summary of photovoltaic parameters of polymer:$PC_{71}BM$ devices.

	J_{SC} (mA cm^{-2})	V_{OC} (V)	*FF*	PCE (%)	J_{CAL} (mA cm^{-2})[b]
PCTTPD[a]	2.70	0.94	0.45	1.14	2.60
PCTTTPD	3.86	0.90	0.36	1.25	3.61
PCBTTPD	7.79	0.86	0.51	3.42	7.25

[a] With 2% 1,8-diiodoocatane as a processing additive. [b]Calculated J_{SC} from the IPCE curve.

Several factors can account for the improved J_{SC} value for **PCBTTPD**:$PC_{71}BM$ compared to the other polymers. First, the higher molar absorption coefficient of the **PCBTTPD** film enables a strong light absorption with a similar active layer thickness. In addition, the film morphology has a significant effect on the photo-induced charge generation and their transport to the electrodes. The surface morphology of the polymer:$PC_{71}BM$ blended films was measured by atomic force microscopy (AFM) (**Figure 7.6**). In the case of **PCTTPD**:$PC_{71}BM$, a large phase separation with a domain size of 300~400 nm (in diameter) was measured, suggesting that it is difficult for the generated excitons to reach the polymer/$PC_{71}BM$ interfaces before recombination. This can explain why the **PCTTPD**:$PC_{71}BM$ device shows a poor J_{SC} value. The **PCTTTPD** and **PCBTTPD** blend films showed a well distributed

intermixed surface morphology. Surprisingly, the **PCTTTPD**:$PC_{71}BM$ (domain size ~100 nm) blend generates a much smaller J_{SC} compared to **PCBTTPD**:$PC_{71}BM$ (domain size ~150 nm).

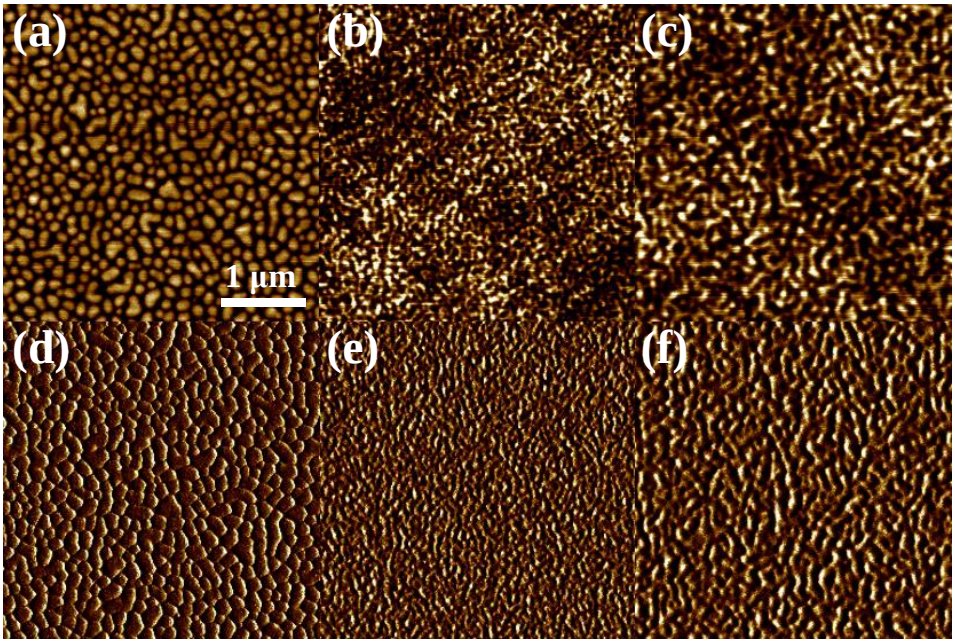

Figure 7.6 AFM topography (a~c) and phase (d~f) images of (a, d) **PCTTPD** (b, e) **PCTTTPD** (c, f) **PCBTTPD** blend films with $PC_{71}BM$.

To compare the photo-induced charge transfer processes of the three polymer blends, the photoluminescence (PL) spectra of polymer films were measured with and without blending $PC_{71}BM$ (**Figure 7.7**). Efficient PL quenching can be understood in terms of the efficient dissociation of photo-generated excitons.[28] Although this comparison is only approximate, the estimated PL quenching efficiencies of the **PCTTPD**, **PCTTTPD** and **PCBTTPD** blend films were 93, 97 and 98%, respectively.

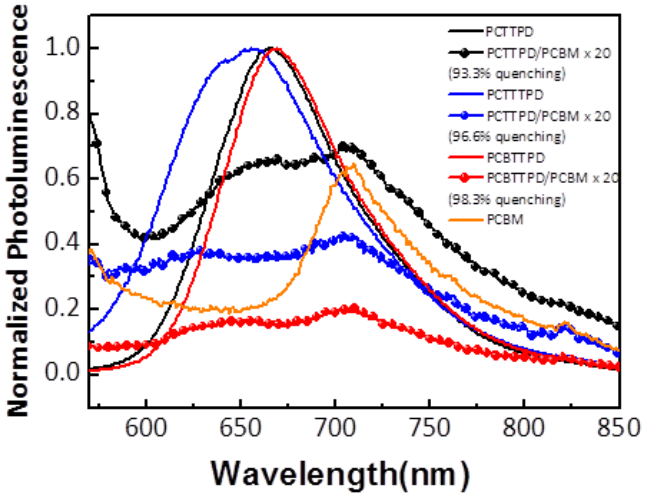

Figure 7.7 PL spectra of polymers with and without blending $PC_{71}BM$. Spectra were measured by exciting at 520 nm.

The relatively low PL quenching for **PCTTPD**:$PC_{71}BM$ may be related (partially) to the film morphology (see **Figure 7.6**), suppressing exciton diffusion and dissociation at the polymer/$PC_{71}BM$ interface.[29] **PCTTTPD**:$PC_{71}BM$ showed similar PL quenching with **PCBTTPD**:$PC_{71}BM$ but the former exhibited much smaller J_{SC} values (3.86 vs. 7.79 mA cm^{-2}). The relatively poor J_{SC} of **PCTTPD** and **PCTTTPD** devices might be related to their deeper HOMO energy levels (relative to **PCBTTPD**), yielding less efficient hole transfer from $PC_{71}BM$ to the polymers.[22] Previously, McGehee et al. reported the energy offset between the HOMOs of fullerene and the donor polymer for efficient hole transfer with minimized electron-hole recombinations.[21] A sufficient energy offset for the **PCBTTPD**:$PC_{71}BM$ blend (ca. -0.3 eV) enables efficient hole transfer from $PC_{71}BM$ to the polymer. On the other hand, the relatively small energy offset between the HOMOs of $PC_{71}BM$ and **PCTTPD** (or **PCTTTPD**) suggests potential significant electron-hole recombination at the polymer/$PC_{71}BM$ interfaces, decreasing the J_{SC}.

To understand the underlying mechanism for the different device characteristics for three polymers, charge recombination was also examined by comparing the saturated photocurrent (J_{ph}) as a function of the bias and light intensity. The photocurrent ($J_{ph} = J_L - J_D$) was analyzed by subtracting the current density in the dark (J_D) from the current density under illumination (J_L) with changing illumination intensity. According to the J_{ph}-V characteristics, the compensation voltage (V_0) at which $J_{ph} = 0$ was obtained.

Figure 7.8 shows the measured photocurrent as a function of the effective voltage (V_0-V). In the case of **PCBTTPD**:$PC_{71}BM$, the photocurrent showed two regimes: a linear regime and a saturation regime, where the J_{ph} was saturated quickly at V_0-$V > 0.3$ V. This field-independent region suggests that the **PCBTTPD**:$PC_{71}BM$ system has negligible trapped charges and most of the generated charge carriers

are extracted and collected by the electrodes with insignificant recombination.

In contrast, the J_{ph} of the other polymer blends (**PCTTPD**, **PCTTTPD**) showed a strong field dependence across a large bias range without showing a clear saturation regime, suggesting serious electron-hole recombination. A stronger electric field is needed to sweep out the photo-generated charge carriers before recombination and separate the geminate electron-hole pairs. From the measured J_{ph} data, the higher photovoltaic properties of **PCBTTPD**:$PC_{71}BM$ can be understood in terms of the suppressed charge recombination by efficient hole transfer from the polymer to $PC_{71}BM$.

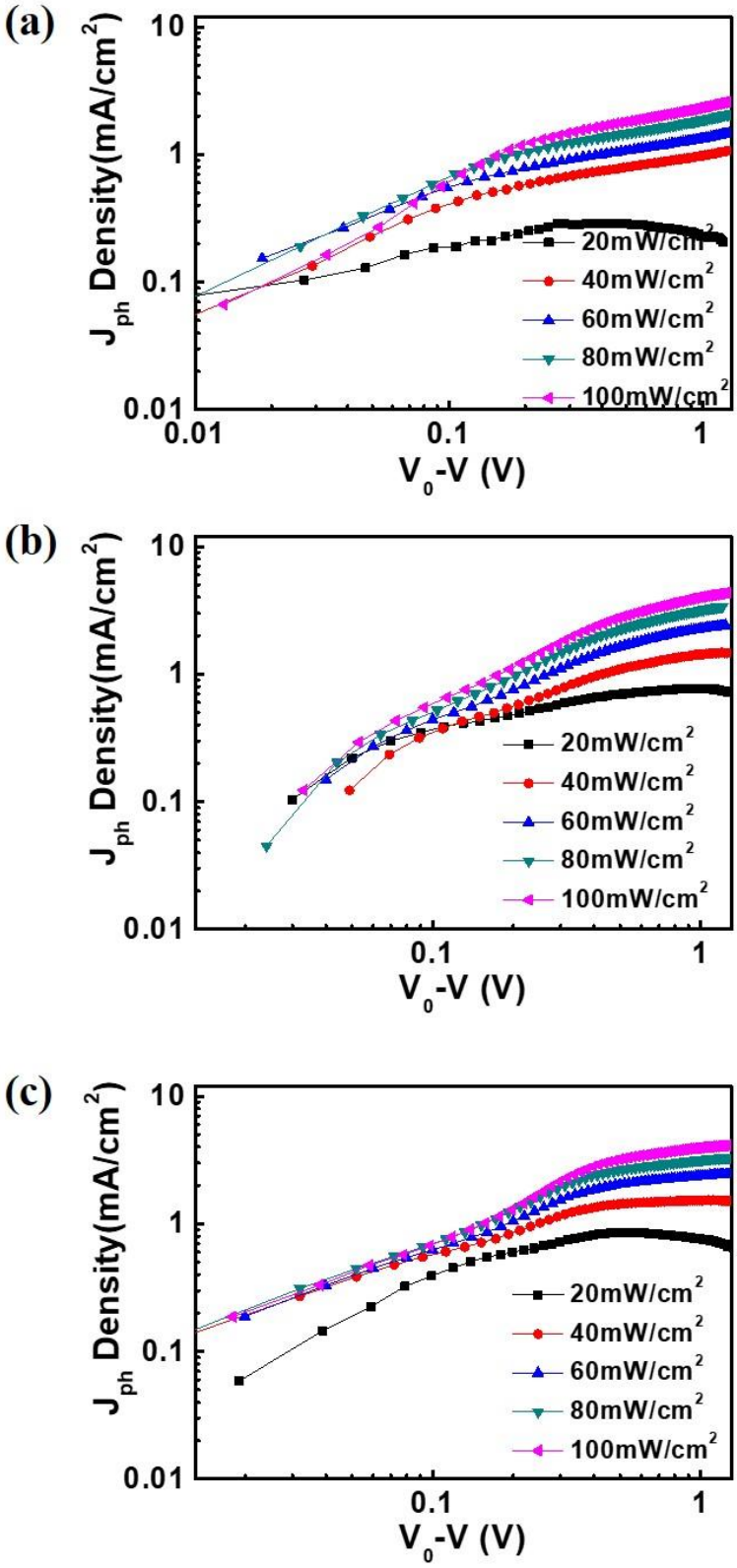

Figure 7.8 Photocurrent measurement as a function of effective voltage for (a) **PCTTPD**:$PC_{71}BM$, (b) **PCTTTPD**:$PC_{71}BM$ and (c) **PCBTTPD**:$PC_{71}BM$.

The charge carrier transport characteristics were also evaluated by fabricating hole-only and electron-only devices with a configuration of ITO/PEDOT:PSS/polymer:$PC_{71}BM$/Au and FTO (fluorine-doped tin oxide)/polymer:$PC_{71}BM$/Al. Space-charge-limited current measurements were used to calculate the hole- and electron mobility (**Figure 7.9** and **Table 7.3**).[30,31] The extension of the conjugation length from **PCTTPD** to **PCTTTPD** resulted in ~ 1 order higher mobility with a more balanced hole/electron mobility ratio (μ_h/μ_e) (μ_h = 3.5 × 10^{-6}, 2.3 × 10^{-5}; μ_e = 4.4 × 10^{-5}, 1.3 × 10^{-4} $cm^2/V{\cdot}s$ for **PCTTPD**:$PC_{71}BM$ and **PCTTTPD**:$PC_{71}BM$). The **PCBTTPD**:$PC_{71}BM$ blend with further extended π-conjugation showed slightly higher charge mobilities (μ_h = 3.9 × 10^{-5}, μ_e = 1.4 × 10^{-4} $cm^2/V{\cdot}s$). Therefore, the higher hole mobility of **PCBTTPD**:$PC_{71}BM$ with the more balanced μ_h/μ_e value might also account for the higher J_{SC} compared to the other polymeric systems.

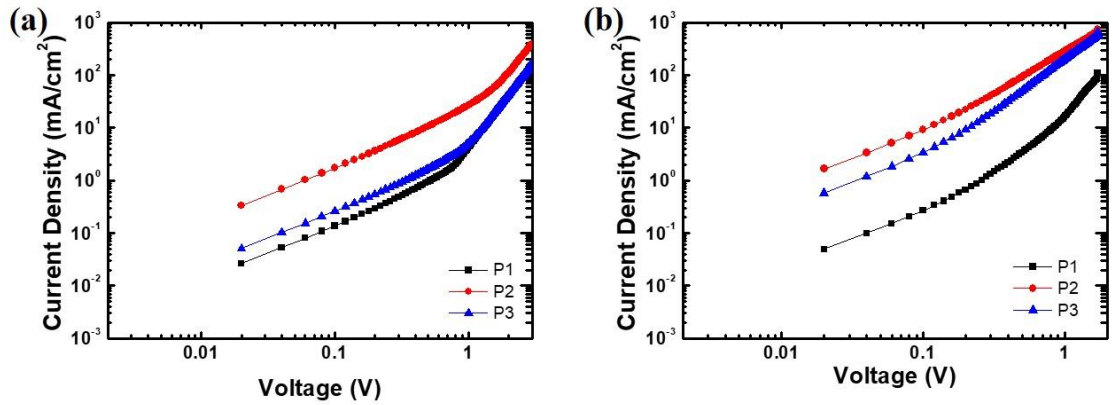

Figure 7.9 Current-voltage characteristics of (a) hole-only and (b) electron-only devices for polymer:$PC_{71}BM$ by a SCLC method.

Table 7.3 Summary of hole- and electron mobilities.

Polymer	μ_h (cm^2/Vs)	μ_e (cm^2/Vs)	μ_h/μ_e
PCTTPD:$PC_{71}BM$	3.5 × 10^{-6}	4.4 × 10^{-5}	12.5
PCTTTPD:$PC_{71}BM$	2.3 × 10^{-5}	1.3 × 10^{-4}	5.9
PCBTTPD:$PC_{71}BM$	3.9 × 10^{-5}	1.4 × 10^{-4}	3.7

7.4 Conclusion

This paper reported three types of D-A conjugated polymers with a deep HOMO, based on the carbazole and TPD moieties with different thiophene spacers to fine-tune the HOMO level. Extending the conjugation length by the incorporation of thiophene, thieno[3,2-b]thiophene and bithiophene yielded an up-shift of the HOMO level from -5.72 to -5.57 eV. The deeper HOMO level of **PCTTPD** and **PCTTTPD** (compared to **PCBTTPD**) afforded a higher V_{OC} of 0.94 and 0.90 V, respectively. On the other hand, a poor J_{SC} (2.7 ~ 3.86 mA cm^{-2}) was measured for both **PCTTPD**:$PC_{71}BM$ and **PCTTTPD**:$PC_{71}BM$ devices, yielding PCEs of ~1%. The voltage and light intensity-dependent photocurrent and PL quenching measurements suggested significant electron-hole recombination at the polymer/$PC_{71}BM$ interfaces due to the insufficient energy offset for hole transfer between the HOMOs of the polymer and $PC_{71}BM$. The **PCBTTPD** polymer with the higher HOMO level showed the best PCE of 3.42% with a significantly improved J_{SC} of 7.79 mA cm^{-2}. The HOMO level of the photovoltaic polymers should be fine-adjusted carefully by considering efficient hole transfer as well as a high V_{OC}.

Chapter 8. Summary

In this thesis, I reported various engineering strategies employing novel TCE materials such as AgNW electrode by alignment process, and hybridized surface plasmon effect using plasmonic electrode consisting of align AgNW and Ag@SiO_2 NPs electrode, enhancing planarity of molecular backbone of PBTTFB and development of ternary PSC using two acceptors with $PC_{71}BM$ and ITIC mixture with a promising conjugated donor polymer PBTTFB and introducing several processing additives with conjugated polymers resulting in enhanced electromagnetic field to maximize light harvesting to active layer, overcoming problem of binary BHJ solar cells and finely-distributed nano morphology to make good pathway for electron and holes, respectively, for the highly efficient polymer solar cells.

Firstly, I have demonstrated a high-throughput, one-step capillary printing strategy for the fabrication of TCEs based on aligned AgNWs. In the capillary printing process, the unidirectional dragging of AgNW solutions by a trigonal prismatic PDMS stamp with nano-patterned channels produced highly aligned AgNW arrays. The aligned AgNW networks showed lower electrical percolation thresholds than random AgNW networks, which led to higher T at similar R_s or lower R_s at similar T. Notably, partially misaligned NWs are necessary for the formation of the electrical percolation network. The TCEs based on aligned AgNW networks exhibited outstanding performances of 19.5 Ω/sq at 96.7% transmittance and a high FoM value of 571.3, which can be favorably compared to the performances of other NW-based TCEs. For the potential applications of aligned AgNW TCEs in optoelectronic devices such as Polymer Solar Cells (PSCs) and Polymer Light Emitting Diodes (PLEDs), we demonstrated highly efficient, flexible PSCs and PLEDs. The observed PCE of 8.57% in PSCs, as well as the luminance efficiency of 14.25 cd/A and power efficiency of 10.62 lm/W in PLEDs, currently represent the highest efficiencies reported for AgNW-based devices. Moreover, the flexible PSC fabricated using aligned AgNWs had a PCE of 8.00%, 80% of which was maintained after 1,000 bending cycles. This work demonstrates that aligned Ag NW networks are excellent candidates for low-cost ITO-free TCEs used in optoelectronic devices and future flexible electronics.

Secondly, we have demonstrated the use of NP-enhanced plasmonic AgNW electrodes, consisting of aligned AgNW networks decorated by core-shell Ag@SiO_2NPs, for the improvement of device efficiency in both OLEDs and OSCs. The NP-enhanced plasmonic AgNW electrodes functioned as outstanding transparent electrodes as well as performing as hybrid plasmonic structures. In the NP-NW hybrid plasmonic system, AgNPs played an important role as nanoantennae, serving to couple incoming light into NW plasmons propagating along the NW, resulting in large near-field enhancement, which affected light absorption efficiency in OSCs. In addition, simulated near-field distributions of the NP-NW system exhibited giant local E-field enhancement at NP-NW junctions due to strong gap plasmon

coupling between LSPs of AgNPs and propagating SPPs of AgNWs. Raman mapping results revealed that strong plasmon coupling in the NW-NP system provides large E-field enhancement at NP-NW junctions. Additionally, we achieved high EL efficiencies of up to 25.33 cd/A (at 3.2 V) and power efficiency of 25.14 lm/W (3.0 V) in fluorescent LEDs as well as a PCE of 9.19% in OSCs using Ag@SiO_2NP-AgNW electrodes. These significant results represent the highest efficiency reported for OLEDs and OSCs based on AgNW electrodes. Furthermore, NP-enhanced plasmonic AgNW films may be further explored for use in a variety of optoelectronic devices and other plasmonic applications.

Finally, we studied the charge carrier dynamics in PBTTFB:ITIC:$PC_{71}BM$ TPSCs based on the observation that JV characteristics of TPSCs with various acceptor ratio exhibited unintended V_{OC} pinning phenomenon to the highest possible value formed by PBTTFB and ITIC junction. This bizarre phenomenon was direct contradictory to our previous observations in TPSC studies. We compared previously suggest models such as parallel-like, alloy, or energy cascade structure, but nothing can explain our observations. The PL measurement on electron accepters revealed that rare charge transfer between ITIC and $PC_{71}BM$ by showing remained PL from ITIC even after mixing with $PC_{71}BM$. Spectral overlap of PBTTFB PL spectrum with ITIC absorption spectrum confirmed the FRET exists in the ternary blend. The competition between CT from PBTTFB to $PC_{71}BM$ and ET from PBTTFB to ITIC was clarified via TAS, confirming that ET dominates over CT. The collaboration of two physical phenomena allowed the selective charge transfer resulting in the improvement of both J_{SC} and V_{OC} simultaneously in TPSCs. This selective charge transfer is unusual and unfamiliar in the polymer solar cell community, but our study could provide the new and efficient way to improve the performance of solar cells. Considering previously researched studies, the selective charge transfer does not always occur in two acceptor TPSCs. It still requires more studies and the cumulative experimental data on the prerequisite for this efficient CT in the ternary blend.

Furthermore, I have demonstrated promising p-type conjugated polymers with several processing additives resulting in to maximize light harvesting to active layer finely-distributed nano-network to make good pathway for charge carriers for the high-performance polymer solar cells.

These successful various stretegies need to be addressed in the future and further explored and applied for great utility in the development and mass production of next-generation optoelectronic devices.

Chapter 9. References

1. Becquerel, A. E. *Comptes Rendus de L´Academie des Sciences* **1839,** 9.
2. Adams, W. G.; Day, R. E. *Proceedings of the Royal Society of London* **1876,** 25, (171-178), 113-117.
3. Volmer, M. *Annalen der Physik* **1913,** 345, (4), 775-796.
4. Tang, C. W. *Applied Physics Letters* **1986,** 48, (2), 183-185.
5. Sariciftci, N. S.; Smilowitz, L.; Heeger, A. J.; Wudl, F. *Science* **1992,** 258, (5087), 1474-1476.
6. Yu, G.; Gao, J.; Hummelen, J. C.; Wudl, F.; Heeger, A. J. *Science* **1995,** 270, (5243), 1789-1791.
7. Siddiki, M. K.; Li, J.; Galipeau, D.; Qiao, Q. *Energy & Environmental Science* **2010,** 3, (7), 867-883.
8. Saunders, B. R.; Turner, M. L. *Advances in Colloid and Interface Science* **2008,** 138, (1), 1-23.
9. Heremans, P.; Cheyns, D.; Rand, B. P. *Accounts of Chemical Research* **2009,** 42, (11), 1740-1747.
10. Brédas, J.-L.; Norton, J. E.; Cornil, J.; Coropceanu, V. *Accounts of Chemical Research* **2009,** 42, (11), 1691-1699.
11. Brabec, C. J.; Cravino, A.; Meissner, D.; Sariciftci, N. S.; Fromherz, T.; Rispens, M. T.; Sanchez, L.; Hummelen, J. C. *Advanced Functional Materials* **2001,** 11, (5), 374-380.
12. Peumans, P.; Yakimov, A.; Forrest, S. R. *Journal of Applied Physics* **2003,** 93, (7), 3693-3723.
13. Li, G.; Shrotriya, V.; Yao, Y.; Huang, J.; Yang, Y. *Journal of Materials Chemistry* **2007,** 17, (30), 3126-3140.
14. Ameri, T.; Dennler, G.; Lungenschmied, C.; Brabec, C. J. *Energy & Environmental Science* **2009,** 2, (4), 347-363.
15. Gur, I.; Fromer, N. A.; Chen, C.-P.; Kanaras, A. G.; Alivisatos, A. P. *Nano Letters* **2007,** 7, (2), 409-414.
16. Schilinsky, P.; Waldauf, C.; Hauch, J.; Brabec, C. J. *Journal of Applied Physics* **2004,** 95, (5), 2816-2819.
17. Waldauf, C.; Scharber, M. C.; Schilinsky, P.; Hauch, J. A.; Brabec, C. J. *Journal of Applied Physics* **2006,** 99, (10), 104503.
18. Novotny, C. J.; Yu, E. T.; Yu, P. K. L. *Nano Letters* **2008,** 8, (3), 775-779.
19. Schilinsky, P.; Waldauf, C.; Brabec, C. J. *Advanced Functional Materials* **2006,** 16, (13), 1669-1672.
20. Kippelen, B.; Bredas, J.-L. *Energy & Environmental Science* **2009,** 2, (3), 251-261.
21. Potscavage, W. J.; Sharma, A.; Kippelen, B. *Accounts of Chemical Research* **2009,** 42, (11), 1758-1767.
22. Li, X.; Choy, W. C.; Huo, L.; Xie, F.; Sha, W. E.; Ding, B.; Guo, X.; Li, Y.; Hou, J.; You, J.; Yang, Y. *Adv Mater* **2012,** 24, (22), 3046-52.
23. Erwin, W. R.; Zarick, H. F.; Talbert, E. M.; Bardhan, R. *Energy Environ. Sci.* **2016,** 9, (5), 1577-1601.
24. Lu, L.; Luo, Z.; Xu, T.; Yu, L. *Nano Lett* **2013,** 13, (1), 59-64.
25. Jung, K.; Song, H.-J.; Lee, G.; Ko, Y.; Ahn, K.; Choi, H.; Kim, J. Y.; Ha, K.; Song, J.; Lee, J.-K.; Lee, C.; Choi, M. *ACS Nano* **2014,** 8, (3), 2590-2601.
26. Niesen, B.; Rand, B. P.; Van Dorpe, P.; Cheyns, D.; Tong, L.; Dmitriev, A.; Heremans, P. *Advanced Energy Materials* **2013,** 3, (2), 145-150.
27. Wu, B.; Wu, X.; Guan, C.; Fai Tai, K.; Yeow, E. K.; Jin Fan, H.; Mathews, N.; Sum, T. C. *Nat Commun* **2013,** 4, 2004.
28. Atwater, H. A.; Polman, A. *Nat Mater* **2010,** 9, (3), 205-13.
29. Brus, L. *Accounts of Chemical Research* **2008,** 41, (12), 1742-1749.
30. Kelly, K. L.; Coronado, E.; Zhao, L. L.; Schatz, G. C. *The Journal of Physical Chemistry B* **2003,** 107, (3), 668-677.
31. Burda, C.; Chen, X.; Narayanan, R.; El-Sayed, M. A. *Chemical Reviews* **2005,** 105, (4), 1025-1102.
32. El-Sayed, M. A. *Accounts of Chemical Research* **2001,** 34, (4), 257-264.
33. Xia, Y.; Xiong, Y.; Lim, B.; Skrabalak, S. E. *Angewandte Chemie International Edition* **2009,** 48,

(1), 60-103.
34. Rycenga, M.; Cobley, C. M.; Zeng, J.; Li, W.; Moran, C. H.; Zhang, Q.; Qin, D.; Xia, Y. *Chemical Reviews* **2011,** 111, (6), 3669-3712.
35. Rubio, G.; Agraït, N.; Vieira, S. *Physical Review Letters* **1996,** 76, (13), 2302-2305.
36. Krans, J. M.; van Ruitenbeek, J. M.; Fisun, V. V.; Yanson, I. K.; de Jongh, L. J. *Nature* **1995,** 375, 767.
37. Olesen, L.; Laegsgaard, E.; Stensgaard, I.; Besenbacher, F.; Schio/tz, J.; Stoltze, P.; Jacobsen, K. W.; No/rskov, J. K. *Physical Review Letters* **1994,** 72, (14), 2251-2254.
38. Hong, B. H.; Bae, S. C.; Lee, C.-W.; Jeong, S.; Kim, K. S. *Science* **2001,** 294, (5541), 348-351.
39. Rodrigues, V.; Fuhrer, T.; Ugarte, D. *Physical Review Letters* **2000,** 85, (19), 4124-4127.
40. Kassubek, F.; Stafford, C. A.; Grabert, H. *Physical Review B* **1999,** 59, (11), 7560-7574.
41. Bürki, J.; Stafford, C. A. *Applied Physics A* **2005,** 81, (8), 1519-1525.
42. Rodrigues, V.; Bettini, J.; Rocha, A. R.; Rego, L. G. C.; Ugarte, D. *Physical Review B* **2002,** 65, (15), 153402.
43. Yanson, A. I.; Yanson, I. K.; van Ruitenbeek, J. M. *Physical Review Letters* **2000,** 84, (25), 5832-5835.
44. Ponrouch, A.; Garbarino, S.; Bertin, E.; Andrei, C.; Botton, G. A.; Guay, D. *Advanced Functional Materials* **2012,** 22, (19), 4172-4181.
45. Rathmell, A. R.; Bergin, S. M.; Hua, Y.-L.; Li, Z.-Y.; Wiley, B. J. *Advanced Materials* **2010,** 22, (32), 3558-3563.
46. Mohl, M.; Pusztai, P.; Kukovecz, A.; Konya, Z.; Kukkola, J.; Kordas, K.; Vajtai, R.; Ajayan, P. M. *Langmuir* **2010,** 26, (21), 16496-16502.
47. Chang, Y.; Lye, M. L.; Zeng, H. C. *Langmuir* **2005,** 21, (9), 3746-3748.
48. Sachse, C.; Müller-Meskamp, L.; Bormann, L.; Kim, Y. H.; Lehnert, F.; Philipp, A.; Beyer, B.; Leo, K. *Organic Electronics* **2013,** 14, (1), 143-148.
49. Sachse, C.; Weiß, N.; Gaponik, N.; Müller-Meskamp, L.; Eychmüller, A.; Leo, K. *Advanced Energy Materials* **2014,** 4, (2), n/a-n/a.
50. Fan, S.; Chapline, M. G.; Franklin, N. R.; Tombler, T. W.; Cassell, A. M.; Dai, H. *Science* **1999,** 283, (5401), 512-514.
51. Fung, M. K.; Sun, Y. C.; Ng, A.; Ng, A. M. C.; Djurišić, A. B.; Chan, H. T.; Chan, W. K. *ACS Applied Materials & Interfaces* **2011,** 3, (2), 522-527.
52. Hu, L.; Hecht, D. S.; Grüner, G. *Nano Letters* **2004,** 4, (12), 2513-2517.
53. Seager, C. H.; Pike, G. E. *Physical Review B* **1974,** 10, (4), 1435-1446.
54. Pike, G. E.; Seager, C. H. *Physical Review B* **1974,** 10, (4), 1421-1434.
55. Kumar, S.; Murthy, J. Y.; Alam, M. A. *Physical Review Letters* **2005,** 95, (6), 066802.
56. Kalowekamo, J.; Baker, E. *Solar Energy* **2009,** 83, (8), 1224-1231.
57. Paetzold, R.; Heuser, K.; Henseler, D.; Roeger, S.; Wittmann, G.; Winnacker, A. *Applied Physics Letters* **2003,** 82, (19), 3342-3344.
58. Khodorov, A.; Piechowiak, M.; Gomes, M. J. M. *Thin Solid Films* **2007,** 515, (20–21), 7829-7833.
59. Kim, J. H.; Ahn, B. D.; Lee, C. H.; Jeon, K. A.; Kang, H. S.; Kim, G. H.; Lee, S. Y. *Thin Solid Films* **2007,** 515, (7–8), 3580-3583.
60. Meng, L.-J.; Gao, J.; dos Santos, M. P.; Wang, X.; Wang, T. *Thin Solid Films* **2008,** 516, (7), 1365-1369.
61. Armstrong, N. R.; Veneman, P. A.; Ratcliff, E.; Placencia, D.; Brumbach, M. *Accounts of Chemical Research* **2009,** 42, (11), 1748-1757.
62. Aziz, H.; Popovic, Z. D. *Chemistry of Materials* **2004,** 16, (23), 4522-4532.
63. Wu, C. C.; Wu, C. I.; Sturm, J. C.; Kahn, A. *Applied Physics Letters* **1997,** 70, (11), 1348-1350.
64. Elbahri, M.; Hedayati, M. K.; Kiran Chakravadhanula, V. S.; Jamali, M.; Strunkus, T.; Zaporojtchenko, V.; Faupel, F. *Advanced Materials* **2011,** 23, (17), 1993-1997.
65. Stec, H. M.; Williams, R. J.; Jones, T. S.; Hatton, R. A. *Advanced Functional Materials* **2011,** 21, (9), 1709-1716.
66. Lindquist, N. C.; Luhman, W. A.; Oh, S.-H.; Holmes, R. J. *Applied Physics Letters* **2008,** 93, (12),

123308.
67. Luhman, W. A.; Lee, S. H.; Johnson, T. W.; Holmes, R. J.; Oh, S.-H. *Applied Physics Letters* **2011,** 99, (10), 103306.
68. Reilly, T. H.; III; Lagemaat, J. v. d.; Tenent, R. C.; Morfa, A. J.; Rowlen, K. L. *Applied Physics Letters* **2008,** 92, (24), 243304.
69. Kang, M.-G.; Kim, M.-S.; Kim, J.; Guo, L. J. *Advanced Materials* **2008,** 20, (23), 4408-4413.
70. Kang, M.-G.; Xu, T.; Park, H. J.; Luo, X.; Guo, L. J. *Advanced Materials* **2010,** 22, (39), 4378-4383.
71. Chen, X.; Zhao, C.; Rothberg, L.; Ng, M.-K. *Applied Physics Letters* **2008,** 93, (12), 123302.
72. Ding, I. K.; Zhu, J.; Cai, W.; Moon, S.-J.; Cai, N.; Wang, P.; Zakeeruddin, S. M.; Grätzel, M.; Brongersma, M. L.; Cui, Y.; McGehee, M. D. *Advanced Energy Materials* **2011,** 1, (1), 52-57.
73. You, J.; Li, X.; Xie, F.-x.; Sha, W. E. I.; Kwong, J. H. W.; Li, G.; Choy, W. C. H.; Yang, Y. *Advanced Energy Materials* **2012,** 2, (10), 1203-1207.
74. Chou, S. Y.; Ding, W. *Opt. Express* **2013,** 21, (S1), A60-A76.
75. Garnett, E. C.; Cai, W.; Cha, J. J.; Mahmood, F.; Connor, S. T.; Greyson Christoforo, M.; Cui, Y.; McGehee, M. D.; Brongersma, M. L. *Nat Mater* **2012,** 11, (3), 241-249.
76. Atwater, H. A.; Polman, A. *Nat Mater* **2010,** 9, (3), 205-213.
77. Dunbar, R. B.; Hesse, H. C.; Lembke, D. S.; Schmidt-Mende, L. *Physical Review B* **2012,** 85, (3), 035301.
78. Sha, W. E. I.; Choy, W. C. H.; Liu, Y. G.; Chew, W. C. *Applied Physics Letters* **2011,** 99, (11), 113304.
79. Kim, S. S.; Na, S. I.; Jo, J.; Kim, D. Y.; Nah, Y. C. *Applied Physics Letters* **2008,** 93, 073307.
80. Morfa, A. J.; Rowlen, K. L.; Reilly, T. H.; III; Romero, M. J.; Lagemaat, J. v. d. *Applied Physics Letters* **2008,** 92, (1), 013504.
81. Lee, J. H.; Park, J. H.; Kim, J. S.; Lee, D. Y.; Cho, K. *Organic Electronics* **2009,** 10, (3), 416-420.
82. Chen, F.-C.; Wu, J.-L.; Lee, C.-L.; Hong, Y.; Kuo, C.-H.; Huang, M. H. *Applied Physics Letters* **2009,** 95, (1), 013305.
83. Wu, J.-L.; Chen, F.-C.; Hsiao, Y.-S.; Chien, F.-C.; Chen, P.; Kuo, C.-H.; Huang, M. H.; Hsu, C.-S. *ACS Nano* **2011,** 5, (2), 959-967.
84. Yoon, W.-J.; Jung, K.-Y.; Liu, J.; Duraisamy, T.; Revur, R.; Teixeira, F. L.; Sengupta, S.; Berger, P. R. *Solar Energy Materials and Solar Cells* **2010,** 94, (2), 128-132.
85. Pei, J.; Tao, J.; Zhou, Y.; Dong, Q.; Liu, Z.; Li, Z.; Chen, F.; Zhang, J.; Xu, W.; Tian, W. *Solar Energy Materials and Solar Cells* **2011,** 95, (12), 3281-3286.
86. Qiao, L.; Wang, D.; Zuo, L.; Ye, Y.; Qian, J.; Chen, H.; He, S. *Applied Energy* **2011,** 88, (3), 848-852.
87. Oo, T. Z.; Mathews, N.; Xing, G.; Wu, B.; Xing, B.; Wong, L. H.; Sum, T. C.; Mhaisalkar, S. G. *The Journal of Physical Chemistry C* **2012,** 116, (10), 6453-6458.
88. Lu, L.; Luo, Z.; Xu, T.; Yu, L. *Nano Letters* **2012,** 13, (1), 59-64.
89. Liu, H.; Goh, W.-P.; Leung, M.-Y.; Li, Y.; Norsten, T. B. *Solar Energy Materials and Solar Cells* **2012,** 96, (0), 302-306.
90. Wang, X.; Ho, J. W.; Yang, Q.; Tam, H. L.; Li, G. X.; Cheah, K. W.; Zhu, F. *Organic Electronics* **2011,** 12, (11), 1943-1947.
91. Yakimov, A.; Forrest, S. R. *Applied Physics Letters* **2002,** 80, (9), 1667-1669.
92. Atwater, H. A.; Polman, A. *Nature Mater.* **2010,** 9, 205-213.
93. Yang, J.; You, J.; Chen, C.-C.; Hsu, W.-C.; Tan, H.-r.; Zhang, X. W.; Hong, Z.; Yang, Y. *ACS Nano* **2011,** 5, (8), 6210-6217.
94. Kalfagiannis, N.; Karagiannidis, P. G.; Pitsalidis, C.; Panagiotopoulos, N. T.; Gravalidis, C.; Kassavetis, S.; Patsalas, P.; Logothetidis, S. *Solar Energy Materials and Solar Cells* **2012,** 104, (0), 165-174.
95. Wudl, F.; Srdanov, G., 1993.
96. Peumans, P.; Yakimov, A.; Forrest, S. R. *J. Appl. Phys.* **2003,** 93, 3693-3723.
97. Brabec, C. J.; Shaheen, S. E.; Winder, C.; Sariciftci, N. S.; Denk, P. *Appl. Phys. Lett.* **2002,** 80, 1288-1290.

98. Wienk, M. M. *Angew. Chem. Int. Ed.* **2003,** 42, 3371-3375.
99. Padinger, F.; Rittberger, R. S.; Sariciftci, N. S. *Adv. Funct. Mater.* **2003,** 13, 85-88.
100. Bao, Z.; Dodabalapur, A.; Lovinger, A. J. *Appl. Phys. Lett.* **1996,** 69, 4108-4110.
101. Li, G. *Nature Mater.* **2005,** 4, 864-868.
102. Ma, W. L.; Yang, C. Y.; Gong, X.; Lee, K.; Heeger, A. J. *Adv. Funct. Mater.* **2005,** 15, 1617-1622.
103. Muhlbacher, D. *Adv. Mater.* **2006,** 18, 2884-2889.
104. Peet, J.; Kim, J. Y.; Coates, N. E.; Ma, W. L.; Moses, D.; Heeger, A. J.; Bazan, G. C. *Nat Mater* **2007,** 6, (7), 497-500.
105. Blouin, N.; Michaud, A.; Leclerc, M. *Adv. Mater.* **2007,** 19, 2295-2300.
106. Park, S. H. *Nature Photon.* **2009,** 3, 297-302.
107. Liang, Y. Y. *J. Am. Chem. Soc.* **2009,** 131, 56-57.
108. Liang, Y. Y. *J. Am. Chem. Soc.* **2009,** 131, 7792-7799.
109. Chen, H.-Y.; Hou, J.; Zhang, S.; Liang, Y.; Yang, G.; Yang, Y.; Yu, L.; Wu, Y.; Li, G. *Nat Photon* **2009,** 3, (11), 649-653.
110. Price, S. C.; Stuart, A. C.; Yang, L. Q.; Zhou, H. X.; You, W. *J. Am. Chem. Soc.* **2011,** 133, 4625-4631.
111. Amb, C. M.; Chen, S.; Graham, K. R.; Subbiah, J.; Small, C. E.; So, F.; Reynolds, J. R. *Journal of the American Chemical Society* **2011,** 133, (26), 10062-10065.
112. Su, M.-S.; Kuo, C.-Y.; Yuan, M.-C.; Jeng, U. S.; Su, C.-J.; Wei, K.-H. *Advanced Materials* **2011,** 23, (29), 3315-3319.
113. Chu, T.-Y.; Lu, J.; Beaupré, S.; Zhang, Y.; Pouliot, J.-R.; Wakim, S.; Zhou, J.; Leclerc, M.; Li, Z.; Ding, J.; Tao, Y. *Journal of the American Chemical Society* **2011,** 133, (12), 4250-4253.
114. Zhou, H.; Yang, L.; Stuart, A. C.; Price, S. C.; Liu, S.; You, W. *Angewandte Chemie International Edition* **2011,** 50, (13), 2995-2998.
115. Cheng, Y. J.; Yang, S. H.; Hsu, C. S. *Chem. Rev.* **2009,** 109, 5868-5923.
116. Liang, Y. Y.; Yu, L. P. *Polym. Rev.* **2010,** 50, 454-473.
117. Scharber, M. C.; Mühlbacher, D.; Koppe, M.; Denk, P.; Waldauf, C.; Heeger, A. J.; Brabec, C. J. *Advanced Materials* **2006,** 18, (6), 789-794.
118. Yun, J. J. *Appl. Phys. Lett.* **2005,** 87, 123102.
119. McCullough, R. D.; Tristramnagle, S.; Williams, S. P.; Lowe, R. D.; Jayaraman, M. *J. Am. Chem. Soc.* **1993,** 115, 4910-4911.
120. Zhou, Q. M. *Appl. Phys. Lett.* **2004,** 84, 1653-1655.
121. Gadisa, A. *Adv. Funct. Mater.* **2007,** 17, 3836-3842.
122. Vandewal, K.; Tvingstedt, K.; Gadisa, A.; Inganas, O.; Manca, J. V. *Nature Mater.* **2009,** 8, 904-909.
123. Liang, Y. Y.; Yu, L. P. *Acc. Chem. Res.* **2010,** 43, 1227-1236.
124. Havinga, E. E.; Tenhoeve, W.; Wynberg, H. *Synth. Met.* **1993,** 55, 299-306.
125. Zhang, Q. T.; Tour, J. M. *J. Am. Chem. Soc.* **1997,** 119, 5065-5066.
126. Huang, F. *J. Am. Chem. Soc.* **2009,** 131, 13886-13887.
127. Hou, J. H.; Chen, H. Y.; Zhang, S. Q.; Li, G.; Yang, Y. *J. Am. Chem. Soc.* **2008,** 130, 16144-16145.
128. Chen, H.-Y.; Hou, J.; Hayden, A. E.; Yang, H.; Houk, K. N.; Yang, Y. *Advanced Materials* **2010,** 22, (3), 371-375.
129. Zhang, Y. *Chem. Mater.* **2011,** 23, 2289-2291.
130. He, F. *J. Am. Chem. Soc.* **2011,** 133, 3284-3287.
131. Chen, D.; Liu, F.; Wang, C.; Nakahara, A.; Russell, T. P. *Nano Lett.* **2011,** 11, 2071-2078.
132. Piliego, C.; Holcombe, T. W.; Douglas, J. D.; Woo, C. H.; Beaujuge, P. M.; Fréchet, J. M. J. *Journal of the American Chemical Society* **2010,** 132, (22), 7595-7597.
133. Lenes, M. *Adv. Mater.* **2008,** 20, 2116-2119.
134. Laird, D. W., Organic photovoltaic devices comparising fullerenes and derivatives thereof. 2008.
135. Ross, R. B. *Nature Mater.* **2009,** 8, 208-212.
136. He, Y. J.; Chen, H. Y.; Hou, J. H.; Li, Y. F. *J. Am. Chem. Soc.* **2010,** 132, 1377-1382.
137. Zhao, G. J.; He, Y. J.; Li, Y. F. *Adv. Mater.* **2010,** 22, 4355-4358.
138. He, Y.; Li, Y. *Physical Chemistry Chemical Physics* **2011,** 13, (6), 1970-1983.

139. Li, S.; Ye, L.; Zhao, W.; Zhang, S.; Mukherjee, S.; Ade, H.; Hou, J. *Advanced Materials* **2016,** 28, (42), 9423-9429.
140. Padinger, F.; Rittberger, R. S.; Sariciftci, N. S. *Advanced Functional Materials* **2003,** 13, (1), 85-88.
141. Li, G.; Shrotriya, V.; Huang, J.; Yao, Y.; Moriarty, T.; Emery, K.; Yang, Y. *Nature Materials* **2005,** 4, 864.
142. Li, G.; Yao, Y.; Yang, H.; Shrotriya, V.; Yang, G.; Yang, Y. *Advanced Functional Materials* **2007,** 17, (10), 1636-1644.
143. Shaheen, S. E.; Brabec, C. J.; Sariciftci, N. S.; Padinger, F.; Fromherz, T.; Hummelen, J. C. *Applied Physics Letters* **2001,** 78, (6), 841-843.
144. Zhang, F.; Jespersen, K. G.; Björström, C.; Svensson, M.; Andersson, M. R.; Sundström, V.; Magnusson, K.; Moons, E.; Yartsev, A.; Inganäs, O. *Advanced Functional Materials* **2006,** 16, (5), 667-674.
145. Peet, J.; Kim, J. Y.; Coates, N. E.; Ma, W. L.; Moses, D.; Heeger, A. J.; Bazan, G. C. *Nature Materials* **2007,** 6, 497.
146. Mihailetchi, V. D.; Xie, H. X.; de Boer, B.; Koster, L. J. A.; Blom, P. W. M. *Advanced Functional Materials* **2006,** 16, (5), 699-708.
147. Li, G.; Shrotriya, V.; Yao, Y.; Yang, Y. *Journal of Applied Physics* **2005,** 98, (4), 043704.
148. Ma, W.; Yang, C.; Gong, X.; Lee, K.; Heeger, A. J. *Advanced Functional Materials* **2005,** 15, (10), 1617-1622.
149. Shrotriya, V.; Yao, Y.; Li, G.; Yang, Y. *Applied Physics Letters* **2006,** 89, (6), 063505.
150. Zhao, Y.; Xie, Z.; Qu, Y.; Geng, Y.; Wang, L. *Applied Physics Letters* **2007,** 90, (4), 043504.
151. Hoppe, H.; Glatzel, T.; Niggemann, M.; Schwinger, W.; Schaeffler, F.; Hinsch, A.; Lux-Steiner, M. C.; Sariciftci, N. S. *Thin Solid Films* **2006,** 511-512, (Supplement C), 587-592.
152. Hoppe, H.; Sariciftci, N. S. *Journal of Materials Chemistry* **2006,** 16, (1), 45-61.
153. Hoth, C. N.; Schilinsky, P.; Choulis, S. A.; Brabec, C. J. *Nano Letters* **2008,** 8, (9), 2806-2813.
154. Liu, J.; Shi, Y.; Yang, Y. *Advanced Functional Materials* **2001,** 11, (6), 420-424.
155. Hoppe, H.; Niggemann, M.; Winder, C.; Kraut, J.; Hiesgen, R.; Hinsch, A.; Meissner, D.; Sariciftci, N. S. *Advanced Functional Materials* **2004,** 14, (10), 1005-1011.
156. Soci, C.; Hwang, I. W.; Moses, D.; Zhu, Z.; Waller, D.; Gaudiana, R.; Brabec, C. J.; Heeger, A. J. *Advanced Functional Materials* **2007,** 17, (4), 632-636.
157. Mühlbacher, D.; Scharber, M.; Morana, M.; Zhu, Z.; Waller, D.; Gaudiana, R.; Brabec, C. *Advanced Materials* **2006,** 18, (21), 2884-2889.
158. Yao, Y.; Hou, J.; Xu, Z.; Li, G.; Yang, Y. *Advanced Functional Materials* **2008,** 18, (12), 1783-1789.
159. Chen, F.-C.; Tseng, H.-C.; Ko, C.-J. *Applied Physics Letters* **2008,** 92, (10), 103316.
160. Moulé, A. J.; Meerholz, K. *Advanced Materials* **2008,** 20, (2), 240-245.
161. Lee, J. K.; Ma, W. L.; Brabec, C. J.; Yuen, J.; Moon, J. S.; Kim, J. Y.; Lee, K.; Bazan, G. C.; Heeger, A. J. *Journal of the American Chemical Society* **2008,** 130, (11), 3619-3623.
162. Hwang, I.-W.; Cho, S.; Kim, J. Y.; Lee, K.; Coates, N. E.; Moses, D.; Heeger, A. J. *Journal of Applied Physics* **2008,** 104, (3), 033706.
163. Lu, H.; Xu, X.; Bo, Z. *Science China Materials* **2016,** 59, (6), 444-458.
164. Cheng, P.; Zhan, X. *Materials Horizons* **2015,** 2, (5), 462-485.
165. Lu, L.; Kelly, M. A.; You, W.; Yu, L. *Nature Photonics* **2015,** 9, 491.
166. An, Q.; Zhang, F.; Zhang, J.; Tang, W.; Deng, Z.; Hu, B. *Energy & Environmental Science* **2016,** 9, (2), 281-322.
167. Zhao, W.; Li, S.; Zhang, S.; Liu, X.; Hou, J. *Advanced Materials* **2017,** 29, (2), 1604059-n/a.
168. Nian, L.; Gao, K.; Liu, F.; Kan, Y.; Jiang, X.; Liu, L.; Xie, Z.; Peng, X.; Russell, T. P.; Ma, Y. *Advanced Materials* **2016,** 28, (37), 8184-8190.
169. Cha, H.; Chung, D. S.; Bae, S. Y.; Lee, M.-J.; An, T. K.; Hwang, J.; Kim, K. H.; Kim, Y.-H.; Choi, D. H.; Park, C. E. *Advanced Functional Materials* **2013,** 23, (12), 1556-1565.
170. Kang, H.; Kim, K.-H.; Kang, T. E.; Cho, C.-H.; Park, S.; Yoon, S. C.; Kim, B. J. *ACS Applied Materials & Interfaces* **2013,** 5, (10), 4401-4408.

171. An, Q.; Zhang, F.; Yin, X.; Sun, Q.; Zhang, M.; Zhang, J.; Tang, W.; Deng, Z. *Nano Energy* **2016,** 30, (Supplement C), 276-282.
172. Cheng, P.; Yan, C.; Wu, Y.; Wang, J.; Qin, M.; An, Q.; Cao, J.; Huo, L.; Zhang, F.; Ding, L.; Sun, Y.; Ma, W.; Zhan, X. *Advanced Materials* **2016,** 28, (36), 8021-8028.
173. Chen, Y.; Ye, P.; Zhu, Z.-G.; Wang, X.; Yang, L.; Xu, X.; Wu, X.; Dong, T.; Zhang, H.; Hou, J.; Liu, F.; Huang, H. *Advanced Materials* **2017,** 29, (6), 1603154-n/a.
174. Zhang, J.; Zhang, Y.; Fang, J.; Lu, K.; Wang, Z.; Ma, W.; Wei, Z. *Journal of the American Chemical Society* **2015,** 137, (25), 8176-8183.
175. Hecht, D. S.; Hu, L.; Irvin, G. *Advanced Materials* **2011,** 23, (13), 1482-1513.
176. Du, J.; Pei, S.; Ma, L.; Cheng, H.-M. *Advanced Materials* **2014,** 26, (13), 1958-1991.
177. Ellmer, K. *Nature Photonics* **2012,** 6, 809.
178. Kumar, A.; Zhou, C. *ACS Nano* **2010,** 4, (1), 11-14.
179. Hu, L.; Wu, H.; Cui, Y. *MRS Bulletin* **2011,** 36, (10), 760-765.
180. Kuang, P.; Park, J.-M.; Leung, W.; Mahadevapuram, R. C.; Nalwa, K. S.; Kim, T.-G.; Chaudhary, S.; Ho, K.-M.; Constant, K. *Advanced Materials* **2011,** 23, (21), 2469-2473.
181. De, S.; Higgins, T. M.; Lyons, P. E.; Doherty, E. M.; Nirmalraj, P. N.; Blau, W. J.; Boland, J. J.; Coleman, J. N. *ACS Nano* **2009,** 3, (7), 1767-1774.
182. Garnett, E. C.; Cai, W.; Cha, J. J.; Mahmood, F.; Connor, S. T.; Greyson Christoforo, M.; Cui, Y.; McGehee, M. D.; Brongersma, M. L. *Nature Materials* **2012,** 11, 241.
183. Daniel, L.; Gaël, G.; Céline, M.; Caroline, C.; Daniel, B.; Jean-Pierre, S. *Nanotechnology* **2013,** 24, (45), 452001.
184. van de Groep, J.; Spinelli, P.; Polman, A. *Nano Letters* **2012,** 12, (6), 3138-3144.
185. Wu, Z.; Chen, Z.; Du, X.; Logan, J. M.; Sippel, J.; Nikolou, M.; Kamaras, K.; Reynolds, J. R.; Tanner, D. B.; Hebard, A. F.; Rinzler, A. G. *Science* **2004,** 305, (5688), 1273-1276.
186. Zhang, D.; Ryu, K.; Liu, X.; Polikarpov, E.; Ly, J.; Tompson, M. E.; Zhou, C. *Nano Letters* **2006,** 6, (9), 1880-1886.
187. Bae, S.; Kim, H.; Lee, Y.; Xu, X.; Park, J.-S.; Zheng, Y.; Balakrishnan, J.; Lei, T.; Ri Kim, H.; Song, Y. I.; Kim, Y.-J.; Kim, K. S.; Özyilmaz, B.; Ahn, J.-H.; Hong, B. H.; Iijima, S. *Nature Nanotechnology* **2010,** 5, 574.
188. Bonaccorso, F.; Sun, Z.; Hasan, T.; Ferrari, A. C. *Nature Photonics* **2010,** 4, 611.
189. Gomez De Arco, L.; Zhang, Y.; Schlenker, C. W.; Ryu, K.; Thompson, M. E.; Zhou, C. *ACS Nano* **2010,** 4, (5), 2865-2873.
190. Kim, K. S.; Zhao, Y.; Jang, H.; Lee, S. Y.; Kim, J. M.; Kim, K. S.; Ahn, J.-H.; Kim, P.; Choi, J.-Y.; Hong, B. H. *Nature* **2009,** 457, 706.
191. Wang, X.; Zhi, L.; Müllen, K. *Nano Letters* **2008,** 8, (1), 323-327.
192. Kiruthika, S.; Gupta, R.; Rao, K. D. M.; Chakraborty, S.; Padmavathy, N.; Kulkarni, G. U. *Journal of Materials Chemistry C* **2014,** 2, (11), 2089-2094.
193. Kirchmeyer, S.; Reuter, K. *J. Mater. Chem.* **2005,** 15, (21), 2077-2088.
194. Yim, J. H.; Joe, S.-y.; Pang, C.; Lee, K. M.; Jeong, H.; Park, J.-Y.; Ahn, Y. H.; de Mello, J. C.; Lee, S. *ACS nano* **2014,** 8, (3), 2857-2863.
195. Lee, J.-Y.; Connor, S. T.; Cui, Y.; Peumans, P. *Nano Letters* **2008,** 8, (2), 689-692.
196. Liu, C. H.; Yu, X. *Nanoscale Res Lett* **2011,** 6, (1), 75.
197. Hu, L.; Kim, H. S.; Lee, J.-Y.; Peumans, P.; Cui, Y. *ACS Nano* **2010,** 4, (5), 2955-2963.
198. Zhu, R.; Chung, C.-H.; Cha, K. C.; Yang, W.; Zheng, Y. B.; Zhou, H.; Song, T.-B.; Chen, C.-C.; Weiss, P. S.; Li, G. *ACS nano* **2011,** 5, (12), 9877-9882.
199. Scardaci, V.; Coull, R.; Lyons, P. E.; Rickard, D.; Coleman, J. N. *Small* **2011,** 7, (18), 2621-8.
200. Kim, T.; Canlier, A.; Kim, G. H.; Choi, J.; Park, M.; Han, S. M. *ACS Applied Materials & Interfaces* **2013,** 5, (3), 788-794.
201. Madaria, A. R.; Kumar, A.; Zhou, C. *Nanotechnology* **2011,** 22, (24), 245201.
202. Chung, C.-H.; Song, T.-B.; Bob, B.; Zhu, R.; Yang, Y. *Nano Research* **2012,** 5, (11), 805-814.
203. Lee, Y.; Suh, M.; Kim, D.; Lee, D.; Chang, H.; Lee, H. S.; Kim, Y. W.; Kim, T.; Suh, K. S.; Jeon, D. Y. *Advanced Functional Materials* **2014,** 24, (41), 6465-6472.
204. Gaynor, W.; Burkhard, G. F.; McGehee, M. D.; Peumans, P. *Adv Mater* **2011,** 23, (26), 2905-10.

205. Araki, T.; Jiu, J.; Nogi, M.; Koga, H.; Nagao, S.; Sugahara, T.; Suganuma, K. *Nano Research* **2014,** 7, (2), 236-245.
206. Liang, J.; Li, L.; Tong, K.; Ren, Z.; Hu, W.; Niu, X.; Chen, Y.; Pei, Q. *ACS Nano* **2014,** 8, (2), 1590-1600.
207. Tokuno, T.; Nogi, M.; Karakawa, M.; Jiu, J.; Nge, T. T.; Aso, Y.; Suganuma, K. *Nano Research* **2011,** 4, (12), 1215-1222.
208. Zeng, X.-Y.; Zhang, Q.-K.; Yu, R.-M.; Lu, C.-Z. *Advanced Materials* **2010,** 22, (40), 4484-4488.
209. Liu, Y.; Chang, Q.; Huang, L. *Journal of Materials Chemistry C* **2013,** 1, (17), 2970-2974.
210. Mutiso, R. M.; Sherrott, M. C.; Rathmell, A. R.; Wiley, B. J.; Winey, K. I. *ACS Nano* **2013,** 7, (9), 7654-7663.
211. De, S.; Coleman, J. N. *MRS Bulletin* **2011,** 36, (10), 774-781.
212. White, S. I.; Mutiso, R. M.; Vora, P. M.; Jahnke, D.; Hsu, S.; Kikkawa, J. M.; Li, J.; Fischer, J. E.; Winey, K. I. *Advanced Functional Materials* **2010,** 20, (16), 2709-2716.
213. Madaria, A. R.; Kumar, A.; Ishikawa, F. N.; Zhou, C. *Nano Research* **2010,** 3, (8), 564-573.
214. Lee, J.; Lee, P.; Lee, H.; Lee, D.; Lee, S. S.; Ko, S. H. *Nanoscale* **2012,** 4, (20), 6408-6414.
215. Hsu, P.-C.; Wang, S.; Wu, H.; Narasimhan, V. K.; Kong, D.; Ryoung Lee, H.; Cui, Y. *Nature Communications* **2013,** 4, 2522.
216. Han, B.; Pei, K.; Huang, Y.; Zhang, X.; Rong, Q.; Lin, Q.; Guo, Y.; Sun, T.; Guo, C.; Carnahan, D.; Giersig, M.; Wang, Y.; Gao, J.; Ren, Z.; Kempa, K. *Advanced Materials* **2014,** 26, (6), 873-877.
217. Gao, T.; Wang, B.; Ding, B.; Lee, J.-k.; Leu, P. W. *Nano Letters* **2014,** 14, (4), 2105-2110.
218. Wu, H.; Kong, D.; Ruan, Z.; Hsu, P.-C.; Wang, S.; Yu, Z.; Carney, T. J.; Hu, L.; Fan, S.; Cui, Y. *Nature Nanotechnology* **2013,** 8, 421.
219. Hsu, P.-C.; Kong, D.; Wang, S.; Wang, H.; Welch, A. J.; Wu, H.; Cui, Y. *Journal of the American Chemical Society* **2014,** 136, (30), 10593-10596.
220. He, T.; Xie, A.; Reneker, D. H.; Zhu, Y. *ACS Nano* **2014,** 8, (5), 4782-4789.
221. Tao, A.; Kim, F.; Hess, C.; Goldberger, J.; He, R.; Sun, Y.; Xia, Y.; Yang, P. *Nano Letters* **2003,** 3, (9), 1229-1233.
222. Fan, Z.; Ho, J. C.; Jacobson, Z. A.; Yerushalmi, R.; Alley, R. L.; Razavi, H.; Javey, A. *Nano Letters* **2008,** 8, (1), 20-25.
223. Bang, J.; Choi, J.; Xia, F.; Kwon, S. S.; Ashraf, A.; Park, W. I.; Nam, S. *Nano Letters* **2014,** 14, (6), 3304-3308.
224. Yao, J.; Yan, H.; Lieber, C. M. *Nature Nanotechnology* **2013,** 8, 329.
225. Zhou, X.; Zhou, Y.; Ku, J. C.; Zhang, C.; Mirkin, C. A. *ACS Nano* **2014,** 8, (2), 1511-1516.
226. Huang, Y.; Duan, X.; Wei, Q.; Lieber, C. M. *Science* **2001,** 291, (5504), 630-633.
227. Song, M.; Park, J. H.; Kim, C. S.; Kim, D.-H.; Kang, Y.-C.; Jin, S.-H.; Jin, W.-Y.; Kang, J.-W. *Nano Research* **2014,** 7, (9), 1370-1379.
228. Gerdes, S.; Ondarçuhu, T.; Cholet, S.; Joachim, C. *EPL (Europhysics Letters)* **1999,** 48, (3), 292.
229. Noy, A.; Frisbie, C. D.; Rozsnyai, L. F.; Wrighton, M. S.; Lieber, C. M. *Journal of the American Chemical Society* **1995,** 117, (30), 7943-7951.
230. Arianna, L. W.; Giuseppe, R. P. *Materials Research Express* **2014,** 1, (3), 035013.
231. Du, F.; Fischer, J. E.; Winey, K. I. *Physical Review B* **2005,** 72, (12), 121404.
232. Kocabas, C.; Pimparkar, N.; Yesilyurt, O.; Kang, S. J.; Alam, M. A.; Rogers, J. A. *Nano Letters* **2007,** 7, (5), 1195-1202.
233. White, S. I.; DiDonna, B. A.; Mu, M.; Lubensky, T. C.; Winey, K. I. *Physical Review B* **2009,** 79, (2), 024301.
234. Lee, M.-S.; Lee, K.; Kim, S.-Y.; Lee, H.; Park, J.; Choi, K.-H.; Kim, H.-K.; Kim, D.-G.; Lee, D.-Y.; Nam, S.; Park, J.-U. *Nano Letters* **2013,** 13, (6), 2814-2821.
235. Lee, J.; Lee, P.; Lee, H. B.; Hong, S.; Lee, I.; Yeo, J.; Lee, S. S.; Kim, T.-S.; Lee, D.; Ko, S. H. *Advanced Functional Materials* **2013,** 23, (34), 4171-4176.
236. Ko, S.-J.; Choi, H.; Lee, W.; Kim, T.; Lee, B. R.; Jung, J.-W.; Jeong, J.-R.; Song, M. H.; Lee, J. C.; Woo, H. Y.; Kim, J. Y. *Energy & Environmental Science* **2013,** 6, (6), 1949-1955.
237. Kim, A.; Won, Y.; Woo, K.; Kim, C.-H.; Moon, J. *ACS Nano* **2013,** 7, (2), 1081-1091.

238. Yu, Z.; Zhang, Q.; Li, L.; Chen, Q.; Niu, X.; Liu, J.; Pei, Q. *Advanced Materials* **2011,** 23, (5), 664-668.
239. Lee, S. J.; Kim, Y.-H.; Kim, J. K.; Baik, H.; Park, J. H.; Lee, J.; Nam, J.; Park, J. H.; Lee, T.-W.; Yi, G.-R.; Cho, J. H. *Nanoscale* **2014,** 6, (20), 11828-11834.
240. Kang, H.; Jung, S.; Jeong, S.; Kim, G.; Lee, K. *Nature Communications* **2015,** 6, 6503.
241. Li, L.; Yu, Z.; Chang, C.-h.; Hu, W.; Niu, X.; Chen, Q.; Pei, Q. *Physical Chemistry Chemical Physics* **2012,** 14, (41), 14249-14254.
242. Gaynor, W.; Hofmann, S.; Christoforo, M. G.; Sachse, C.; Mehra, S.; Salleo, A.; McGehee, M. D.; Gather, M. C.; Lüssem, B.; Müller-Meskamp, L.; Peumans, P.; Leo, K. *Advanced Materials* **2013,** 25, (29), 4006-4013.
243. Li, L.; Yu, Z.; Hu, W.; Chang, C.-h.; Chen, Q.; Pei, Q. *Advanced Materials* **2011,** 23, (46), 5563-5567.
244. Liao, S. H.; Jhuo, H. J.; Cheng, Y. S.; Chen, S. A. *Adv Mater* **2013,** 25, (34), 4766-71.
245. Song, M.; You, D. S.; Lim, K.; Park, S.; Jung, S.; Kim, C. S.; Kim, D.-H.; Kim, D.-G.; Kim, J.-K.; Park, J.; Kang, Y.-C.; Heo, J.; Jin, S.-H.; Park, J. H.; Kang, J.-W. *Advanced Functional Materials* **2013,** 23, (34), 4177-4184.
246. Kim, Y.; Ryu, T. I.; Ok, K.-H.; Kwak, M.-G.; Park, S.; Park, N.-G.; Han, C. J.; Kim, B. S.; Ko, M. J.; Son, H. J.; Kim, J.-W. *Advanced Functional Materials* **2015,** 25, (29), 4580-4589.
247. Wang, B.-Y.; Yoo, T.-H.; Lim, J. W.; Sang, B.-I.; Lim, D.-S.; Choi, W. K.; Hwang, D. K.; Oh, Y.-J. *Small* **2015,** 11, (16), 1905-1911.
248. Yang, L.; Zhang, T.; Zhou, H.; Price, S. C.; Wiley, B. J.; You, W. *ACS Applied Materials & Interfaces* **2011,** 3, (10), 4075-4084.
249. Bundgaard, E.; Livi, F.; Hagemann, O.; Carlé, J. E.; Helgesen, M.; Heckler, I. M.; Zawacka, N. K.; Angmo, D.; Larsen-Olsen, T. T.; dos Reis Benatto, G. A.; Roth, B.; Madsen, M. V.; Andersson, M. R.; Jørgensen, M.; Søndergaard, R. R.; Krebs, F. C. *Advanced Energy Materials* **2015,** 5, (10), 1402186-n/a.
250. Søndergaard, R.; Hösel, M.; Angmo, D.; Larsen-Olsen, T. T.; Krebs, F. C. *Materials Today* **2012,** 15, (1), 36-49.
251. Chen, H.-Y.; Hou, J.; Zhang, S.; Liang, Y.; Yang, G.; Yang, Y.; Yu, L.; Wu, Y.; Li, G. *Nature Photonics* **2009,** 3, (11), 649-653.
252. Park, S. H.; Roy, A.; Beaupré, S.; Cho, S.; Coates, N.; Moon, J. S.; Moses, D.; Leclerc, M.; Lee, K.; Heeger, A. J. *Nature Photonics* **2009,** 3, (5), 297-302.
253. Choi, H.; Ko, S. J.; Kim, T.; Morin, P. O.; Walker, B.; Lee, B. H.; Leclerc, M.; Kim, J. Y.; Heeger, A. J. *Adv Mater* **2015,** 27, (21), 3318-24.
254. Liang, Y.; Xu, Z.; Xia, J.; Tsai, S. T.; Wu, Y.; Li, G.; Ray, C.; Yu, L. *Adv Mater* **2010,** 22, (20), E135-8.
255. Dou, L.; You, J.; Yang, J.; Chen, C.-C.; He, Y.; Murase, S.; Moriarty, T.; Emery, K.; Li, G.; Yang, Y. *Nature Photonics* **2012,** 6, (3), 180-185.
256. Yang, Y.; Chen, W.; Dou, L.; Chang, W.-H.; Duan, H.-S.; Bob, B.; Li, G.; Yang, Y. *Nature Photonics* **2015,** 9, (3), 190-198.
257. Kim, J. Y.; Lee, K.; Coates, N. E.; Moses, D.; Nguyen, T.-Q.; Dante, M.; Heeger, A. J. *Science* **2007,** 317, (5835), 222-225.
258. Heo, M.; Cho, H.; Jung, J.-W.; Jeong, J.-R.; Park, S.; Kim, J. Y. *Advanced Materials* **2011,** 23, (47), 5689-5693.
259. Kim, J. Y.; Kim, S. H.; Lee, H. H.; Lee, K.; Ma, W.; Gong, X.; Heeger, A. J. *Advanced Materials* **2006,** 18, (5), 572-576.
260. Choi, H.; Ko, S.-J.; Choi, Y.; Joo, P.; Kim, T.; Lee, B. R.; Jung, J.-W.; Choi, H. J.; Cha, M.; Jeong, J.-R.; Hwang, I.-W.; Song, M. H.; Kim, B.-S.; Kim, J. Y. *Nature Photonics* **2013,** 7, (9), 732-738.
261. Kim, C.-H.; Cha, S.-H.; Kim, S. C.; Song, M.; Lee, J.; Shin, W. S.; Moon, S.-J.; Bahng, J. H.; Kotov, N. A.; Jin, S.-H. *ACS Nano* **2011,** 5, (4), 3319-3325.
262. Wang, D. H.; Park, K. H.; Seo, J. H.; Seifter, J.; Jeon, J. H.; Kim, J. K.; Park, J. H.; Park, O. O.; Heeger, A. J. *Advanced Energy Materials* **2011,** 1, (5), 766-770.
263. Li, X.; Choy, W. C. H.; Lu, H.; Sha, W. E. I.; Ho, A. H. P. *Advanced Functional Materials* **2013,**

23, (21), 2728-2735.
264. Choi, H.; Lee, J.-P.; Ko, S.-J.; Jung, J.-W.; Park, H.; Yoo, S.; Park, O.; Jeong, J.-R.; Park, S.; Kim, J. Y. *Nano Letters* **2013,** 13, (5), 2204-2208.
265. Jeong, S.-H.; Choi, H.; Kim, J. Y.; Lee, T.-W. *Particle & Particle Systems Characterization* **2015,** 32, (2), 164-175.
266. Rycenga, M.; Cobley, C. M.; Zeng, J.; Li, W.; Moran, C. H.; Zhang, Q.; Qin, D.; Xia, Y. *Chem Rev* **2011,** 111, (6), 3669-712.
267. Krantz, J.; Richter, M.; Spallek, S.; Spiecker, E.; Brabec, C. J. *Advanced Functional Materials* **2011,** 21, (24), 4784-4787.
268. Wang, B. Y.; Yoo, T. H.; Lim, J. W.; Sang, B. I.; Lim, D. S.; Choi, W. K.; Hwang, D. K.; Oh, Y. J. *Small* **2015,** 11, (16), 1905-11.
269. Knight, M. W.; Grady, N. K.; Bardhan, R.; Hao, F.; Nordlander, P.; Halas, N. J. *Nano Letters* **2007,** 7, (8), 2346-2350.
270. Pan, D.; Wei, H.; Jia, Z.; Xu, H. *Scientific Reports* **2014,** 4, (1).
271. Hao, F.; Nordlander, P. *Applied Physics Letters* **2006,** 89, (10), 103101.
272. Kang, S.; Kim, T.; Cho, S.; Lee, Y.; Choe, A.; Walker, B.; Ko, S. J.; Kim, J. Y.; Ko, H. *Nano Lett* **2015,** 15, (12), 7933-42.
273. Mock, J. J.; Hill, R. T.; Degiron, A.; Zauscher, S.; Chilkoti, A.; Smith, D. R. *Nano Letters* **2008,** 8, (8), 2245-2252.
274. Park, B.; Bae, I. G.; Huh, Y. H. *Sci Rep* **2016,** 6, 19485.
275. Akimov, A. V.; Mukherjee, A.; Yu, C. L.; Chang, D. E.; Zibrov, A. S.; Hemmer, P. R.; Park, H.; Lukin, M. D. *Nature* **2007,** 450, (7168), 402-6.
276. Hutchison, J. A.; Centeno, S. P.; Odaka, H.; Fukumura, H.; Hofkens, J.; Uji-i, H. *Nano Letters* **2009,** 9, (3), 995-1001.
277. Wei, H.; Hao, F.; Huang, Y.; Wang, W.; Nordlander, P.; Xu, H. *Nano Letters* **2008,** 8, (8), 2497-2502.
278. Sun, Y.; Yin, Y.; Mayers, B. T.; Herricks, T.; Xia, Y. *Chemistry of Materials* **2002,** 14, (11), 4736-4745.
279. Yang, L.; Zhang, T.; Zhou, H.; Price, S. C.; Wiley, B. J.; You, W. *ACS Appl Mater Interfaces* **2011,** 3, (10), 4075-84.
280. Seo, J. H.; Hwang, I.; Um, H.-D.; Lee, S.; Lee, K.; Park, J.; Shin, H.; Kwon, T.-H.; Kang, S. J.; Seo, K. *Advanced Materials* **2017,** 29, (30), 1701479-n/a.
281. Mat Teridi, M. A.; Sookhakian, M.; Basirun, W. J.; Zakaria, R.; Schneider, F. K.; da Silva, W. J.; Kim, J.; Lee, S. J.; Kim, H. P.; Mohd Yusoff, A. R. b.; Jang, J. *Nanoscale* **2015,** 7, (16), 7091-7100.
282. Heeger, A. J. *Advanced Materials* **2014,** 26, (1), 10-28.
283. Li, G.; Zhu, R.; Yang, Y. *Nature Photonics* **2012,** 6, 153.
284. Zhao, J.; Li, Y.; Yang, G.; Jiang, K.; Lin, H.; Ade, H.; Ma, W.; Yan, H. *Nature Energy* **2016,** 1, 15027.
285. Lu, L.; Xu, T.; Chen, W.; Landry, E. S.; Yu, L. *Nature Photonics* **2014,** 8, 716.
286. Zhang, Y.; Deng, D.; Lu, K.; Zhang, J.; Xia, B.; Zhao, Y.; Fang, J.; Wei, Z. *Advanced Materials* **2015,** 27, (6), 1071-1076.
287. Gupta, V.; Bharti, V.; Kumar, M.; Chand, S.; Heeger, A. J. *Advanced Materials* **2015,** 27, (30), 4398-4404.
288. Yang, Y.; Chen, W.; Dou, L.; Chang, W.-H.; Duan, H.-S.; Bob, B.; Li, G.; Yang, Y. *Nature Photonics* **2015,** 9, 190.
289. Liu, S.; You, P.; Li, J.; Li, J.; Lee, C.-S.; Ong, B. S.; Surya, C.; Yan, F. *Energy & Environmental Science* **2015,** 8, (5), 1463-1470.
290. Benten, H.; Nishida, T.; Mori, D.; Xu, H.; Ohkita, H.; Ito, S. *Energy & Environmental Science* **2016,** 9, (1), 135-140.
291. Gasparini, N.; Lucera, L.; Salvador, M.; Prosa, M.; Spyropoulos, G. D.; Kubis, P.; Egelhaaf, H.-J.; Brabec, C. J.; Ameri, T. *Energy & Environmental Science* **2017,** 10, (4), 885-892.
292. Zhang, S.; Zuo, L.; Chen, J.; Zhang, Z.; Mai, J.; Lau, T.-K.; Lu, X.; Shi, M.; Chen, H. *Journal of*

Materials Chemistry A **2016,** 4, (5), 1702-1707.
293. Lu, L.; Chen, W.; Xu, T.; Yu, L. *Nature Communications* **2015,** 6, 7327.
294. Xiao, L.; Liang, T.; Gao, K.; Lai, T.; Chen, X.; Liu, F.; Russell, T. P.; Huang, F.; Peng, X.; Cao, Y. *ACS Applied Materials & Interfaces* **2017,** 9, (35), 29917-29923.
295. An, Q.; Zhang, F.; Sun, Q.; Wang, J.; Li, L.; Zhang, J.; Tang, W.; Deng, Z. *Journal of Materials Chemistry A* **2015,** 3, (32), 16653-16662.
296. An, Q.; Zhang, F.; Sun, Q.; Zhang, M.; Zhang, J.; Tang, W.; Yin, X.; Deng, Z. *Nano Energy* **2016,** 26, (Supplement C), 180-191.
297. Wang, J.; Peng, J.; Liu, X.; Liang, Z. *ACS Applied Materials & Interfaces* **2017,** 9, (24), 20704-20710.
298. Wang, C.; Xu, X.; Zhang, W.; Dkhil, S. B.; Meng, X.; Liu, X.; Margeat, O.; Yartsev, A.; Ma, W.; Ackermann, J.; Wang, E.; Fahlman, M. *Nano Energy* **2017,** 37, (Supplement C), 24-31.
299. Coughlin, J. E.; Henson, Z. B.; Welch, G. C.; Bazan, G. C. *Accounts of Chemical Research* **2014,** 47, (1), 257-270.
300. Gao, F.; Inganas, O. *Physical Chemistry Chemical Physics* **2014,** 16, (38), 20291-20304.
301. Thompson, B. C.; Fréchet, J. M. J. *Angewandte Chemie International Edition* **2008,** 47, (1), 58-77.
302. Liu, Y.; Zhao, J.; Li, Z.; Mu, C.; Ma, W.; Hu, H.; Jiang, K.; Lin, H.; Ade, H.; Yan, H. *Nature Communications* **2014,** 5, 5293.
303. Kan, B.; Zhang, Q.; Li, M.; Wan, X.; Ni, W.; Long, G.; Wang, Y.; Yang, X.; Feng, H.; Chen, Y. *Journal of the American Chemical Society* **2014,** 136, (44), 15529-15532.
304. Cao, J.; Qian, L.; Lu, F.; Zhang, J.; Feng, Y.; Qiu, X.; Yip, H.-L.; Ding, L. *Chemical Communications* **2015,** 51, (59), 11830-11833.
305. Zhang, Q.; Wang, Y.; Kan, B.; Wan, X.; Liu, F.; Ni, W.; Feng, H.; Russell, T. P.; Chen, Y. *Chemical Communications* **2015,** 51, (83), 15268-15271.
306. Subbiah, J.; Purushothaman, B.; Chen, M.; Qin, T.; Gao, M.; Vak, D.; Scholes, F. H.; Chen, X.; Watkins, S. E.; Wilson, G. J.; Holmes, A. B.; Wong, W. W. H.; Jones, D. J. *Advanced Materials* **2015,** 27, (4), 702-705.
307. Zhou, H.; Zhang, Y.; Mai, C.-K.; Collins, S. D.; Bazan, G. C.; Nguyen, T.-Q.; Heeger, A. J. *Advanced Materials* **2015,** 27, (10), 1767-1773.
308. Sun, K.; Xiao, Z.; Lu, S.; Zajaczkowski, W.; Pisula, W.; Hanssen, E.; White, J. M.; Williamson, R. M.; Subbiah, J.; Ouyang, J.; Holmes, A. B.; Wong, W. W. H.; Jones, D. J. *Nature Communications* **2015,** 6, 6013.
309. Wang, T.; Pearson, A. J.; Lidzey, D. G. *Journal of Materials Chemistry C* **2013,** 1, (44), 7266-7293.
310. Xiao, T.; Xu, H.; Grancini, G.; Mai, J.; Petrozza, A.; Jeng, U. S.; Wang, Y.; Xin, X.; Lu, Y.; Choon, N. S.; Xiao, H.; Ong, B. S.; Lu, X.; Zhao, N. *Scientific Reports* **2014,** 4, 5211.
311. Zheng, Y.; Li, S.; Zheng, D.; Yu, J. *Organic Electronics* **2014,** 15, (11), 2647-2653.
312. Kovacik, P.; Assender, H. E.; Watt, A. A. R. *Solar Energy Materials and Solar Cells* **2013,** 117, (Supplement C), 22-28.
313. Ma, T.; Jiang, K.; Chen, S.; Hu, H.; Lin, H.; Li, Z.; Zhao, J.; Liu, Y.; Chang, Y.-M.; Hsiao, C.-C.; Yan, H. *Advanced Energy Materials* **2015,** 5, (20), 1501282-n/a.
314. Boudreault, P.-L. T.; Najari, A.; Leclerc, M. *Chemistry of Materials* **2011,** 23, (3), 456-469.
315. Duan, C.; Huang, F.; Cao, Y. *Journal of Materials Chemistry* **2012,** 22, (21), 10416-10434.
316. Zhang, S.; Yang, B.; Liu, D.; Zhang, H.; Zhao, W.; Wang, Q.; He, C.; Hou, J. *Macromolecules* **2016,** 49, (1), 120-126.
317. Kranthiraja, K.; Gunasekar, K.; Cho, W.; Park, Y. G.; Lee, J. Y.; Shin, Y.; Kang, I.-N.; Song, M.; Chae, K. H.; Kim, B.; Jin, S.-H. *Journal of Materials Chemistry C* **2015,** 3, (4), 796-808.
318. You, J.; Dou, L.; Yoshimura, K.; Kato, T.; Ohya, K.; Moriarty, T.; Emery, K.; Chen, C.-C.; Gao, J.; Li, G.; Yang, Y. *Nature Communications* **2013,** 4, 1446.
319. Nguyen, T. L.; Choi, H.; Ko, S. J.; Uddin, M. A.; Walker, B.; Yum, S.; Jeong, J. E.; Yun, M. H.; Shin, T. J.; Hwang, S.; Kim, J. Y.; Woo, H. Y. *Energy & Environmental Science* **2014,** 7, (9), 3040-3051.

320. Dou, L.; Liu, Y.; Hong, Z.; Li, G.; Yang, Y. *Chemical Reviews* **2015,** 115, (23), 12633-12665.
321. Yao, B.; Zhou, X.; Ye, X.; Zhang, J.; Yang, D.; Ma, D.; Wan, X. *Organic Electronics* **2015,** 26, (Supplement C), 305-313.
322. Wang, L.; Cai, D.; Zheng, Q.; Tang, C.; Chen, S.-C.; Yin, Z. *ACS Macro Letters* **2013,** 2, (7), 605-608.
323. Li, H.; Sun, S.; Mhaisalkar, S.; Zin, M. T.; Lam, Y. M.; Grimsdale, A. C. *Journal of Materials Chemistry A* **2014,** 2, (42), 17925-17933.
324. Nielsen, C. B.; Ashraf, R. S.; Treat, N. D.; Schroeder, B. C.; Donaghey, J. E.; White, A. J. P.; Stingelin, N.; McCulloch, I. *Advanced Materials* **2015,** 27, (5), 948-953.
325. Lee, W.; Choi, H.; Hwang, S.; Kim, J. Y.; Woo, H. Y. *Chemistry – A European Journal* **2012,** 18, (9), 2551-2558.
326. Guo, X.; Quinn, J.; Chen, Z.; Usta, H.; Zheng, Y.; Xia, Y.; Hennek, J. W.; Ortiz, R. P.; Marks, T. J.; Facchetti, A. *Journal of the American Chemical Society* **2013,** 135, (5), 1986-1996.
327. Guo, X.; Kim, F. S.; Jenekhe, S. A.; Watson, M. D. *Journal of the American Chemical Society* **2009,** 131, (21), 7206-7207.
328. Beljonne, D.; Pourtois, G.; Silva, C.; Hennebicq, E.; Herz, L. M.; Friend, R. H.; Scholes, G. D.; Setayesh, S.; Müllen, K.; Brédas, J. L. *Proceedings of the National Academy of Sciences* **2002,** 99, (17), 10982-10987.
329. Brédas, J. L.; Street, G. B.; Thémans, B.; André, J. M. *The Journal of Chemical Physics* **1985,** 83, (3), 1323-1329.
330. Street, R. A.; Northrup, J. E.; Salleo, A. *Physical Review B* **2005,** 71, (16), 165202.
331. Li, Y.; Lee, T. H.; Park, S. Y.; Uddin, M. A.; Kim, T.; Hwang, S.; Kim, J. Y.; Woo, H. Y. *Polymer Chemistry* **2016,** 7, (28), 4638-4646.
332. Lee, W.; Kim, G.-H.; Ko, S.-J.; Yum, S.; Hwang, S.; Cho, S.; Shin, Y.-H.; Kim, J. Y.; Woo, H. Y. *Macromolecules* **2014,** 47, (5), 1604-1612.
333. Minnaert, B.; Burgelman, M. *Progress in Photovoltaics: Research and Applications* **2007,** 15, (8), 741-748.
334. Kirkpatrick, J.; Nielsen, C. B.; Zhang, W.; Bronstein, H.; Ashraf, R. S.; Heeney, M.; McCulloch, I. *Advanced Energy Materials* **2012,** 2, (2), 260-265.
335. Deng, P.; Liu, L.; Ren, S.; Li, H.; Zhang, Q. *Chemical Communications* **2012,** 48, (55), 6960-6962.
336. Choi, H.; Ko, S.-J.; Kim, T.; Morin, P.-O.; Walker, B.; Lee, B. H.; Leclerc, M.; Kim, J. Y.; Heeger, A. J. *Advanced Materials* **2015,** 27, (21), 3318-3324.
337. Gomez, E. D.; Barteau, K. P.; Wang, H.; Toney, M. F.; Loo, Y.-L. *Chemical Communications* **2011,** 47, (1), 436-438.
338. Blom, P. W. M.; de Jong, M. J. M.; van Munster, M. G. *Physical Review B* **1997,** 55, (2), R656-R659.
339. Kyaw, A. K. K.; Wang, D. H.; Gupta, V.; Leong, W. L.; Ke, L.; Bazan, G. C.; Heeger, A. J. *ACS Nano* **2013,** 7, (5), 4569-4577.
340. Lu, L.; Yu, L. *Advanced Materials* **2014,** 26, (26), 4413-4430.
341. Li, Y. *Accounts of Chemical Research* **2012,** 45, (5), 723-733.
342. He, Z.; Zhong, C.; Su, S.; Xu, M.; Wu, H.; Cao, Y. *Nature Photonics* **2012,** 6, 591.
343. Dou, L.; You, J.; Hong, Z.; Xu, Z.; Li, G.; Street, R. A.; Yang, Y. *Advanced Materials* **2013,** 25, (46), 6642-6671.
344. Zhou, H.; Yang, L.; You, W. *Macromolecules* **2012,** 45, (2), 607-632.
345. Fan, Q.; Liu, Y.; Xiao, M.; Su, W.; Gao, H.; Chen, J.; Tan, H.; Wang, Y.; Yang, R.; Zhu, W. *Journal of Materials Chemistry C* **2015,** 3, (24), 6240-6248.
346. Zhou, H.; Yang, L.; Price, S. C.; Knight, K. J.; You, W. *Angewandte Chemie* **2010,** 122, (43), 8164-8167.
347. Li, K.; Li, Z.; Feng, K.; Xu, X.; Wang, L.; Peng, Q. *Journal of the American Chemical Society* **2013,** 135, (36), 13549-13557.
348. He, R.; Yu, L.; Cai, P.; Peng, F.; Xu, J.; Ying, L.; Chen, J.; Yang, W.; Cao, Y. *Macromolecules* **2014,** 47, (9), 2921-2928.

349. Liu, D.; Zhao, W.; Zhang, S.; Ye, L.; Zheng, Z.; Cui, Y.; Chen, Y.; Hou, J. *Macromolecules* **2015,** 48, (15), 5172-5178.
350. Fan, Q.; Xiao, M.; Liu, Y.; Su, W.; Gao, H.; Tan, H.; Wang, Y.; Lei, G.; Yang, R.; Zhu, W. *Polymer Chemistry* **2015,** 6, (23), 4290-4298.
351. Wang, E.; Hou, L.; Wang, Z.; Hellström, S.; Zhang, F.; Inganäs, O.; Andersson, M. R. *Advanced Materials* **2010,** 22, (46), 5240-5244.
352. Su, W.; Xiao, M.; Fan, Q.; Zhong, J.; Chen, J.; Dang, D.; Shi, J.; Xiong, W.; Duan, X.; Tan, H.; Liu, Y.; Zhu, W. *Organic Electronics* **2015,** 17, (Supplement C), 129-137.
353. Chen, H.-C.; Chen, Y.-H.; Liu, C.-H.; Hsu, Y.-H.; Chien, Y.-C.; Chuang, W.-T.; Cheng, C.-Y.; Liu, C.-L.; Chou, S.-W.; Tung, S.-H.; Chou, P.-T. *Polymer Chemistry* **2013,** 4, (11), 3411-3418.
354. Zhang, M.; Guo, X.; Zhang, S.; Hou, J. *Advanced Materials* **2014,** 26, (7), 1118-1123.
355. Dutta, G. K.; Kim, T.; Choi, H.; Lee, J.; Kim, D. S.; Kim, J. Y.; Yang, C. *Polymer Chemistry* **2014,** 5, (7), 2540-2547.
356. Dang, D.; Chen, W.; Himmelberger, S.; Tao, Q.; Lundin, A.; Yang, R.; Zhu, W.; Salleo, A.; Müller, C.; Wang, E. *Advanced Energy Materials* **2014,** 4, (15), 1400680-n/a.
357. Li, J.; Grimsdale, A. C. *Chemical Society Reviews* **2010,** 39, (7), 2399-2410.
358. Cheng, Y.-J.; Wu, J.-S.; Shih, P.-I.; Chang, C.-Y.; Jwo, P.-C.; Kao, W.-S.; Hsu, C.-S. *Chemistry of Materials* **2011,** 23, (9), 2361-2369.
359. Kim, J.; Yun, M. H.; Kim, G.-H.; Lee, J.; Lee, S. M.; Ko, S.-J.; Kim, Y.; Dutta, G. K.; Moon, M.; Park, S. Y.; Kim, D. S.; Kim, J. Y.; Yang, C. *ACS Applied Materials & Interfaces* **2014,** 6, (10), 7523-7534.
360. Kim, Y.; Yeom, H. R.; Kim, J. Y.; Yang, C. *Energy & Environmental Science* **2013,** 6, (6), 1909-1916.
361. Zhou, H.; Yang, L.; Stoneking, S.; You, W. *ACS Applied Materials & Interfaces* **2010,** 2, (5), 1377-1383.
362. Gu, C.; Xiao, M.; Bao, X.; Han, L.; Zhu, D.; Wang, N.; Wen, S.; Zhu, W.; Yang, R. *Polymer Chemistry* **2014,** 5, (22), 6551-6557.
363. Kim, J.; Yun, M. H.; Kim, G.-H.; Kim, J. Y.; Yang, C. *Polymer Chemistry* **2012,** 3, (12), 3276-3281.
364. Kim, G.; Han, A. R.; Lee, H. R.; Oh, J. H.; Yang, C. *Physical Chemistry Chemical Physics* **2015,** 17, (40), 26512-26518.
365. Lee, J.; Han, A. R.; Yu, H.; Shin, T. J.; Yang, C.; Oh, J. H. *Journal of the American Chemical Society* **2013,** 135, (25), 9540-9547.
366. Kim, B.; Yeom, H. R.; Yun, M. H.; Kim, J. Y.; Yang, C. *Macromolecules* **2012,** 45, (21), 8658-8664.
367. Zhou, H.; Yang, L.; Stuart, A. C.; Price, S. C.; Liu, S.; You, W. *Angewandte Chemie* **2011,** 123, (13), 3051-3054.
368. Stuart, A. C.; Tumbleston, J. R.; Zhou, H.; Li, W.; Liu, S.; Ade, H.; You, W. *Journal of the American Chemical Society* **2013,** 135, (5), 1806-1815.
369. Sze, S. M.; Ng, K. K., Physics and Properties of Semiconductors—A Review. In *Physics of Semiconductor Devices*, John Wiley & Sons, Inc.: 2006; pp 5-75.
370. Yun, M. H.; Lee, E.; Lee, W.; Choi, H.; Lee, B. R.; Song, M. H.; Hong, J.-I.; Kwon, T.-H.; Kim, J. Y. *Journal of Materials Chemistry C* **2014,** 2, (47), 10195-10200.
371. Hoke, E. T.; Vandewal, K.; Bartelt, J. A.; Mateker, W. R.; Douglas, J. D.; Noriega, R.; Graham, K. R.; Fréchet, J. M. J.; Salleo, A.; McGehee, M. D. *Advanced Energy Materials* **2013,** 3, (2), 220-230.
372. Ren, G.; Schlenker, C. W.; Ahmed, E.; Subramaniyan, S.; Olthof, S.; Kahn, A.; Ginger, D. S.; Jenekhe, S. A. *Advanced Functional Materials* **2013,** 23, (10), 1238-1249.
373. Kim, J. Y.; Lee, K.; Coates, N. E.; Moses, D.; Nguyen, T.-Q.; Dante, M.; Heeger, A. J. *Science* **2007,** 317, (5835), 222-225.
374. Park, S. H.; Roy, A.; Beaupré, S.; Cho, S.; Coates, N.; Moon, J. S.; Moses, D.; Leclerc, M.; Lee, K.; Heeger, A. J. *Nature Photon.* **2009,** 3, (5), 297-302.
375. Chen, H.-Y.; Hou, J.; Zhang, S.; Liang, Y.; Yang, G.; Yang, Y.; Yu, L.; We, Y.; Li, G. *Nature*

Photon. **2009,** 3, (11), 649-653.
376. Cabanetos, C. m.; Labban, A. E.; Bartelt, J. A.; Douglas, J. D.; Mateker, W. R.; Fréchet, J. M. J.; McGehee, M. D.; Beaujuge, P. M. *J. Am. Chem. Soc.* **2013,** 135, (12), 4656-4659.
377. Scharber, M. C.; Mühlbacher, D.; Koppe, M.; Denk, P.; Waldauf, C.; Heeger, A. J.; Brabec, C. H. *Adv. Mater.* **2006,** 18, (6), 789-794.
378. Blouin, N.; Michaud, A.; Leclerc, M. *Adv. Mater.* **2007,** *19* (17), 2295-2300.
379. Zhao, G.; He, Y.; Li, Y. *Adv. Mater.* **2010,** 22, (39), 4355-4358.
380. Blouin, N.; Michaud, A.; Gendron, D.; Wakim, S.; Blair, E.; Neagu-Plesu, R.; Michel, B. t.; Durocher, G.; Tao, Y.; Leclerc, M. *J. Am. Chem. Soc.* **2008,** 130, (2), 732-742.
381. Cheng, Y.-J.; Yang, S.-H.; Hsu, C.-S. *Chem. Rev.* **2009,** 109, (11), 5868-5923.
382. Sun, Y.; Takacs, C. J.; Cowan, S. R.; Seo, J. H.; Gong, X.; Roy, A.; Heeger, A. J. *Adv. Mater.* **2011,** 23, (19), 2226-2230.
383. Chu, T.-Y.; Alem, S.; Tsang, S.-W.; Tse, S.-C.; Wakim, S.; Lu, J.; Dennler, D.; Waller, D.; Gaudiana, R.; Tao, Y. *Appl. Phys. Lett.* **2011,** 98, (25), 253301-203303.
384. Wang, X.; Sun, Y.; Chen, S.; Guo, X.; Zhang, M.; Li, X.; Li, Y.; Wang, H. *Macromolecules* **2012,** 45, (3), 1208-1216.

Chapter 10. Acknowledgements

Since beginning of my research in UNIST, I'm pleased to thank the many people who help me to complete my Master & Ph.D course.

First of all, I gratefully thank my advisor, Prof. Jin Young Kim to give me encouragement and compliment during my Master & Ph. D course. I am also thankful and would like to acknowledge my committee members, Prof. Hyunhyub Ko, Prof. Myoung Hoon Song, Prof. Tae-Hyuk Kwon, and Prof. Han Young Woo (Korea Univ.), to give me good directions and advices. They deserve my deepest appreciation because of their devoted help and support including professional discussions and collaboration opportunities. Moreover, I also feel gratitude to Prof. Changduk Yang and Prof. Hongsuk Suh (PNU) for helpful, assistance and encouragement.

In addition, I would like to thank all NGEL members for their help for my study. In addition, I would like to express my thanks to, Prof. Hyosung Choi (Han Yang Univ.), Dr. Seo-Jin Ko (UCSB), Prof. Bo Ram Lee (PKNU), Dr. Jae Hwan Chu(UCSB), Dr. Gyoungsik Kim (LG Chem) and OPOL members as well as ATOMS members.

Lastly, I wish to express my love and gratitude to my family whom have provided great mental support during this journey. It was truly with their endless love and encouragement that I could come this far. If it had not been for help from everyone, I could not have made great achievement and finished my M.S & Ph. D program in seven years.

I will always cherish the time at UNIST as a precious memory and a great part of my life.
I would like to really thank everyone once more.

감사의 글

어느덧 논문을 마치고 감사의 글을 쓰려고 하니 감회가 참 새로운 것 같습니다. 선배들의 졸업논문이 하나둘씩 책장을 채워지는 것을 보며 마냥 부럽기도 하고 아쉬워하던 NGEL의 막내였던 제가 어느새 실험실 선배가 되어 졸업한다는 사실이 아직 실감이 되지 않는 것 같습니다. 에너지 분야에 관심이 많았던 저는 친구를 통해 처음 UNIST라는 학교를 알게 되고 지금의 지도교수님이신 김진영 교수님과의 면담을 통해서 '열심히 하면 된다' 라는 말씀과 함께 저의 유니스트에서의 대학원 생활을 시작된 것 같습니다. 학부 전공이 달랐던 저에게는 교수님의 말씀이 남들보다 더 열심히 해야 되겠다는 자극제가 되었고 지금의 제가 될 수 있었던 것 같습니다. 수업시간때 교수님께서 '우리랩은 진정한 융합된 실험실이다 생명공학과 출신도 있다.'라며 하셨던 말씀이 저에게 해이해지지 않고 꾸준히 대학원 생활을 마칠 수 있게 해준 밑거름이 되었던 것 같습니다.

다사다난했던 7년간의 대학원 생활동안 부족한 저에게 지도교수님이신 김진영 교수님의 뛰어난 지도력과 따뜻한 격려에 대해 다시 한번 감사의 인사를 드리고 싶습니다. 또한 연구적으로 많은 조언과 지도를 해주신 고현협 교수님, 송명훈 교수님, 권태혁 교수님, 우한영 교수님, 양창덕 교수님께도 감사하다는 말씀을 전합니다. 물론 UNIST에서 제일 좋은 실험실이라 얘기할 수 있는 저희 실험실과 NGEL 멤버들의 도움 덕분에 잘 마무리할 수 있었던 것 같습니다. 더불어 유니스트의 최첨단 연구 시설과 활발한 공동연구 덕분에 저를 더욱 발전 시켜 준 것 같습니다.

박사과정 동안 동고동락했던 유니스트 모든 연구실 분들께 감사의 인사를 전합니다. 작은 부탁도 항상 친절하게 도와주시고 연구적 조언을 아낌없이 해주시는 브라이트 박사님, NGEL의 역사를 함께해 온 김박사님이 된 기환이행님, 합성에 이어 새롭게 소자를 연구하고 계신 이정훈 박사님, 묵묵히 자기일을 열심히 패로브 스카이트를 열심히 동갑 친구인 재기와 학범이, 연구에 누구보다 열정적이고 긍정적인 세영이, 박학다식하며 많은 도움을 주는 정우, 친절하게 부탁을 잘 들어주는 송이, 학부생때부터 같이 지낸 현재 NGEL의 랩짱인 택호와 UNIST대학원생 회장이 된 강택이, UPS 전문가가 된 영진이, 항상 열심히 일하는 나경이와 재원이, 엔젤 막내인 혜원이 윤섭이. 모두들 너무 감사합니다. 앞으로도 NGEL의 멤버로써 서로 잘 이끌어주며 좋은 연구 성과를 많이 내서 NGEL을 더욱 더 비상할 수 있도록 노력합니다. 그리고 먼저 졸업한 선배, 고등학교 친구이자 실험실 선배인 최효성 교수님(?), 실험실에서 가장 오래 동거동락하며 많은 도움

을 준 코코형 서진이형, 어느덧 엄마가 된 명희 그리고 다정하며 온화한 과학자 마인드를 가진 김성범 교수님 에게도 감사의 인사를 전합니다. 그리고 나의 동기이자 두 아이의 엄마가 되어 돌아올 혜림이, 뭐든지 친절하게 잘 알려주는 형민이형, 항상 많은 도움을 주는 교수가 된 이보람 교수님, 그리고 자주 커피 타임을 갖던 경식이, 규철이형, 지훈이형 한샘이형에게도 진심으로 감사드립니다. 또 유니스트가 맺어 준 인연인 승민이형, 재환이, 시혁이 등등 모두들 진심으로 감사합니다.

제가 어떤 선택과 결정을 하든 항상 저를 믿고 응원해준 저의 든든한 지원군! 아버지, 어머니, 동생에게 감사의 말씀을 전합니다. 그리고 학위 기간동안 항상 옆에서 묵묵히 불평없이 도와준 여자친구 세화에게도 감사의 말을 전합니다.

여러분들의 큰 도움이 없었다면 지금의 저는 없었다고 생각합니다. 지금까지 여러분께 받은 크나큰 감사함에 조금이나마 보답할 수 있도록 노력하겠습니다. 다시 한 번 진심으로 감사 드립니다.

김태효 올림